Finite Element Analysis of RC Walls with Complex Configurations

Kamal A. Ahmed

A dissertation
submitted in partial fulfillment of the
requirements for the degree of

Doctor of Philosophy

University of Washington

2021

Reading Committee:

Laura N. Lowes, Chair

Dawn E. Lehman, Chair

Michael Motley

Paolo M. Calvi

Program Authorized to Offer Degree:
Department of Civil & Environmental Engineering

University of Washington

Abstract

Finite Element Analysis of RC Walls with Complex Configurations

Kamal A. Ahmed

Co-Chairs of the Supervisory Committee:
Professor Laura N. Lowes
Civil & Environmental Engineering

Professor Dawn E. Lehman
Civil & Environmental Engineering

Slender RC walls are used commonly in mid- and high-rise buildings to resist lateral loads arising from earthquakes and wind forces. To accommodate architectural constraints, facilitate construction, and maximize structural efficiency, the majority of these walls have complex configurations, comprising planar and non-planar wall elements that often include regular or irregular patterns of openings. To date most laboratory testing of slender RC walls has employed wall specimens with relatively simple configurations and without openings and coupling action which provides only limited understanding of the impact on performance of the variations in configuration and reinforcement detailing observed in real-world construction.

This study here employed nonlinear high resolution numerical model to improve understanding of the behavior of walls with complex configurations and support recommendations for design of these systems. Planar wall data were used to calibrate the continuum-type modeling approach; experimental data characterizing the response of non-planar walls and walls with openings are used to validate the model.

A broad parametric study was conducted using the validated model for both non-planar walls and walls with openings. Simulated stress, strain, and damage fields are used to provide improved understanding of wall response and failure mechanisms. Simulation and

experimental data support recommendations for design of complex wall systems.

TABLE OF CONTENTS

LIST OF FIGURES

Figure Number Page

LIST OF TABLES

Table Number Page

LIST OF SYMBOLS

ALR: axial load ratio (%), where the applied axial load is normalized by $A_g f'_c$

A_{cv}: gross area of concrete section bounded by web thickness and length of section in the direction of shear force considered in the case of walls, mm^2

A_s: area of steel reinforcement crossing the concrete surface, mm^2

A_g: gross area of concrete section, mm^2. For a section with openings, A_g is the area of the concrete only and does not include the area of the opening(s)

a_g: maximum aggregate size, mm

b_f: flange width in tension, mm

b'_f: flange width in compression, mm

c: depth neutral axis

c: parameter that controls the hardening/softening for the Menetrey and Willam yield surface, $c \in \langle 0, 1 \rangle$

c_{ACI}: location of neutral axis from the extreme compressive fiber according to ACI 318-19 code

c_{FEM}: location of neutral axis from the extreme compressive fiber in numerical simulation

C_{ts}: residual tensile strength to the concrete, MPa

COV: coefficient of variation

CSAR: cross-sectional aspect ratio defined as ℓ_w/t_w

CSAR$_{\text{cp}}$: cross-sectional aspect ratio of compression pier next to an openings defined as $\ell_{\text{cp}}/t_{\text{cp}}$

e: parameter that defines the smoothness of the failure surface, $e \in \langle 0.5, 1.0 \rangle$

$\mathbf{E}$: elasticity tensor

E'^{cr}: crack stiffness

E_c: Elastic modulus, MPa

f'_c: compressive strength of concrete, MPa

f'_{co}: onset of nonlinear behavior for Menetrey and Willam model, MPa

f'_t: tensile strength of concrete, MPa

F^p: failure surface developed by Menetrey and Willam

$G(\sigma)$: flow rule

$G^p(\sigma)$: return direction for the flow rule

h_{eff}: effective wall height, defined as the constant ratio between the base moment and base shear

I_1: first invariant of stress tensor

J_2: second invariant of stress tensor

ℓ_w: length of entire wall, or length of wall segment considered in direction of shear force, mm

ℓ_{cp}: length of wall pier in compression (considered in direction of shear force), mm

L_c: parameter representing the projection of the element size into the direction of minimal principal stresses (characteristic length of finite element mesh in compression), mm

M_b: base moment resisted by the wall, N.mm

M_n: nominal moment strength for the base section, defined by the extreme compression fiber strain in the boundary element core reaching a strain value of -0.003, N.mm

NC2: ATENA concrete constitutive model "NonLinearCementitious2"

P: axial load, N

Shear span: $M_b/(V_b\ell_w) = h_{\text{eff}}/\ell_w$

Sigma ZZ: vertical stress, MPa

S_F: shear factor coefficient that defines a relationship between the normal and shear crack stiffness

s_{ho}: center-to-center horizontal spacing between openings, mm

t_f: thickness of flange, mm

t_w: thickness of wall, mm

t_{cp}: thickness of wall pier in compression (considered in direction of shear force), mm

V_b: base shear resisted by the wall, N

$V_{\max}$: peak base shear, N

w: maximum crack width, mm

W_d: concrete plastic displacement at zero compressive stress, mm

β: defines the return direction (dilation parameter)

$\Delta\varepsilon$: increments of strain

$\Delta\varepsilon_p$: increments of plastic strain

$\Delta\varepsilon_f$: increments of fracturing strain

Δ_u: maximum displacement reached by the specimen at which the lateral load carrying capacity of the wall drops to 80% if the historic maximum, mm

Δ_{vert}: displacement in the vertical direction, mm

Δ_y: specimen displacement at section yield, mm

ε: strain

ε_c^p: strain at compressive length L_c

ε_e: elastic strain

ε_{eq}^p: equivalent plastic strain

ε_f: fracture strain

ε_p: plastic strain

ε_u: steel fracture strain

ε_y: steel yield strain

θ: third Heigh-Vestergaard coordinate

ξ: first Heigh-Vestergaard coordinate

ρ: reinforcement ratio defined as the ratio of A_s to cross-sectional area

ρ: second Heigh-Vestergaard coordinate

ρ_{be}: longitudinal reinforcement ratio for the wall boundary element region

ρ_h: horizontal reinforcement ratio for the wall

ρ_t: transverse reinforcement ratio for the wall boundary element region

ρ_v: vertical reinforcement ratio for the wall

σ_n: new stress state, MPa

σ_{n-1}: stress state at previous stage, MPa

σ_{trial}: predictor stress state, MPa

ACKNOWLEDGMENTS

I would first like to express my sincerest gratitude to my advisers, Professor Laura N. Lowes and Professor Dawn E. Lehman, for the indispensable knowledge and support they provided during my studies. Since I first met them, they have always been thoughtful mentors, experienced advisers, and good friends to me for the past few years. There is no doubt that without their vision, inspirations, trust and patience, I could not have achieved any of the work presented herein. They showed me perfect examples of scholars and mentors that I wish to pursue in my upcoming career. Whenever I reflect on my time at the graduate school, I realize how fortunate I was to work with them.

I would like to sincerely thank my committee members, Professors Michael Motley, Paolo Calvi, and Tyler Sprague. It was a true honor for me to have these members in my committee. All of them are respected experts in my research field and gave me valuable advice and insights. Their suggestions and inputs helped this dissertation become more complete.

I would also like to extend my sincere gratitude to Ministry of Higher Education and Scientific Research at Kurdistan Regional Government in Kurdistan, Applied Technology Council, and University of Washington's Department of Civil & Environmental Engineering for their financial support of this research.

Without my mentors, colleagues, and family, I could not have completed my degree successfully. I would like to thank my friends and colleagues at the University of Washington, Han-Gyu Kim, Sarah Wichman, Andrew O. Winter, Eleonora Bruschi, Abbas Ganji, Alborz Ghofrani, Krishnendu Shekhar, Tianye (Andrew) Yang, Farnaz

Asl, and Chi-Pu (Tom) Lin for their great help throughout my graduate program. Thank you to Sevda Molani, Evan Apolis, Deborah Rohan, Jim Borgford-Parnell and Ken Yasuhara for your precious friendship and for making this journey an enjoyable experience for me.

Finally, I would like to thank my lovely family for giving me their support and love. I enjoyed endless support from my parents and my siblings.

DEDICATION

to my parents and my siblings

Chapter 1

INTRODUCTION

Slender reinforced concrete walls are used commonly in mid- and high-rise buildings to resist lateral loads arising from earthquakes and wind forces. To accommodate architectural constraints, facilitate construction, and maximize structural efficiency, the majority of these walls have complex configurations, comprising coupled planar and non-planar wall elements that often include regular or irregular patterns of openings. As building owners, building occupants, and communities seek both efficient structural designs that facilitate rapid construction as well as a high level of performance under earthquake and wind loading, it becomes critical to understand the load paths, response mechanisms, and damage patterns that develop in wall systems with complex configurations.

To date most laboratory testing of slender reinforced concrete walls has employed wall specimens with relatively simple configurations and without openings and coupling action. Fewer tests have investigated the more complex wall configurations found typically in modern buildings. For example, in one of the largest compilations of international laboratory test data for concrete walls, without openings and/or coupling action [1]; L, I and T–shaped walls represented only 20 percent of the data set, and data collection for the current study found only 52 laboratory tests in the last approximately three decades considering coupled walls and walls with openings. Given the many wall configurations found in real-world construction, existing laboratory testing provides only limited understanding of the impact on performance of the variations in configuration and reinforcement detailing observed in real-world construction. Additional research is required to improve understanding of the behavior of walls will complex configurations; this study employs nonlinear finite element simulation to provide this understanding.

The current study employs nonlinear finite element analysis to improve understanding of the behavior of walls with complex configurations and support recommendations for design of these systems. An experimental data set comprising planar, non-planar and planar walls with openings is assembled by extending the planar wall dataset assembled by Lowes et al. [40]. Planar wall data are used to calibrate a continuum-type modeling approach employing the ATENA (2019) software; experimental data characterizing the response of non-planar walls and walls with openings are used to validate the model. Simulated stress, strain, and damage fields are used to provide improved understanding of wall response and failure mechanisms. Simulation and experimental data support recommendations for design of complex wall systems.

1.1 Research Objectives and Activities

This PhD Research effort comprises (1) validation of the FEM approach for simulation of the response of non-planar walls and walls with openings subjected to lateral and axial loading via comparison of simulated and measured response data, (2) application of validated modeling approach to investigate the impact of configuration and design parameters on the response of non-planar walls and walls with openings, and (3) recommendations for design

1.2 Outline of Document

Chapter 2 introduces the finite element program used for this study. Chapter 3 presents some previous experimental work and a comprehensive numerical study of the non-planar walls and a discussion of the observations versus measured results. The study includes validation of the commercial software used for the purpose of analyses. Chapter 4 presents several previous experimental work for walls with openings and validation of the software platform used for the analyses. Chapter 5 presents a parametric study to recognize impacts of flanges, length of confined region, axial load ratio and shear stress demand on the performance of non-planar walls. Chapter 6 includes a detailed design procedure used for the design of planar walls with openings following the requirements of the ASCE 7-16 and ACI 318-14 codes and presents a parametric study to recognize impacts of vertical irregularity, opening size and arrangement, axial load ratio and shear stress demand on the performance of walls with openings. Ultimately, Chapter 7 presents conclusions based on the study results and proposes design recommendations and future work.

Chapter 2

FINITE ELEMENT ANALYSIS OF RC WALLS

2.1 Introduction

This chapter presents the continuum-type finite element modeling approach used in the current study to investigate reinforced concrete wall behavior; this chapter includes also a review of previous research employing finite element modeling to provide a basis for the current research approach. Section 2.2 presents previous research studies, and Section 2.3 presents the finite element analysis approach used in the current study. Both sections include discussion of software platforms, modeling approaches for simulation, the response of reinforced concrete walls, element formulations, concrete and other material models, and approaches for considering geometric nonlinearity.

2.2 Previous Researches by Others Addressing Different Modeling Approaches

This section identifies the different modeling approaches that have been used for walls and links these different approaches to the modeling approach employed in this study as explained in Section 2.3. This section is not a comprehensive review, however, it includes representative versions of multiple types of models including beam-column elements, plane stress elements, layered shell elements and solid elements.

2.2.1 Orakcal and Wallace (2006)

Orakcal and Wallace [51] formulated, implemented in OpenSees and calibrated a nonlinear macro-model (Multiple-Vertical-Line-Element Model (MVLEM)) using experimental results for RC walls having slender aspect ratios.

The MVLEM model consists of a spring at the center of rotation of the element measured relative to dimension ch (shown in Figure 2.1a). This spring is responsible for shear response of the wall and it is independent of the flexural deformation (i.e, shear strength and deformation are no influenced by bending deformations). A sequence of micro-fibers (uniaxial elements) are responsible for the flexural response. The micro-fibers are connected to rigid beams on both ends. The wall model consists of several elements stacked on top of each other as shown in Figure 2.1b.

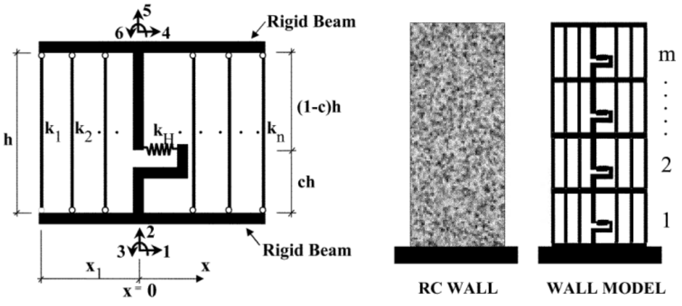

(a) (b)

Figure 2.1: Multiple-vertical-line-element model, (a) MVLEM element and (b) model of wall [51].

Orakcal and Wallace calibrated the model for simulating slender planar and non-planar wall response using data from two specimens (RW2 and TW2) tested by Thomsen and Wallace [59]. Specimen RW2 had a planar cross-section and Specimen TW2 had a T–shaped cross-section.

While Orakcal and Wallace show that the MVLEM model provides a relatively efficient and robust approach to simulating wall response, there are several features of the model that make it inappropriate for the current study. First, like traditional fiber-type beam-column elements, the MVLEM formulation ignores flexure-shear interaction and assumes plane sections remain plane with a linearly varying vertical strain field. Thus, this element formulation cannot be used to investigate the impact of shear on flexural deformation capacity or effective flange width which is a simplification used to represent the impact of nonlinear vertical strain fields in the wall flanges.

2.2.2 Lee, Guan, Fragomeni, and Doh (2007)

Lee et al. [35, 36] employed nonlinear layered finite element method (LFEM) (layered shell elements) to study the behavior of RC wall panels with openings. The FE model employed degenerated shell elements that consisted of several layers. The layered shell includes layers for unconfined and confined concrete. Steel reinforcement in all directions were fully smeared with layers of analogous thicknesses. The construction of the layered system is shown in Figure 2.2. For each layer the stresses were assumed to be constant across the layer thickness and therefore, the stress distribution across the thickness of the structure is a stepwise estimation.

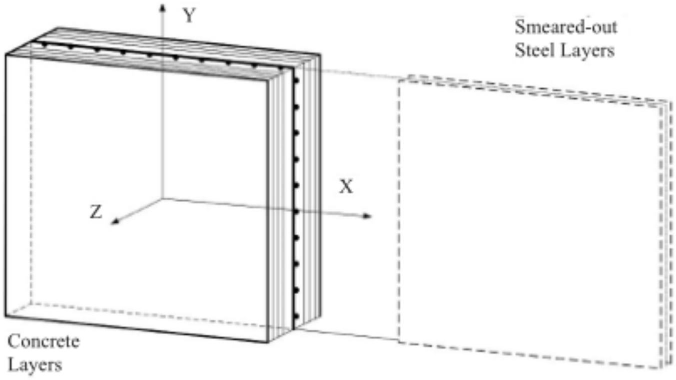

Figure 2.2: Construction of typical layered system [35, 36].

The numerical was validated using data from laboratory tests [25] for four wall panels with single opening and double horizontal openings different opening patterns and slenderness ratio subjected to axial in-plane loading with eccentricity to failure [25, 36]. According to Lee et al. the LFEM approach well predicted the strength, deflection and crack patterns of walls with openings tested in the laboratory.

Additionally, Lee et al. [35] tested thirty-five RC wall panels with different concrete strengths, slenderness ratios and patterns of openings and one- and two-way actions (see Figure 2.3). The experimental data were compared with simulations using the nonlinear layered finite element method (LFEM) that was developed by Lee et al. [36]. Lee et al. concluded that LFEM can accurately predict the strength of wall panels with openings (a mean ratio of 0.993 and a standard deviation of 0.141).

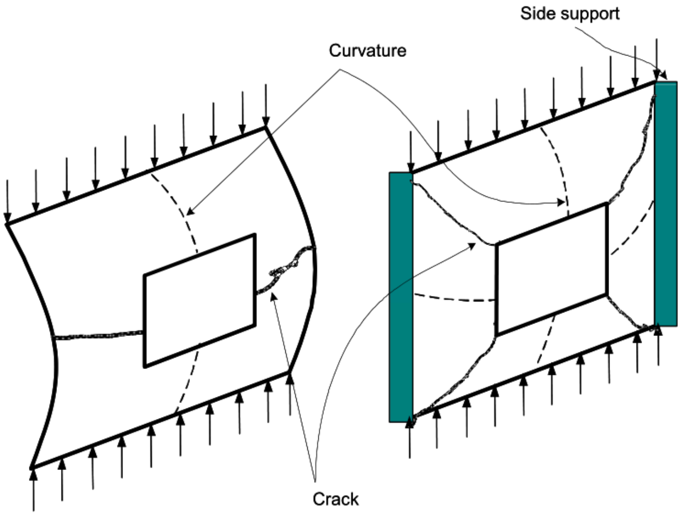

(a) One-way behavior **(b)** Two-way behavior

Figure 2.3: Behavior of axially loaded wall panels [35].

While Lee et al. show that the LFEM model provides a relatively efficient approach to simulating wall panel response, the model has not been tested for flexure-controlled RC walls subjected to axial and reversed cyclic lateral loading. The model is expected to well predict the nonlinear strain fields, however, the crushing of the concrete cannot be well predicted since confined and unconfined concrete material need to be defined rather than explicitly representing confinement and concrete expansion under compression loading. Thus, this element formulation cannot be used to investigate the impact of shear on flexural deformation capacity or effect of confinement on the performance of walls.

2.2.3 Lu, Xie, Guan, Huang, and Lu (2015)

Lu et al. [43] formulated, implemented in OpenSees and calibrated a multi-layer shell element (ShellMITC4) to simulate the behavior of RC shear walls. The elements are four-node shell elements and consist of multiple layers that are fully bonded in the out-of-plane direction. Each layer could have different thickness and material properties depending on the size and reinforcement distribution. The local coordinate system and details of the multi-layer element are shown in Figure 2.4. The reinforcing steel is smeared into one or multiple layers as shown in Figure 2.5.

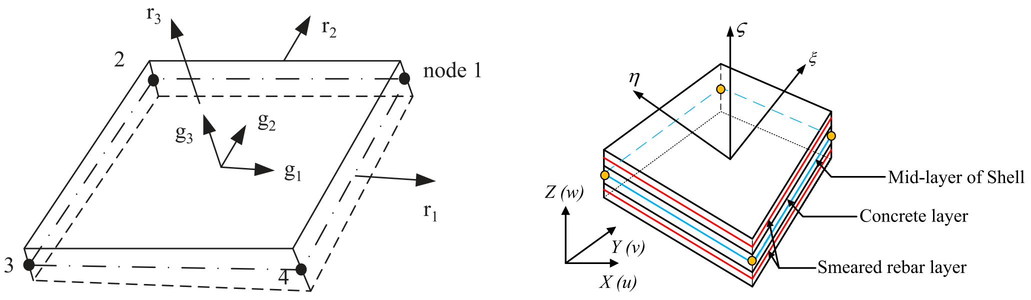

(a) Local cartesian coordinate system

(b) Multi-layer shell element

Figure 2.4: Local coordinate system and multi-layer shell element [43].

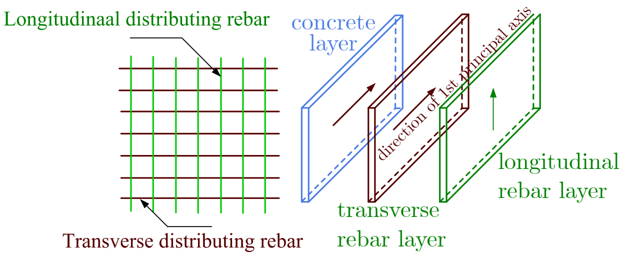

Figure 2.5: Distribution of the rebar layer.

A two-dimensional material constitutive model based on smeared crack model is used to simulate the behavior of concrete. The model assumes that the concrete is in the plane stress condition. The model treats concrete as an orthotropic material when cracks are formed due to the surpass of the principal tensile stress from concrete tensile strength. The displacements and rotations at the nodes are used to interpolate the strains and curvature at the in-plane integration points.

Lu et al. validated the model for simulating RC wall response using data from twelve planar specimens tested by Lu et al. [42] and six non-planar specimens (H– and T–shaped) presented by Chen [20], Lu and Chen [41], Lu et al. [43]. The specimens included a range of axial load ratios, aspect ratios, confinement lengths and reinforcement ratios. The results of the FE model were compared with the experiments for displacement and strength at yield and peak strength and according to Lu et al., the predictions were in good agreement with experimental results.

While Lu et al. show that the multi-layer shell element model provides a relatively efficient approach to simulating wall response, the model has not been tested for the deformation capacity and failure mode observed in the laboratory. Additionally, the model has not been tested for walls with openings subjected to axial and reversed cyclic lateral loading. Thus, this element formulation cannot be used to investigate the impact of shear on flexural deformation capacity or failure modes caused by bar buckling and failure modes influenced by shear in RC slender walls.

2.2.4 Kolozvari, Tran, Orakcal, and Wallace (2015)

Kolozvari et al. [32, 33] formulated, implemented and calibrated a nonlinear two-dimensional macroscopic fiber model called shear-flexure interaction multiple vertical line element model (SFI-MVLEM) using experimental results for RC walls having slender aspect ratios.

The SFI-MVLEM model replaces the macro-fiber (axial) elements that are responsible to capture the axial/flexural response in the MVLEM model [51] with RC panel elements that are under membrane actions. Figure 2.6 shows the SFI–MVLEM element. Coupling of the axial and shear fields enables coupling of axial/flexural and shear responses at the element level. Assuming plane sections remain plane and shear strain is uniform across the length of the wall, shear (γ_{xy}) and axial (ε_y) strains in the model are computed by nodes having six degrees of freedom at the top and bottom level of the element. Additional horizontal degrees of freedom are used to capture the axial strain in the horizontal direction assuming the resultant horizontal stress from both steel rebars and concrete is equal to zero. The model uses a cyclic two-dimensional constitutive relationship based on the fixed strut angle model (FSAM) and includes a shear-resistance mechanism along the crack surface to capture the RC panel response. Two independent models are employed to describe the aggregate interlock and dowel action in the SFI-MVLEM model.

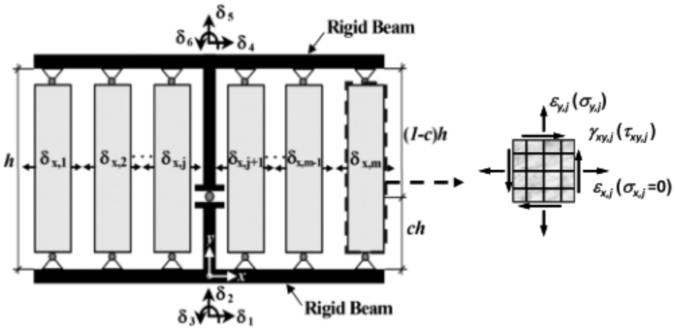

(a) **(b)**

Figure 2.6: SFI-MVLEM element [33].

Kolozvari et al. calibrated the model for simulating slender planar and non-planar wall response using data from five specimens tested by Tran [60]. Kolozvari et al. concluded that the model well simulated the coupling between nonlinear flexural and shear responses observed in the experiments. The model also accurately predicted the load-deformation responses including wall stiffness degradation and pinching. Kolozvari et al. acknowledged that since the model could not simulate the failure mechanisms observed in the laboratory that involves bar-buckling, lateral instability of the confined region and sliding shear near wall base, the strength deterioration observed in the tests were not captured.

While Kolozvari et al. show that the SFI-MVLEM model provides a relatively efficient and robust approach to simulating wall response, there are several features of the model that make it inappropriate for the current study. Like traditional fiber-type beam-column elements, the SFI-MVLEM formulation assumes plane sections remain plane with a linearly varying vertical strain field. Also, the model cannot predict the observed failure modes. Thus, this element formulation cannot be used to investigate the impact of shear on flexural deformation capacity or effective flange width which is a simplification used to represent the impact of nonlinear vertical strain fields in the wall flanges.

2.2.5 Niroomandi, Pampanin, Dhakal, and Soleymani Ashtiani (2016)

Niroomandi et al. [49] employed an FE model with layered curved shell elements in DIANA software package to simulate rectangular doubly reinforced concrete shear walls under bi-directional loading. For reinforcing bars embedded elements were used (see Figure 2.7). The simulations depicted walls under seismic loading. The main objective was to investigate the main parameters impact the performance of rectangular RC shear walls subjected to bi-directional lateral loading. Additionally, using the results of the study in addition to experimental data, the study aimed to make recommendations for design of walls under bi-directional loading and to assess existing walls.

The FE model was validated by comparing simulated load-deformation envelopes and failure mechanism with the experiments. Curved shell elements utilize iso-parametric degenerated solid methods that is based on two assumptions [49]: Straight-normals which assumes normals remain straight after deformation, and Zero-normal-stress which assumes the stress component in the normal direction is zero. Each node consists of five degrees of freedom (DOF) in the shell elements; three translational and two rotational DOFs as shown in Figure 2.7c and d

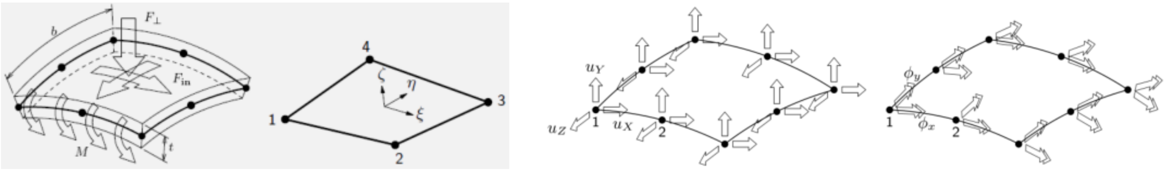

(a) (b) (c) (d)

Figure 2.7: Curved shell elements, **(a)** characteristics, **(b)** element Q20SH (DIANA), **(c)** translational displacements, and **(d)** rotational displacements [49].

Ultimately, Niroomandi et al. proposed a numerical model to simulate cyclic response of RC walls subjected to uni- and bi-directional loading.

While Orakcal and Wallace show that the curved shell model provides a relatively efficient approach to simulating wall response under uni- and bi-directional loading, there are several features of the model that make it inappropriate for the current study. First, the model ignores flexure-shear interaction and assumes plane sections remain plane with a linearly varying vertical strain field. The model also assumes the the element is under plane stress condition. Additionally, the model has not been tested for non-planar walls and walls with openings subjected to axial and reversed cyclic lateral loading. Thus, this element formulation cannot be used to investigate the impact of shear on flexural deformation capacity or effective flange width which is a simplification used to represent the impact of nonlinear vertical strain fields in the wall flanges.

2.2.6 Kolozvari, Miller, and Orakcal (2017)

Kolozvari et al. [34] developed and tested a nonlinear numerical model for analysis of RC walls in OpenSees [45]. The objective was to propose an FE modeling approach in OpenSees to accurately simulate nonlinear behavior of RC structural walls subjected to seismic loading.

The FE model is based on a plane stress constitutive model that is used for RC panels and utilizes a fixed crack approach for determining the onset of cracks. The model uses a four-node quadrilateral element formulations (Figure 2.8). The constitutive model called the

Fixed Strut Angle Model (FSAM). Concrete behavior is depicted using a uniaxial stress-strain relationship and it is applied in orthogonal directions. The orientation of principal stresses at first cracking establishes the orientation of the orthogonal 1D concrete constitutive model. Shear stress on the crack surface is modeled using a friction-based aggregate interlock model and it is combined with a linear-elastic model to account for dowel action on the steel rebars (Figure 2.9c and e). Reinforcing steel is modeled as embedded truss elements and assumed to be perfectly bonded to concrete (Figure 2.9d).

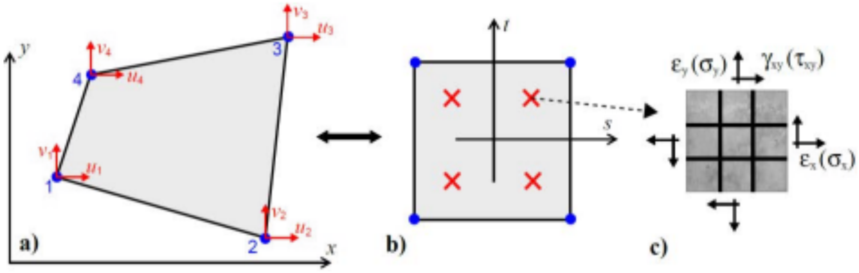

Figure 2.8: Four-node iso-parametric quadrilateral element, **(a)** actual element, **(b)** parent element, and **(c)** 2D constitutive material model FSAM [34].

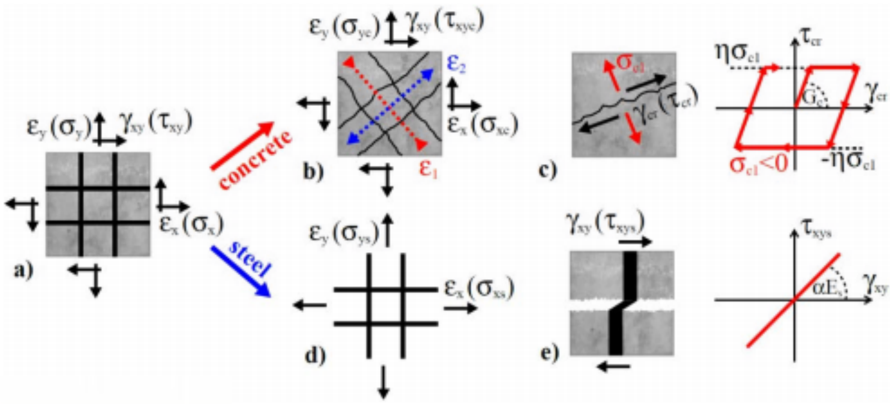

Figure 2.9: Behavior and modeling parameters of the constitutive RC panel model FSAM, **(a)** strain-stress field, **(b)** concrete biaxial behavior, **(c)** concrete shear aggregate interlock, **(d)** steel behavior, and **(e)** dowel action on reinforcement [34].

The FE model was validated by simulating the responses of two RC wall specimens that exhibit shear-flexure interaction. The model accurately predicted stiffness, stiffness deterioration, strength, hysteretic response history that was observed in the laboratory. The model also, accurately estimated nonlinear flexural and shear deformations [34].

Kolozvari et al. concluded that the proposed numerical model's depiction of localized response characteristics (strain and stress fields) are in reasonable agreements with the experiments.

2.2.7 Lowes, Lehman, and Whitman (2019)

A UW research team (Lowes et al. [40], Whitman [68]) employed the ATENA software package and high-resolution solid-element models to investigate the behavior of slender, planar concrete walls and develop recommendations for improving the performance of these walls. The ATENA model used solid elements for concrete and line elements for reinforcing bars and a perfect bond was assumed between concrete and reinforcing bars.

The numerical model was calibrated using experimental data from twenty-three planar wall tests; tests employed slender concrete walls for which strength loss resulted from one of three flexural failure modes: i) bar-buckling followed by bar rupture (BR), ii) concrete crushing and reinforcing bar buckling initiate in the extreme compression zone (CB), and iii) concrete crushing initiating at the interface of the lightly reinforced web region of the wall and the more heavily confined and reinforced boundary element region of the wall (CS failure). The calibrated model was used to perform a parametric study to investigate the impact of design parameters, including cross-sectional aspect ratio, shear stress demand, and axial load ratio on failure mode and ductility.

The research team [40, 68] concluded that failure mode and deformation capacity are influenced primarily by the cross-sectional aspect ratio and peak shear stress demand. The less ductile compression-shear (CS) failure is more likely when the wall has a large cross-sectional aspect ratio and high shear stress demand. Walls with lower cross-sectional aspect ratios and lower shear stress demands exhibit compression-buckling (CB) and buckling-rupture (BR) failure modes and increased ductility. Extending the confined boundary element region of the wall from the ACI Code requirement of half the neutral axis depth to the full neutral axis depth can push a wall that would be expected to exhibit a low-ductility CS failure to a higher ductility BR or CB failure mode. Additionally, walls failing in compression-buckling and buckling-rupture, exhibit similar deformation capacities.

This approach is a viable FE model for the current study since it can capture not only the design parameters such as stiffness, strength and deformation capacity, but it is also capable of simulating the shear-flexure interaction. The three-dimensional model is capable of simulating cracking and stiffness loss in tension, employs a multi-dimensional yield surface that enables simulation of strength and deformation capacity of confining pressure and is mesh independent. It can also simulate the failure mode.

2.2.8 Gullu and Orakcal (2021)

Gullu and Orakcal [26] presented a finite element approach called Strut-Angle Finite Element (FSAFE) model for nonlinear simulation of RC structural walls subjected to cyclic lateral loading. The model consists of rectangular four-node membrane elements that only possess in-plane translational degrees of freedom at each node. Stress field in each element is defined by a single Gauss integration point that results in a single average stress and corresponding strain field. FSAM formulation [34] was utilized to simulate constitutive axial/shear response in the plane-stress loading.

The FSAM model was modified for the membrane elements in FSAFE model. The first crack in the concrete occurs when the principal tensile strain in reaches cracking strain in concrete and the principal strain direction for the first crack is the “fixed strut”. It is assumed that the direction of the principal stresses in the concrete are fixed. No shear stress is assumed to be developing along the crack. When the second crack is developed, the single fixed-strut mechanism is over and a second fixed-strut is activated parallel to the crack in the model.

2.3 Finite Element Modeling and Analysis

Previous research by others has employed a number of different models to simulate the non-linear response of RC flexural walls [11, 53, 66, 67, 68]. In general, modeling approaches include *2D Beam-Column Elements*, *Shell and Membrane Elements* and *3D-Continuum Type Elements*. Line-element models are computationally efficient and are capable to accurately simulate response of flexure-controlled walls. However, previous research [9, 11, 53] have shown that line-element models poorly estimate the response of walls with flexure-shear interaction. Beam-column elements assume plane sections remain plane across the section. Also, a linear shear response is assumed in these models and higher shear demand does not affect flexural failure and higher axial load does not facilitate shear failure.

Shell and membrane element models (2D plane stress elements and layered shell elements) can simulate non-linear vertical strain distributions along the cross-section of walls and flexure-shear interaction using a 2D material model. Disadvantages of using these elements include definition of the response of confined and unconfined concrete by the user which can lead to an over or under prediction of the deformation capacity.

3D-Continuum Type elements unlike are computationally expensive but have advantages over 2D elements which include [11]:

- Simulation of non-linear vertical strain distribution on wall cross-sections.
- Accurate prediction of shear stiffness and onset of strength loss due to flexure-shear interaction by simulating flexure-shear interaction at the material level.
- Explicit simulation of confining provided by transverse reinforcement and additional strength and deformation capacity developed by confined concrete.
- Accurate prediction of stiffness, strength and deformation capacity.
- Enabling 3D elements to represent 3D geometry and loading.

Some finite element analysis software packages that support 3D modeling and include advanced three-dimensional constitutive models for concrete are ABAQUS, ADINA, ATENA, DIANA, LS-DYNA, and VecTor3. Whitman [68] compared ABAQUS and ATENA for modeling confined concrete prisms that represent the confined boundary regions in RC shear walls. A comprehensive comparison of many of the above software packages was conducted by Johnson [30]. ATENA software platform was selected for the purpose of this research study following the reviews made by Johnson [30] and Whitman [68].

The current study investigates the behavior and provides recommendations for design to achieve a high level of performance for reinforced concrete walls exhibiting flexure-controlled response and with non-planar configuration as well as configuration that include openings. On the basis of the literature review above, the ATENA software developed by Červenka Consulting was used for the current study. As discussed above,

1. the software has been shown to provide accurate simulation of wall response, including failure mode and deformation capacity, for walls exhibiting flexure and flexure-shear controlled behavior,

2. in comparison with other modeling approaches, the nonlinear solid-element modeling approach provided by the ATENA software minimizes the assumptions and simplifications introduced into the models and provides maximum generality of the model,

3. the research team has experience using this software, and

4. ATENA includes advanced pre- and post-processor tools that facilitates model building and visualization of simulation data including strain and stress fields, crack orientation, and crack width, . . . [11, 19, 40].

The objective of these analyses was to validate the software for simulation of stiffness, strength and deformation capacity of non-planar flexural walls as well as provide additional understanding of the mechanisms controlling behavior. The results of previous research [68] and pilot studies conducted for this project demonstrated that the software could not provide numerical robustness for the case of cyclic loading; thus, simulations in this study was limited to monotonic, uni-directional loading. This section below describes the finite element modeling approach employed for simulation purposes in this study.

2.3.1 ATENA

ATENA is a Finite Element software developed by Červenka Consulting for the non-linear analysis of reinforced concrete. It employs a sophisticated 3D concrete constitutive model that simulates concrete cracking, crushing as well as crack closure under cyclic loading. It also supports both 2D and 3D environments [11, 19, 40].

The modeling approach used for current study was calibrated and validated by Whitman [68] for planar walls. As part of this study the same modeling approach is validated and used for simulation of non-planar walls and walls with openings. Details of the model, configuration, mesh size, element type, material model calibration procedure are presented in the next section.

2.3.2 Model Definition

2.3.2.1 Model Configuration

Figure 2.10 shows the geometric layout and characteristic mesh scheme for the finite element models used in the study. To reduce computational demand and increase computational stability, the models employed different material constitutive models, levels of mesh refinement, and methods for modeling reinforcing steel in different regions of the test specimens where different levels of inelastic action were observed in the laboratory or expected in newly designed walls. Also, to reduce computational demand, symmetry was used to reduce mesh size for planar walls and non-planar walls subjected to loading parallel to the axis of symmetry. Figure 2.10) shows a typical wall model; modeling details for the different regions of the model were as follows:

- Regions 1 and 2 are the wall foundation and loading block where minimal inelastic action was observed in the laboratory. An elastic concrete material model and larger elements (element size approximately 10 in.) were used in these regions.

- Regions 3 and 4 are the boundary element and web regions of the wall where significant inelastic action could be expected and was observed in the laboratory. For walls without openings these regions are limited to the area above the wall-foundation interface; for walls with openings these regions comprise the entire specimen except the foundation and loading block (regions 1 and 2). Here, inelastic concrete and reinforcing steel material models were used and smaller element sizes were used, with elements sizes measuring approximately 50 mm (2 in.) and at least four elements were used to model the total thickness of the model. In these regions 90 percent of the reinforcing steel vertical reinforcing steel was modeled discretely, as embedded truss elements, and 10 percent of the reinforcement volume was modelled as "smeared" throughout the region. Providing a small percentage of smeared reinforcement was found to produce greater numerical stability [68].

    - In Region 3 (wall boundary element above the wall-foundation interface), 90 percent of the confining reinforcement was modeled discretely as embedded truss elements with 10 percent modeled as smeared reinforcement.

    - In Region 4 (wall web above the wall-foundation interface), horizontal reinforcement was modeled with 50 percent as discrete bars and 50 percent as smeared reinforcement; this approach was necessary to provide numerical stability given the low horizontal reinforcement ratio and significant inelastic action in this region.

- Regions 5 and 6 are the boundary element and web regions of the walls without openings, approximately half the length of the wall above the wall-foundation interface. In these regions a larger element size was used, with element lengths of approximately 100 mm (4 in.) and fewer than four elements were used to represent the thickness of the wall. Ninety percent of the vertical reinforcement was modeled discretely, as embedded truss elements, with 10 percent modeled as smeared reinforcement. Also in these regions, 100 percent of the horizontal and confining reinforcement was modeled as smeared to simplify model building; use of 100 percent smeared reinforcement was found to have no impact on simulated response.

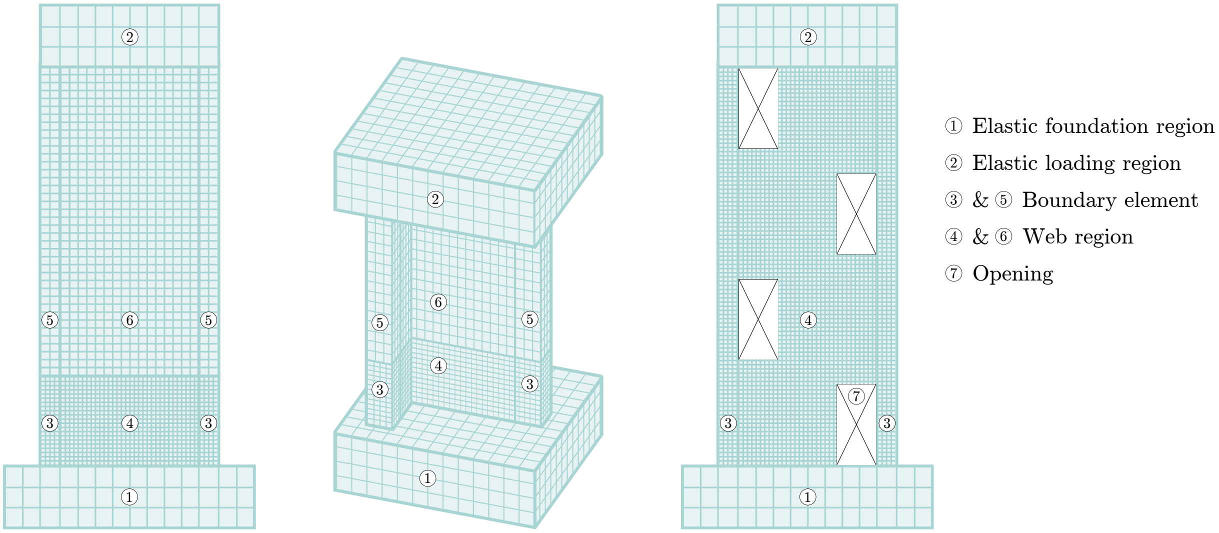

Planar solid wall

Non-planar wall

Wall with openings

Figure 2.10: Geometric layout and characteristic mesh scheme of the model.

2.3.2.2 Modeling Concrete Material Response using ATENA

There are multiple concrete constitutive models included in the ATENA software package. The `CC3DNonLinCementitious2` (NC2) was used because it simulates (1) cracking and stiffness loss in tension, (2) nonlinear compression response with a multi-dimensional yield surface that enables simulation of the impact on strength and deformation capacity of confining pressure, (3) crack closer under cyclic loading, and (4) softening in tension and compression using material regularization with user-defined fracture energy (tension) and deformation at strength loss (compression) to minimize mesh sensitivity. Figure 2.11 shows

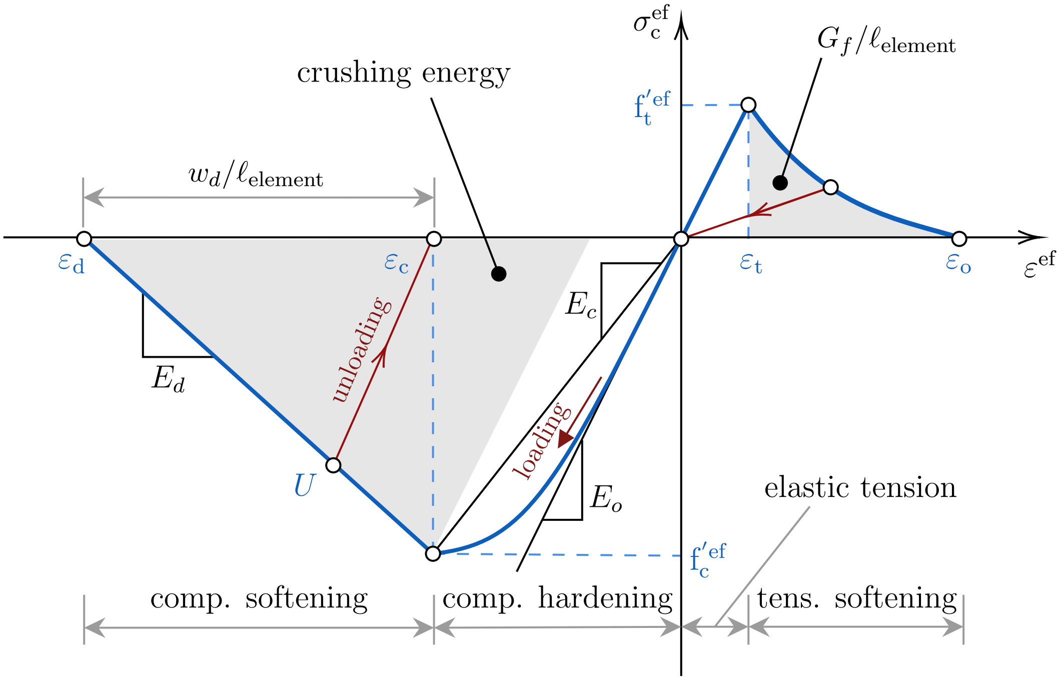

Figure 2.11: Uniaxial stress-strain law for concrete.

the uniaxial stress-strain model embedded in the ATENA NC2 model. In this figure (1) f_c' and f_t' are, respectively, the compressive and tensile strengths of concrete, (2) ε_d, and ε_o are, respectively, the compressive and tensile strains at which concrete strength is lost and are defined as a function of the element size to reduce mesh sensitivity, (3) ε_c is the compressive strain at peak compressive strength, and ε_t is the strain at peak tensile strength, (4) G_f is the fracture energy and W_d is the length beyond peak at which the peak strength reaches zero. Table A.1 tabulates list of concrete parameters used in ATENA analysis. Details of the model are presented in Appendix A and summarized here:

- Compression response is simulated using a multi-dimensional plasticity model with non-associated flow. The yield surface is defined by the Menetrey and Willam [47] yield surface, which provides accurate simulation of concrete strength under three-dimensional compressive loading; post-peak softening is defined on the basis of Van Mier 1986 [62].

Plastic flow is defined by the Drucker-Prager yield surface, which simulated volumetric expansion with compression softening. User-defined variables include uniaxial concrete compressive strength (f'_c), deformation at compressive strength loss (W_d), rate of volumetric expansion under compressive loading (β).

- Tension response is simulated using a continuum damage model, in which increasing post-peak strain reduces the elastic modulus in tension. The Rankine criteria determines onset of cracking; cracking may be simulated as fixed, rotating, or hybrid (initially rotating and switching to fixed when a user-specified level of tensile strength is reached). User-defined variables include fracture energy (G_f), crack spacing $s_{\max}$, and tension stiffening (c_{ts}).
- Shear on the crack surface
- Compression and tension response are linked via strain decomposition, with total strain assumed equal to elastic strain plus plastic strain plus an effective fracture strain normal to the crack surface, $\varepsilon_t = E_{\text{eff}}/\sigma$.

2.3.2.3 Modeling Steel Material Response and Concrete-Steel Bond in ATENA

The stress-strain response of reinforcing steel was defined on the basis of coupon test data provided by the researchers; the envelop was defined as multilinear curves. Neither bar buckling nor bar fracture was explicitly modeled. Reinforcing steel was assumed to be perfectly bonded to surrounding concrete with no slip at the bar-concrete interface.

2.3.2.4 Simulating Geometric Nonlinearity in ATENA

A series of preliminary analyses of a selection of walls from Table 3.1 indicated that load-displacement response simulated using updated Lagrangian and total Lagrangian approaches approximately identical. Thus, the updated Lagrangian approach was used for all analyses.

2.3.3 Boundary Conditions and Loading

In this study, walls are subjected to vertical (gravity) and lateral loading. Lateral Load is applied to the top layer of the wall, using displacement control; the load is applied as displacements to the top portion of the wall and it is usually applied to multiple nodes to achieve distributed loading rather than point load. Elements at the top of the wall are elastic to ensure that local stress concentrations associated with loading do not affect the results. If the wall has a moment applied to it in addition to the lateral load, then the height of the wall specimen is extended to the effective height of the applied shear load and lateral loading is applied as a shear load at the effective height.

For T– and C–shaped walls loaded perpendicular to the wall axis of symmetry, loading results in twisting, unless loading is applied at the shear center. However, nonlinear material response causes the shear center to move and makes it impractical to calculate the location of the shear center throughout the load history. To determine the best loading protocol for these asymmetric walls, a series of preliminary analyses were conducted for C– and T–shaped walls in which load was first applied, via displacement-controlled increments, to the four corners of the stiff, elastic loading block placed at the top of the laboratory specimen (Figure 2.12); for these initial analyses equal displacements perpendicular to the axis of symmetry was imposed at all load points on the loading block and rotation was restrained. A second series of analyses was conducted in which lateral load was applied via displacement control at the corners of the load block but the loading block was allowed to twist (Figure 2.13). Comparison of simulated and measured response indicated that the allowing rotation of the loading block resulted in the greatest similarity between simulated and measured load-displacement response (see Figure 2.14).

When the loading is applied in the direction of symmetry, application of the lateral load results in twisting of the cross-section unless the load is applied at the shear center. Because the wall responds nonlinearly, the shear center changes during analysis, and it is not possible to load through the shear center. Instead, loading is applied, via displacement-controlled

(a) T-shaped, asymmetrical cross-sections **(b)** C-shaped, asymmetrical cross-sections

Figure 2.12: Application of displacement-controlled loading in the asymmetrical direction with out plane constraints (top view). Note that gray square represents the load block at the top of most of the specimens.

(a) T-shaped, asymmetrical cross-sections **(b)** T-shaped, symmetrical cross-sections

(c) C-shaped, asymmetrical cross-sections **(d)** C-shaped, symmetrical cross-sections

Figure 2.13: Application of displacement-controlled loading in the symmetrical and asymmetrical directions used in the simulations (top view). Note that gray square represents the load block at the top of most of the specimens.

increments, at corners of the loading block at the top of the specimen and the corners of the loading block are restrained to prevent rotation as shown in Figure 2.12. However, when compared to the case without any restraints, it was observed that out-of-plane restraints cause additional strength in the simulation (see Figure 2.14). Thus, all the wall simulations were performed without any restraints as illustrated in Figure 2.13. More details are given on the results in Section 3.4.

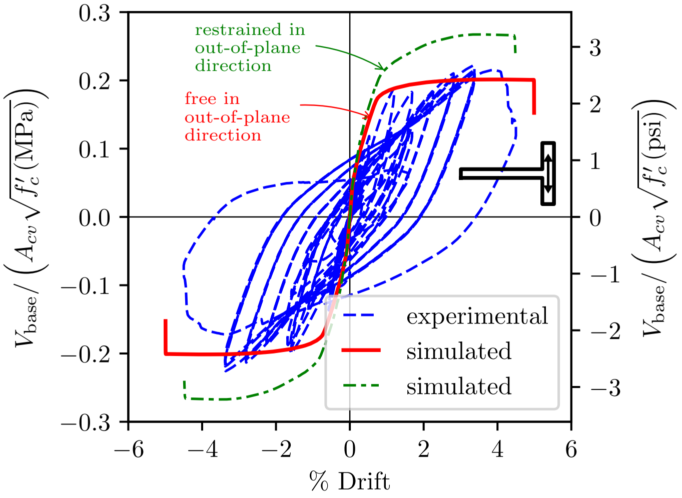

Figure 2.14: Load-deformation relationship for specimens NTW1 (tested by Brueggen), simulated for loading in the direction perpendicular to web, with and without restraint in the out-of-plane direction.

Gravity loads were applied uniformly over the top elastic region of the specimens in the simulations.

2.3.4 Cyclic Response

The wall specimens included in this study were all loaded cyclically in the laboratory, and after a few cycles the program fails to converge in the inelastic range. Multiple approaches were tried to achieve convergence under cyclic loading, including smaller step sizes, change of mesh size, employing different solution algorithms, recommendations provided by Cervenka Consulting [19] documentation, . . . ; however, none were successful. Figure 2.15 shows a simulated (ATENA) versus measured response history for specimen W2, tested by Liu [38]. Thus, all simulations employed monotonically increasing lateral displacement demand. Lowes et al. [40] and Whitman [68] showed that monotonic loading combined with non-simulated failure modes provided accurate simulation of failure mode and deformation capacity.

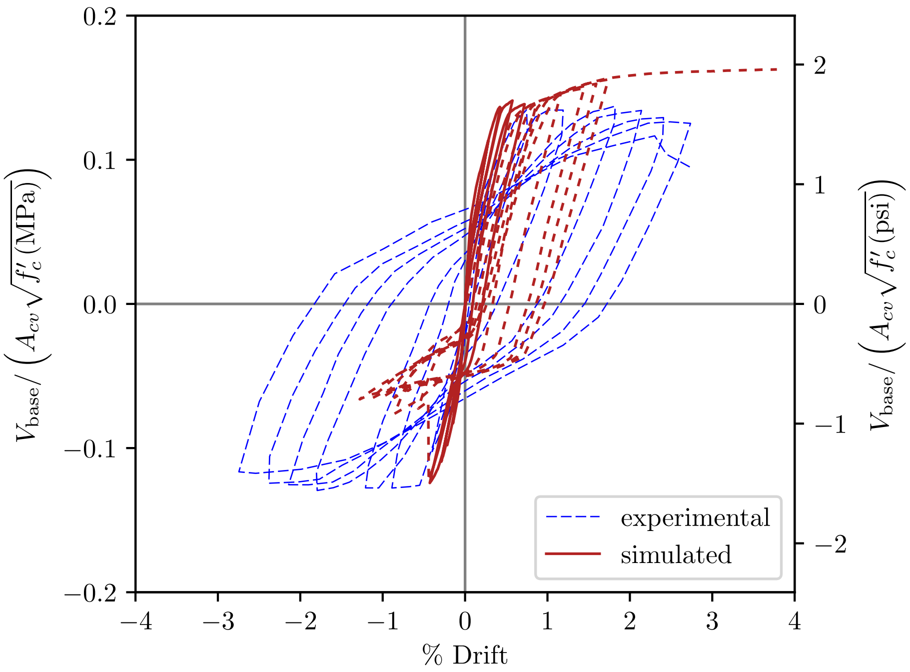

Figure 2.15: Cyclic response of wall specimen W2 (tested by Liu [38]) simulated in ATENA. (*Note*: simulated cyclic history includes unconverged points and shown in dashed lines).

2.3.5 Identifying Onset of Lateral Strength Loss and Failure Mode

Previous work by others [53, 68] shows that for flexural walls, loss of lateral load carrying capacity mainly is due to either *Compression-Buckling* (CB) failure, characterized by simultaneous crushing of boundary element concrete and buckling of boundary element longitudinal reinforcement, or *Buckling-Rupture* (BR) characterized by rupture of previously buckled longitudinal reinforcement. It is possible for the wall to respond in both shear and flexure and fail due to concrete crushing in the web and/or confined region. This failure is a *compression-shear* failure type. As the reinforcing steel model in ATENA does not simulate bar buckling, Whitman [68] established criteria for identifying the onset of lateral strength loss and the failure mechanism. These criteria are described below and listed in Table 2.1. In the paragraphs below and Table 2.1, ε_t is the simulated tensile strain in the boundary element longitudinal reinforcement at point of experimental wall failure (20% strength loss from peak strength) and $\varepsilon_{u,\mathrm{BE}}$ is the specified rupture strain of the boundary element reinforcement.

Case 1) Failure determined by simulated lateral strength loss in excess of 20% of maximum strength:

- If the concrete is crushed (i.e., minimum principal stress less than 30% of historic maximum) and $\varepsilon_t/\varepsilon_{u,\mathrm{BE}}$ is less than 33%, failure is classified as a CB type failure.
- If the concrete is crushed and $\varepsilon_t/\varepsilon_{u,\mathrm{BE}}$ is greater than 33%, it is necessary to consider the solution step at which $\varepsilon_t/\varepsilon_{u,\mathrm{BE}}$ equaled 33%. If the concrete was crushed at that point, failure is classified as a CB failure. If the concrete had not crushed, a BR failure has occurred.

Case 2) ATENA reports a numerical error (i.e., zero pivot error):

- If $\varepsilon_t/\varepsilon_{u,\mathrm{BE}}$ is greater than 33% and the concrete is not crushed, thus a BR failure has occurred.
- If $\varepsilon_t/\varepsilon_{u,\mathrm{BE}}$ is smaller than 33% and the concrete is not crushed, the numerical instability (i.e., zero pivot error) has caused termination of the analysis and the numerical stability of the model must be improved to enable simulation of response to failure.

- If $\varepsilon_t/\varepsilon_{u,\mathrm{BE}}$ is greater than 33% and the concrete is crushed, Case 1 apply.

Case 3) ATENA does not fail and the load protocol completed successfully:

- If $\varepsilon_t/\varepsilon_{u,\mathrm{BE}}$ is greater than 33% and concrete is not crushed, the failure is classified as a BR failure.
- If the concrete is crushed at an earlier point and load transferred into the compression reinforcement, apply rules from Case 1 to that point. This phenomenon is identified when there is a large strength loss and regained upon activation of the longitudinal reinforcement in compression.

Table 2.1: Determination of a CB versus a BR failure mode.

$\frac{\sigma_{\mathbf{c}}}{\sigma_{\mathbf{c},\mathrm{peak}}}$ 1)	$\frac{\varepsilon_t}{\varepsilon_{u,\mathrm{BE}}}$ 2)	**ATENA Output message**	**Failure Mode**
$\leq 30\%$	$\geq 33\%$	-	CB
$> 30\%$	$\geq 33\%$	-	BR
$> 30\%$	$< 33\%$	numerical error (i.e., zero pivot error)	Failure not reached

1) $\sigma_{\mathbf{c}}$ = compressive stress, $\sigma_{\mathbf{c},\mathrm{peak}}$ = peak compressive strength.

2) ε_t = steel strain, $\varepsilon_{u,\mathrm{BE}}$ = ultimate strain of longitudinal steel.

In order to verify the above criteria, Whitman [68] performed a comprehensive investigation using measured data for twenty-three mostly flexure-controlled reinforced concrete walls subjected to cyclic loading and constant axial load. All wall specimens were planar and ATENA 3D was used for simulation purposes. Twenty simulations to failure were successfully completed of the twenty-three wall specimens and the accuracy of simulated versus measured response are shown in Table 2.2. In Table 2.2, Δ_y is yield deformation, $V_{\max}$ is normalized peak shear stress demand and Δ_u is the deformation capacity of the wall.

Table 2.2: Simulation results for experimental wall database conducted by Whitman [68].

Specimen	Yield Displacement		Strength		Deformation Capacity		Failure Mode
	$\Delta_{y,\text{meas.}}$	sim./meas.	$V_{\max}$	sim./meas.	$\Delta_{u,\text{meas.}}$	sim./meas.	
	%	-	kips	-	%	-	-
WSH2	0.38	0.90	81.1	0.98	1.75	1.00	BR
WSH3	0.41	0.96	102.4	0.97	2.07	0.91	BR
WSH4	0.36	0.89	99.0	1.03	1.60	1.10	CB
WSH5	0.25	0.91	97.4	0.99	1.52	0.86	BR
WSH6	0.36	0.91	135.4	0.99	2.04	0.98	CB
W1	0.52	0.92	58.8	1.06	2.98	0.96	CB
W2	0.49	0.94	62.1	1.06	2.91	1.13	BR
PW4	0.41	0.76	218	1.08	1.01	1.87	CB
RW1	0.37	0.98	33.4	0.98	2.26	1.01	BR
RW2	0.35	0.94	35.7	0.91	2.35	0.93	CB
S6	0.41	0.93	194.3	0.98	1.65	0.96	CB
WR10	0.47	0.56	96.7	1.04	2.82	0.98	CB
WR0	0.52	0.50	95.4	1.04	2.14	0.99	CB
R1	0.15	1.81	27.4	0.93	2.52	1.12	BR
R2	0.34	0.95	50.4	0.92	3.25	1.01	BR
RW-A20-P10-S38	0.14	0.90	108.0	0.93	3.14	0.99	CB
RW-A20-P10-S63	0.55	0.88	166.9	0.97	3.00	1.09	CB
RW-A15-P10-S51	0.34	0.61	135.5	0.99	3.31	0.96	CB
RW-A15-P10-S78	0.40	0.87	193.2	1.05	3.00	0.92	CB

1)		Yield Displacement	Strength	Deformation Capacity
Total	Median	0.91	0.99	0.98
	COV	0.29	0.05	0.06
BR	Median	0.95	0.98	1.01

Table 2.2: (continued)

Specimen		Yield Displacement		Strength		Deformation Capacity		Failure Mode
		$\Delta_{y,\text{meas.}}$	sim./meas.	V_{max}	sim./meas.	$\Delta_{u,\text{meas.}}$	sim./meas.	
		%	-	kips	-	%	-	-
	COV		0.31		0.05		0.1	
CB	Median		0.89		1.01		0.98	
	COV		0.2		0.05		0.07	

[1] Note that these are statistics for sim./meas. values shown in the table.

2.3.6 Summary

A selected literature review of the previous work on the numerical approaches used to simulating RC walls was presented. To enable investigation of behavior of RC walls with complex configurations a numerical model is required that not only provides accurate predictions for wall strength, stiffness, and deformation capacity but also provides no assumption of plane sections remaining plane, capable of simulating the localized behavior and uses 3D elements to model 3D geometry. A review of the previous modeling approaches and analysis software resulted in identifying ATENA (which is previously calibrated and validated using RC slender planar wall data) as the preferred software package for this study.

Chapter 3

FINITE ELEMENT MODELING OF NON-PLANAR RC WALLS TO INVESTIGATE BEHAVIOR

3.1 Introduction

Slender, flexure-controlled reinforced concrete walls are used commonly as the lateral load resisting system in mid- and high-rise buildings. Architectural constraints as well as strength and stiffness design requirements often result in walls with non-planar configurations (Figure 3.1). In general, walls are designed to exhibit approximately elastic response under wind and service-level earthquake loading and to exhibit damage and nonlinear response under design-level earthquake loading. Experimental and simulation data [10, 11, 12, 39, 68] show that under design-level loading, wall configuration and nonlinear material behavior result in stress and strain fields that are not represented well by simplified models (e.g., plane sections are assumed to remain plane and/or simplified shear-strain distributions are assumed) and are represented best using three-dimensional continuum-type models that inherently simulate the 3D nonlinear strain fields resulting from interaction of flexure and shear response mechanisms. Thus, three-dimensional continuum modeling is used in the current study of non-planar wall behavior and design.

This chapter presents the 3D continuum modeling approach employed in the current study, validates the modeling via comparison of simulated and observed response for walls tested in the laboratory, and advances understanding of non-planar wall behavior via evaluation of simulation and experimental data. Specifically:

- Section 3.2 presents an experimental data set comprising 13 non-planar (T– and C–shaped) walls exhibiting flexure controlled response when subjected to constant axial loading and quasi-static, unidirectional and bi-directional, cyclic lateral loading in the

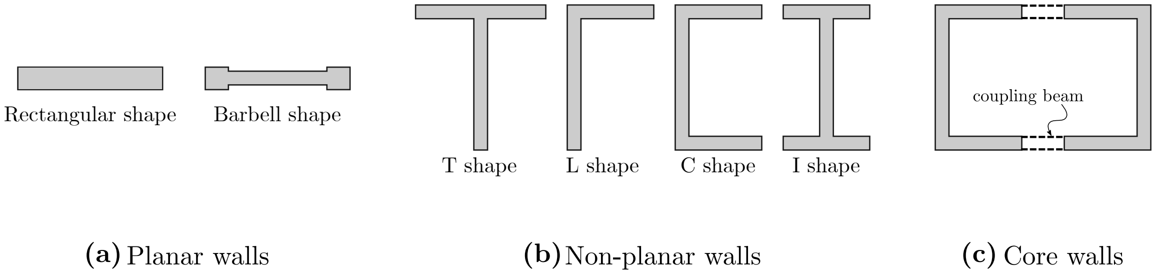

(a) Planar walls (b) Non-planar walls (c) Core walls

Figure 3.1: Commonly used wall cross-sectional configurations.

laboratory.

- Section 3.3 presents the response observed in the laboratory for the specimens considered in this study.
- Section 3.4 validates the modeling approach through comparison of simulated and measured response.
- Section 3.5 employs simulation data, including stress, strain, and damage fields, as well as damage patterns observed in the laboratory to improve understanding of non-planar wall behavior and failure modes.

3.2 *Experimental Investigations of Non-planar Wall Behavior Conducted Previously by Others*

The results of previous experimental research were reviewed to assemble a data set for use in validating the ATENA finite element modeling procedure for non-planar walls. Tables 3.1 and 3.2 present relevant design and response data for the T– and C–shaped test specimens used in the study because they are the simplest configurations that produce response modes of interest to the current study. Specifically, these shapes can be loaded along an axis of symmetry to produce uni-directional response, without twist-induced out-of-plane deformation, which greatly simplifies boundary conditions in the laboratory and simulation, and these shapes result in heavy compression loading of the “toes” of the wall as well as nonlinear vertical stress-strain distributions in the “flange” of the wall. I–shaped wall specimens were not used because, when loaded along an axis of symmetry, they do not provide stress/strain distributions that differ from those developed in planar, T– and C–shaped walls. Barbel shaped walls were not considered because they are not used commonly in modern construction and do not provide stress/strain fields that differ substantially from those that can develop in T–shaped walls.

Wall specimens listed in Tables 3.1 and 3.2 had the following characteristics:

- flexure-controlled response with onset of strength loss resulting from a compression-buckling (characterized by simultaneous crushing of boundary element concrete and buckling of boundary element longitudinal reinforcement) or buckling-rupture (characterized by rupture of previously buckled longitudinal reinforcement) or compression-shear (characterized by concrete crushing in the web and/or confined region caused by the influence of both shear and flexure),

- aspect ratio (h_w/ℓ_w) greater than 2.5. Previous research [53] indicates that RC walls with aspect ratios in excess of 1.5 and designed in accordance with modern codes typically exhibit flexure-controlled response when subjected to moderate axial loading and cyclic lateral loading.

- loaded under constant axial load and cyclic lateral loading applied uni-directionally or bi-directionally via displacement–controlled increments,

- wall thickness in the laboratory greater than 3 inches (76 mm) as a specimen thickness of less than 3 in.was considered to increase the likelihood of the specimen exhibiting failure modes not typically associated with full-scale walls,

- two layers of vertical and horizontal reinforcement, as this is a modern code requirement.

Additionally, walls having one curtain of reinforcement were not considered as they are not relevant to modern construction. The specimens represented a range of axial load ratios (1.34 to 9.0%) and peak shear stress demands (ranged from about $2A_{cv}\sqrt{f'_c}$ to $10A_{cv}\sqrt{f'_c}$). Parameters in Tables 3.1 and 3.2 are defined as follows:

- Load: U = uni-directional and B = bi-directional.
- ALR: axial load ratio = $P/(A_g f'_c)$
- Cross-Sectional Aspect Ratio (CSAR): ℓ_w/t_w, where ℓ_w is the wall in-plane length and t_w is the wall thickness.
- Scale: wall with 12 in.thickness is considered a full-scale wall.
- ρ_{BE}: vertical reinforcement ratio in the boundary element.
- ρ_v: vertical reinforcement ratio in the web region of the wall.
- ρ_t: transverse reinforcement ratio in the boundary element.
- ρ_h: horizontal reinforcement ratio in the web region of the wall.
- f'_c: concrete compressive strength.
- ACI: ACI 318-14 [3] Compliant: Y = yes, N = no, Al = almost.
- FM: failure mode.
- $V_{b,\max}$: maximum base shear resisted by the wall.
- $M_{b,\max}$: maximum base moment resisted by the wall.
- V_n: nominal shear strength of the wall per ACI 318-19 [4]. Calculated using reported material strengths.

- M_n: nominal moment strength for the base section, defined by the extreme compression fiber strain in the boundary element core reaching a strain value of -0.003.

- A_{cv}: gross area of concrete section bounded by web thickness and length of section in the direction of shear force considered in the case of walls.

- Drift: lateral displacement at the point of applied load divided by the height from the wall-foundation interface to the point of the applied load.

- Ductility: maximum displacement (Δ_u) reached by the model divided by the displacement at yielding (Δ_y).

- (+): Toe in compression.

- (-): Toe in tension

Due to their cross-sectional geometry, non-planar walls have different stiffness in perpendicular directions. Therefore, drift capacity is not the most suitable measure of deformation capacity. Ductility tends to be a better measure of the deformation capacity for such walls and is employed in this study. Following section explains two commonly used approaches for computation of ductility in structural walls.

3.2.1 Methods for Computing Displacement Ductility

Two commonly used methods for defining drift capacity are those proposed by Park [52]. Both techniques are based on an elastic-perfectly-plastic model for the envelope of the load-displacement response of the system as shown in Figure 3.2. For both methods the plastic portion is defined as the horizontal tangent to the maximum load of the response envelope. For the 75% method the elastic stiffness is calculated using the secant to the response envelope between points of zero load and 75% of maximum load. For the energy equivalent method the elastic stiffness is defined to achieve zero energy error between the

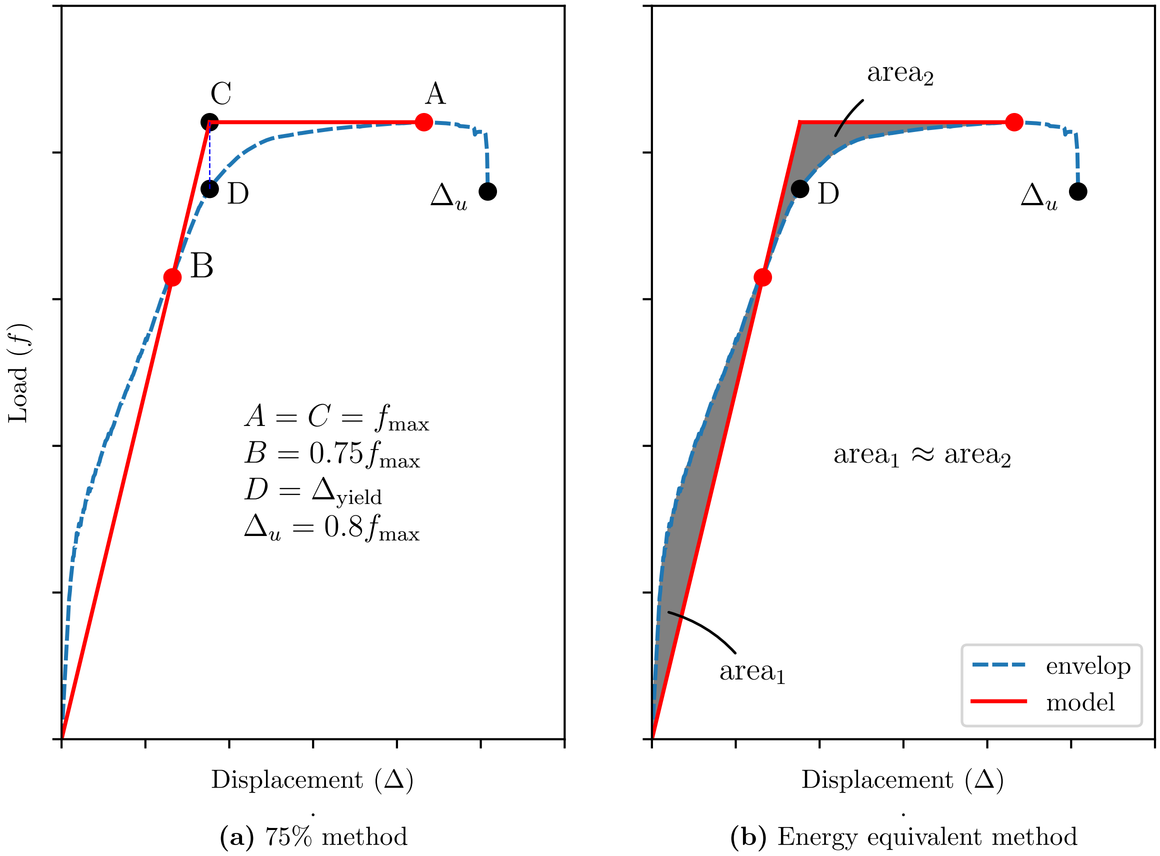

(a) 75% method

(b) Energy equivalent method

Figure 3.2: Comparison of methods used to predict the elastic-perfectly-plastic response model from the experimental envelope of the load-displacement.

bilinear model and measured/simulated $P - \Delta$ history. In this study, for simplicity, the 75% method is employed. Study performed by Behrouzi [11] shows both methods lead to similar results. Ductility is defined by the ratio of the displacement at 20% loss in lateral load capacity to the displacement at yield. Displacement at yield is the displacement at which the maximum strength of the bilinear model is reached (point D on Figure 3.2).

Table 3.1: Design parameters of non-planar structural walls.

Author	ID	Shape	Load	ALR	CSAR	Scale	ρ_{BE}	ρ_v	ρ_t	ρ_h	f'_c	ACI	FM
				%			%	%	%	%	ksi		
Thomsen and Wallace [58]	TW1	T	U	9.0	12	1/3	3.09	0.29	0.46	0.33	6.33	Al	CB
	TW2	T	U	7.5	12	1/3	1.43	0.41	1.01	0.33	6.05	Y	CB
Brueggen [14]	NTW1	T	B	6.5	15	1/2	3.70	0.30	0.81	0.61	7.30	Y	CB
	NTW2	T	B	7.5	15	1/2	3.34	0.25	0.81	0.61	6.60	Y	CB
Choi et al. [21]	TC	T	U	6.0	10	-	2.10	1.30	1.27	2.99	5.47	N	CB
	TCaw	T	U	6.0	10	-	2.10	1.30	1.27	4.03	5.63	N	CB
Lowes et al. [11]	CW6	C	U	5.0	20	1/2	3.93	0.30	0.73	0.73	4.94	Al	BR
	CW7	C	B	5.0	20	1/2	3.93	0.30	0.73	0.73	5.25	Al	BR
Beyer et al. [12]	TUA	C	B	2.0	8.7	1/2	1.33	0.21	0.75	0.30	11.3	N	BR
	TUB	C	B	4.0	8.7	1/3	2.77	0.30	1.13	0.45	7.93	N	CS
Ile and Reynouard [29]	IleX	C	B	1.34	6.0	5/6	1.20	0.13	0.45	0.32	3.44	N	BR
	IleY	C	B	1.34	6.0	5/6	1.20	0.13	0.45	0.32	3.44	N	BR

Table 3.2: Measured properties of non-planar structural walls.

Author	ID	ALR	Shape	Loading ∥ to Axis of Symm.					Loading ⊥ to Axis of Symm. (+)					Loading ⊥ to Axis of Symm. (-)					ACI	FM
		%	ksi	$\frac{V_{b,\max}}{\sqrt{f'_c}A_{cv}}$ (psi)	$\frac{V_{b,\max}}{V_n}$	$\frac{M_{b,\max}}{M_n}$	Drift %	Ductility	$\frac{V_{b,\max}}{\sqrt{f'_c}A_{cv}}$ (psi)	$\frac{V_{b,\max}}{V_n}$	$\frac{M_{b,\max}}{M_n}$	Drift %	Ductility	$\frac{V_{b,\max}}{\sqrt{f'_c}A_{cv}}$ (psi)	$\frac{V_{b,\max}}{V_n}$	$\frac{M_{b,\max}}{M_n}$	Drift %	Ductility		
Thomsen & Wallace [59]	TW1	9.0	T	-	-	-	-	-	4.3	0.86	0.74	1.49	3.65	2.9	0.58	0.99	2.40	4.11	Al	CB
	TW2	7.5	T	-	-	-	-	-	5.5	0.89	0.94	2.61	4.2	2.8	0.46	0.97	3.44	2.39	Y	CB
Brueggen [14]	NTW1	6.5	T	2.7	0.62	0.96	3.92	3.85	5.0	0.69	1.12	2.22	2.6	2.6	0.36	0.92	2.29	4.25	Y	CB
	NTW2	7.5	T	2.5	0.57	1.01	1.95	4.70	5.6	0.74	1.19	2.71	3.51	3.1	0.41	0.98	1.94	4.22	Y	CB
Choi et al. [21]	TC	6.0	T	-	-	-	-	-	9.92	0.80	0.96	2.65	5.30	6.9	0.39	0.97	4.57	8.02	N	CB
	TCaw	6.0	T	-	-	-	-	-	9.45	0.81	0.99	2.68	3.83	6.1	0.39	0.98	4.42	7.37	N	CB
Lowes et al. [39]	CW6	5.0	C	4.3	0.43	1.0	2.06	4.23	-	-	-	-	-	-	-	-	-	-	Al	BR
	CW7	5.0	C	4.0	0.41	0.97	1.88	3.51	2.2	0.10	1.03	1.3	1.50	4.12	0.06	1.01	2.25	3.96	Al	BR
Beyer et al. [12]	TUA	2.0	C	3.2	0.78	0.92	2.50	8.0	1.9	0.47	0.91	2.67	7.57	1.7	0.41	0.91	3.51	8.12	N	BR
	TUB	4.0	C	5.7	0.99	0.98	2.47	6.1	6.7	0.57	1.03	2.60	6.06	5.6	0.48	0.95	3.05	6.3	N	CS
Ile & Reynouard [29]	IleX	1.34	C	6.0	0.68	1.11	3.09	6.65	-	-	-	-	-	-	-	-	-	-	N	BR
	IleY	1.34	C	-	-	-	-	-	2.8	0.45	1.13	3.08	6.87	2.8	0.50	1.11	3.08	6.40	N	BR
	IleXY	1.34	C	6.0	0.65	1.05	2.06	3.50	2.8	0.44	1.08	2.10	3.96	2.4	0.37	0.83	2.06	3.75	N	CS

3.2.2 Thomsen and Wallace (1995)

Thomsen and Wallace [59] tested two planar and two T-shaped walls (TW1 and TW2) (Figure 3.3) to verify the design approach proposed by Wallace (1994) [64, 65]. Figure 3.4 shows the laboratory test set up for the T-shaped walls, and Figure 3.3 shows the two wall cross-sections. The two T–shaped walls were nominally identical with the exception that in TW2 the length of confinement in the toe of the wall web was increased and vertical hoop spacing was decreased. Cyclic lateral loading was applied via displacement controlled increments along the web of the wall and parallel to the wall axis of symmetry; a constant axial load was applied. Specimen TW1 lost lateral load capacity at a drift[1] (at point of applied load) of 1.25% due to buckling of all longitudinal reinforcements in the toe of the web of the wall. Specimen TW2 lost lateral load capacity at a drift of 2.5% when the toe of the web wall buckled out of plane [22, 59]. Measured response of both walls is shown in Figure 3.5.

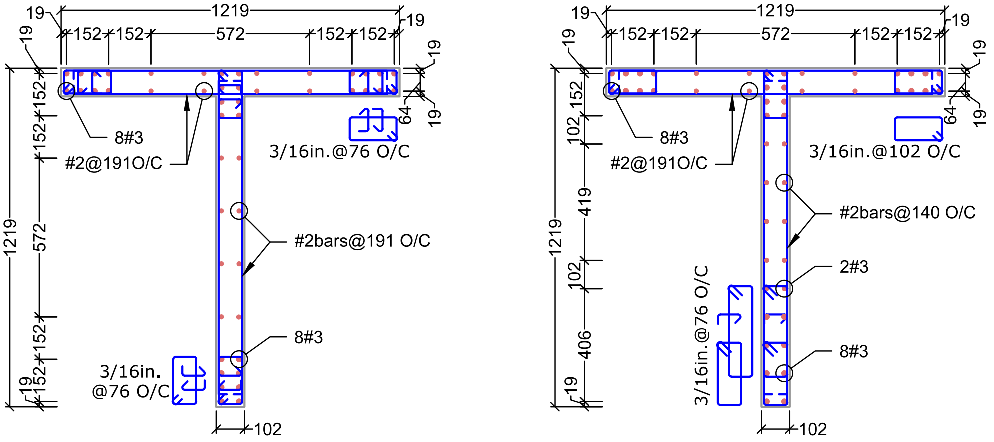

(a) Specimen TW1

(b) Specimen TW2

Figure 3.3: Cross-sectional configurations for T–shaped walls tested by Thomsen and Wallace (dimensions in mm).

---

[1] defined as the lateral displacement at the point of applied load divided by the height from the wall-foundation interface to the point of the applied load.

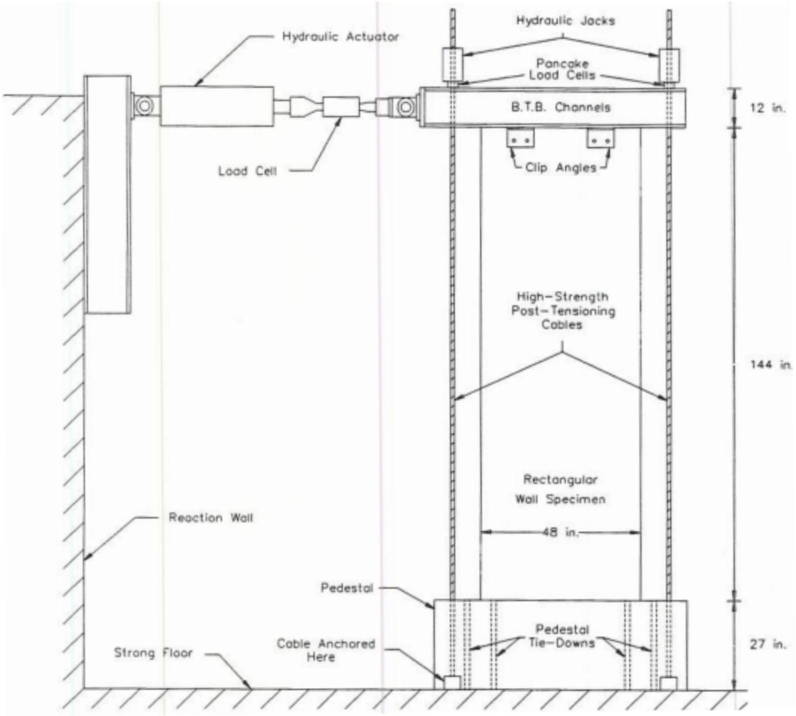

Figure 3.4: Test setup for T–shaped walls tested by Thomsen and Wallace [59].

Thomsen and Wallace [58] state that measured response was affected by pedestal (foundation block) rotation and by eccentric application of the axial load but not by pedestal sliding. Potentiometer data indicated that sliding of the pedestal represented less than 1% of the measured displacement at the top of the wall; thus, data characterizing lateral displacement at the top of the wall were not corrected to remove pedestal sliding. As shown in Figure 3.4, axial load was applied to the wall specimens via four jacks and a loading frame. Thomsen and Walls state that the jacks were not placed symmetrically about the wall, such that the applied axial load was accompanied by an applied moment. The data presented in Figure 3.5 have been modified such that the lateral load is not the applied lateral load, but the lateral load applied +/- the lateral load associated with the gravity-induced base moment. Pedestal rotation resulted in a non-trivial displacement at the point of load application and, therefore, the data presented in Figure 3.5 have been modified also to include the impact of pedestal rotation on displacement at the point of applied load.

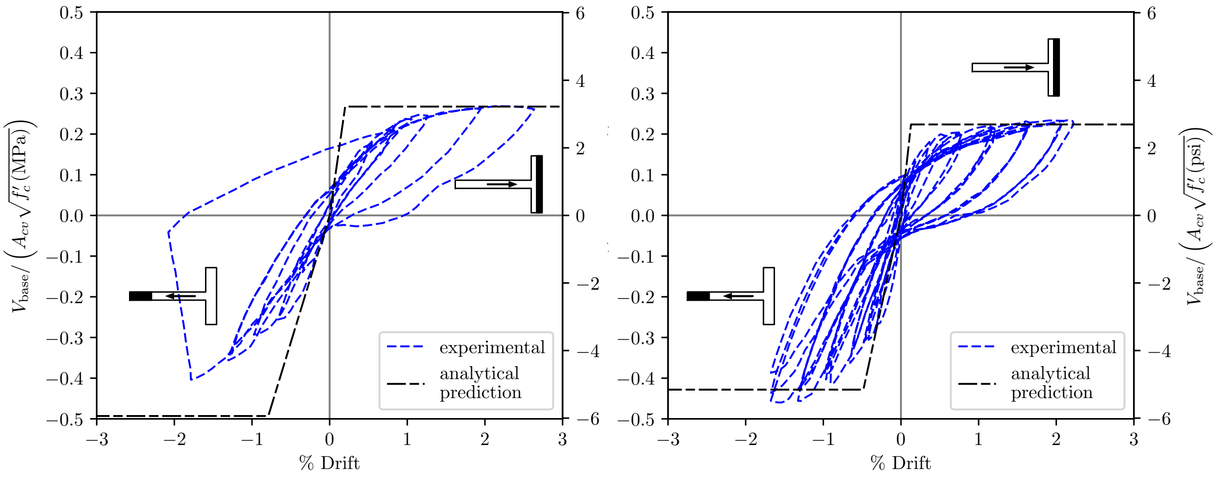

(a) Specimen TW1

(b) Specimen TW2

Figure 3.5: Measured load-deformation relationship for wall specimens tested by Thomsen and Wallace.

Figure 3.6 shows the damage pattern experienced by specimens TW1 and TW2. Thomsen and Wallace, found that specimen TW2 performed much better compared to TW1 due to the higher rate of transverse reinforcement in the confined region at the toe of the wall [59].

3.2.3 Choi, Ha, Lee, Oh, and Yun (2004)

Choi et al. [21] tested two specimens (TC and TC-aw) with confinement details that complied with the provisions of both ACI 318-99 [5] and UBC-97 (Figure 3.7). Tests along with sectional analyses were expected to provide data to determine deformation capacities (drift and ductilty) for T–shaped walls. Figure 3.7 shows the cross-section of the walls. Cyclic lateral loading was applied parallel to the web of the specimen. Specimens were nominally identical with the exception that the confined regions of specimen TC and TC-aw were 15% and 10% of the wall length, respectively. A constant axial load of $0.06A_g f'_c$ was applied to

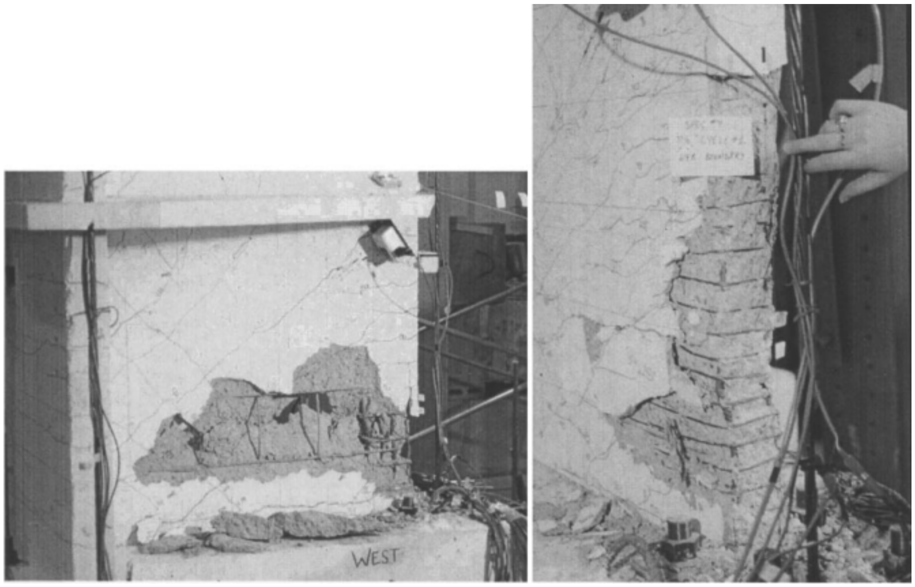

(a) Specimen TW1 **(b)** Specimen TW2

Figure 3.6: Damage patterns for Specimens TW1 and TW2 [59].

both specimens.

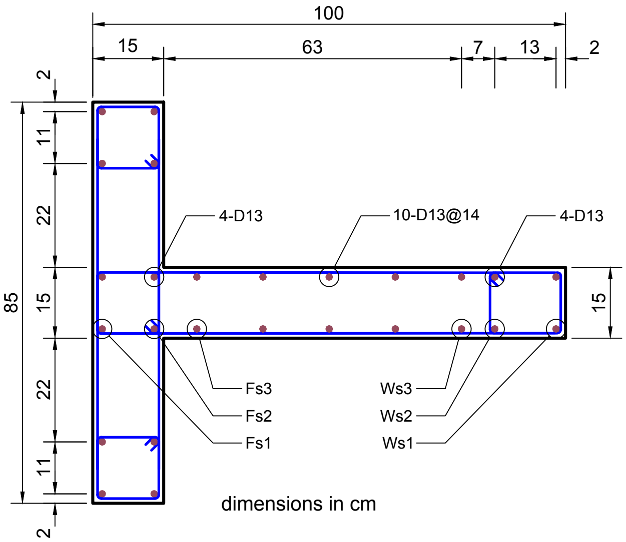

Figure 3.7: Cross-sectional details of the specimens tested by Choi et al..

Specimen TC, lost lateral load carrying capacity at a drift of 1.79% when toe was in compression and maintained the applied axial load to a drift demand of more than 2%. Specimen TC-aw lost lateral load carrying capacity at a drift of about 1.82% (toe in compression) and maintained axial load capacity to a drift of more than 2%. Both specimens maintained lateral load carrying capacity to a drift demand of approximately 4% in the direction resulting in flange compression. Figure 3.8 shows the experimental response of both specimens.

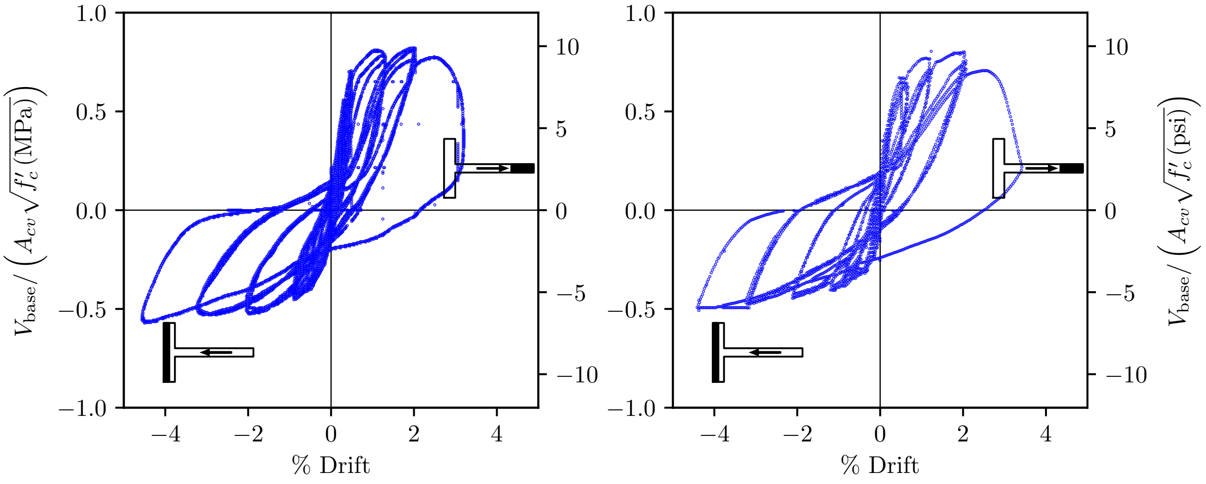

(a) Specimen TC

(b) Specimen TC-aw

Figure 3.8: Measured load-deformation relationship for wall specimens tested by Choi et al..

Choi et al. concluded that since the specimens did not maintain lateral load carrying capacity to drifts in excess of the UBC-97 limit of 2%, in both loading directions, wall detailing, specifically the length of the boundary element was not adequate. Additionally, Choi et al. concluded that, specimens TC and TC–aw, were not provided with adequate confinement to sustain specified deformation capacity required by UBC-97 when flange is in compression. Though, the deformation capacities exhibited in the opposite direction, were satisfactory. Additionally, it is conceivable to attain large deformation capacities withou the need of special transverse reinforcement in the flange when axial load ratio is less that 10% [21].

3.2.4 Ile and Reynouard (2005)

Ile and Reynouard [29] tested three nominally identical C-shaped wall specimens under cyclic lateral loadings to investigate the performance of a full scale C–shaped wall in uniaxial and biaxial bending and shear while comparing design requirements in two versions of EC8. The first specimen (IleX) was loaded parallel to the web, the second specimen (IleY) was loaded in the direction parallel to the flanges and the third (IleXY) was loaded biaxially (Figure 3.9). Specimens were designed to meet the requirements of CEN, ENV1998 [15] with the exception that the longitudinal reinforcement ratio at the corner boundary element was below the allowed ratio. Due to the geometry of the walls, the shear span in the web and flange directions differs and the authors predicted different shear influence in the walls prior to the design. For this reason, the spacing provided in the web direction for horizontal rebars is about half of that provided in the flanges. More shear reinforcement is provided in the direction of the web. A constant axial load ratio of $0.10A_g f_c'$ was applied to all specimens.

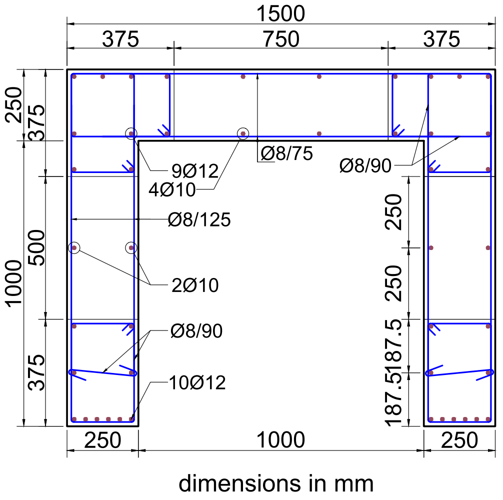

Figure 3.9: Cross-sectional details of the specimens tested by Ile and Reynouard.

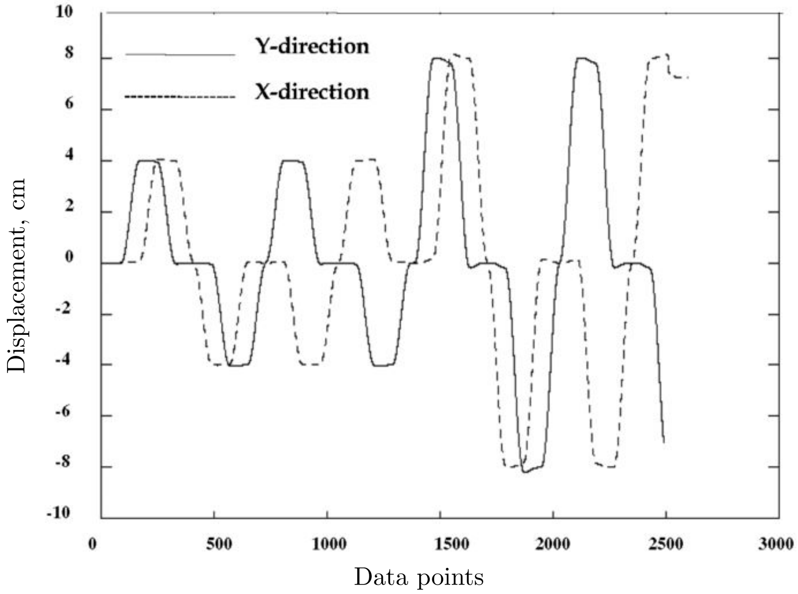

Figure 3.10: Average horizontal displacement time-histories applied to specimen IleXY [29].

Figure 3.11 shows the experimental responses of the three specimens. Specimen IleX failed at a drift of 3 .08% perpendicular to the axis of symmetry due to fracture of previously buckled longitudinal bars in the toes of the flanges. Specimen IleY failed at a drift of 3.08% and parallel to the axis of symmetry due to simultaneous concrete crushing and buckling of reinforcing bars in the toes of the flanges and corners of the wall. Specimen IleXY was subjected to bi-directional loading (Figure 3.10) and reached a maximum drift of 2.05% in both directions with failure due to fracture of previously buckled bars in the toes of flanges. Figure 3.12 shows specimen IleXY at failure.

Ile and Reynouard observed that wall response was stable and determined that wall displacement ductility exceeded 6 under bi-directional loading. Ile and Reynouard concluded that the design requirements included in CEN, ENV1998:1994 [16] and proposed provisions in CEN, preEN1998 [16] are satisfactory.

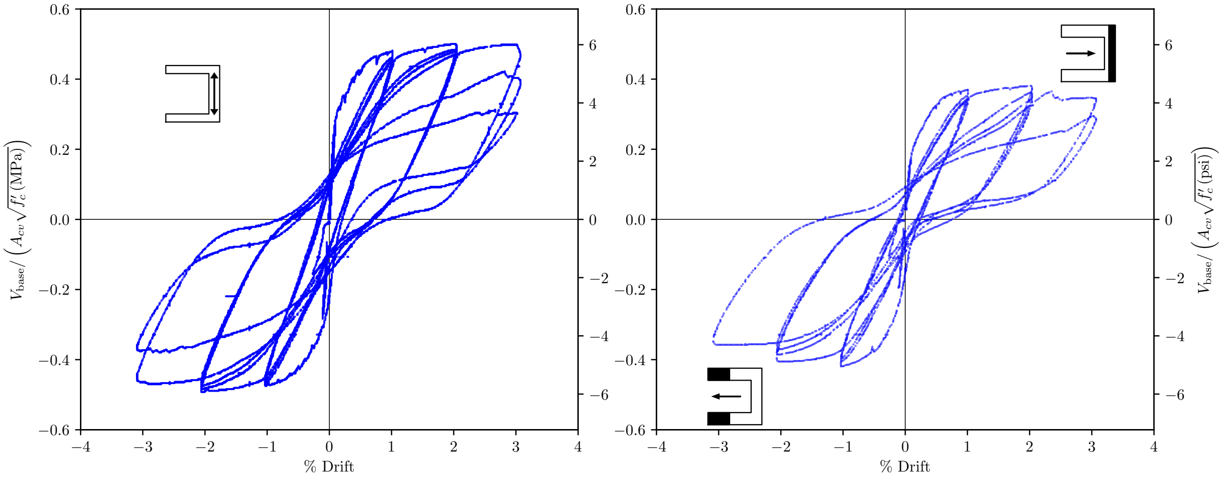

(a) Specimen IleX - parallel to web

(b) Specimen IleY - perpendicular to web

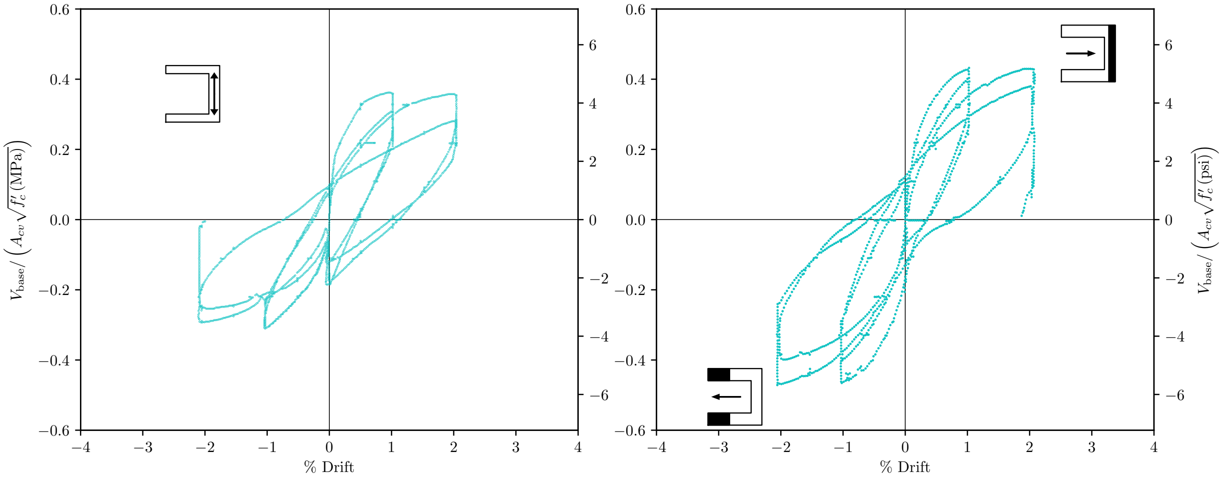

(c) Specimen IleXY - parallel to web

(d) Specimen IleXY - perpendicular to web

Figure 3.11: Measured load-deformation relationship for wall specimens tested by Ile and Reynouard. Specimens IleX and IleY were loaded uni-directionally while specimen IleXY was loaded bi-directionally.

3.2.5 Beyer, Dazio, and Priestley (2008)

Beyer et al. [12] tested two half-scaled C-shaped wall (TUA and TUB) designed and loaded

Figure 3.12: Failure of one flange for the specimen IleXY loaded bi-directionally [29]

to represent the lower three stories of a six-story wall. Figure 3.13 shows the laboratory test setup for the walls, and Figure 3.14 shows the wall cross-sections. Walls were designed with different thicknesses but the same flexural and shear strengths. The walls were subjected to quasi-static cyclic bi-directional lateral loading (Figure 3.15) and constant axial loads of $0.02A_gf'_c$ and $0.04A_gf'_c$ for TUA and TUB, respectively. For each specimen, lateral loads parallel and perpendicular to the axis of symmetry were applied at slightly different heights due to the position of the actuators. Consequently, the shear span ratios were $M/(V\ell_w) = 2.58$ and $M/(V\ell_w) = 3.2$ for parallel and perpendicular to the web directions, respectively. Walls were not designed to meet specific code requirement but were designed to achieve highly ductile response. The main difference between the specimens was the thickness of the walls (150 mm for TUA and 100 mm for TUB). The horizontal reinforcement ratios were the same for both specimens. Amount of vertical reinforcement used in both specimens were the same which led to higher flexural reinforcement ratio in specimen TUB due to thinner walls. The walls were provided with shear keys at the bases to limit sliding at the wall-base interface.

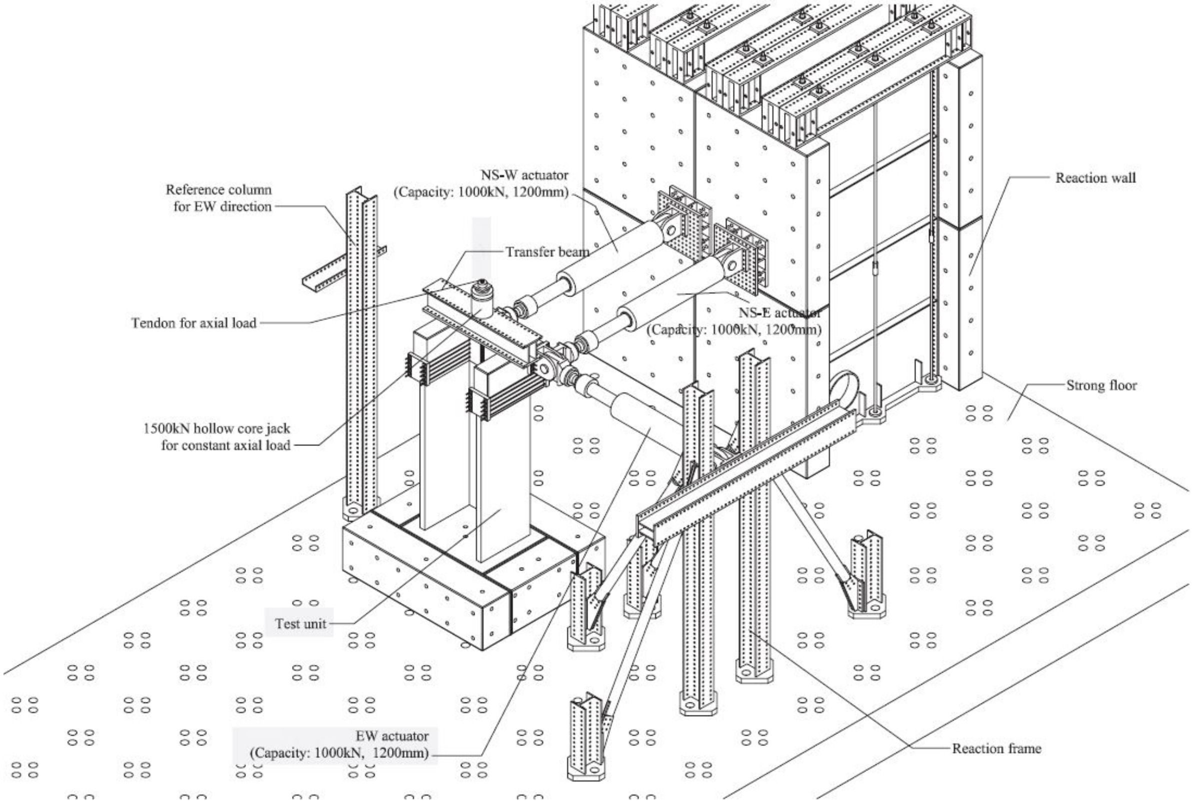

Figure 3.13: Isometric view of the test set up by Beyer et al. [12]

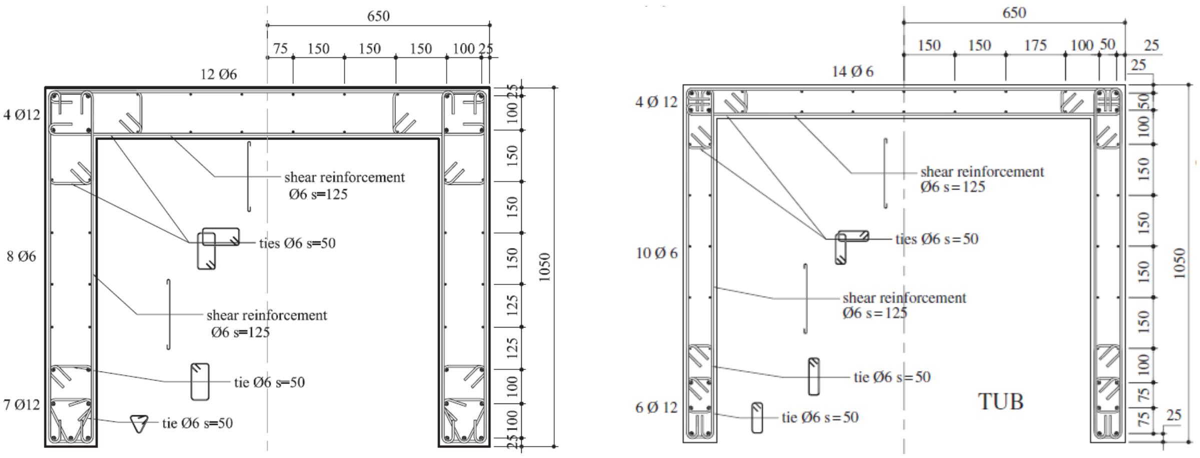

(a) Specimen TUA

(b) Specimen TUB

Figure 3.14: Cross-sectional details of the specimens tested by Beyer et al. [12].

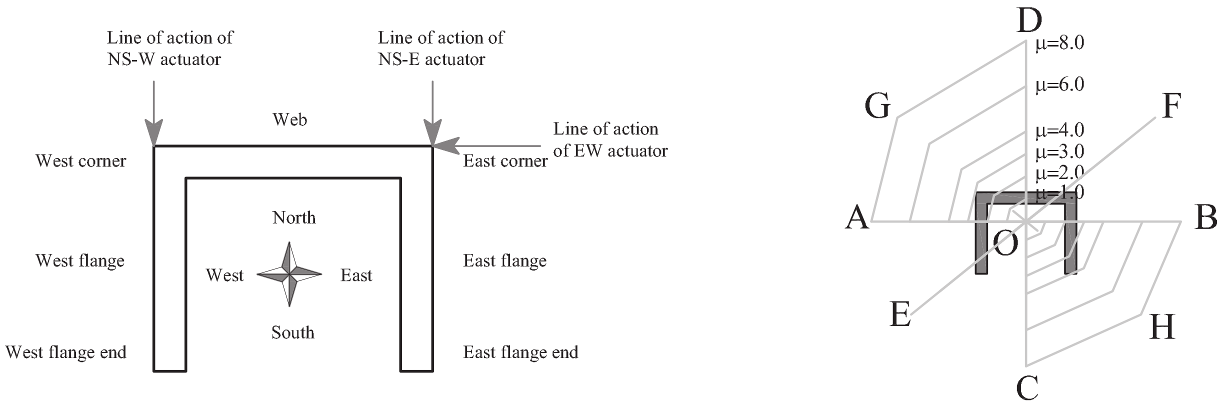

Figure 3.15: Cardinal point (left) and load pattern (right) of the walls tested by Beyer et al. [12]

The experimental responses of both specimens in both directions are shown in Figure 3.16. Specimen TUA lost load carrying capacity due to fracture following buckling of longitudinal bars at the toe of the flanges at a drift of 2.4% in the direction parallel to the axis of symmetry. Specimen TUB lost lateral load carrying capacity due to the crushing of concrete in the unconfined region of the web after reaching a drift of 2.7% in the direction parallel to the web [11, 12, 22].

Beyer et al. observed that

- the diagonal direction is the most critical loading direction for non-planar walls based on the observation that measured wall flexural capacity in the diagonal direction was less than that calculated using plastic hinge models,
- ultimate moment capacity of the walls, computed assuming plane sections remain plane,
- the high ductility design methodology was successful for TUA because TUA achieved a displacement ductility of 8,
- the same “high ductility design methodology” was less success for TUB, because TUB achieved a ductility of 6 due to web crushing; though axial load was maintained, which was attributed to well-detailed boundary elements.

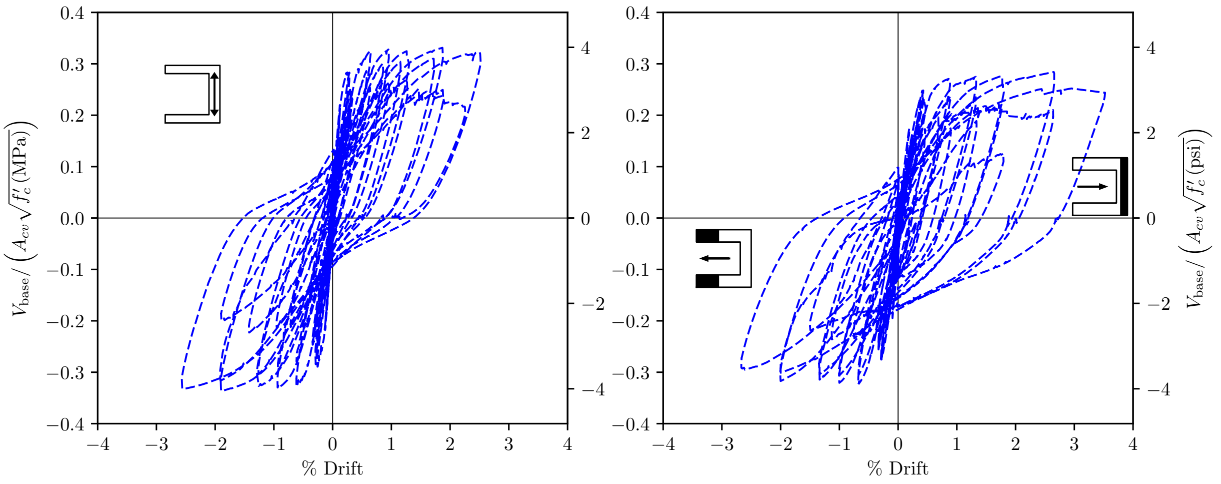

(a) Specimen TUA - parallel to web

(b) Specimen TUA - perpendicular to web

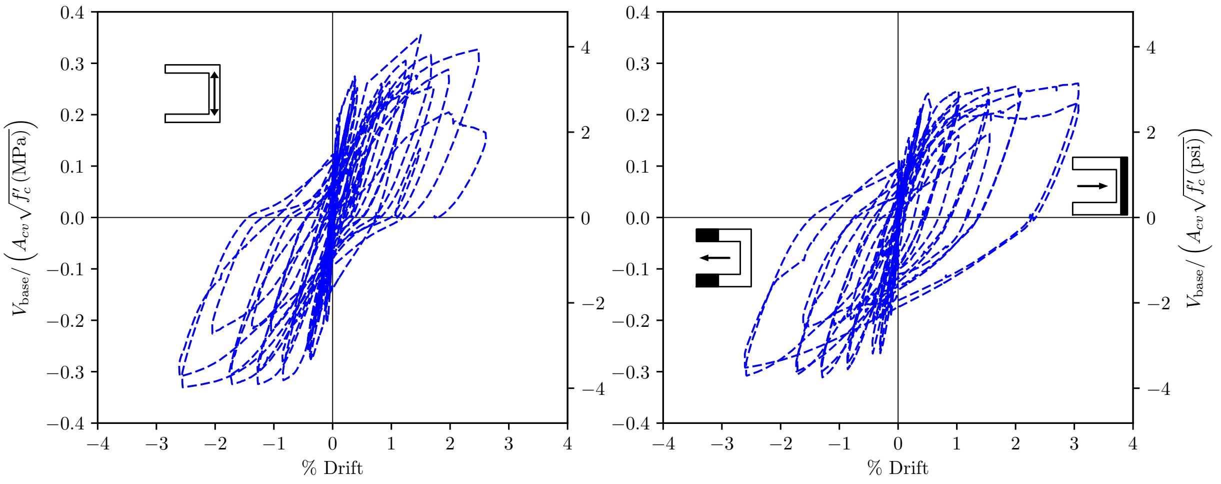

(c) Specimen TUB - parallel to web

(d) Specimen TUB - perpendicular to web

Figure 3.16: Measured load-deformation relationship for wall specimens tested by Beyer et al..

3.2.6 Brueggen (2009)

Brueggen [14] tested two half-scale T-shaped walls (NTW1 and NTW2) under quasi-static bi-directional cyclic loading to explore the performance of the T-shaped wall under multidirectional loading. Figure 3.17 shows the cross-section design details of both specimens. The walls were designed and loaded to represent the lower portion of a six-story prototype building. The walls were designed to meet the requirements of ACI 318-02 [2] and IBC 2003 [28] for seismic category D. The first specimen represented the bottom four stories of the prototype wall while the second represented bottom two stories. Specimen NTW2 was designed based on the results of the first test (NTW1) with changes made to the reinforcement configuration to study the effects of lap splice, distribution of longitudinal reinforcement, length of boundary element and number of stories included in specimen. Specimen NTW2 was constructed with a uniform reinforcement distribution in the flange while NTW1 was designed with heavily reinforced boundary elements at the toes of the wall flanges; the web region of both walls had a heavily reinforced boundary element. Wall NTW2 was constructed with lap splices in the second story [14, 22]. An axial load of $0.03A_gf'_c$ was applied to specimen NTW1 and held constant during the test. Initially, the same axial load ratio (186.5 kips) was applied to specimen NTW2 but after three cycles (at 75% of nominal yield displacement) raised to 201.2 kips for remainder of the test to account for the self-weight of the third and fourth stories that were not included in the NTW2 specimen [13, 14].

Both NTW1 and NTW2 were tested using the same base moment to shear ratio. In the laboratory, moment and shear and axial load were applied at the top of the specimens to develop base reactions expected for the 6-story prototype (see Figure 3.18). This resulted walls NTW1 and NTW2 being subjected to different moment and shear demands at the top of the specimens due to the difference in the specimen heights. The cyclic displacement history for each specimen is shown in Figure 3.19.

Specimen NTW1, when loaded perpendicular to the axis of symmetry, lost lateral load carrying capacity at a drift of 2%; strength loss was attributed to crushing of the "toe" of the wall and sliding was observed following crushing. Following strength loss in the direction perpendicular to the axis of symmetry, testing was continued with load applied only parallel to the axis of symmetry. I this direction, strength loss was observed at a drift of 4% due to crushing of the flange ends. This specimen was able to carry axial load after this point

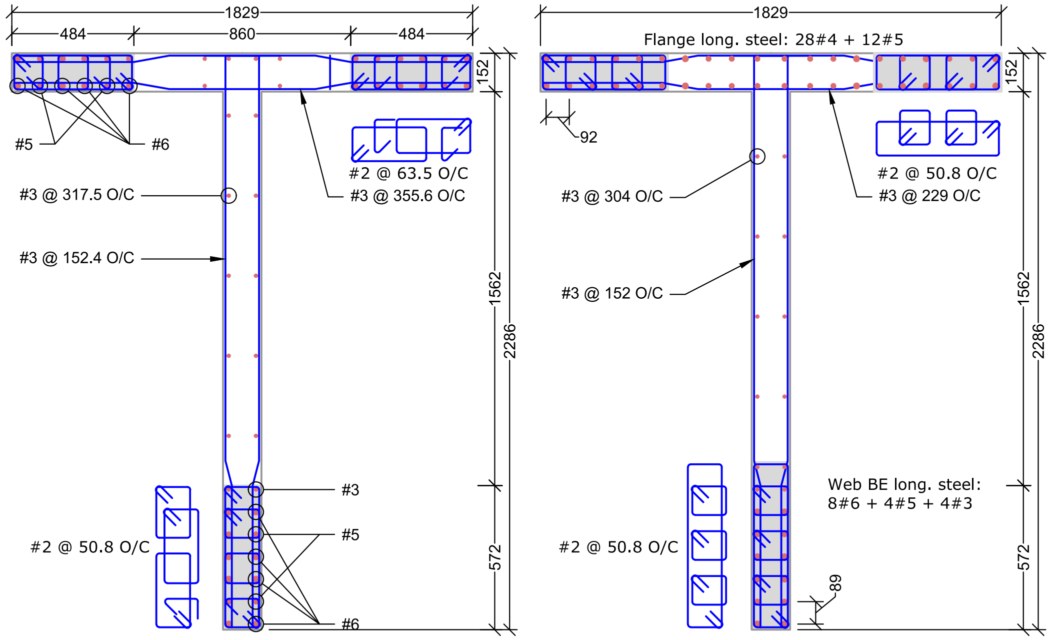

(a) Specimen NTW1 **(b)** Specimen NTW2

Figure 3.17: Cross-sectional details of the specimens tested by Brueggen et al. (bottom story, dimensions in mm).

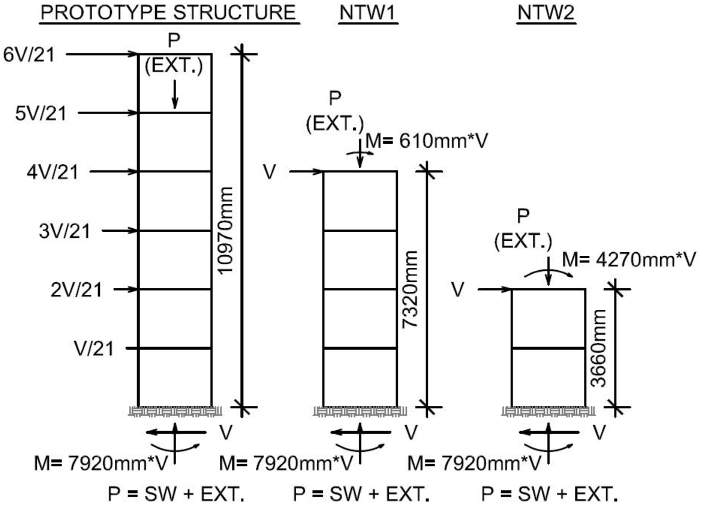

Figure 3.18: Test setup: translating prototype loading to specimens NTW1 and NTW2 [13].

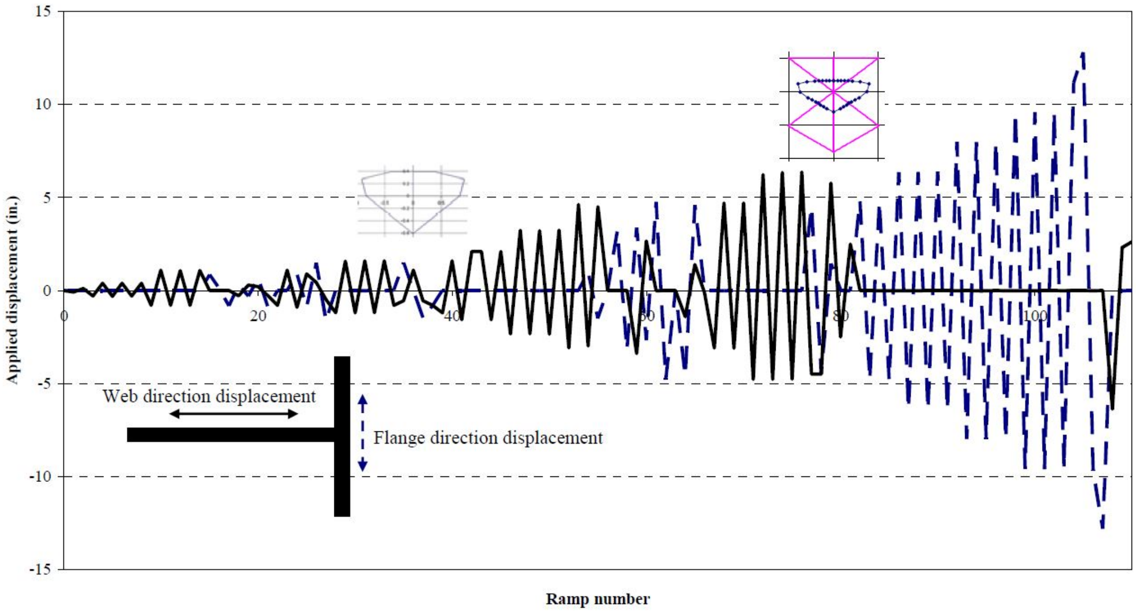

Figure 3.19: Load pattern of the walls tested by Brueggen [14]

but resulted in fracture of the previously buckled bars and led to the crushing of the web where the wall was no longer able to hold axial load. The damages of this test are shown in Figure 3.20.

Specimen NTW2 lost lateral load carrying capacity at a drift of 2.5% when loaded in the direction perpendicular to the axis of symmetry. The strength loss was due to buckling of four longitudinal bars and rupture of transverse hoops within the web boundary element. The buckled bars fractured upon the load reversals at this drift load. After this loading was continued in the direction parallel to the axis of symmetry and the wall reached a drift of 4% before losing lateral load carrying capacity. After spalling of concrete in the toe of the south flange, one longitudinal bar fractured and two more buckled in the other flange toe. Additional bars fractured under increased drift demand and after web region crushed the wall was no longer able to carry the axial load. The damage of this wall is also shown in Figure 3.20. The experimental responses of both specimens in both directions are shown in

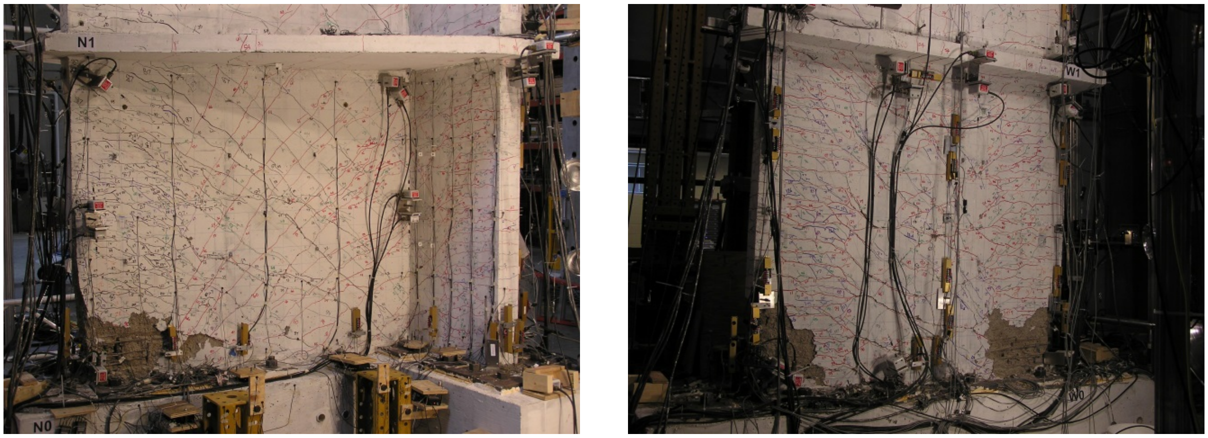

(a) Web failure (NTW1) **(b)** Flange failure (NTW1)

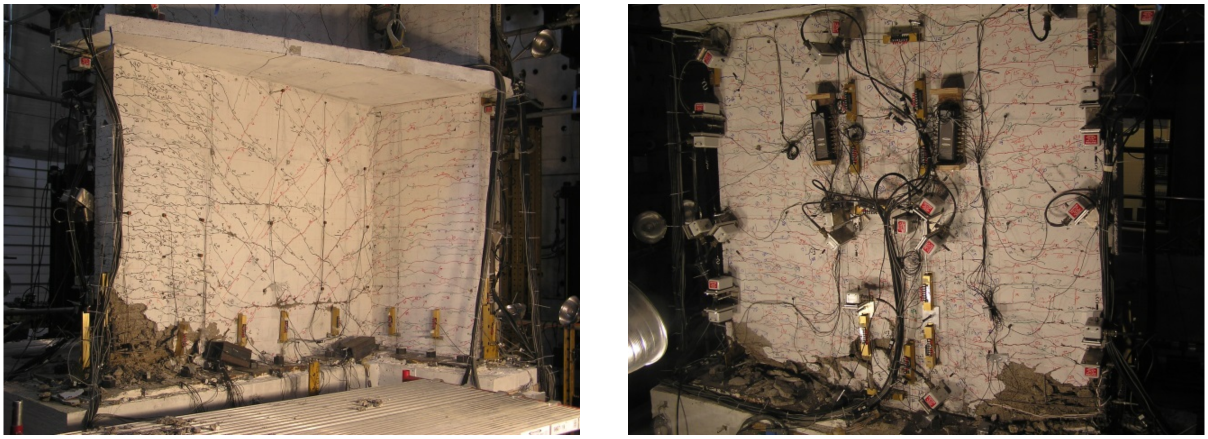

(c) Web failure (NTW2) **(d)** Flange failure (NTW2)

Figure 3.20: First story failures for the walls tested by Brueggen [14].

Figure 3.21.

Brueggen et al. observed that

- damage to the wall including crack width and shear sliding were reduced by employing distributed longitudinal reinforcement across the flange, instead of lumped heavier reinforcement in the boundary elements,
- effects of shear lag increase when using lumped reinforcement in the flange tips when

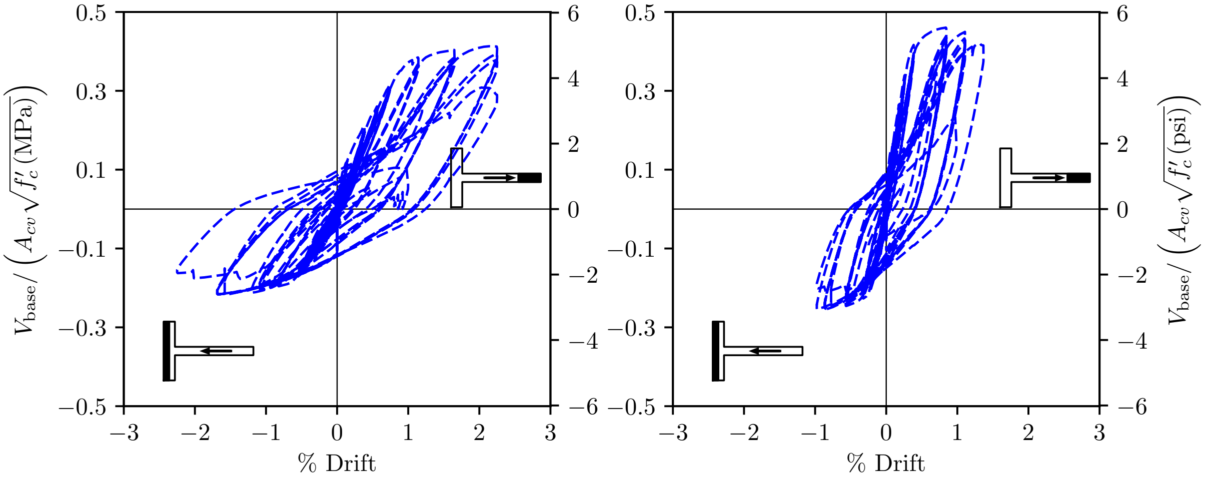

(a) Specimen NTW1 - parallel to web

(b) Specimen NTW2 - parallel to web

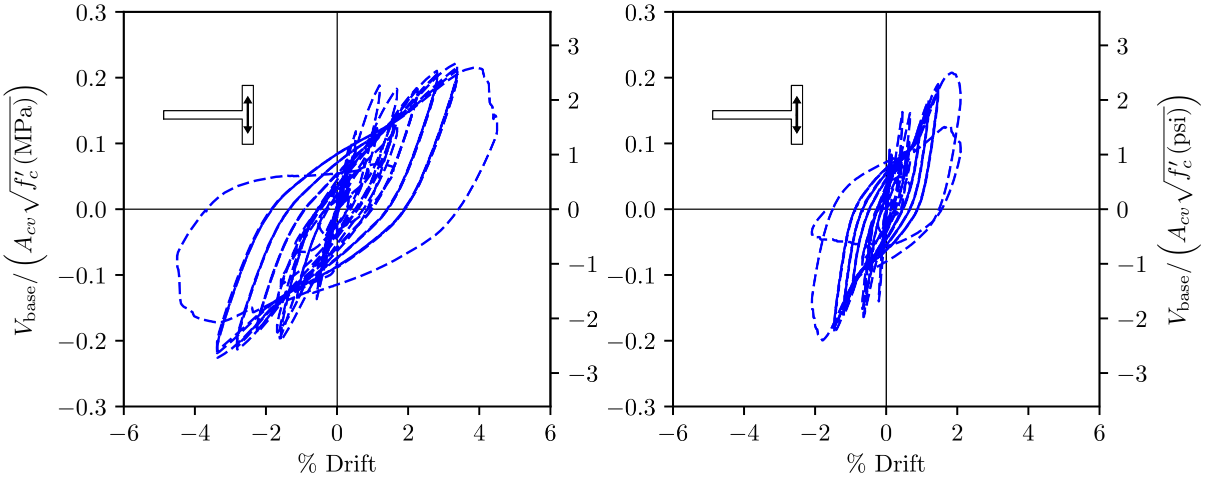

(c) Specimen NTW1 - perpendicular to web

(d) Specimen NTW2 - perpendicular to web

Figure 3.21: Measured load-deformation relationship for wall specimens tested by Beyer et al..

loading parallel to the web,

- relocating the lap splices to the second story avoided the damage caused by lap splices at the wall-flange interface, and

- behavior of the walls was not affected by the increasing shear reinforcement ratio nor by the dimension of the boundary element.

3.2.7 Behrouzi, Welt, Lehman, Lowes, LaFave, and Kuchma (2017)

A team of researchers from the University of Washington and University of Illinois at Urbana-Champaign [9] tested three, one-third scale C-shaped walls (CW6, CW7 and CW8) under quasi-static cyclic lateral loading to study impacts of unidirectional and bidirectional lateral loading on the modern ACI Code compliant non-planar walls. Wall specimens represented the bottom three stories of a 10-story wall. Moment, lateral load, and axial load were applied at the top of the specimen to represent idealized lateral loading at the base of the wall. Cross-section of the walls are shown in Figure 3.22. Specimen CW6 was subjected to uni-directional cyclic lateral loading parallel to the web of the C-shaped wall and a constant axial load of $0.05A_gf'_c$ (Figure 3.23). Specimen CW7 was subjected to bi-directional lateral loading and the same constant axial load (Figure 3.24). Specimen CW8 was subjected to a load history intended to represent that which would develop in a C-shaped pier in a coupled core-wall system. For CW8 Lateral loading parallel to the web of the wall was accompanied by the application of a constant axial load $(0.05A_gf'_c)$ while loading parallel to wall flanges was accompanied by the application of a compressive or tensile axial load to represent the change in pier axial load induced by couling action [11, 39].

Specimen CW6 lost lateral load carrying capacity at a drift of 3.52%. A large number of longitudinal bars fractured in boundary element in the east flange and reduced wall strength. After failure of the boundary element in the east flange, longitudinal bars in the west flange boundary element fractured successively. Loss of lateral strength in specimen CW6 was also associated with sliding along the web in addition to fracture of confining reinforcement in the boundary element. Final damage of the wall test is shown in Figure 3.25.

Specimen CW7 lost lateral load carrying capacity due to buckling and fracture of longitudinal bars in the corner boundary elementt; this was followed by sliding within the web of the wall and fracture of vertical reinforcement in the boundary elements in the toes of the wall.

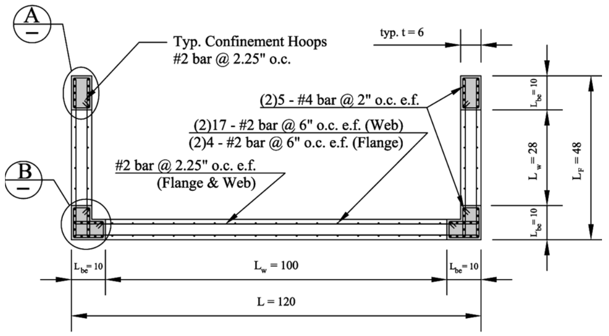

(a) Wall 6/7/8

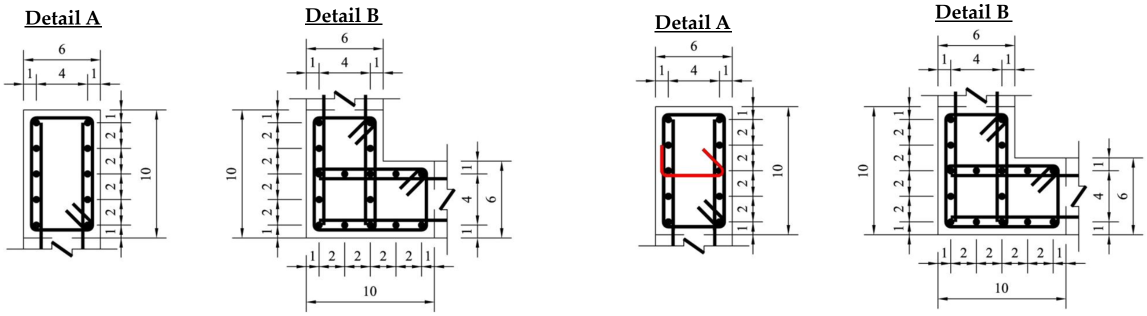

(b) Wall 6 boundary element details

(c) Wall 7/8 boundary element details

Figure 3.22: Cross-sectional details of the specimens tested by Behrouzi et al. [9].

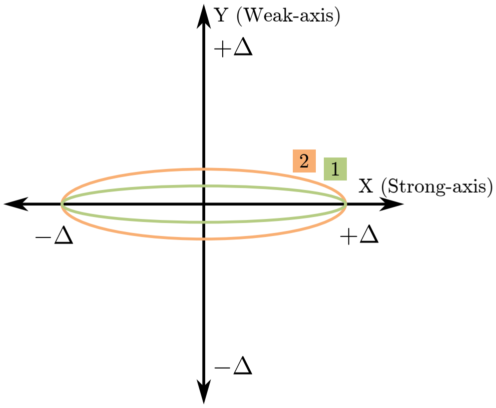

Figure 3.23: Uni-directional loading pattern for specimen CW6 tested by Behrouzi et al..

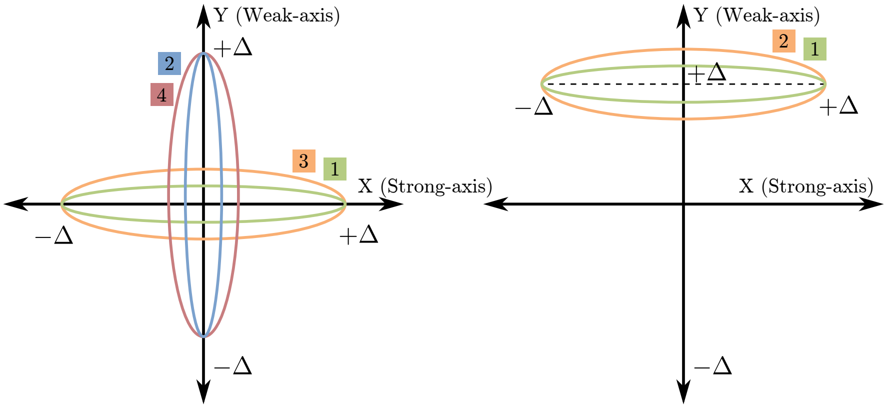

Figure 3.24: Bi-directional loading patterns for specimen CW7 tested by Behrouzi et al..

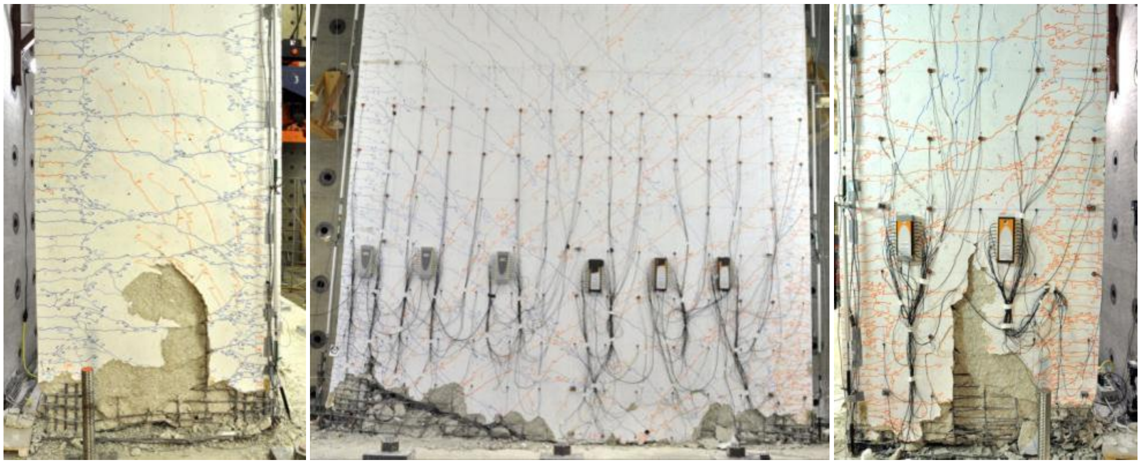

(a) West flange (b) Web (c) East flange

Figure 3.25: Failure images of specimen CW6 [11, 39].

Specimen CW7 reached a drift of 1.9% in the direction parallel to the web (strong direction) and 2% in the perpendicular direction. Figure 3.26 shows damage of specimen CW7 at the end of the test.

Specimen CW8, similar to the previous two tests, lost lateral load carrying capacity due to buckling and fracture of longitudinal reinforcement in the tension pier and small failure in the compression pier. Sliding along the web and fracture of confining reinforcement in

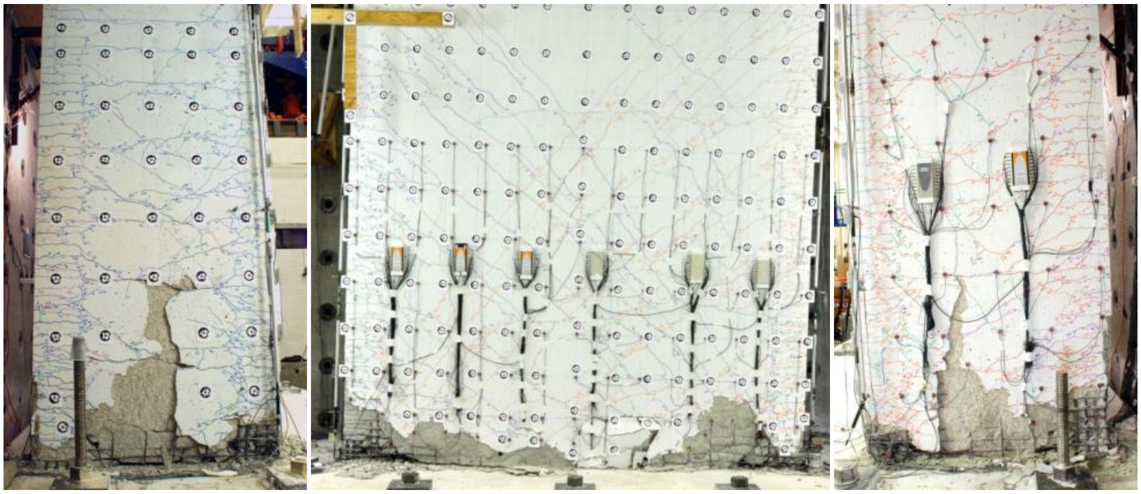

(a) West flange (b) Web (c) East flange

Figure 3.26: Failure images of specimen CW7 [11, 39].

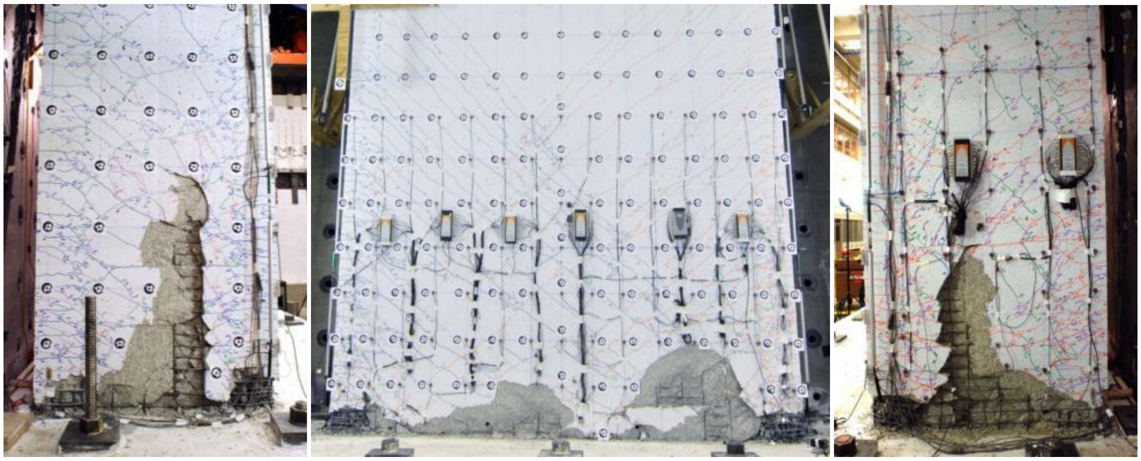

(a) West flange (b) Web (c) East flange

Figure 3.27: Failure images of specimen CW8 [11, 39].

the boundary element was also observed in this test. Final damaged state of the wall test is shown in Figure 3.27. The load-deformation relationship for specimens CW6 and CW7 are shown in Figure 3.28.

Behrouzi et al. observed that

- displacement ductility of greater than 6 and drift ratios of greater than 2% can be sustained for well-detailed non-planar walls subjected to uni-directional and bi-directional cyclic loading,
- increasing axial load ratio reduces the deformation capacity,
- increasing reinforcement ratio in the boundary element as well as providing deeper confining regions, result in higher deformation capacities,
- increased axial load increases the likelihood of compression-controlled failure,
- bidirectional loading reduces the deformation capacity but has no impact on the strength of the wall, and
- due to complexity of shear transfer in non-planar walls, crushing of the unconfined region of the web could occur where shear stress develops out-of-plane bending of the wall and sliding shear failure of the web region of the wall.

3.3 Material Behavior and Response Observed in the Laboratory

The data presented in the previous section show that most non-planar walls tested in the laboratory fail due to crushing of the toe of the wall at drift levels that are low in comparison with planar walls with comparable axial load ratios [40]. This is likely due to the large compression forces that are required to equilibrate large tension forces that develop due to the larger volume of reinforcement in the flange of the wall. Additionally, employing a uniform reinforcement configuration in the flanges mitigates the damage experienced by the wall. When bidirectional loading was applied to the walls the strength of the walls was not affected. Similar observations are made by Behrouzi et al. [10] and summarized in following section.

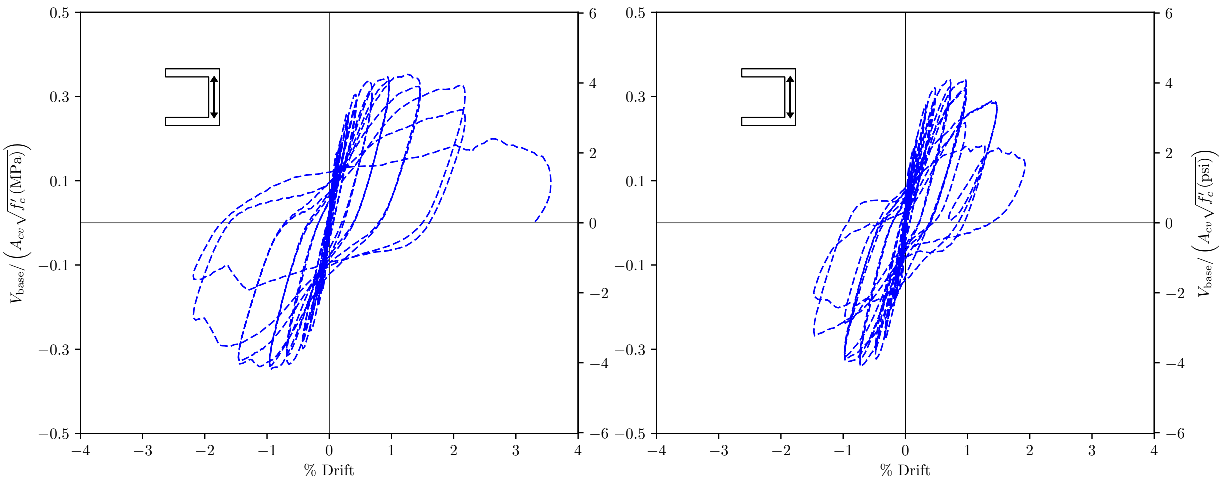

(a) Specimen CW6 - parallel to web

(b) Specimen CW7 - parallel to web

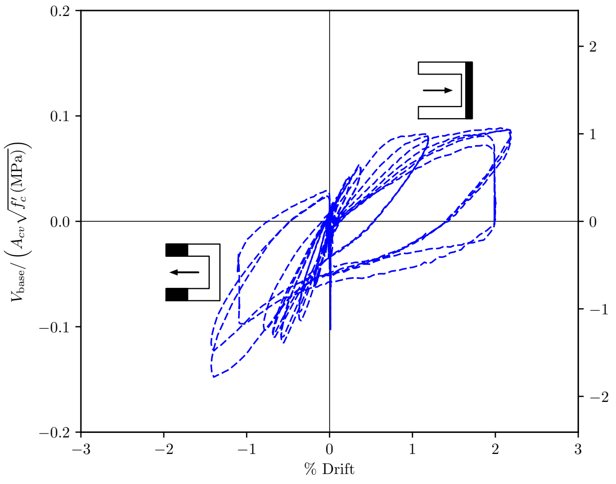

(c) Specimen CW7 - perpendicular to web

Figure 3.28: Measured load-deformation relationship for wall specimens tested by Behrouzi et al.. Specimen CW6 was loaded uni-directionally and specimen CW7 was loaded bi-directionally.

3.3.1 Experimental Observations on the Behavior of Non-Planar Walls [10]

Behrouzi et al. [10] reviewed the results of experimental research, conducted by the authors and by others, investigating the response of non-planar walls subjected to uni-directional and bi-directional loading. This review resulted in the following observations and conclusions:

- Non-planar wall deformation capacity is increased by reduction in wall axial load ratio, reduction in maximum concrete compression strain at onset of steel tension yielding, reduction in steel reinforcement ratio, and expansion of confined boundary element regions. Non-planar walls that are well detailed and designed to reduce local compression demands can sustain lateral loads to large displacement capacities (greater than 6%) and large drift capacities (greater than 2%).

- Where non-planar configurations increase the size of the compression zone and, thereby reduced compression demands, wall deformation capacity is increased. However, where non-planar configurations result in large tension regions that increase compression demands elsewhere in the wall, deformation capacity is reduced.

- Bi-directional loading does not influence the strength but reduces the deformation capacity.

- "Framing action" was used to characterize the flanges of the wall contributing to shear strength and stiffness for loading parallel to the web and perpendicular to the flanges of a C–shaped wall. It was observed near the end of the test in the C–shaped walls when loaded parallel to the web of the wall once web damage reduced web shear capacity.

- The vertical cross-sectional strain distribution of walls are not linear based on the previous data. Therefore, assuming linear strain distribution for numerical calculation of moment-curvature, as employed by many fiber-type section analysis software packages, might not always lead to accurate results. Further studies are suggested to find conditions at which the use of linear sectional analyses is inaccurate.

3.4 *Validation of the Finite Element Analysis Method for Simulating the Response of Non-planar Walls*

The results of the simulations for wall dataset considered in this study are shown in the following section. For the sake of comparison, wall specimens are categorized according to *symmetrical strength* and *asymmetrical strength* (Figure 3.29). The term *symmetrical strength* means the wall has the same strengths if loaded in positive and negative directions. For instance when a C–shaped wall is loaded parallel to the web of the wall and perpendicular to the wall axis of symmetry, then the wall exhibits same strength in both positive and negative loading directions. But if the same wall is loaded in the direction perpendicular to the web, then strength of the wall, when web is tension, is different than when the web is in compression. Figure 3.29 illustrates axis of symmetry for a T–shaped wall and *toe in tension* versus *toe in compression* directions of loading.

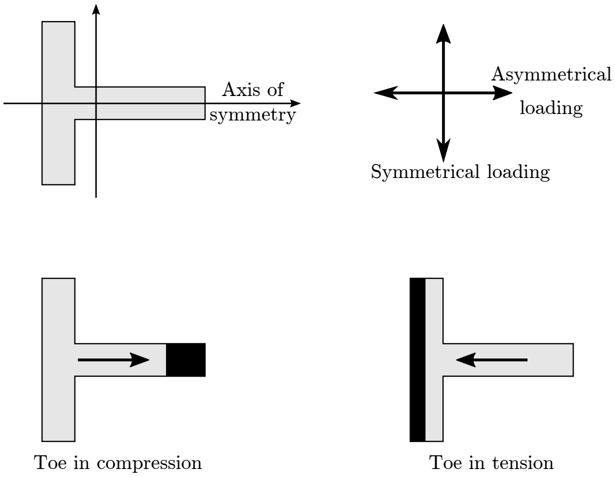

Figure 3.29: Illustration of loading direction and axis of symmetry for a T-shaped cross-section (loading parallel to the web).

Previous research by Lowes et al. [40] and Whitman [68] validated the finite element model approach for simulating the response of planar walls. This section extends that work to validate the modeling approach for simulating the response of non-planar walls subjected to uni-directional and bi-directional loading. As with planar walls, the model is validated for non-planar walls by demonstrating tha modeling approach provides accurate simulation of strength, deformation capacity in the direction of initial strength loss, and failure mode.

3.4.1 Wall Behavior and Response, Symmetric Loading

Table 3.3: Results of the simulated non-planar walls, symmetrical strength.

ID	**Stiffness to yield**1) (simu./meas.)	**Strength** (simu./meas.)	**Deformation capacity**2) (simu./meas.)	**Failure mode** (meas.)	 (simu.)
			(a) Uni-directional loading		
CW6	1.51	0.98	1.05	BR	BR
IleX	0.93	0.90	0.91	BR	BR
Mean	**1.22**	**0.94**	**0.98**		
COV	**0.24**	**0.04**	**0.07**		
			(b) Bi-directional loading		
NTW1	1.40	0.90	NA3)	NA	NA
NTW2	2.50	1.02	NA	NA	NA
CW7	2.67	0.98	1.49	BR	BR
TUA	1.44	1.05	NA	NA	NA
TUB	1.08	0.97	NA	NA	NA
IleXY	2.23	0.90	NA	NA	NA
Mean	**1.89**	**0.97**			
COV	**0.32**	**0.06**			

1) ratio of simulated to measured stiffness at yield,

2) data for wall specimens that failed in the laboratory due to loading in the perpendicular direction are not reported since bi-directional loading was not simulated,

3) not applicable.

All the walls were flexure-controlled and failed due to either compression-buckling, buckling rupture or compression-buckling. The symmetric loading direction refers to the direction at which the wall exhibits the same strength in both positive and negative direction. However, if loading is in the perpendicular direction (asymmetric strength), the strength of the wall will be different for the positive and negative directions.

Table 3.3 shows the simulated results for the wall specimens subjected to a symmetric load case in which cyclic lateral loading is applied perpendicular to an axis of symmetry with approximately equal load and deformation capacities in the positive and negative directions. All the wall specimens in Table 3.3 are loaded bi-directionally except for specimen IleX and CW6. Deformation capacity and failure mode are affected by bi-directional loading and the data provided in Table 3.3 only where failure first occurs in the symmetric load direction.

Previous research applying ATENA to simulate the response of planar RC wall test specimens validated a set of rules for post-processing simulation data characterising response under monotonic loading to accurately determine onset of strength loss (see Section 2.3.5) under cyclic loading. This approach was validated for walls subjected to unidirectional loading. Table 3.3 only compares deformation capacity and failure mode if the wall fails in this particular load direction.

Figures 3.30 to 3.33 show simulated and experimental response of walls, for the symmetrical loading condition, which includes NTW1, NTW2, CW6, CW7, TUA, TUB, IleX and IleXY. The following paragraphs, discuss comparison of simulated and measured capacity.

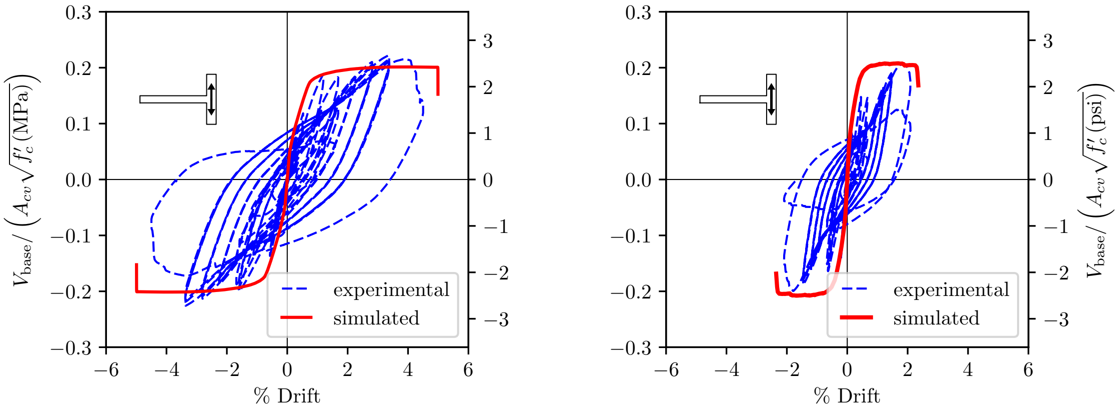

(a) Specimen NTW1, symmetric load case

(b) Specimen NTW2, symmetric load case

Figure 3.30: Measured and simulated load-deformation histories for specimens NTW1 & NTW2 tested by Brueggen [14].

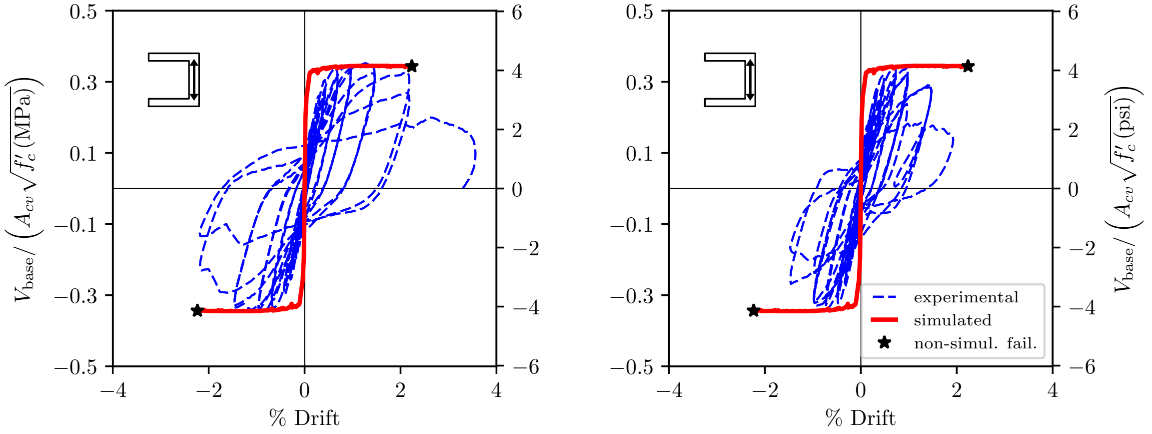

(a) Specimen CW6, uni-directional loading

(b) Specimen CW7, bi-directional loading

Figure 3.31: Measured and simulated load-deformation histories for specimens CW6 & CW7 tested by Behrouzi et al. [9] (symmetric load case).

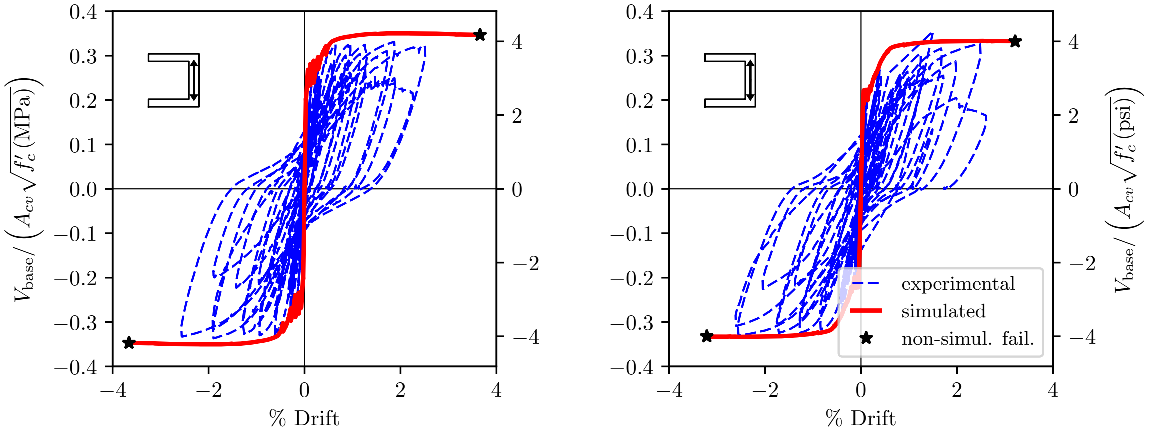

(a) Specimen TUA, web direction

(b) Specimen TUB, web direction

Figure 3.32: Measured and simulated load-deformation histories for specimens TUA & TUB (tested by Beyer et al.) [12] (symmetric load case).

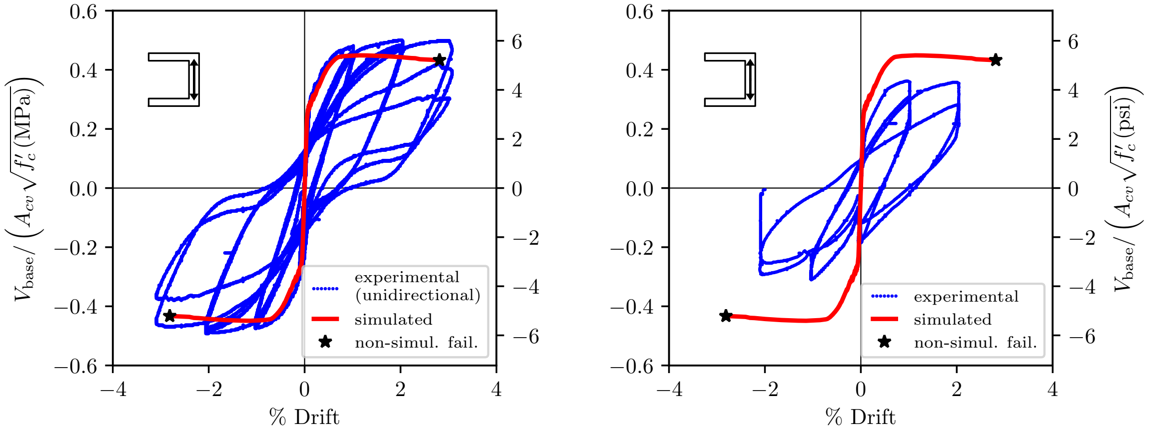

(a) Specimen IleX, uni-directional loading

(b) Specimen IleXY, bi-directional loading

Figure 3.33: Measured and simulated load-deformation histories for specimens IleX & IleXY tested by Ile and Reynouard [29] (symmetric load case).

3.4.1.1 Response History

The envelope to the shape of the hysteretic curve is well predicted by the FEM program when the loading is uni-directional. When the specimen is subjected to bi-directional loading, the envelope to the shape of the hysteretic curve is not precisely predicted. Figures 3.31 and 3.33 indicate how the response of walls affected by the effect of bi-directional loading in the laboratory. The monotonic responses from the simulation are in good agreements with the walls subjected to the uni-directional loading.

3.4.1.2 Secant Stiffness to Yield

For both laboratory and simulation data, stiffness to yield was computed as described in Section 3.2.1. Results of the average (for positive and negative loading) ratio of simulated to measured stiffness are presented in the first column of Table 3.3. These data show that simulated stiffness exceeds measured stiffness; this is typical for RC components [10, 11, 66, 67, 68]. Overestimation is typically attributed to the fact that the simulation models do not include cracking associated with shrinkage cracking, which can be significant in the laboratory where reduced-scale test specimens are much thinner than in full-scale specimens. Overestimation likely results also from failure to simulate bond-slip between concrete and steel [73]. Overestimation of stiffness is not considered to significantly affect the results of this study, which focuses primarily on failure modes and relative deformation capacity and ductility.

3.4.1.3 Strength

As is typically observed with FEM analysis, the analyses provide accurate simulation of strength; the mean ratio of simulated to measured strength for all the wall specimens in Table 3.3 is 0.97 with a coefficient of variation of 5%. For all specimens the error in simulated strength was 10% or less. This is consistent with most simulation-based studies of reinforced concrete components exhibiting flexure-controlled response, and considered adequate for the current study.

3.4.1.4 Deformation Capacity and Failure Mode

Table 3.3 provides the ratio of simulated to measure deformation capacity and failure mode for walls CW6, CW7 and IleX, as these are the only walls that exhibited strength loss due to loading in the "symmetric" loading direction. All other specimens exhibited failure due to loading in the "asymmetric" direction, either under uni-directional loading or bi-direction loading. Note that the criteria used to identify failure modes from simulation and laboratory data are presented in Section 2.3.5.

The data in Table 3.3 show that the ratio of simulated to measured deformation capacity for CW7 is large (1.49), while Specimens CW6 and CW7 had the same configuration and reinforcement layout. Specimen CW6 was loaded cyclically in the direction parallel to the web while specimen CW7 was loaded bi-directionally. The predicted to measured ratio for deformation capacity for specimen CW6 is 1.05. Specimen CW7 reached a drift capacity of 1.5% when lost its lateral load carrying capacity while CW6 reached a drift of 2.25%. Specimen CW7 loaded bi-directionally and therefore, the failure occurred in a sooner stage compared to CW6. Specimen CW6 exhibited a more ductile behavior due to uni-directional loading exposure. The ($\star$) sign in Figures 3.30 to 3.33 indicates the non-simulated failure point using the criteria described in Section 2.3.5. Failure modes are similar for both simulated and measured responses.

Figure 3.33 shows simulated and measured responses for specimens IleX and IleXY. Simulated results are close to the response of IleX which is loaded uni-directionally. These specimens were reinforced lightly and when subjected to bi-directional loading (IleXY), both strength and deformation capacities dropped significantly as it can be seen in Figure 3.33. The criteria suggested by Whitman [68], underestimates the deformation capacity of the wall when subjected to uni-directional loading but overestimates it for the bi-directional case, supporting the observation by Behrouzi et al. that bi-directional loading reduces deformation capacity.

Other specimens in Table 3.3 failed when loaded in the asymmetric direction. Therefore, deformation capacities are shown for specimens CW6, CW7 and IleX only. For both specimens the simulated failure modes are consistent with the observed failure modes in the laboratory.

3.4.2 Wall Behavior and Response, Asymmetric Strength

Table 3.4 and Figures 3.34 to 3.39 show simulated results for the wall specimens loaded parallel to axis of symmetry resulting in asymmetric strength. Table 3.1 indicates if loading was bi-directional or uni-directional. All the walls were flexure-controlled and failed due to either compression-buckling, buckling rupture or compression-buckling. The asymmetric loading direction refers to the direction at which the wall exhibits the different strengths in positive and negative direction.

Table 3.4: Results of the simulated non-planar walls, asymmetrical strength.

ID	**Yield displacement** (simu./meas.)		**Strength** (simu./meas.)		**Deformation capacity** (simu./meas.)	**Failure mode**	
	+1)	−2)	+	+	−	(meas.)	(simu.)
			(a) Uni-directional loading				
TW1	2.16	2.41	0.84	1.14	0.91	CB	CB
TW2	2.28	3.19	1.15	0.92	0.90	CB	CB
TC	0.94	1.42	0.89	0.72	1.09	CB	CB
TC-aw	1.13	1.68	0.95	0.82	1.13	CS	CS
IleY	1.31	1.00	0.92	0.92	1.18	BF	BF
Mean	**1.56**	**1.94**	**0.95**	**1.09**	**1.04**		
COV	**0.35**	0.40	**0.11**	**0.08**	**0.11**		
			(b) Bi-directional loading				
NTW1	1.13	1.19	0.98	1.04	1.11	CB	CB
NTW2	1.20	1.18	0.97	1.05	1.22	CB	CB
CW7	1.59	1.79	0.93	1.08	NA3)	NA	BF
TUA	2.12	1.57	1.03	1.01	1.20	BF	BF
TUB	1.06	1.49	1.05	1.06	1.31	CS	CB
IleXY	1.66	1.04	0.82	0.81	1.73	CS	NA
Mean	**1.46**	**1.38**	**0.96**	**1.01**	**1.31**		
COV	**0.25**	**0.19**	**0.08**	**0.09**	**0.17**		

1) Toe in compression, 2) Toe in tension, 3) not applicable

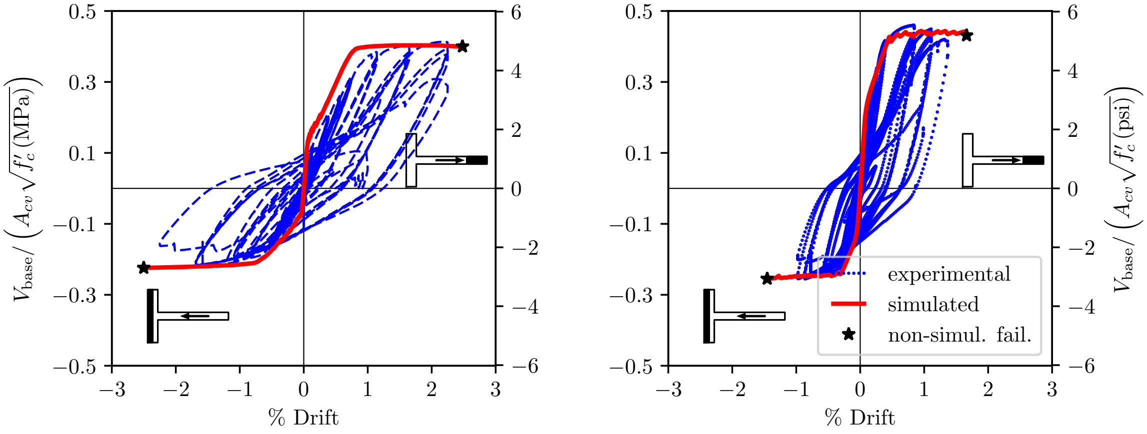

(a) Specimen NTW1, web direction

(b) Specimen NTW2, web direction

Figure 3.34: Measured and simulated load-deformation histories for specimens NTW1 & NTW2 tested by Brueggen [14].

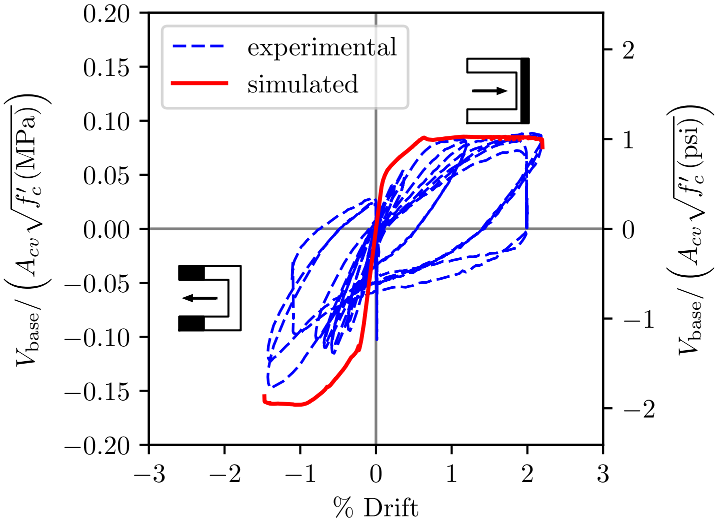

Figure 3.35: Measured and simulated load-deformation histories for specimen CW7 tested by Behrouzi et al. [9] (asymmetric load case).

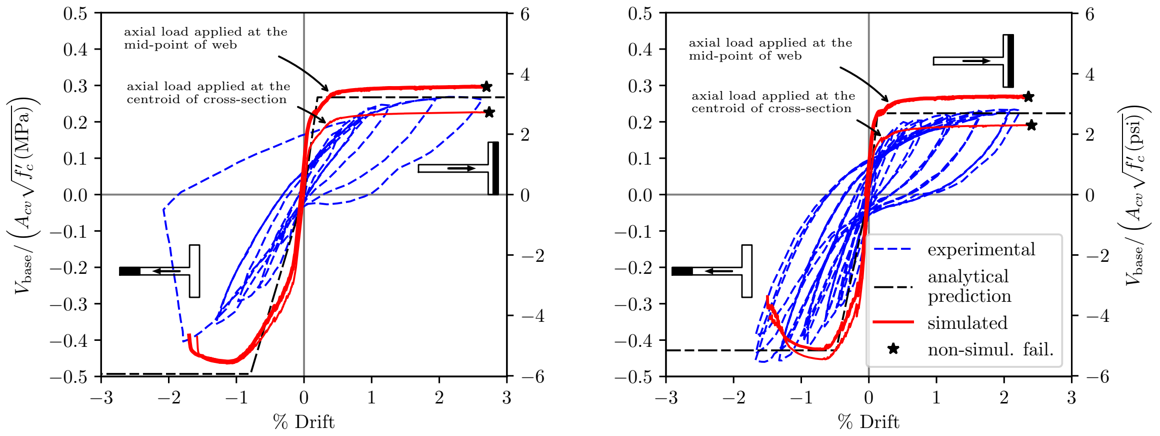

(a) Specimen TW1

(b) Specimen TW2

Figure 3.36: Measured and simulated load-deformation histories for specimens TW1 & TW2 tested by Thomsen and Wallace [59] (asymmetric load case).

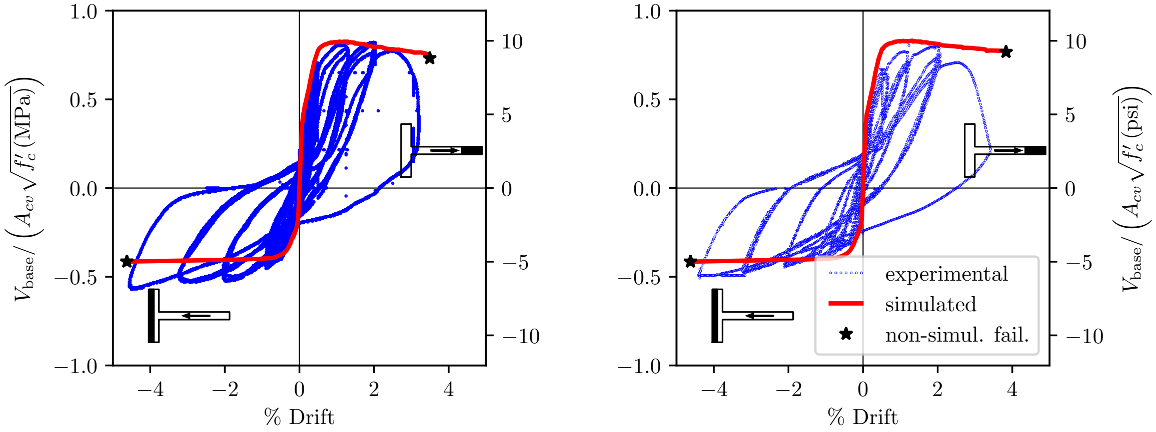

(a) Specimen TC

(b) Specimen TC-aw

Figure 3.37: Measured and simulated load-deformation histories for specimens tested by Choi et al. [21].

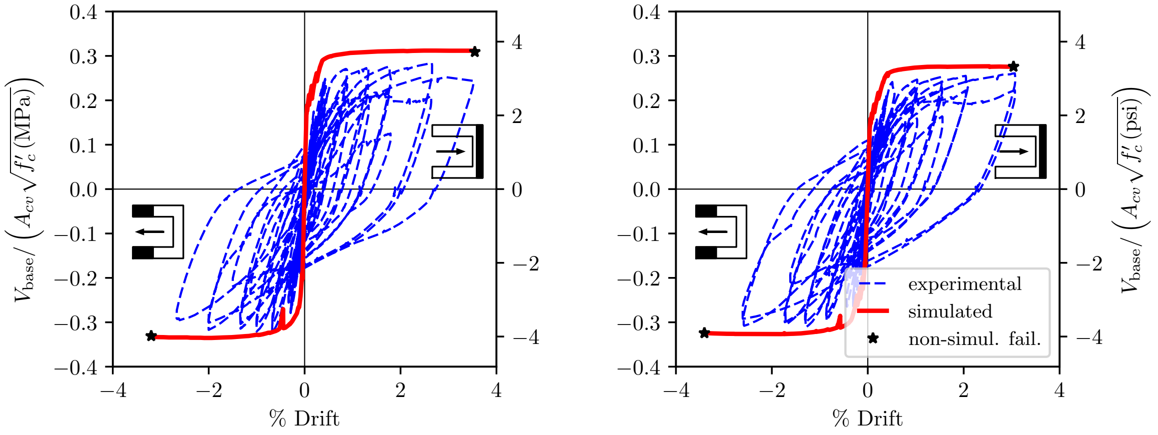

(a) Specimen TUA

(b) Specimen TUB

Figure 3.38: Measured and simulated load-deformation histories for specimens tested by Beyer et al. [12] (asymmetric load case).

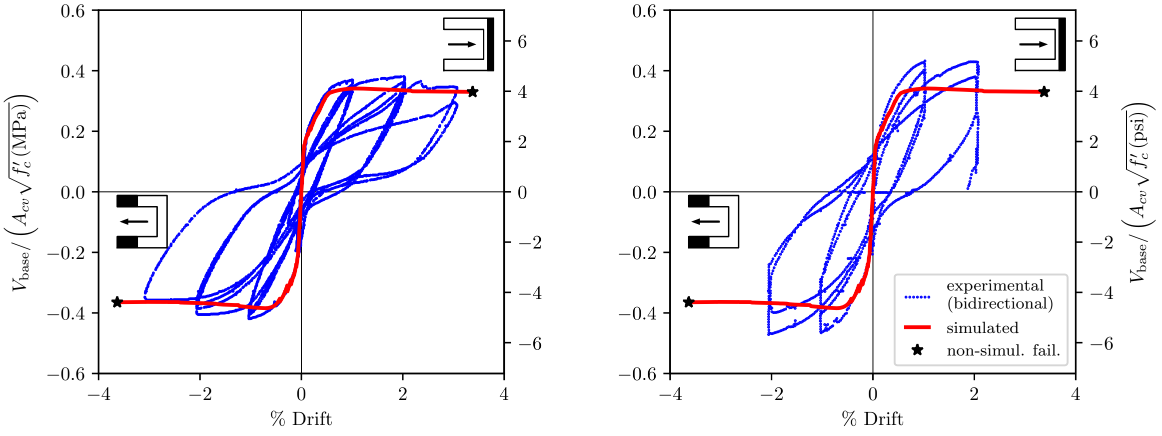

(a) Specimen IleY

(b) Specimen IleXY

Figure 3.39: Measured and simulated load-deformation histories for specimen IleY tested by Ile and Reynouard [29] (asymmetric load case).

As discussed in Section 3.2.2, Thomsen and Wallace [58] do not provide information about the location of the applied load. Since the axial load produces a moment if not applied at the center of the specimen, it will affect the overall results, mainly the deformation capacity. To account for the exact location to apply the axial load, two cases are considered so that the real case is bound in between. In one case, axial load is applied at the centroid of the section while it is applied at the centroid of the web in the second case. Both cases are shown in Figures 3.36a and 3.36b.

Analytical predictions by authors for TW1 and TW2 are also shown in Figure 3.36. When toe is in tension for TW1, the measured strength is smaller than the analytical prediction provided by the authors. The authors attribute this difference to one of the two reasons discussed in the following. First, it is possible that the boundary reinforcement is prevented from acting as flexural reinforcement alone due to the shear demand on the wall specimens, when flange is in compression, and as a result has reduced the measured capacity. The second reason is that the eccentrically applied axial load has caused an initial shift in the lateral load and led to low measured moment capacity.

When flange is in compression, measured strengths are bounded by both cases which suggest that the actual point at which the axial load resultant is applied can be between the centroid of the cross-section and mid-point of the web. This is the case for both specimens as indicated in Figure 3.36. The simulated results shown in Table 3.4, are the average of both cases of axial loading.

3.4.2.1 Envelope Comparison

The envelope to the response history is well predicted by the program for most specimens. For specimen IleXY the simulated result is different from the envelope the response history for both the strength and deformation capacity. However, the same wall, when subjected to uni-directional loading (IleY), the predictions are very similar to the measured response. This difference could be due to the loading mechanism in the laboratory that causes relatively significant difference between both specimens. The envelope to the response histories for specimens TW1 and TW2, are also not exactly predicted and the differences, as mentioned in Sections 3.2.2 and 3.4.2.3, are due to the axial load location and possible loading approach during the test.

3.4.2.2 Secant Stiffness to Yield

As for loading perpendicular to the axis of symmetry, comparison of secand stiffness to yield for simulated and experimental data indicate that the FE model overestimates stiffness. Data suggests that overestimation is not a function of bi- versus uni-directional loading. For uni-directional loading case the mean value for the simulated to measured displacement at yield is 1.75 while it is 1.42 for bi-directional loading case.

3.4.2.3 Strength

The FE model provides accurate and precise simulation of strength. The mean ratio of simulated to measured shear strengths are 0.97 and 0.99 for toe in compression and toe in tension direction, respectively with coefficients of variation of 8% and 12%.

For **most** specimens, the ATENA simulation for monotonic loading provides on accurate representation of the envelope of the measured response history. This is true for both C- and T-shaped walls as well as walls subjected to uni- and bi-directional loading. Two egregious exceptions to this are CW7 and TW1. For these walls, strength gain in the “strong” direction when activates the largest volume of long steel, was slower with increasing displacement demand than was simulated. For CW7 the slower strength gain observed in the laboratory is likely due to reduced stiffness resulting from bi-directional loading. For TW1 and to some extent, TW2, which subjected to uni-directional loading, it is possible to softer lab response is due to the loading approaches where other T-shaped walls were loaded via stiff loading block at the top of the specimen.

3.4.2.4 Deformation Capacity and Failure Mode

Simulated failure modes and non-simulated drift capacities for wall specimens in the asymmetric strength direction are summarized in Table 3.4. Deformation capacities and failure modes reported in Table 3.4 are based on criteria explained in Section 2.3.5. Majority of the wall specimens considered in this research study, failed when toe of the cross-section was in compression in the test. Simulations, resulted in a mean ratio of simulated to measured deformation capacity of 1.07 with a coefficient of variation of 0.13. Specimens loaded bi-directionally, show highest deviation from the experimental results. In other words, deformation capacity is over predicted by the program since simulations are monotonic.

Simulated failure modes in the analyses are consistent with the observed failure modes in the tests except for specimen TUB which exhibited a shear failure mode in the laboratory. This failure occurred when the specimen was loaded in the diagonal direction (from point H to B in Figure 3.15) [12]. Diagonal loading could not be captured in the simulations and as a result the crushing-shear failure mode was not depicted for this specimen. Bi-directional loading can also affect the failure mode of the specimens as observed in the tests performed by Ile and Reynouard [29]. Both IleX and IleY specimens failed due to bar fracture but IleXY, which was identical to both IleX and IleY except loaded bi-directionally, failed due to shear (Figure 3.12).

3.5 Simulated Stress and Strain Fields

Beyond stiffness, strength, deformation capacity and failure mode, continuum analysis provides information also about stress and strain fields, damage patterns, and response mechanisms. Figures 3.40 to 3.52 provide simulated vertical strain and minimum principal stress fields for the test specimens listed in Tables 3.3 and 3.4. These two fields provide the greatest understanding of non-planar wall response mechanisms and failure modes. In all figures, the cyan color line on the cross section, indicates the surface for which the stress/strain field is shown.

Effective flange width influences the strength and deformation capacity by affecting the compression area of the all. Therefore, it is important to understand the effective flange width that is engaged during lateral deformation of the wall. Stress transfer affects the failure mode experienced by the wall and it is essential to understand and investigate the nature of load transfer in walls with flanges for improving design of such walls. The following sections discuss the effective flange width and load transfer in non-planar walls using the simulated stress and strain fields.

3.5.0.1 Effective Flange Width

To simplify and provide conservatism in the the design process, the ACI Code introduces the concept of an "effective flange width" for non-planar walls. The effective flange width is defined as "lesser of one-half the distance to an adjacent wall web and 25 percent of the total wall height". Concrete and steel outside of the effective flange width cannot be considered in determining wall strength or stiffness. The Code commentary states that the portion of the flange that is effective in resisting loads increasing with increasing drift and varies depending on whether the flange is in tension or compression, with the effective flange width used for compression having minimal impact on predicted strength or stiffness.

Simulated strain field data provide an ideal mechanism for investigating the extent which concrete and reinforcing steel in wall flanges are engaged to resist compression and tension resulting from flexural loading. Vertical strain distribution in the flanges of both specimens TW1 and TW2 are shown in Figure 3.40. The main differences between the two specimens are the length and confinement ratio of the boundary element at the toe. The results show a nonlinear vertical strain field. Vertical strain distribution is neither constant across the flange width nor linear as moving towards the toes of the flanges. This nonlinear strain distribution is observed in all of the specimens with heavily reinforced boundary elements and lightly reinforced web region. This is different from the typical design assumption that plane sections remain plane indicating a uniform strain distribution across the flange. This is more clear in Figure 3.41. The left figure shows a completely nonlinear strain distribution in the flange for specimen NTW1 which has a non-uniform reinforcement distribution in the flange. However, having a uniform reinforcement distribution in the flange of the specimen NTW2, right figure, the strain distribution is changed to an almost uniform shape. This behavior is investigated via an "effective flange width study" presented in Section 5.5.

Figure 3.42 shows the minimum principal stress distribution in the web for specimens TW1 and TW2 when toe is in compression. Specimen TW2 is identical to TW1 except it has a longer confinement depth at the toe of the web. The results show that providing longer boundary elements could prevent a CS failure (Figure 3.42a) and result in a CB failure (Figure 3.42b). Specimens NTW1 and NTW2 are both ACI compliant and because they are provided with adequate confinement length in the toe of the web, both exhibited CB failures. The stress field for both specimens are shown in Figure 3.44a and Figure 3.44b, respectively.

When flanges in T–shaped walls are in compression (Figure 3.43c and Figure 3.43d), less demands are expected on the concrete and flange due to smaller depth of neutral axis. The stress fields for both specimens NTW1 and NTW2 when flange is in compression show that the N.A. depth is very small. The same observations can be made for C–shaped walls when web of the wall is in compression. These are shown in Figure 3.45a (specimen TUA), Figure 3.47a (specimen TUB), Figure 3.50a (specimen CW7) and Figure 3.51a (specimen IleY).

Figures 3.46, 3.49 and 3.52 show the stress fields for specimens TUA, TUB, CW6/CW7 and IleX, respectively, when loaded in the direction parallel to the axis of symmetry (parallel to the web). Results show that in all cases the crushing of concrete and failure were initiated in the unconfined region of the flanges and then in some cases it extended into the boundary element.

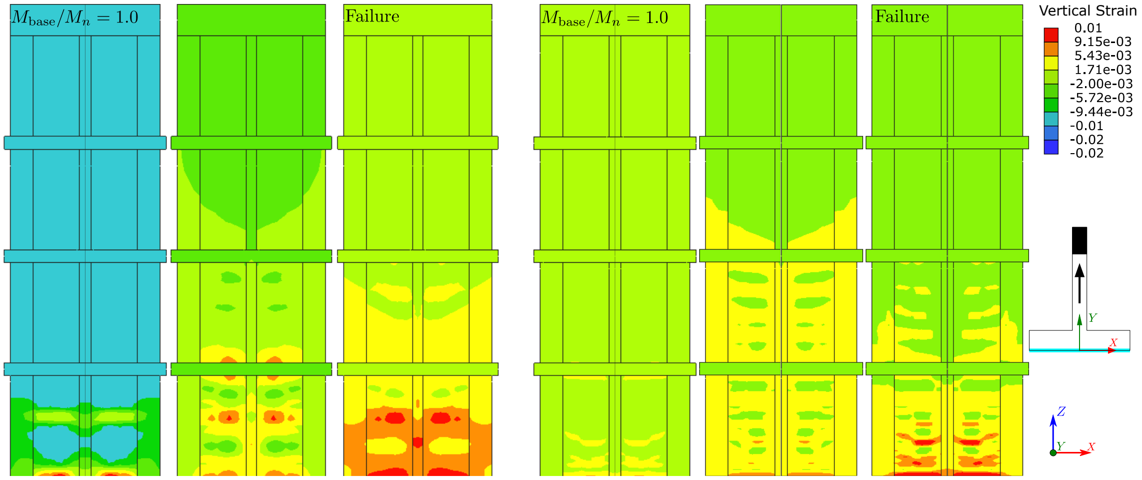

(a) Specimen TW1 **(b)** Specimen TW2

Figure 3.40: Vertical strain distribution in the flange for specimens TW1 and TW2 (tested by Thomsen and Wallace) simulated monotonically in ATENA (Toe in compression).

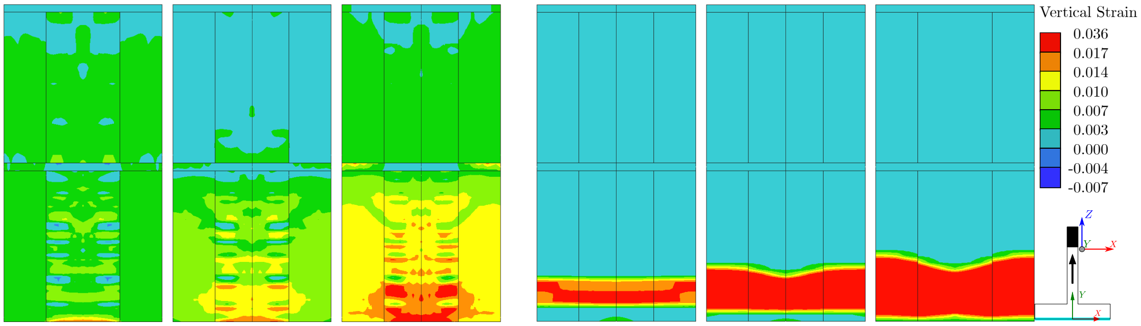

(a) Specimen NTW1, heavily reinforced boundary elements

(b) Specimen NTW2, uniform reinforcement configuration

Figure 3.41: Vertical strain distribution in the flange for specimens NTW1 and NTW2 (tested by Brueggen) simulated monotonically in ATENA (Toe in compression).

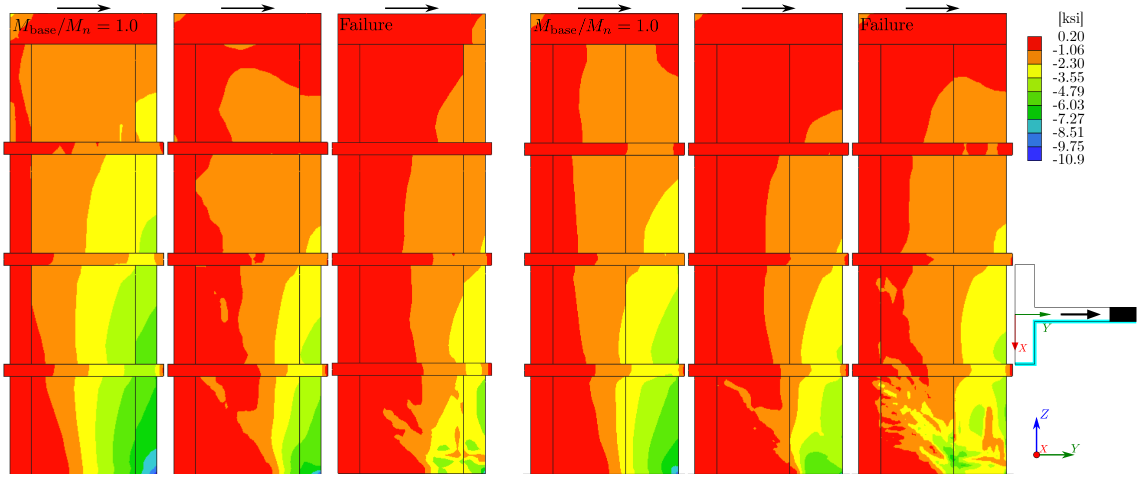

(a) Specimen TW1 **(b)** Specimen TW2

Figure 3.42: Minimum principal stress distribution in the web for specimens TW1 and TW2 (tested by Thomsen and Wallace) simulated monotonically in ATENA (Flange in tension).

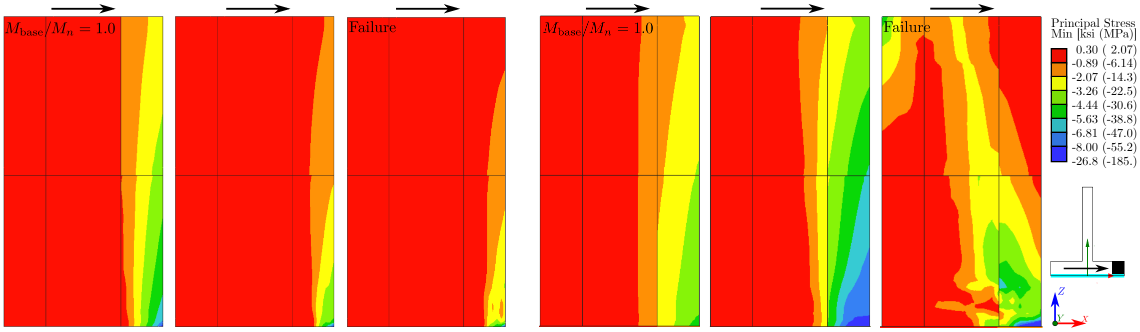

(a) Specimen NTW1 **(b)** Specimen NTW2

Figure 3.43: Minimum principal stress distribution for specimens NTW1 and NTW2 (tested by Brueggen) simulated monotonically in ATENA (Flange elevation).

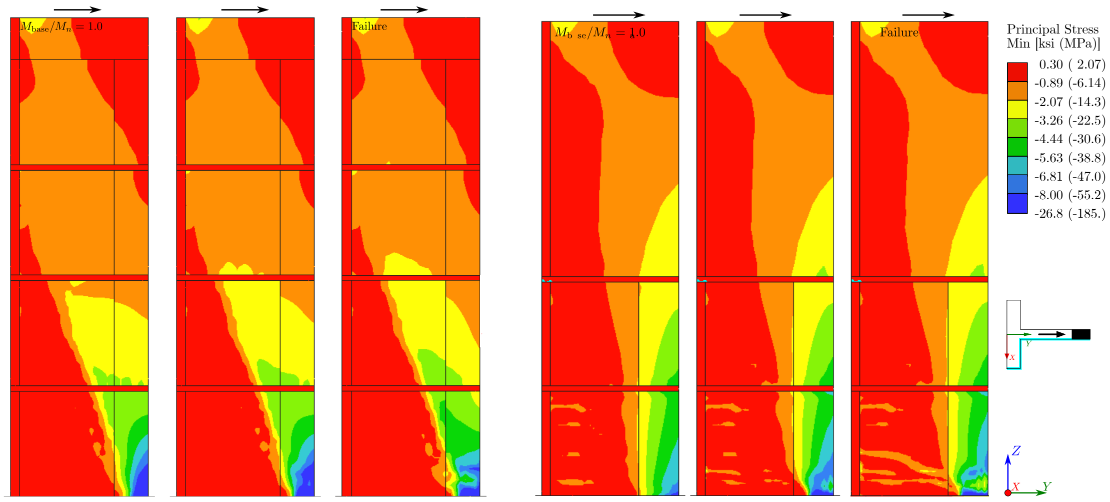

(a) Specimen NTW1, toe in compression **(b)** Specimen NTW2, toe in compression

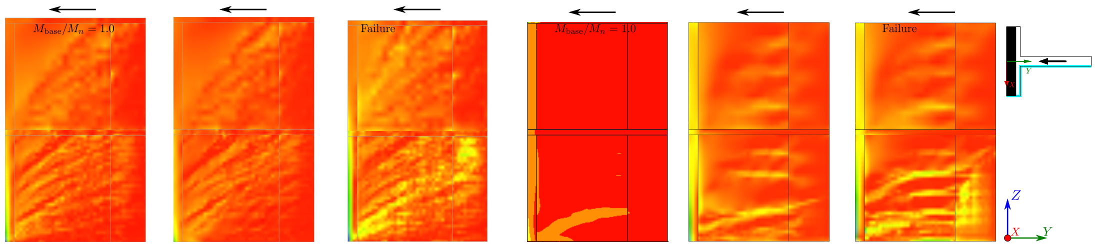

(c) Specimen NTW1, toe in tension (only bottom two stories are shown) **(d)** Specimen NTW2, toe in tension (only bottom two stories are shown)

Figure 3.44: Minimum principal stress distribution for specimen NTW1 & NTW2 (tested by Brueggen) simulated monotonically in ATENA (web elevation).

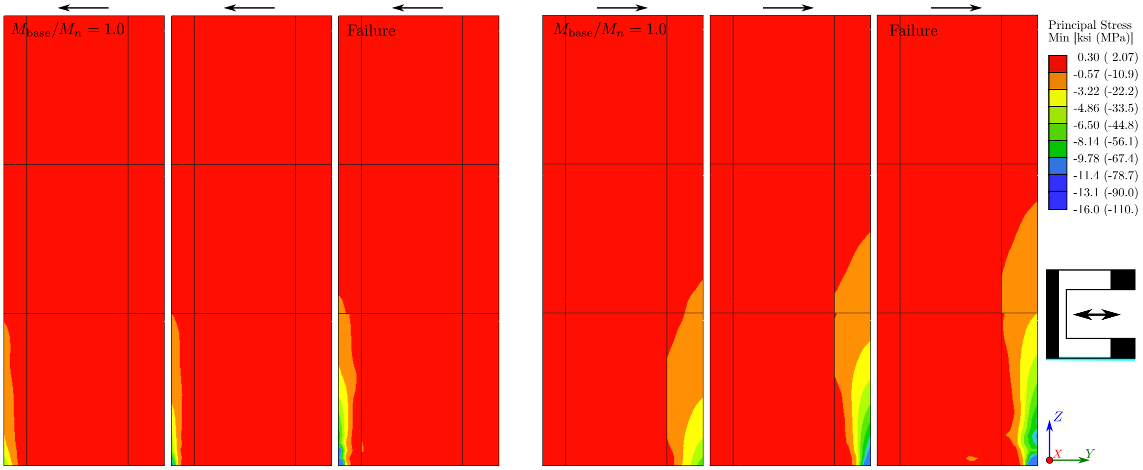

(a) Minimum principal stress, toe in tension **(b)** Minimum principal stress, toe in compression

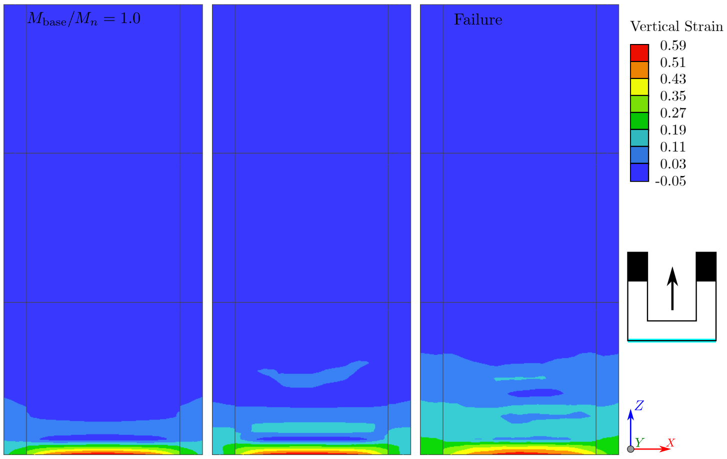

(c) Vertical strain, toe in compression

Figure 3.45: Minimum principal stress and vertical strain distribution for specimen TUA (tested by Beyer et al.) simulated monotonically in ATENA (loading parallel to flange).

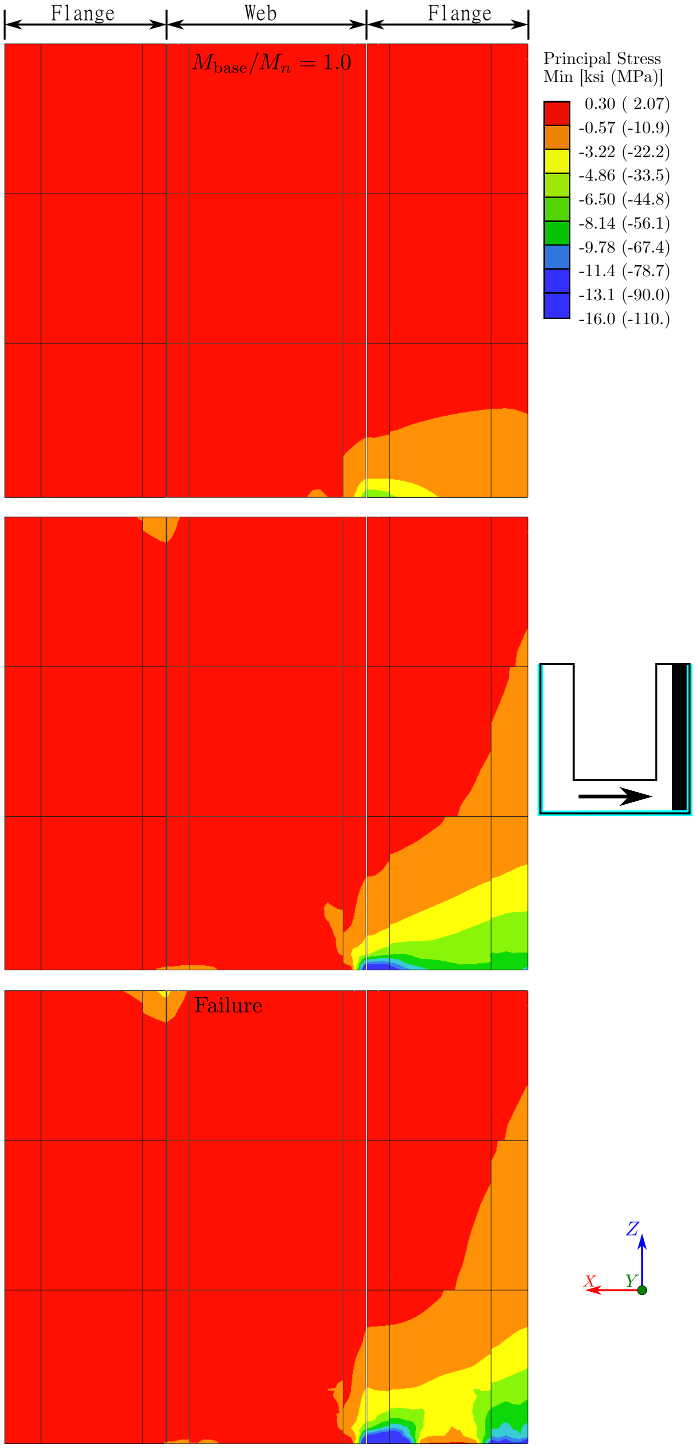

Figure 3.46: Minimum principal stress distribution for specimen TUA (tested by Beyer et al.) simulated monotonically in ATENA (loading parallel to web).

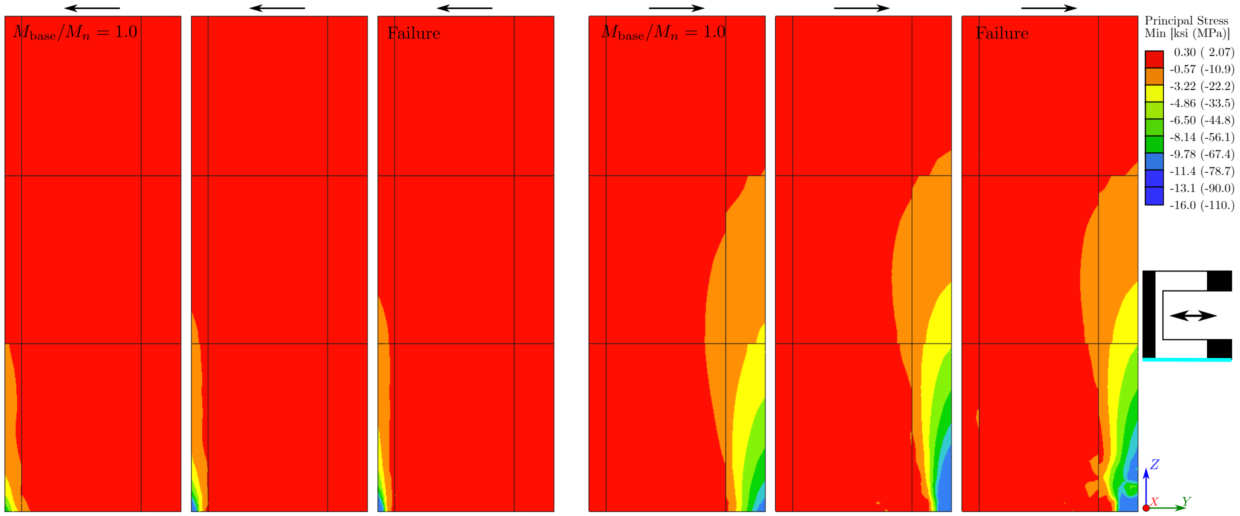

(a) Minimum principal stress, toe in tension **(b)** Minimum principal stress, toe in compression

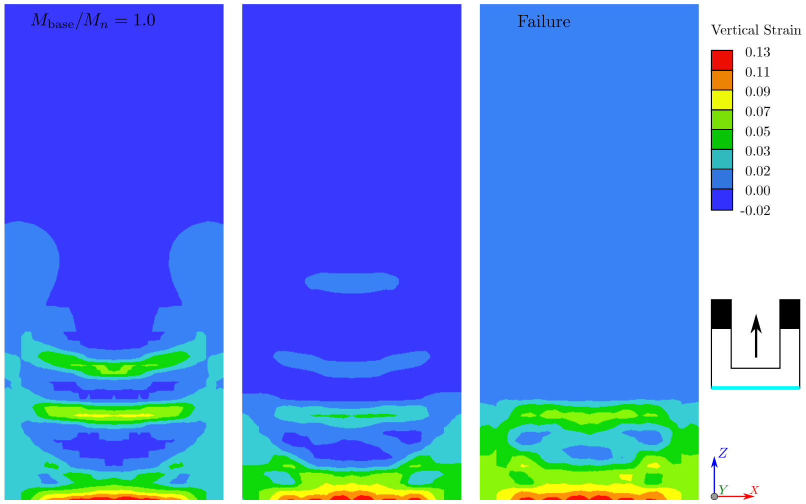

(c) Vertical strain, toe in compression

Figure 3.47: Minimum principal stress and vertical strain distribution for specimen TUB (tested by Beyer et al.) simulated monotonically in ATENA (loading parallel to flange).

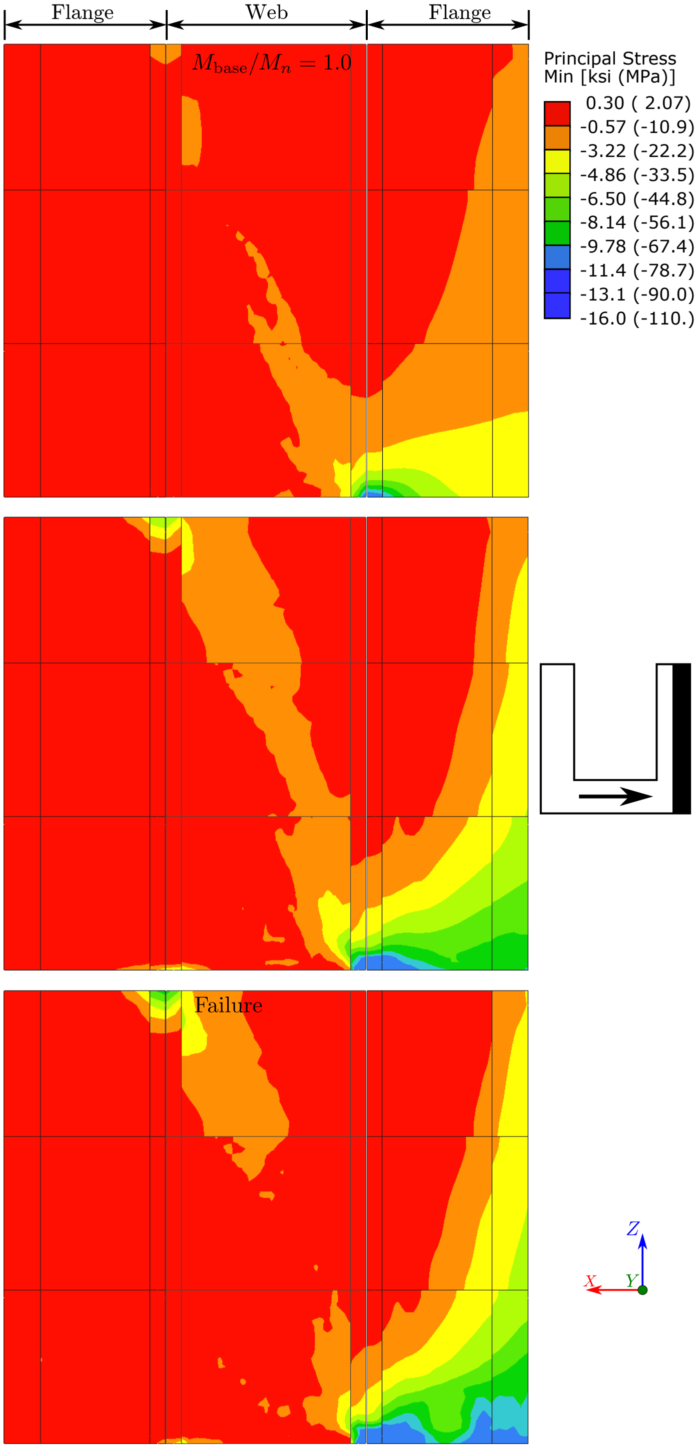

Figure 3.48: Minimum principal stress distribution for specimen TUB (tested by Beyer et al.) simulated monotonically in ATENA (loading parallel to web).

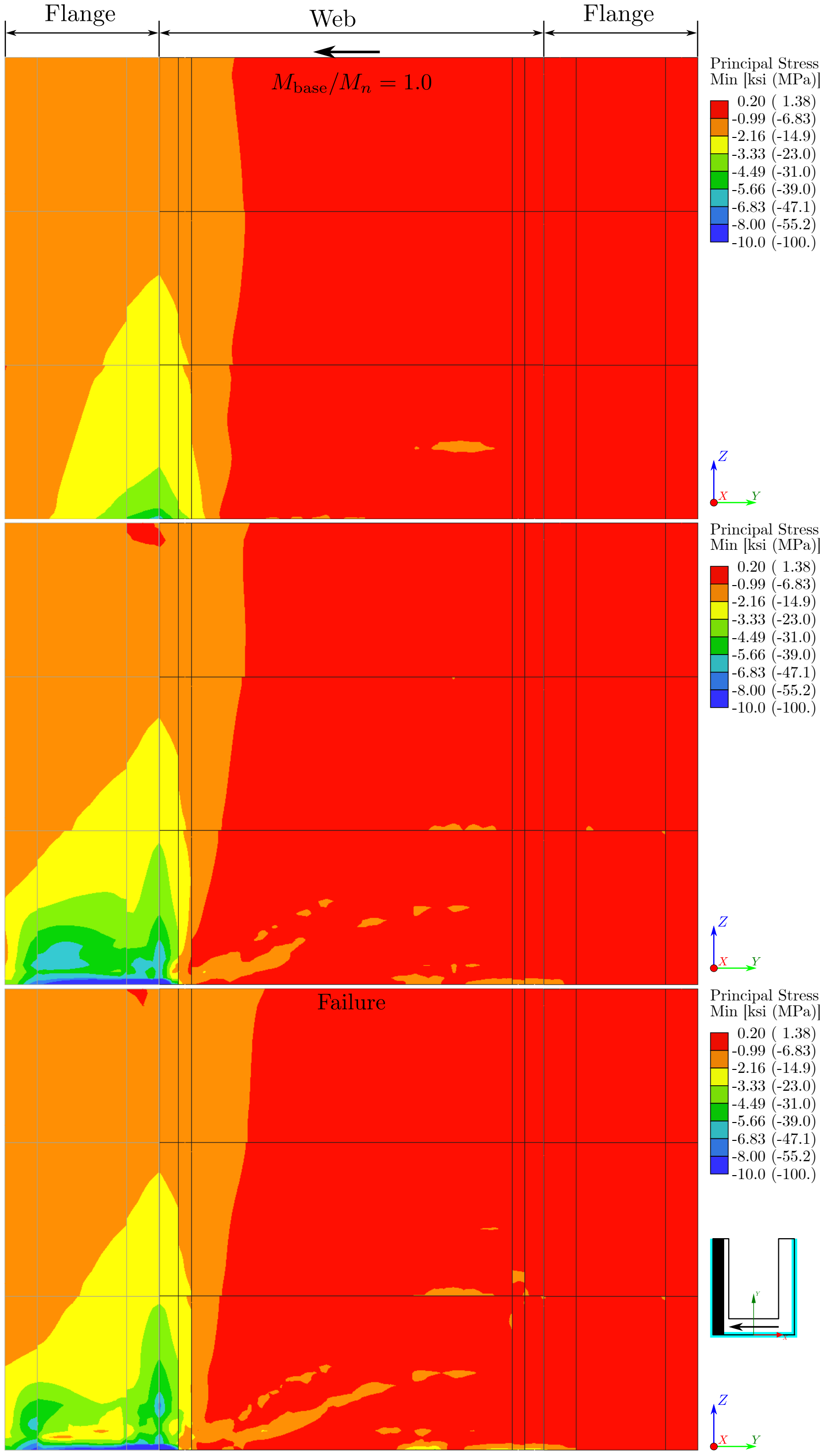

Figure 3.49: Minimum principal stress distribution for specimen CW6 & CW7 (tested by Lowes et al.) simulated monotonically in ATENA (Strong direction). The complete animation showing the minimum principal stress distribution for Specimen CW6 can be viewed at https://youtu.be/MNjDsmjjwhY.

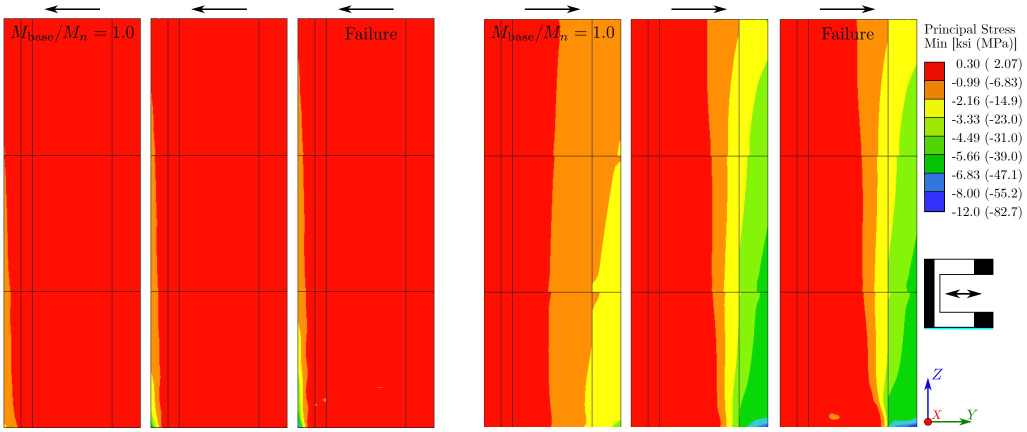

(a) Minimum principal stress, toe in tension

(b) Minimum principal stress, toe in compression

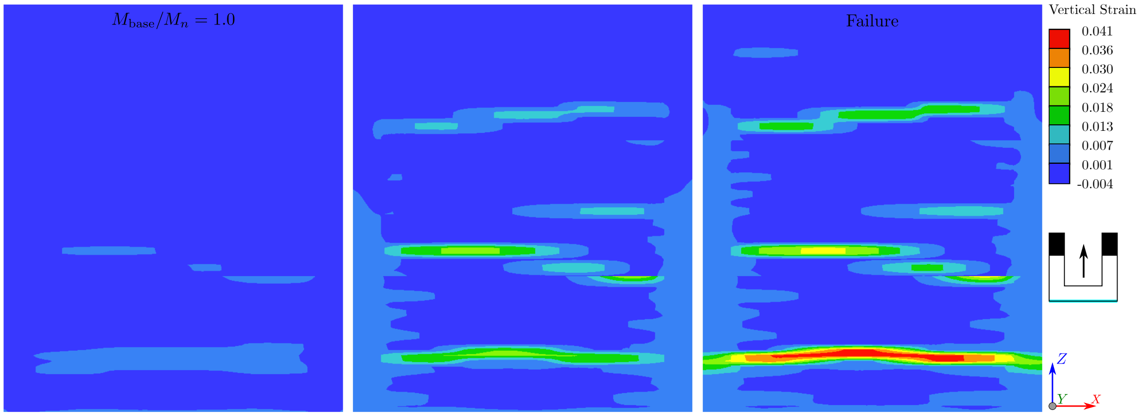

(c) Vertical strain, toe in compression

Figure 3.50: Minimum principal stress and vertical stress distribution for specimen CW7 (tested by Lowes et al.) simulated monotonically in ATENA (Flange in tension).

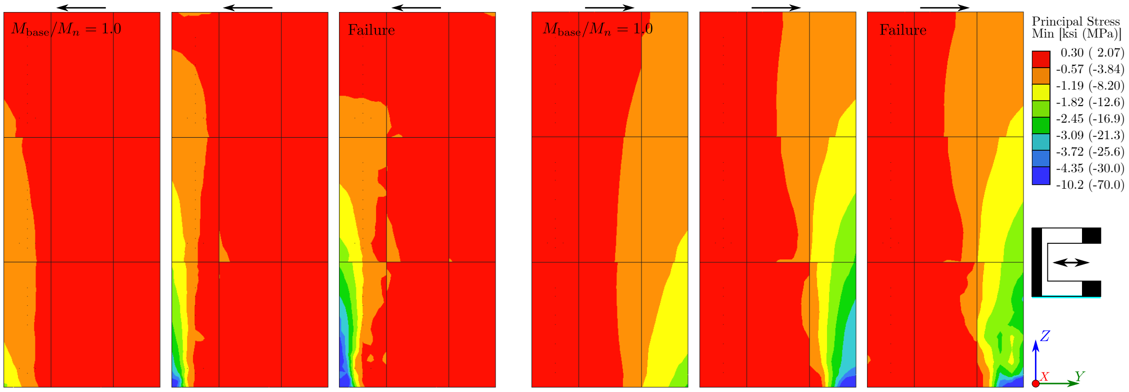

(a) Minimum principal stress, toe in tension **(b)** Minimum principal stress, toe in compression

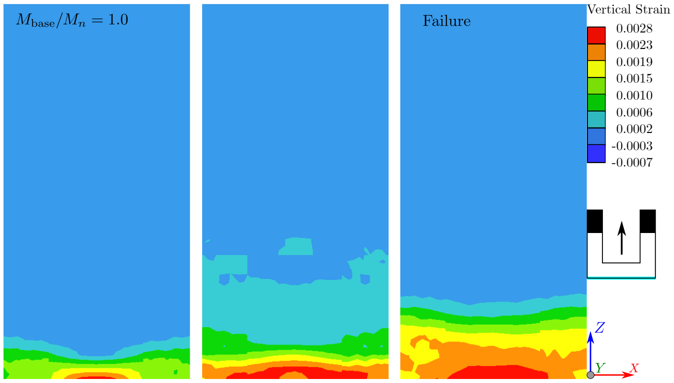

(c) Vertical strain, toe in compression

Figure 3.51: Minimum principal stress and vertical strain distribution for specimen IleY (tested by Ile and Reynouard) simulated monotonically in ATENA.

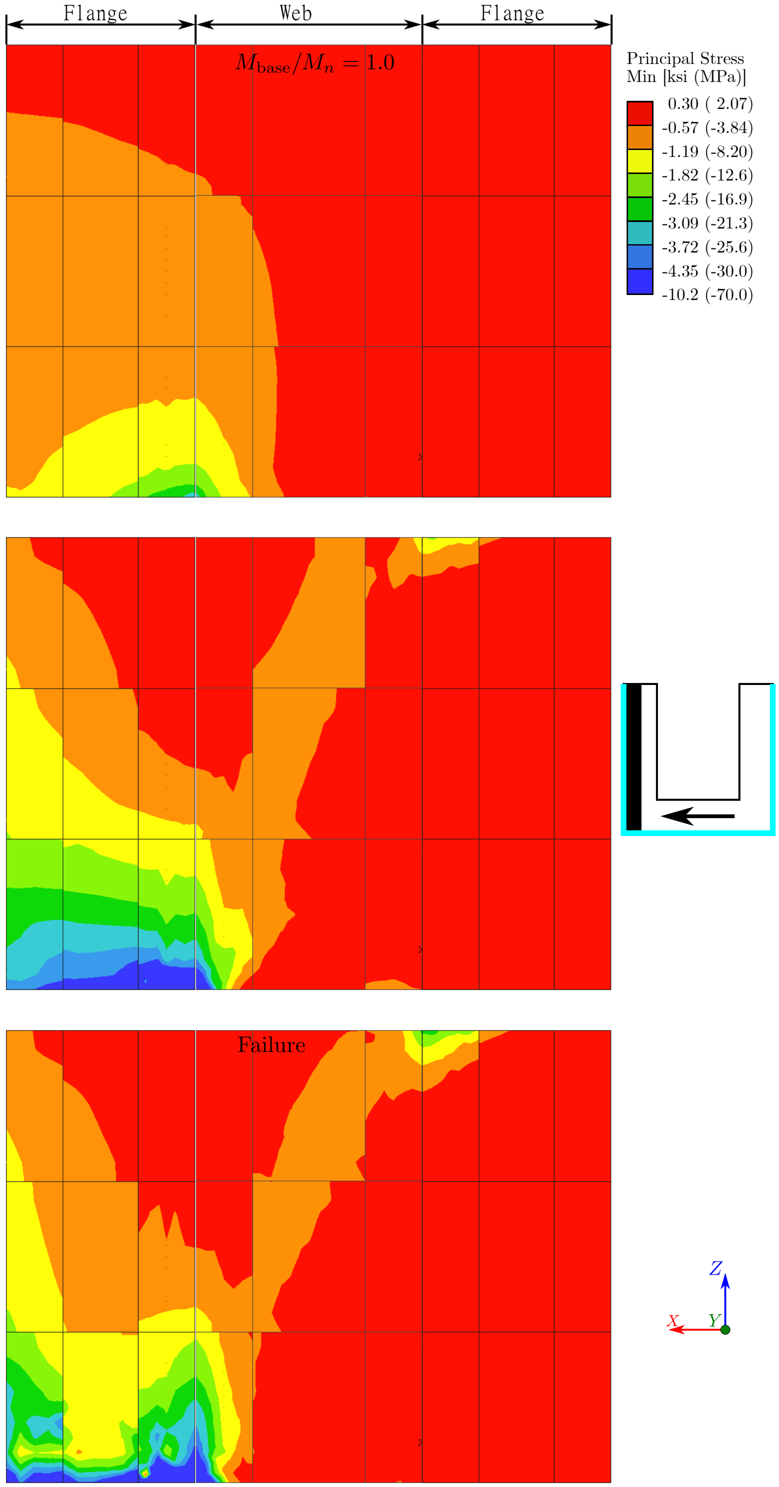

Figure 3.52: Minimum principal stress distribution for specimen IleX (tested by Ile and Reynouard) simulated monotonically in ATENA.

3.5.1 Shear Transfer

Results of continuum analysis of planar walls and experimental data indicate that in planar walls, shear is transferred via a compressive strut and that shear and flexure induced compression interact to reduce deformation capacity for walls with high shear or cross-sectional aspect ratio (wall length divided by wall width [40]). Thus, to investigate shear transfer in flanged walls, minimum principal stress fields were considered. Figure 3.44 shows the minimum principal stress distribution for specimens NTW1 and NTW2 (web elevation). Specimen NTW2 has uniform reinforcement distribution in the flange. Both loading directions (toe in compression and toe in tension) are shown for NTW2. The transfer of shear, when toe is in compression, can be clearly seen and major part of the boundary element contributes in compression stress caused by shear transfer. In fact, neutral axis depth at the base, is a little smaller than the length of the boundary element. On the other hand, when flange is in compression, the depth of the neutral axis is smaller than the flange thickness. Therefore, shear is transfer is different and the wall is expected to undergo a higher deformation for smaller strengths.

3.6 Summary and Conclusion

Continuum analyses were completed for six T–shaped and seven C–shaped concrete walls exhibiting flexure-controlled response under gravity and lateral loading in the laboratory. In the laboratory, wall were subjected to uni-directional or bi-directional cyclic lateral loading; simulations employed lateral loading applied under monotonically increasing displacement demand. Analysis results demonstrates the ability of the software to simulate response observed in the laboratory as well as provide improved understanding of the equivalent behavior of walls with complex configurations.

Comparison of simulated and measured responses supports the following observations:

- Wall strength is accurately and precisely simulated (average error of 0.03 with a COV of 0.12) using continuum analysis with solid elements,

- Simulated stiffness to yield exceeds measured stiffness. This is typical for finite element analyses that do not include simulation of bond-slip and shrinkage induced cracking [11, 68, 73],

- Deformation capacity of the walls were simulated accurately for most of the walls. For uni-directional loading, the deformation capacity were predicted with acceptable accuracy (with average of simulated to measured deformation capacity of 1.04 and COV of 0.10). Deformation capacity was over predicted for most walls subjected to bi-directional loading as the bi-directional loading reduces the deformation capacity of the wall compared to uni-directional loading (average of simulated to measured deformation capacity of 1.34 and COV of 0.16),

- Predicted failure modes are consistent with the observed failure modes in the lab for almost all the specimens.

simulation results including simulated stress and strain fields reinforcing the results of previous studies and provide new insight into non-planar wall behavior under lateral loading

- Vertical strain fields show that plane sections do not remain plane. In particular the distribution of longitudinal reinforcement in wall flanges influences the vertical strain field in the tension region of the wall and the extent to which vertical reinforcing steel is engaged. This has implications for the ACI code's effective flange with definition.

- Shear transfer and formation of compression struts are different for flanged walls compared to planar walls. The depth of neutral axis, in the case of existence of a flange in compression, is reduced significantly and as a result the wall undergoes higher deformation for smaller strengths.

Simulation results for non-planar walls tested in the laboratory suggest the opportunity for further simulation-based research to investigate the impacts of shear stress demand, cross-sectional configuration, flanges and reinforcement distribution. Thus, the simulation results presented in this chapter provide the impetus for the simulation-based parameter studies presented in Chapter 5.

Chapter 4

FINITE ELEMENT MODELING OF RC WALLS WITH OPENINGS TO INVESTIGATE BEHAVIOR

4.1 Introduction

The use of walls with openings is very common in buildings, Openings are necessary for a variety of reasons including doors, windows and utilities. At any given floor, openings may be located in the middle, near the perimeter or at the perimeter of the wall. Vertically, openings may be stacked or staggered; Figure 4.1 shows common vertical opening patterns. Often, the need for "stacked" openings in walls results in a coupled wall system. In a coupled wall system, wall resist load via shear and flexure, but lateral load is primarily resisted through the development of a tension-compression couple in which one of the walls carries primarily tension and the other primarily compression and coupling beams (located between the stacked openings) transfer load between the walls via shear (see Figure 4.2). A wall is considered a coupled wall as the degree of coupling (DOC), which is defined as percentage of the total base moment carried by the tension-compression couple, decreases [27, 61]. Investigation of coupled wall response is outside the scope of the current study.

This study investigates load transfer mechanisms in walls with openings and the impact of these openings on performance. In this chapter, the results of previous experimental tests of walls with openings subjected to gravity and lateral load are simulated to verify the previously presented FEM modeling approach for this class of walls. The results of these simulations are interrogated to provide understanding of the impact of openings on wall performance. Section 4.2 presents experimental tests of walls with openings conducted previously by others; Section 4.3 presents the results of numerical simulation of these test specimens and conclusions about behavior supported by the simulation data. Chapter 6

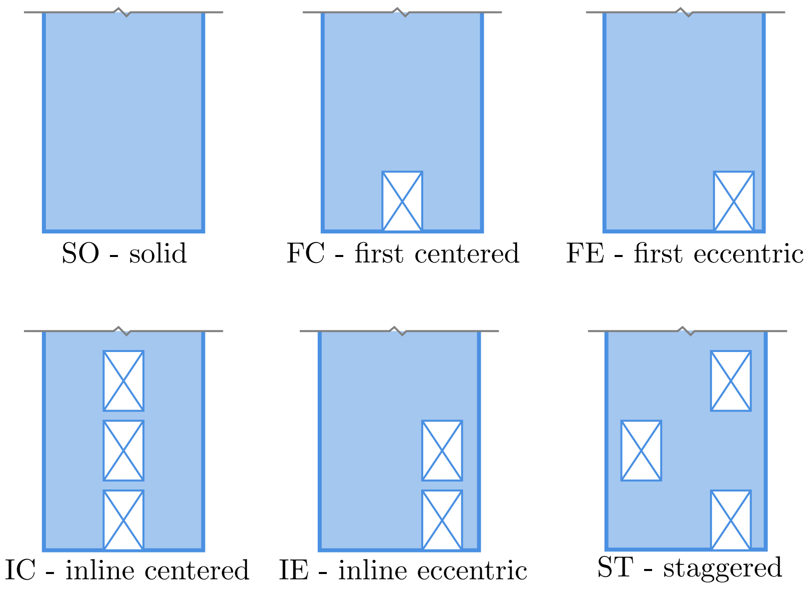

SO - solid FC - first centered FE - first eccentric

IC - inline centered IE - inline eccentric ST - staggered

Figure 4.1: Clarification of the icons used for openings in walls.

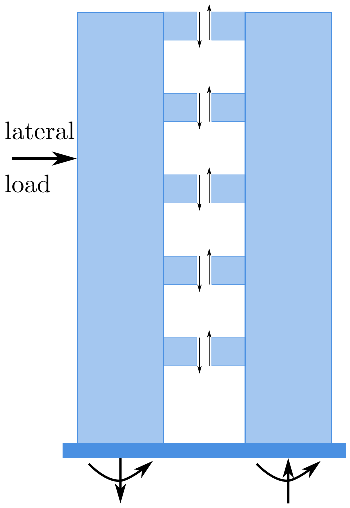

Figure 4.2: Overturning moment resistance of coupling beams.

presents a numerical parameter study conducted to investigate the impact of range of wall opening patterns on wall performance.

4.2 Previous Experimental Investigation of Walls with Openings

Previous research by others has employed experimental testing to investigate the behavior of concrete walls with openings. A review of the literature resulted in seven studies conducted at laboratories around world. Study parameters included horizontal location of an opening at the base of the wall, vertical opening pattern and opening size. Tables 4.1 to 4.3 presents data characterizing the wall tests. In Table 4.1 data are organized by test program; in Table 4.2 data are organized by wall opening pattern. All parameters included in Tables 4.1 and 4.2 are defined in the parameter list in the list of symbols, and newly introduced parameters are defined in table notes. Figure 4.1 clarifies wall configuration icons. All specimens were subjected to reversed cyclic lateral loading under displacement control, with load applied at the top of the specimen. Some specimens, as identified in Tables 4.1 and 4.2 were subjected also to constant axial load.

Table 4.1: Measured properties of walls with openings by author.

Author	**ID**	$\mathbf{\frac{P}{A_g f'_c}}$	$\mathbf{t_w}$	**Opening size**		$\frac{\ell_{\text{opening}}}{\ell_{\mathbf{w}}}$	**Reinforcement**		$\mathbf{V_{max}/\left(A_{cv}\sqrt{f'_c}\right)^{1)}}$		**Failure mode**
				width	**height**		ρ_{BE}	ρ_t	+	-	
			in. (mm)	in. (mm)	in. (mm)		%	%	psi (MPa)	psi (MPa)	
Ali and Wight (1991)	W1	0.07	3 (76)	-	-	0.00	3.0	0.4	3.56 (0.30)	-3.47 (0.29)	CB
	W2	0.07	3 (76)	10 (254)	20 (508)	0.21	3.0	0.4	4.39 (0.36)	-4.77 (0.40)	CS
	W3	0.07	3 (76)	10 (254)	20 (508)	0.21	3.0	0.4	4.49 (0.37)	-4.15 (0.34)	CS
	W4	0.07	3 (76)	10 (254)	20 (508)	0.21	3.0	0.4	4.55 (0.38)	-3.91 (0.32)	CS
Yanez et al. (1992)	S1	0	4.72 (120)	-	-	0.00	0.5	-	2.38 (0.20)	-2.28 (0.19)	CB/BR
	S2	0	4.72 (120)	23.62 (600)	23.62 (600)	0.30	1.25	0.47	3.21 (0.27)	-3.37 (0.28)	CB/BR
	S3	0	4.72 (120)	23.62 (600)	23.62 (600)	0.30	0.84	0.47	2.99 (0.25)	-3.31 (0.27)	CB/BR
	S4	0	4.72 (120)	15.75 (400)	15.75 (400)	0.20	0.63	0.47	3.08 (0.26)	-3.03 (0.25)	CB/BR
	S5	0	4.72 (120)	23.62 (600)	23.62 (600)	0.30	0.5	0.4	2.51 (0.21)	-2.44 (0.20)	CB/BR
	S6	0	4.72 (120)	15.75 (400)	15.75 (400)	0.20	0.5	0.4	3.47 (0.29)	-3.37 (0.28)	CB/BR
Shiu et al. (1981)	CI1	0	4 (101.6)	-	-	0.00	5.6	1.64	4.37 (0.36)	4.37 (0.36)	SS
	PW1	0	4 (101.6)	12.5 (317)	18 (457)	0.17	5.6	1.64	4.77 (0.39)	4.77 (0.39)	FS
Wu (2005)	S-F1	0	4.72 (120)	-	-	0.00	1.3	0.1	3.17 (0.26)	-3.28 (0.27)	CB
	S-F2	0	4.72 (120)	23.62 (600)	23.62 (600)	0.30	1.3	0.1	4.53 (0.38)	-4.71 (0.39)	CB
	S-F3	0	4.72 (120)	23.62 (600)	23.62 (600)	0.30	1.3	0.1	4.40 (0.37)	-4.30 (0.36)	CB
	S-F4	0	4.72 (120)	15.75 (400)	15.75 (400)	0.20	1.3	0.1	4.70 (0.39)	-4.54 (0.38)	CB
	S-F5	0	4.72 (120)	23.62 (600)	23.62 (600)	0.30	1.3	0.1	3.79 (0.31)	-4.24 (0.35)	CB
	S-F6	0	4.72 (120)	15.75 (400)	15.75 (400)	0.20	1.3	0.1	4.09 (0.34)	-4.29 (0.36)	CB

Table 4.1: (continued)

Author	**ID**	$\mathbf{\frac{P}{A_g f'_c}}$	$\mathbf{t_w}$	**Opening size**		$\frac{\ell_{\text{opening}}}{\ell_{\mathbf{w}}}$	**Reinforcement**		$\mathbf{V_{\text{max}}/\left(A_{cv}\sqrt{f'_c}\right)^{1)}}$		**Failure mode**
				width	**height**		ρ_{BE}	ρ_t	+	-	
			in. (mm)	in. (mm)	in. (mm)		%	%	psi (MPa)	psi (MPa)	
Taylor (1995)	RW3-O	0.1	4 (101.6)	12 (304.8)	27 (685.8)	0.25	2.93	0.7	2.89 (0.24)	-2.47 (0.21)	CB
	BW1-O	0.14	4 (101.6)	9 (228.6)	20 (508)	0.19	2.93	0.7	2.91 (0.24)	-2.51 (0.21)	CB
Marius (2013)	SW1	0.01	3.15 (80)	-	-	0.00	1.08	0.53	1.88 (0.16)	-1.88 (0.16)	CB
	SW23	0.01	3.15 (80)	9.84 (250)	19.69 (500)	0.20	2.6	0.53	1.66 (0.14)	-1.59 (0.13)	CB
	SW45	0.01	3.15 (80)	9.84 (250)	19.69 (500)	0.20	2.6	0.53	1.55 (0.13)	-1.30 (0.11)	CB
	SW67	0.01	3.15 (80)	9.84 (250)	19.69 (500)	0.20	2.6	0.53	1.56 (0.13)	-1.34 (0.11)	CB
	SW8	0.01	3.15 (80)	9.84 (250)	19.69 (500)	0.20	2.6	0.53	0.20 (0.10)	-1.22 (0.10)	CB
Noda et al. (1997)	WNO1	0.06	2.95 (75)	16.83 (427.5)	12.20 (310)	0.38	1.26	1.4	6.81 (0.57)	-6.26 (0.52)	CB
	WNO2	0.05	2.95 (75)	16.83 (427.5)	12.20 (310)	0.38	1.26	1.4	6.37 (0.53)	-6.23 (0.52)	CB
	WSO1	0.04	2.95 (75)	16.83 (427.5)	15.25 (387.4)	0.38	1.26	1.4	5.97 (0.50)	-5.91 (0.49)	CB
	WSO2	0.05	2.95 (75)	16.83 (427.5)	15.25 (387.4)	0.38	1.26	1.4	6.04 (0.50)	-5.89 (0.49)	CB
	WSO3	0.04	2.95 (75)	12.20 (310)	14.96 (380)	0.27	1.26	1.4	5.60 (0.47)	-5.10 (0.42)	CB
	WSO4	0.04	2.95 (75)	12.20 (310)	14.96 (380)	0.27	1.26	1.4	5.02 (0.42)	-4.49 (0.37)	CB

[1] $\mathbf{A_{cv}}$ = Cross-sectional area of the wall after deducting area of the opening.

Table 4.2: Measured properties of walls with openings by type.

Config	**ID**	$\frac{\mathbf{P}}{\mathbf{A_g f'_c}}$	$\frac{\ell_{\text{opening}}}{\ell_{\mathbf{w}}}$	**Reinforcement**		$\mathbf{V}_{\text{max}}/\left(\mathbf{A_{cv}}\sqrt{\mathbf{f'_c}}\right)^{1)}$		**Failure mode**
				ρ_{BE}	ρ_t	+	-	
				%	%	psi (MPa)	psi (MPa)	
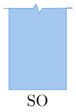	W1	0.07	0.00	3.0	0.4	3.56 (0.30)	-3.47 (0.29)	CB
	S1	0	0.00	0.5	-	2.38 (0.20)	-2.28 (0.19)	CB/BR
	CI1	0	0.00	5.6	1.64	4.37 (0.36)	4.37 (0.36)	FS
	S-F1	0	0.00	1.3	0.1	3.17 (0.26)	-3.28 (0.27)	CB
	SW1	0.01	0.00	1.08	0.53	1.88 (0.16)	-1.88 (0.16)	CB
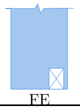	RW3-O	0.1	0.25	2.93	0.7	2.89 (0.24)	-2.47 (0.21)	CB
	BW1-O	0.14	0.19	2.93	0.7	0.91 (0.24)	-2.51 (0.21)	CB
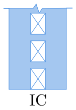	S5	0	0.30	0.5	0.4	2.51 (0.21)	-2.44 (0.20)	CB/BR
	S6	0	0.20	0.5	0.4	3.47 (0.29)	-3.37 (0.28)	CB/BR
	S-F5	0	0.30	1.3	0.1	3.79 (0.31)	-4.24 (0.35)	CB
	S-F6	0	0.20	1.3	0.1	4.09 (0.34)	-4.29 (0.36)	CB
	PW1	0	0.17	5.6	1.64	4.77 (0.39)	4.77 (0.39)	FS
	SW8	0.01	0.20	2.6	0.53	0.00 (0.00)	0.00 (0.00)	CB
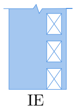	WSO4	0.04	0.27	1.26	1.4	5.02 (0.42)	-4.49 (0.37)	CB
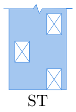	W2	0.07	0.21	3.0	0.4	4.39 (0.36)	-4.77 (0.40)	CS
	W3	0.07	0.21	3.0	0.4	4.49 (0.37)	-4.15 (0.34)	CS
	W4	0.07	0.21	3.0	0.4	4.55 (0.38)	-3.91 (0.32)	CS
	S2	0	0.30	1.25	0.47	3.21 (0.27)	-3.37 (0.28)	CB/BR
	S3	0	0.30	0.84	0.47	2.99 (0.25)	-3.31 (0.27)	CB/BR
	S4	0	0.20	0.63	0.47	3.08 (0.26)	-3.03 (0.25)	CB/BR
	S-F2	0	0.30	1.3	0.1	4.53 (0.38)	-4.71 (0.39)	CB
	S-F3	0	0.30	1.3	0.1	4.40 (0.37)	-4.30 (0.36)	CB
	S-F4	0	0.20	1.3	0.1	4.70 (0.39)	-4.54 (0.38)	CB
	SW23	0.01	0.20	2.6	0.53	1.66 (0.14)	-1.59 (0.13)	CB

Table 4.2: (continued)

Config	**ID**	$\frac{\mathbf{P}}{\mathbf{A_g f'_c}}$	$\frac{\ell_{\text{opening}}}{\ell_{\mathbf{w}}}$	**Reinforcement**		$\mathbf{V}_{\max}/\left(\mathbf{A_{cv}}\sqrt{\mathbf{f'_c}}\right)^{1)}$		**Failure mode**
				ρ_{BE}	ρ_t	+	-	
				%	%	psi (MPa)	psi (MPa)	
	SW45	0.01	0.20	2.6	0.53	1.55 (0.13)	-1.30 (0.11)	CB
	SW67	0.01	0.20	2.6	0.53	1.56 (0.13)	-1.34 (0.11)	CB
	WNO1	0.06	0.38	1.26	1.4	6.81 (0.57)	-6.26 (0.52)	CB
	WNO2	0.05	0.38	1.26	1.4	6.37 (0.53)	-6.23 (0.52)	CB
	WSO1	0.04	0.38	1.26	1.4	5.97 (0.50)	-5.91 (0.49)	CB
	WSO2	0.05	0.38	1.26	1.4	6.04 (0.50)	-5.89 (0.49)	CB
	WSO3	0.04	0.27	1.26	1.4	5.60 (0.47)	-5.10 (0.42)	CB

1) $\mathbf{A_{cv}}$ = Cross-sectional area of the wall after deducting area of the opening.

Table 4.3: Characteristic response of the test specimens.

ID	Config	Shear demand capacity ratio[1)]	Drift (%) +	Drift (%) -	Failure mode
W1	SO	1.32	3.00	-2.93	CB
W2	ST	1.33	2.06	-2.09	CS
W3	ST	1.33	1.60	-1.60	CS
W4	ST	1.33	1.65	-2.05	CS
S1	SO	1.58	66.82	-67.52	CB/BR
S2	ST	1.37	56.00	-58.40	CB/BR
S3	ST	1.41	55.98	-55.56	CB/BR
S4	ST	1.29	60.67	-61.12	CB/BR
S5	IC	1.58	63.61	-66.03	CB/BR
S6	IC	1.58	66.45	-67.43	CB/BR
CI1	SO	2.68	2.83	2.83	SS
PW1	IC	2.75	2.43	0.00	FS
S-F1	SO	1.49	31.09	-34.72	CB
S-F2	ST	1.76	45.41	-45.15	CB
S-F3	ST	1.80	51.42	-51.57	CB
S-F4	ST	1.81	32.50	-32.33	CB
S-F5	IC	1.74	70.49	-71.10	CB
S-F6	IC	1.78	58.72	-57.74	CB
RW3-O	FE	1.31	2.75	2.40	CB
BW1-O	FE	1.25	1.37	1.35	CB
SW1	SO	1.19	1.05	-1.03	CB
SW23	ST	1.21	0.97	-0.87	CB
SW45	ST	1.18	0.83	-0.82	CB
SW67	ST	1.21	0.76	-0.75	CB
SW8	IC	1.07	0.58	-0.58	CB

[1)] defined as $1.25M_n/\phi V_c$ (ACI 318-19 [4]).

4.2.1 Shiu, Daniel, Aristizabal-Ochoa, Fiorato, and Corley (1981)

Shiu et al. [54] tested two wall specimens at the Construction Technology Laboratory of Portland Cement Association (PCA), one solid specimen (CI1) and one specimen (PW1) with opening in the center of each story. The objectives of the tests were to investigate the impacts of openings on the response of walls subjected to reversal loads and to verify the design criteria including reinforcing details for walls with openings in seismic regions. Shiu walls were one-third scale representation of six-story walls. In the laboratory, walls were 4 inches thick, by 75 in. long with a 3 ft. story height (102 mm thick by 1900 mm long by 914 mm high per story), suggesting a 12 inch thick wall, 225 in. long with 9 ft. stories at full-scale (305 mm thick by 5.72 m long by 2.74 m high per story.The opening in specimen PW1 was placed at the center of the wall panel in each story with dimensions of 12.5 in. × 18 in. (317 × 457 mm). As shown in Figure 4.3, openings have a vertical depth equal to half the story height, per Harries [27], Turgeon [61] the expected response of the wall is that of a solid wall with openings rather than a coupled wall; this is consistent with the observed behavior as discussed below. Both specimens had similar reinforcement detailing except reinforcement shifted to the sides of the opening if interrupted by the opening. Geometry and cross-sectional detailing of wall specimens are shown in Figure 4.3. Properties of the materials used in both specimens are shown in Tables 4.4 and 4.5.

Table 4.4: Measured concrete properties for specimens tested by Shiu et al.

Specimen	f'_c (psi)	f_t (psi)	E_c (ksi)
CI1	3375	480	3385
PW1	3030	430	2815

Lateral loading was applied via hydraulic arms at the top of the specimen. An axial load was not applied. Specimen CI1 sustained a maximum shear stress demand of $4.37\sqrt{f'_c}$ psi or $0.36\sqrt{f'_c}$ MPa through multiple cycles to a drift of 2.8%; specimen PW1 sustained a

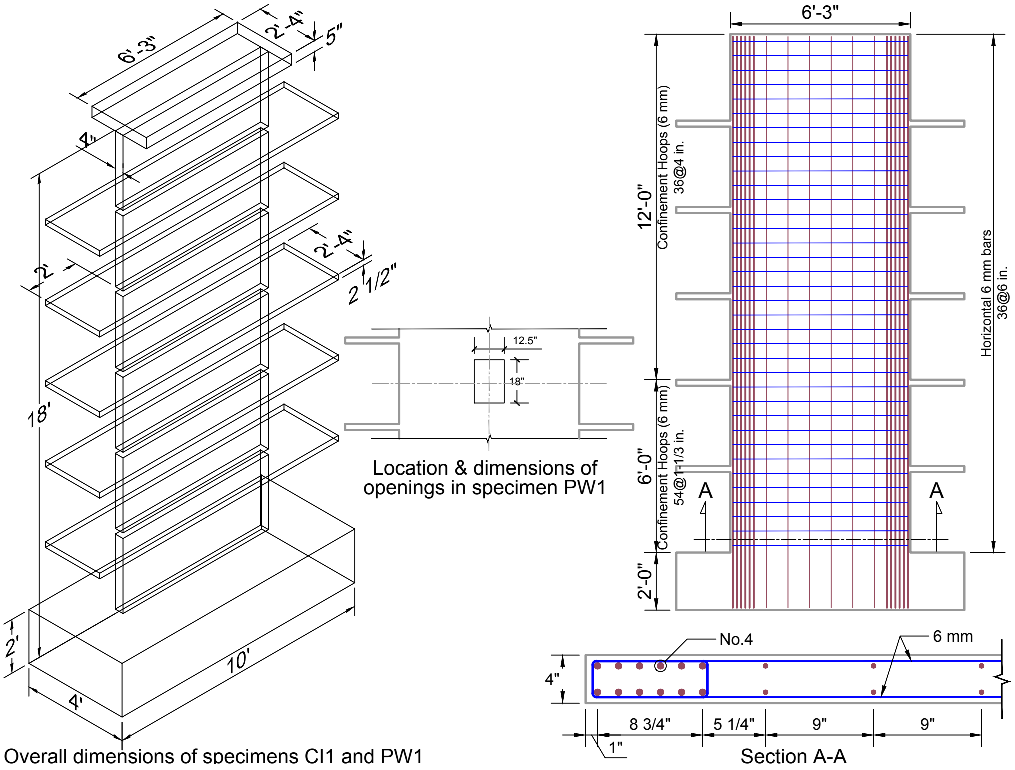

Figure 4.3: Geometry and cross-sectional detailing of specimens tested by Shiu et al.

maximum shear stress demand of $3.98\sqrt{f'_c}$ psi or $0.33\sqrt{f'_c}$ MPa through multiple cycles to a drift of 2.43%. The measured load deformation and final damage pattern of both specimens are shown in Figures 4.4 and 4.5, respectively.

Based on the experimental results, Shiu et al. concluded that the response of the wall specimens were minimally affected by the openings (about 8% reduction in the deformation capacity due to openings). The data show that the two walls exhibited approximately the same strength, deformation capacity and cyclic response history. However, the walls exhibited different damage patterns and failure modes. Specifically,for specimen CI1, at a drift of 2.34% diagonal cracks coalesced into a horizontal crack in the bottom story; this horizontal crack continued to widen under cyclic loading until damage at the crack resulted

Table 4.5: Measured steel properties for specimens tested by Shiu et al..

Specimen	Reinforcing steel	f_y (ksi)	f_{su} (ksi)	E_s (ksi)
CI1	No.4	69.1	110.5	26100
	6 mm	68.6	94.3	29500
	D3 wire	70.8	81.9	27700
PW1	No.4	60.4	110.0	24000
	6 mm	67.0	90.5	35000
	D3 wire	78.0	87.7	28500

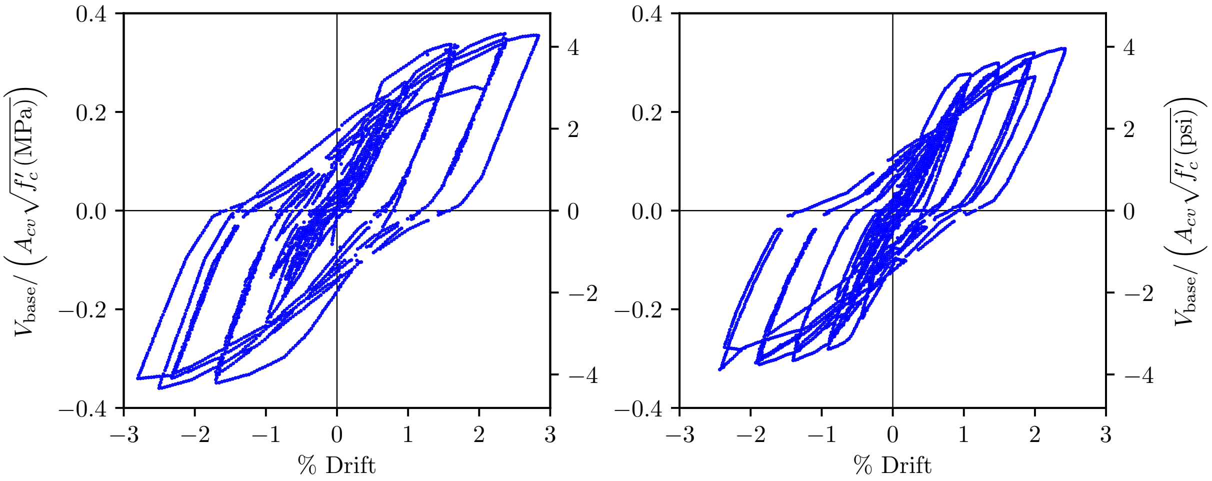

(a) Specimen CI1

(b) Specimen PW1

Figure 4.4: Measured load-deformation relationship for wall specimens tested by Shiu et al..

in strength loss during the second cycle to a drift demand of 2.8%. For specimen PW1, during cycling to maximum drift demands of +/- 2.43%, diagonal cracks in the first story widened substantially and reinforcing steel in the interior of the wall fractured resulting in strength

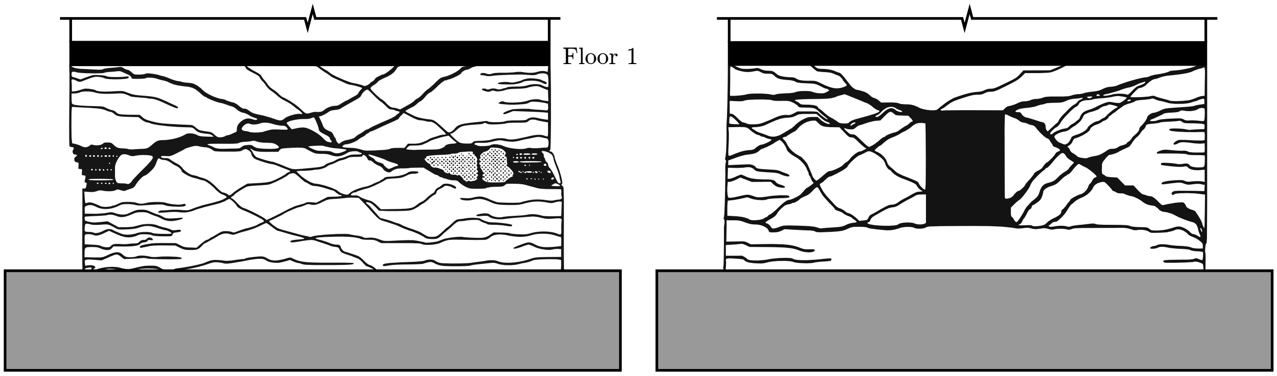

Specimen CI1

Specimen PW1

Figure 4.5: Specimens CI1 and PW1 after failures.

loss. Specimen CI1 failed in a *shear-sliding* mode while the other failed in a *flexural-shear* mode. The failure patterns for both specimens are shown in Figure 4.5.

4.2.2 Ali and Wight (1991)

Ali and Wight [6] tested four wall specimens that were approximately one-fifth scale. The walls represented a five-story prototype building designed for regions of light seismicity, underdesigned for shear associated with flexural strength. The objective of the test was to study the effects of staggered openings on the performance of walls. The reference wall was 3 in. thick, by 48 in. long with a 28 in. story height (76 mm thick by 1.22 m long by 0.71 m high per story), suggesting a 12 inch thick wall, 144 in. long with 7 ft. stories at full-scale (305 mm thick by 3.66 m long by 2.13 m). The cross-section was barbell shaped with a square geometry of 5 in. × 5 in. (127 mm × 127 mm) which acted as the boundary elements for the wall. Three additional walls employed the reference wall gross geometry and had openings on each floor with a staggered vertical layout. Openings were 9 × 20 inches (229 × 508 mm) which is equivalent to 13.4% of the wall area. Confinement reinforcement consisted of 3/16 inches (4.8 mm) diameter wire hoops with a vertical spacing of 2.5 inches (63.5 mm). Additionally, to control the cracking, diagonal wires with 3/16 inch diameters were used at the corners of the openings. Properties of the material used for these specimens are shown in Table 4.6. Geometry and reinforcement detailing of the wall specimens are shown in Figures 4.7 and 4.9.

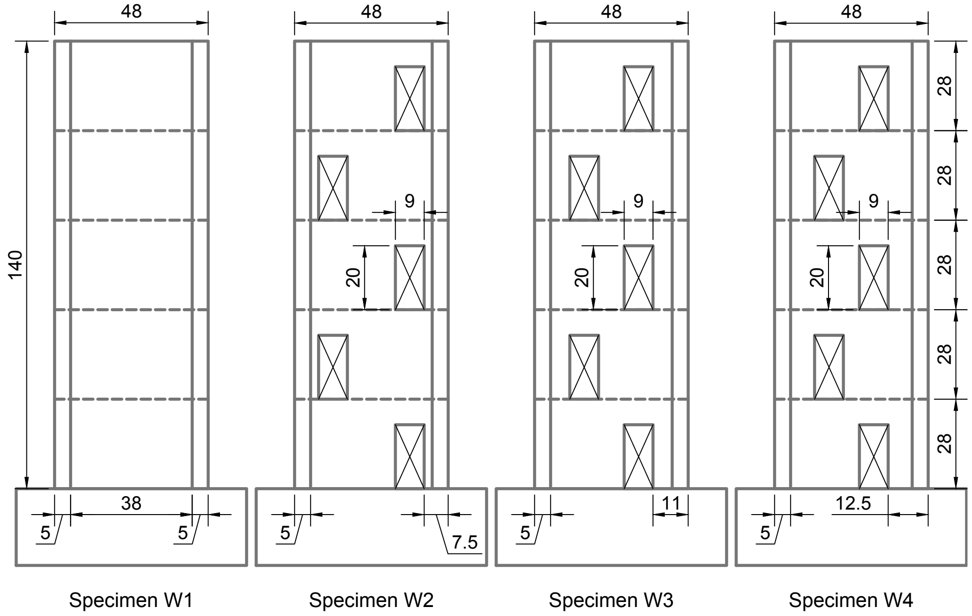

Figure 4.6: Dimensions of wall specimens tested by Ali and Wight (units in inches).

Table 4.6: Measured material properties for specimens tested by Ali and Wight.

	Concrete			Steel	
Specimen	f'_c (psi)	f_t (psi)	f_r (psi)	Type	f_y (ksi)
W1	4960	416	847	No.4 Bar	78.4
W2	4830	425	816	No.2 Bar	81.5
W3	5160	394	814	3/16″ Bar	90.0
W4	5260	409	852		

All the walls were tested under reverse cyclic loading with a constant axial load of

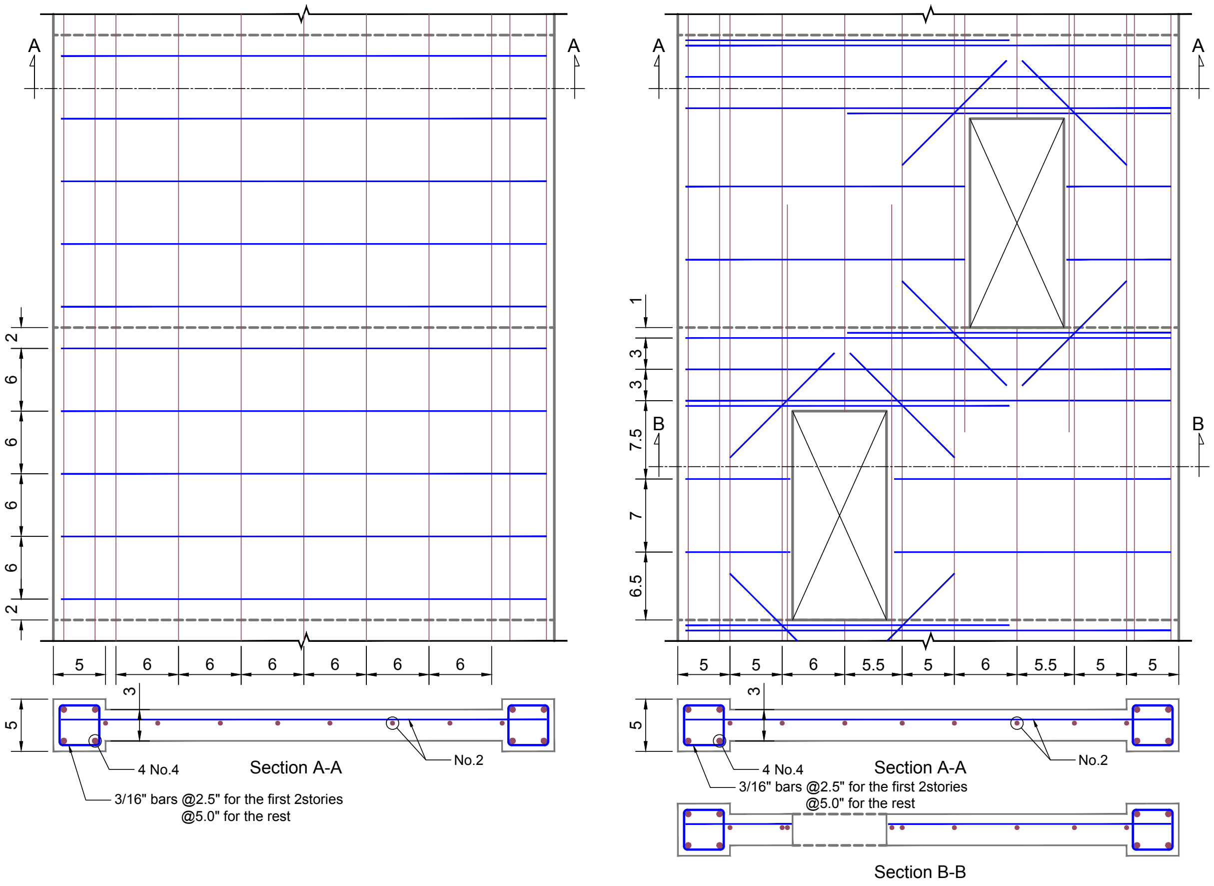

(a) Specimen W-1 **(b)** Specimen W-3

Figure 4.7: Cross-sectional details for specimens tested by Ali and Wight (units in inches).

approximately $0.07A_g f'_c$. The reference specimen experienced a flexure-controlled response with horizontal cracks at the perimeter of the wall that shifted to diagonal cracks in the interior of the wall. As displacement demands increased, horizontal BE cracks widened and concrete spalling and vertical bar buckling was observed; diagonal cracking in the interior of the wall maintained modest widths throughout the test. The specimens with openings exhibited a ductile flexure-controlled behavior until they reached a drift ratio of approximately 1.0%. The three specimens with openings suddenly lost lateral load carrying capacity due to shear compression failure in the web and boundary element in the first story. The failure was followed by crushing of the concrete in the boundary element and compression buckling of the vertical bars. Results indicated that strain profiles across the section of the specimens were not linear and plane sections did not remain plane [6]. Measured load-deformation relationship for all the specimens are shown in Figure 4.8.

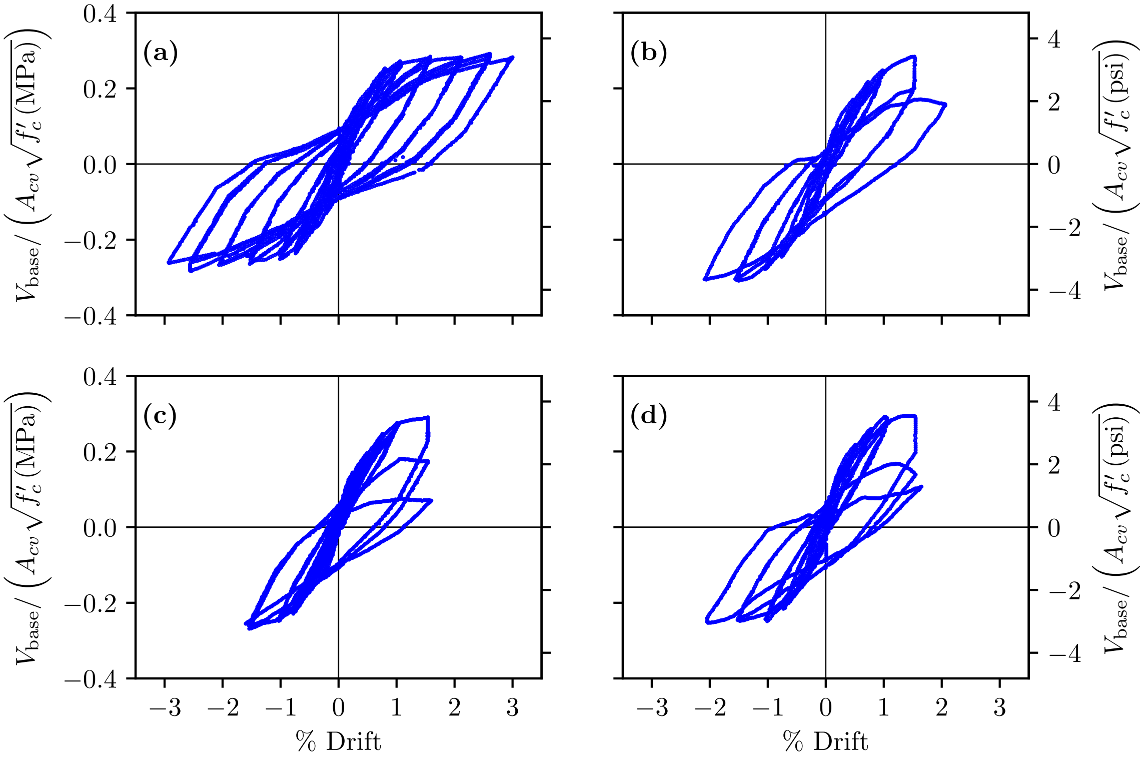

Figure 4.8: Measured load-deformation relationship for specimens **(a)** W1, **(b)** W2, **(c)** W3 and **(d)** W4, tested by Ali and Wight.

Ali and Wight concluded that for slender walls with lightly reinforced sections under axial loads of less than 500 psi (3.5 MPa) and shear stress demands of 3 to $4\sqrt{f'_c}$ psi (0.25 to $0.33\sqrt{f'_c}$ MPa), no severe damage is experienced by the walls up to an average story drift of

1.0%. For higher drifts, the boundary elements need to be more heavily confined. Ali and Wight noted that no distress was observed between the staggered openings as is common, while significant damage to coupling beams is observed in coupled walls. Therefore, they proposed that staggered openings are a practicable alternative to in-line door openings that result in coupled walls. Ali and Wight concluded that, door openings positioned closer to the boundary element edges, can provoke an early shear-compression failure as they remove the in-plane confinement.

4.2.3 Yanez, Park, and Paulay (1992)

Yanez et al. [72] tested six walls with different opening sizes and arrangements (Figure 4.9) to investigate use of strut-and-tie modeling and performance of walls with small or moderate amount of reinforcement and containing openings irregularly distributed. The details of the wall specimens are shown in Figure 4.9. Each wall specimen was 78.74 inches (2 m) long, 4.72 inches (120 mm) thick and 90.55 inches (2.3 m) tall. Reinforcement ratio was 0.5% for all the wall specimens in the vertical direction. The specimens were subjected to reversed cyclic loading under displacement control; no axial load was applied. All wall specimens were planar. The size of openings were 23.6 in. × 23.6 in. (600 mm × 600 mm) for specimens S2, S3 and S5 and 15.8 in. × 15.8 in. (400 mm × 400 mm) for S4 and S6 specimens. Table 4.7 shows concrete and steel material properties for specimens. Axial load was not applied to the specimens during testing. Figure 4.10 shows the measured load-deformation relationship for all the specimens.

All specimens exhibited a ductile response and final failure was attributed to crushing of concrete and fracture of the main vertical bars. Piers (columns) next to the openings also performed quite satisfactory and no shear failure of these regions were observed.

Yanez et al. observed that specimen strengths and damage patterns were consistent with the strut-and-tie models created for each specimen and, thus, concluded that strut and tie models can be used to provide a conservative estimate of the ultimate strength of walls subjected to cyclic lateral loading. Yanez et al. observed also that wall stiffness but not

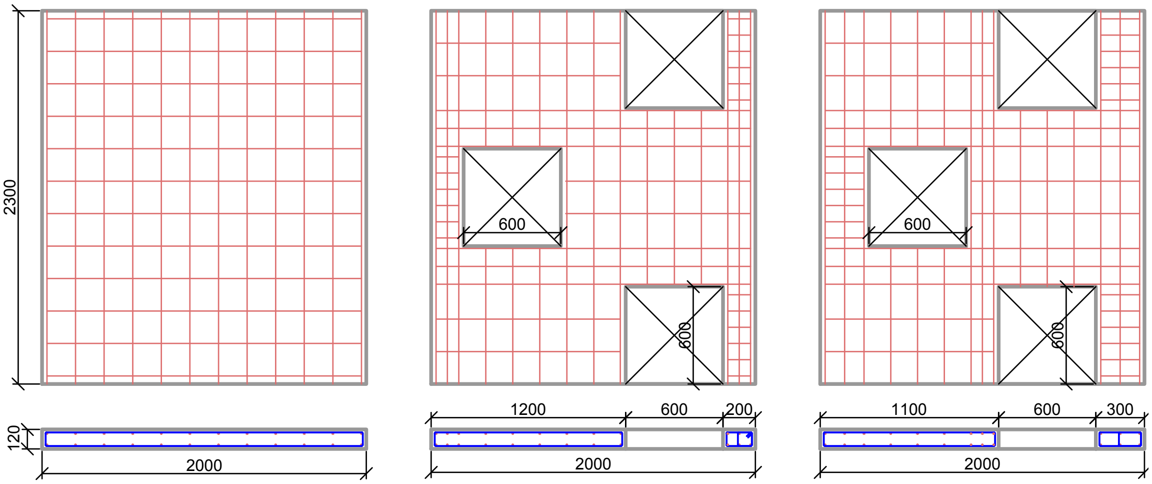

Specimen S1 Specimen S2 Specimen S3

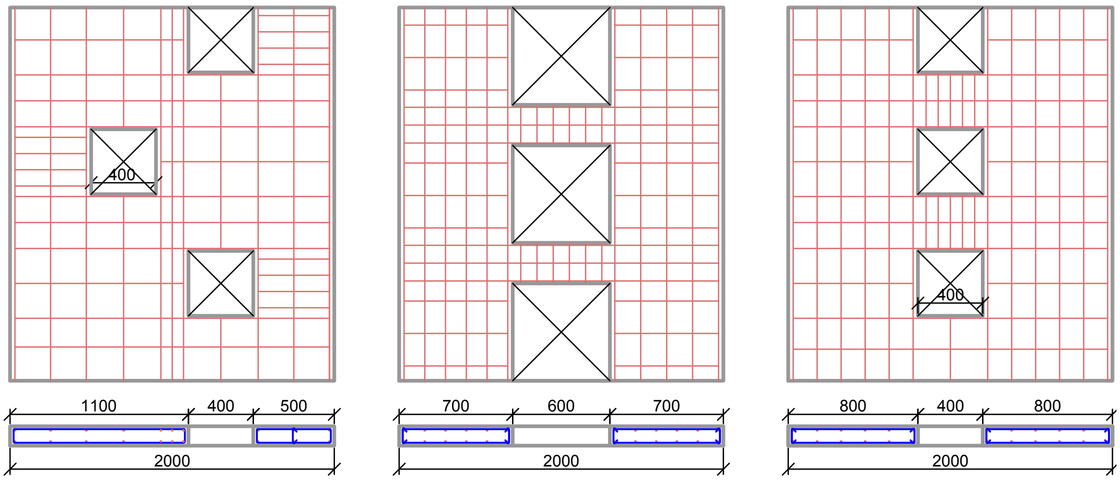

Specimen S4 Specimen S5 Specimen S6

Figure 4.9: Details of the specimens tested by Yanez et al. (units in mm).

strength is affected by openings that represent more than 10% of the gross wall area and concluded that distributed wall openings that represent less than 10% of wall gross area do not significantly affect wall stiffness, strength or deformation capacity.

4.2.4 Taylor (1995)

Taylor [55] tested two quarter-scale, slender reinforced concrete structural walls with openings

Table 4.7: Concrete and steel material properties for specimens tested by Yanez et al..

Concrete		**Reinforcement**		
Wall	$\mathbf{f'_c}$ ksi (MPa)	**Bar**	$\mathbf{f_y}$ ksi (MPa)	$\mathbf{f_u}$ ksi (MPa)
S1	4.93 (34)	HD8	69 (475)	101 (690)
S2	3.34 (23)	R6	51 (350)	68 (470)
S3	3.77 (26)			
S4	3.36 (23)			
S5	6.38 (44)			
S6	3.19 (22)			

at the base. The specimens were tested under reversed cyclic lateral loading with a constant axial load. The objectives of the tests were to evaluate the applicability of displacement-based design to walls with openings and the impact of openings on the shear strength of the walls.

One of the specimens (RW3-O) had a rectangular cross-section while the other (BW3-O) was barbell shaped. Wall geometries and design were chosen so that results would be comparable with those of previous tests [59]. One of the tested specimens (RW3-O) had an overall geometry and reinforcement layout equivalent to that of Specimen RW2 tested by Thomsen and Wallace [59]; the second specimen (BW3-O) employed a barbell configuration with geometry and design parameters comparable to Specimens W1 and W2 tested by Ali and Wight [6]. Figure 4.11 shows the specimen geometries and reinforcement layouts.

The wall specimen was 4 inches thick, by 48 in. long (102 mm thick by 1.22 m long), suggesting a 12 inch thick wall, 144 in. long at full-scale (305 mm thick by 3.66 m long). Elevation and cross-sectional details of the specimen RW3-O are shown in Figure 4.11. Specimen BW1-O, had a barbell shaped cross-section with barbell dimensions of 5 in. × 5 in..

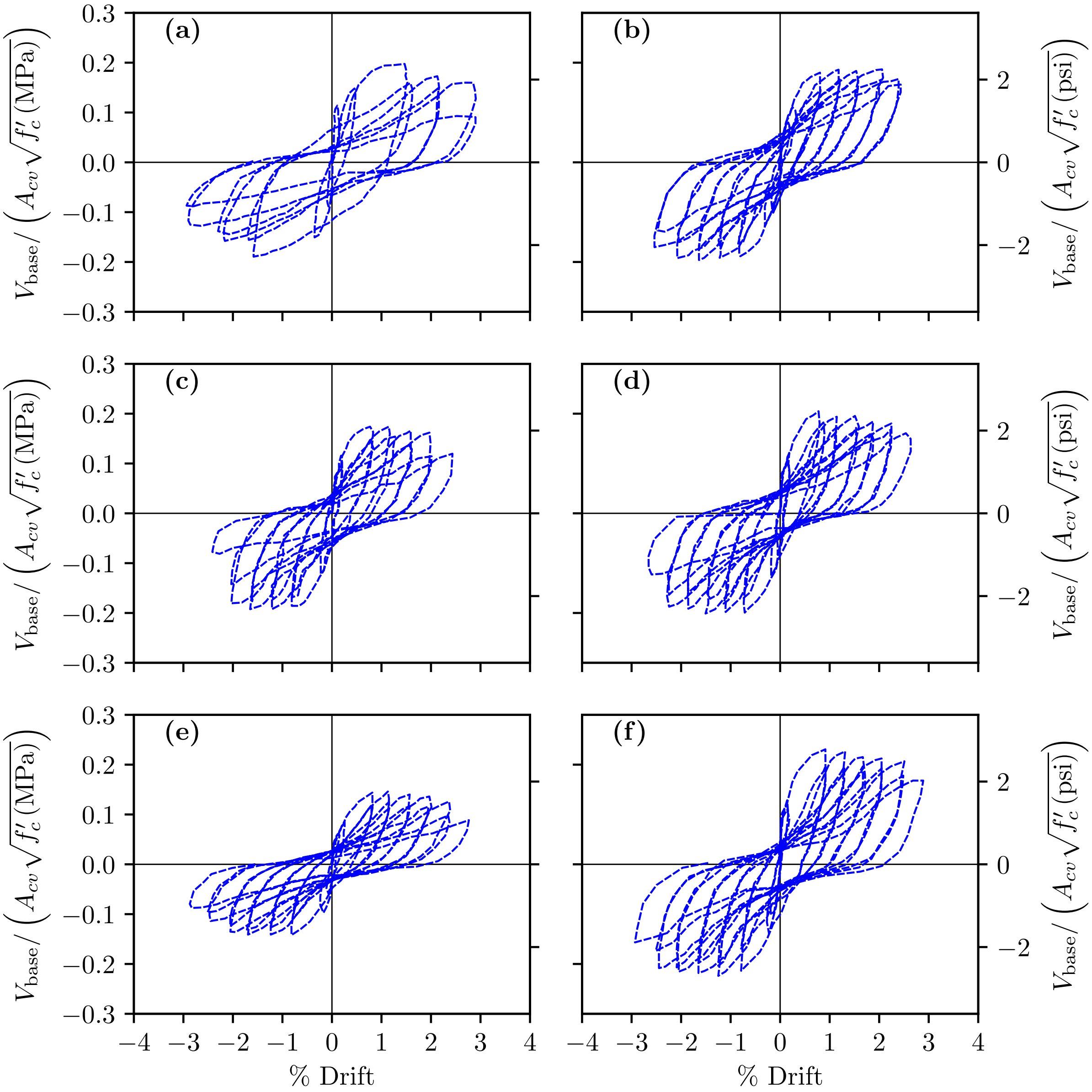

Figure 4.10: Measured load-deformation relationship for specimens **(a)** S1, **(b)** S2, **(c)** S3, **(d)** S4, **(e)** S5 and **(f)** S6 tested by Yanez et al..

This specimen was 3 in. thick but had the same length as specimen RW3-O. Elevation and cross-sectional details of the specimen BW1-O are shown in Figure 4.12. Table 4.8 shows the material properties for specimens tested by Taylor et al. [56].

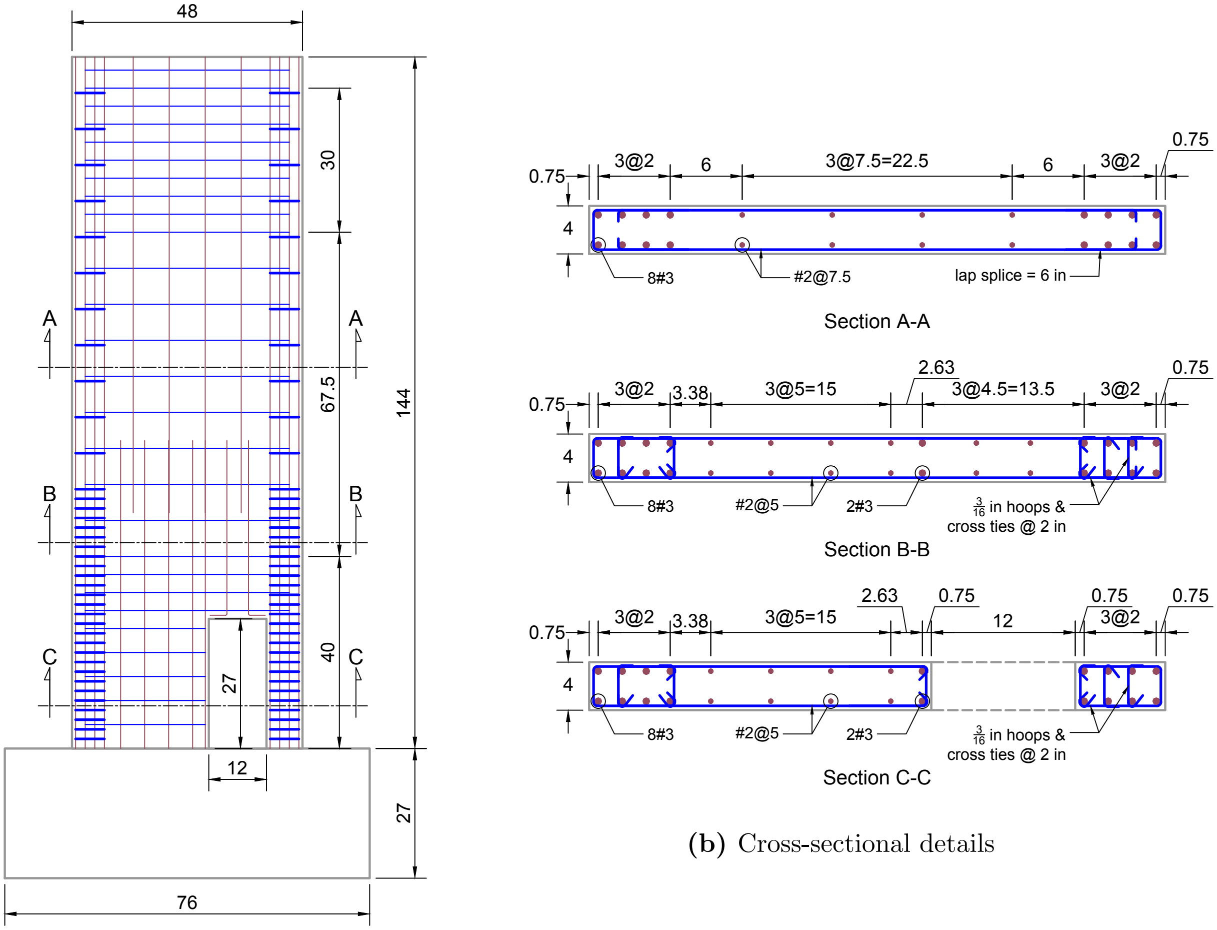

(a) Elevation view

(b) Cross-sectional details

Figure 4.11: Details of specimen RW3-O tested by Taylor (units in inches).

Specimen RW3-O started yielding at 0.75% lateral drift and significant spalling occurred at the first cycle of the 2% drift. The column started buckling at the cycle of 2.5% drift and the specimens boundary element started crushing with main vertical bars buckling at approximately 3% drift. Specimen BW1-O started yielding at 0.75% drift. In the second cycle of 1% drift, top interior side of the column started to spall in the narrow region between the opening and the boundary element. This led to the crushing of this region and buckling

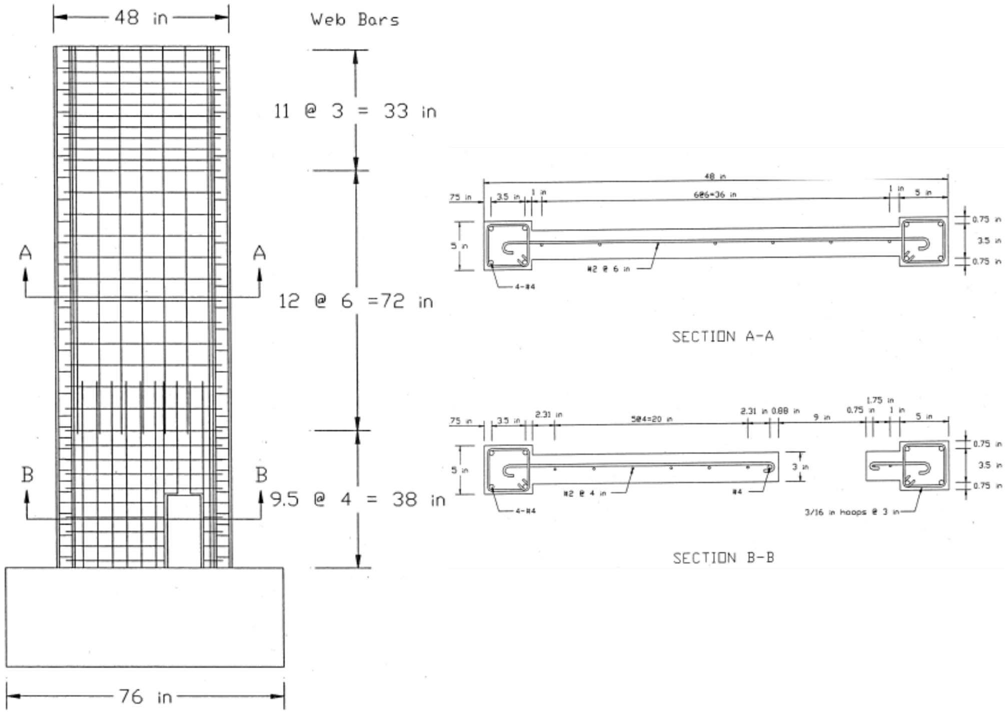

Figure 4.12: Details of specimen BW1-O [55].

Table 4.8: Concrete and steel material properties for specimens tested by Taylor.

Bar	**Yield strength**	**Specimen**	**f$'_c$** (MPa (psi))
	MPa (ksi)		MPa (psi)
3/16″ dia. wire	469 (68)	RW3-O	30.8 (4460)
#2	517 (75)	BW1-O	30.8 (4460)
#3	531 (77)		
#4	510 (74)		

of the bars. The main bar started buckling in the second cylce of 1.5% drift and caused by improperly located hoops. Concrete within the boundary element started crushing during the third cycle of the 1.5% drift and this led to buckling of the remaining vertical bars.

Based on the experimental results, Taylor, concluded that slender reinforced concrete

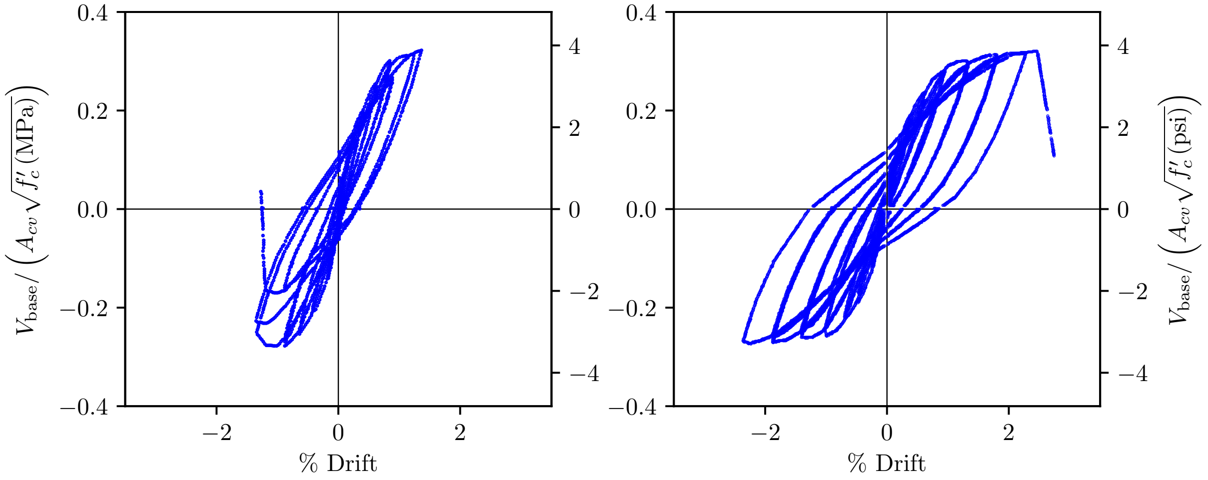

(a) Specimen BW1-O

(b) Specimen RW3-O

Figure 4.13: Measured load-deformation relationship for specimens tested by Taylor.

walls with openings in the base and proper reinforcement detailing can achieve stable hysteretic response to significant ductility demands. Furthermore, using the displacement-based design technique led to providing the amount of confinement needed instead of providing based on the nominal value. Ultimately, whenever code equations are not applicable, strut and tie model is an efficient approach for designing punched walls. Measured load-deformation relationship for both specimens are shown in Figure 4.13.

4.2.5 Noda, Sugishita, and Kato (1997)

Noda et al. designed and tested six two-story walls with openings to validate a set of design recommendations they develop on the basis of review of previous experimental tests and analytical investigations of flexural-controlled walls with and without openings conducted by others. The experimental test specimens were designed to achieve ductile, flexure controlled response by assuming the first story of the wall to be a hinge region and considering the following observations from their review:

1. For walls containing an opening, the failure zone is concentrated compared to the case of continuous (with no openings) walls. In the majority of the cases, sidewalls on either side of the openings were likely to fail,

2. Walls with openings can behave in a ductile manner and fail in flexure similar to solid walls provided sufficient reinforcement is added to both sides of the opening,

3. Diagonal reinforcement around the openings had a major influence in increasing the shear strength of these walls,

4. Summation of the strengths of the sidewalls on both sides of the opening, considering the contribution of peripheral reinforcement around the opening, was the strength of the wall with opening [71].

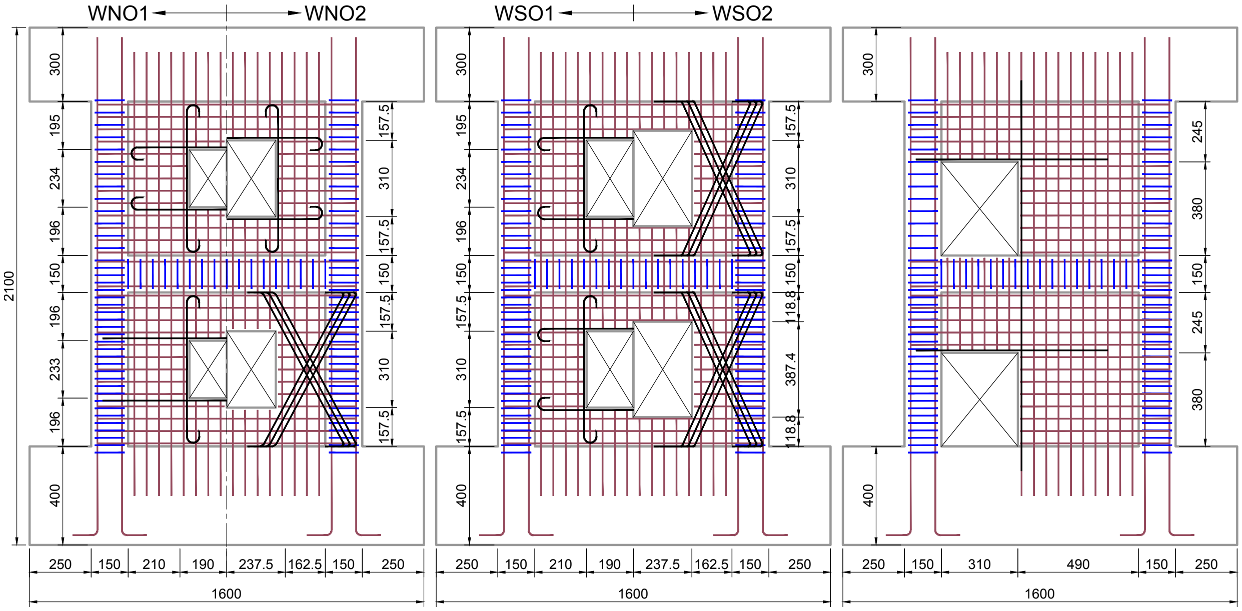

(a) Specimens WNO1 & WNO2 (b) Specimens WSO1 & WSO2 (c) Specimen WSO4

Figure 4.14: Geometry and reinforcement layout of the specimens tested by Noda et al. [50] (units in mm).

Table 4.9: Structural properties of specimens tested by Noda et al. and Kato et al..

(a) Dimension and detail of column

Specimen	Section mm	Main bar	Ratio of Main bar	Hoop (1st floor)	Hoop ratio	Hoop (2nd floor)	Hoop ratio
Common	150 × 150	4-D10	0.0127	2-D6 @ 30 mm	0.0142	D6 @ 50 mm	0.0085

(b) Dimension and detail of wall[1)]

Specimen	Peripheral ratio of opening	Peripheral reinforcement (1st floor)	Peripheral reinforcement (2nd floor)
WNO1	0.3	4-D10 (mesh)	4-D10 (mesh)
WNO2	0.4	12-D6 (diag.)	4-D10 (mesh)
WSO1	0.4	4-D10 (mesh); 4-D6 (mesh)	4-D10 (mesh); 4-D6 (mesh)
WSO2	0.5	8-D6 (diag.); 4-D6 (mesh)	8-D6 (diag.); 4-D6 (mesh)
WSO3	0.4	3-D13 (mesh)	3-D13 (mesh)
WSO4	0.4	2-D13 (mesh)	2-D13 (mesh)

[1)] for all specimens, wall thickness = 75 mm, wall reinforcement is 2 $\phi 4$ @ 50 mm and ratio of wall reinforcement is 0.0069

(c) Dimension and detail of beam

Specimen	Section mm	Main bar	Ratio of Main bar	Stirrup	Stirrup ratio
Common	150 × 150	4-D10	0.0127	2-D6 @ 50 mm	0.0142

Variables studied, included location and size of the openings, peripheral ratios of the panels and the reinforcement next to the openings. A total axial load of 33.72 kips (150 kN) was applied to the wall specimens. Lateral load was applied at a height of 74.8 in. (1900 mm). Each specimen was two-story with one bay only. Each story was surrounded by beams and columns, except the top girder was stiff enough and the loading was applied on top of that. Geometry and reinforcement layout of the specimens are shown in Figure 4.14. And the structural properties of the specimens are tabulated in Tables 4.9 and 4.10

Table 4.10: Mechanical properties of materials used for specimens tested by Noda et al. and Kato et al..

(a) Reinforcement

Reinforcement	f_y ksi (MPa)	f_u ksi (MPa)
$\phi 4$	76.9 (530)	81.2 (560)
D6	46.0 (317)	69.3 (478)
D10	47.9 (330)	68.0 (469)

(b) Concrete

Speciment	f'_c ksi (MPa)	ε_c	E_c ksi (MPa)
WNO1	3.61 (24.9)	2187	3234 (22300)
WNO2	3.95 (27.2)	2417	3394 (23400)
WSO1	4.53 (31.2)	2588	3466 (23900)
WSO2	4.41 (30.4)	2575	3452 (23800)
WSO3	4.54 (31.3)	2591	3466 (23900)
WSO4	4.77 (32.9)	2646	3510 (24200)

Walls performed ductile up to a roof drift of about 1%. After that, as loading continued, the hysteretic curves showed that the walls underwent a pinching-type behavior. Noda et al., based on simplified strut-and-tie models and the shear transfer mechanism based on these strut-and-tie models, classified the walls into flexural type and flexural-shear type. Additionally, for each type, a separate design approach was proposed. For flexure type walls, the deformation capacity of the wall can be evaluated by only considering the compression sidewall by finding the influence of the concrete for shear using the equation proposed for shear. On the other hand, for the flexure shear type walls, both sidewalls are considered. As a result, deformation capacity of walls with openings are expected to decrease. Figure 4.15 shows the experimental load-deflection relationships.

4.2.6 Wu (2005)

Wu [71] tested a total of six flanged walls under reversed cyclic loading to investigate the impacts of opening size, arrangement and irreguliarities on the performance of walls. The specimens were 4.72 inches thick, by 78.74 in. long (0.12 m thick by 2 m long), suggesting a

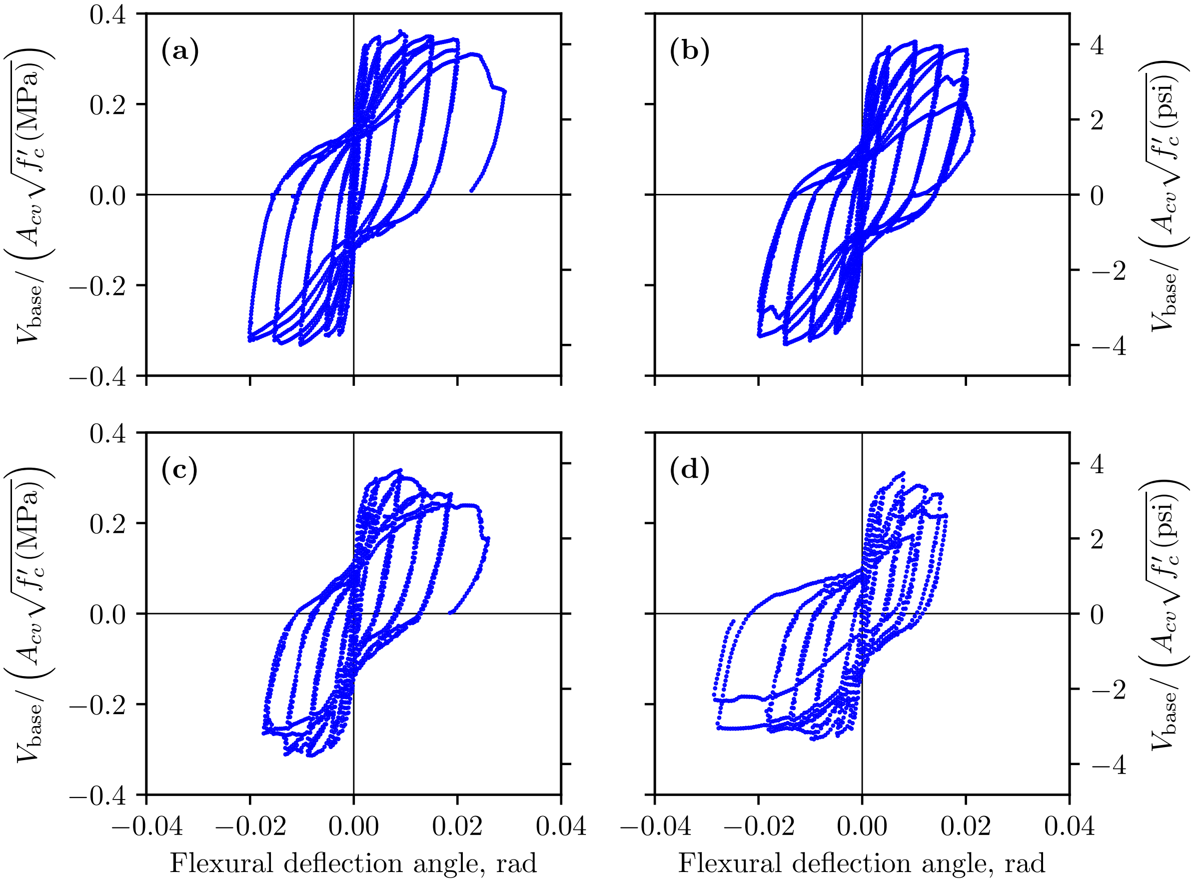

Figure 4.15: Measured load-deformation relationship for specimens **(a)** WNO1, **(b)** WNO2, **(c)** WSO1 and **(d)** WSO4 tested by Noda et al..

12 inch thick wall, 200 in. long at full-scale (305 mm thick by 5.08 m long). The specimens were similar to the specimens tested by Yanez et al. [72] but with flanges. The reference specimen had no openings (S-F1), three walls with irregular openings (S-F2, S-F3 and S-F4) and two walls with regular openings (S-F5 and S-F6). No axial load was applied to the specimens. Opening sizes of 23.62 × 23.62 inches (0.6 × 0.6 m) were used in specimens S-F2, S-F3 and S-F5 and smaller sizes of 15.74 × 15.74 inches (0.4 × 0.4 m) used in the remaining two specimens with openings. Cross-section and reinforcement layout of the specimens are

shown in Figure 4.16. Properties of the steel and concrete materials are shown in Table 4.11.

Table 4.11: Propterties of the materials used in the tests by Wu.

Concrete compressive strength		**Steel bar properties**			
Specimen	$\mathbf{f'_c}$ ksi (MPa)	**Type**[1)]	$\mathbf{f_y}$ ksi (MPa)	$\varepsilon_\mathbf{y}$ %	$\mathbf{f_u}$ ksi (MPa)
S-F1	5.08 (35.02)	R6	42.49 (293)	0.20	58.74 (405)
S-F2	5.35 (36.86)	R10	55.40 (382)	0.19	69.76 (481)
S-F3	5.08 (35.05)	T10	67.73 (467)	0.26	78.46 (541)
S-F4	5.26 (36.26)	T13	71.50 (493)	0.28	84.26 (581)
S-F5	5.20 (35.84)	T20	74.26 (512)	0.35	88.03 (607)
S-F6	5.07 (34.98)				

[1)] R = high yield strength steel deformed bars, T = mild steel plain bars.

Load-displacement relationships for all specimens indicate that pinching is significant but when loading is in the negative direction, the pinching is greater compared to the other direction. Also, these walls exhibit more pinching when compared to the planar walls tested by Yanez et al. [72] (see Section 4.2.3). Additionally, the results show that the solid specimen undergoes less pinching compared to walls with openings. The stiffness for specimens S-F2 and S-F6 was similar to the reference specimen (S-F1) because additional reinforcement was provided at the panel zone to account for the reduction caused by the openings. Specimen S-F3 has a thinner region between the openings compared to the specimen S-F2 which caused a smaller stiffness. And specimen S-F5 exhibited a more significant reduction in the stiffness due to larger openings. Li et al. stated that walls with openings, regardless of the pattern, exhibit reduced stiffness and strength compared to solid specimen S1. This is in contrast to what Yanez et al. concluded [37]. Measured load-deformation relationship for all the specimens are shown in Figure 4.17.

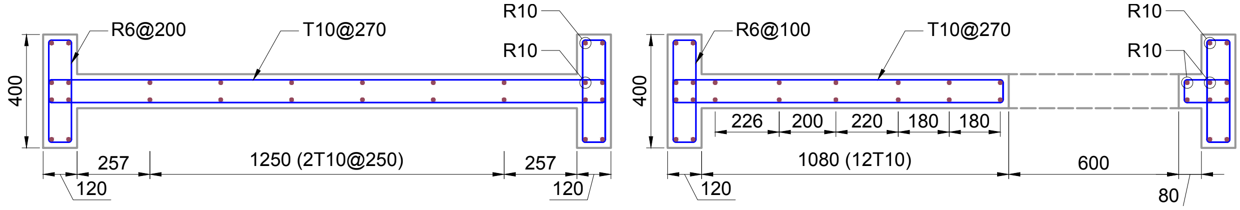

(a) Specimen S-F1 **(b)** Specimen S-F2

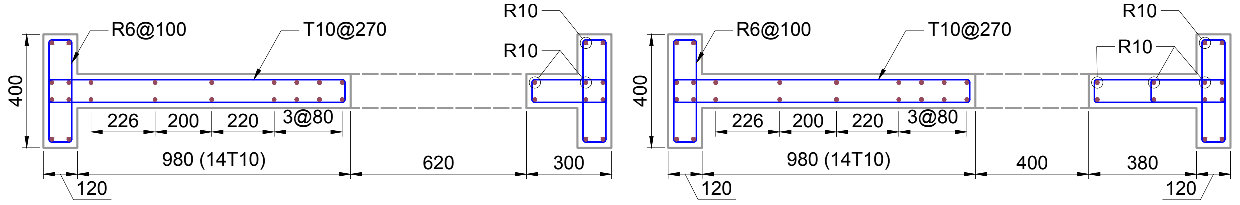

(c) Specimen S-F3 **(d)** Specimen S-F4

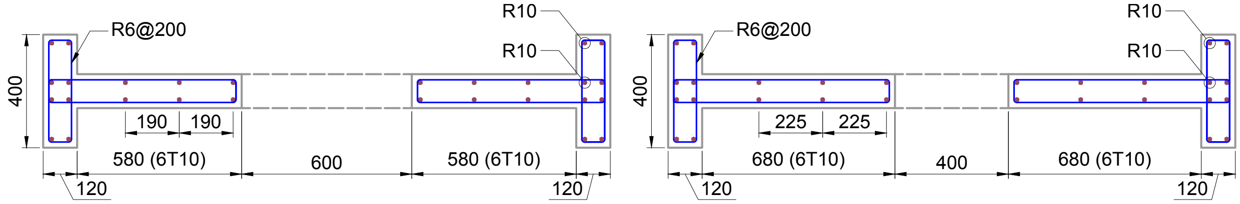

(e) Specimen S-F5 **(f)** Specimen S-F6

Figure 4.16: Cross-section and reinforcement layout of the walls tested by Wu (units in mm).

Deformation capacity seems to be less affected by the presence of openings. Data from the tests showed that specimen S-F4 exhibited similar deformation capacity to the solid reference wall while specimen S-F3 which had larger opening sizes, exhibited a lerger deformation capacity compared to the solid wall. Specimens S-F3 and S-F2 had identical opening sizes however, ultimate drift capacity for S-F2 was smaller compared to S-F3 and even the reference solid wall. The researchers attribute this to the farther distance of openings from the boundaries in specimen S-F3.

Wu concluded that openings, regardless of their pattern, have a significant impact on the stiffness and strength for walls with flanges. When openings are near the edges of the

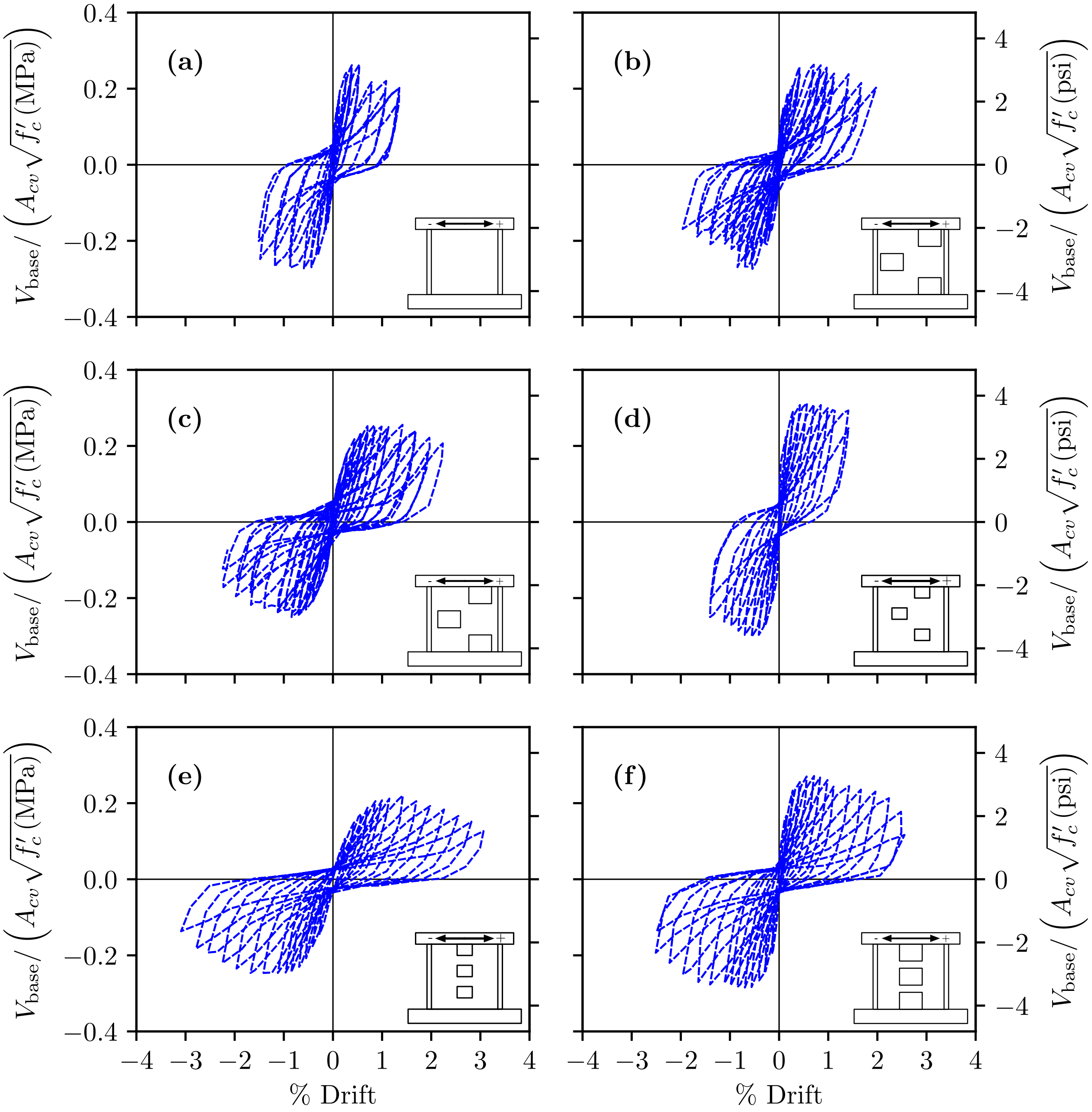

Figure 4.17: Measured load-deformation relationship for specimens **(a)** S-F1, **(b)** S-F2, **(c)** S-F3, **(d)** S-F4, **(e)** S-F5 and **(f)** S-F6 tested by Wu.

wall, the impact is more significant. However, deformation capacity may not be affected by the openings but bigger openings result in more drastic stiffness and strength deterioration.

Additionally, flanges increase the strength of the walls by more than 50% (51% for solid, 93% for walls with irregular openings, 64% for walls with regular openings) while they significantly reduce the deformation capacity. Sliding shear failure is more likely for walls with flanges due to the increase in the strength.

4.2.7 Marius (2013)

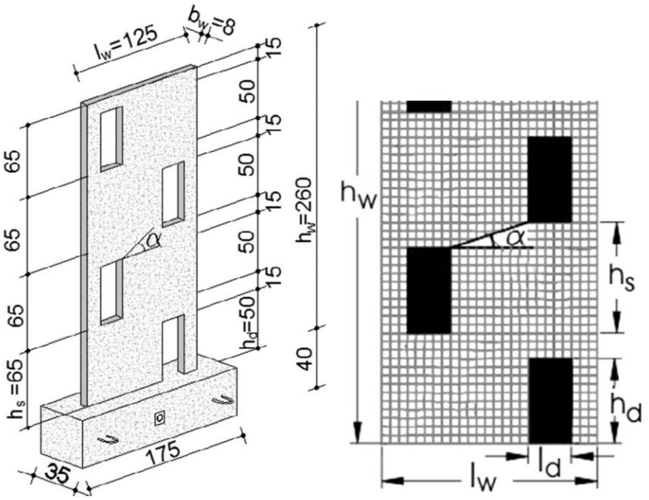

Figure 4.18: Notations of dimensions of walls tested by Marius [44] (units in cm).

Marius [44] tested five one-quarter scale wall specimens. One solid specimen without any openings (SW1), three specimens with staggered openings (SW23, SW45 and SW67) and one coupled wall (SW8). The main objective of the experimental work was to study the advantages of the structural walls with staggered openings under seismic loads. All walls were 49.2 inches (1.25 m) long, 31.5 inches (0.8 m) thick and 102.4 inches (2.6 m) tall. The amount of reinforcement used in all the specimens were the same. Size of each opening was 9.84×19.69 inches (0.25×0.5 m). Notations of the dimensions and cross-sections of the wall specimens are shown in Figures 4.18 and 4.19. Table 4.13 lists the material properties used for all specimens [44].

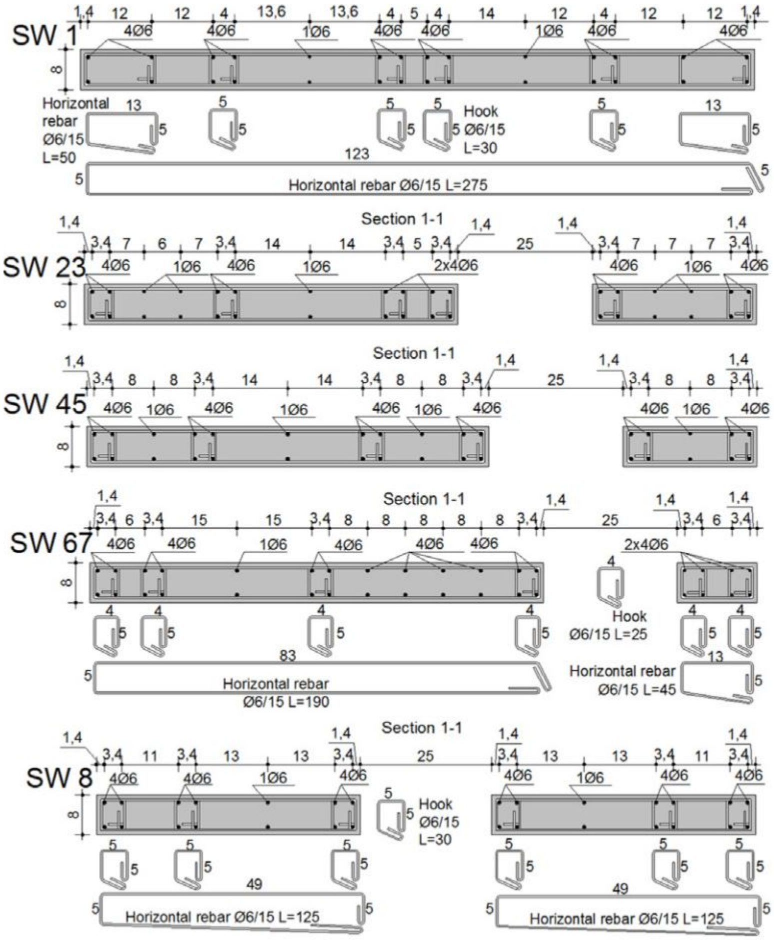

Figure 4.19: Cross-sections at the base story for the walls tested by Marius [44] (units in cm).

Table 4.12: Notation of the walls tested by Marius.

Siemic load direction	**Shear wall with openings**				**Shear wall without opening**
	$\alpha^{1)} = 90°$	$\alpha = 45°$	$\alpha = 32°$	$\alpha = 18°$	
Left seismic load (WEST)	SW8	SW2	SW4	SW6	SW1
Right seismic load (EAST)	SW8	SW3	SW5	SW7	SW1

$^{1)}$ α is the angular distance between the openings, see Figure 4.18

Table 4.13: Concrete and steel material properties for specimens tested by Marius.

Reinforcement				Concrete		
Bar	**f_y** MPa (ksi)	**E** GPa (ksi)	**f_u** MPa (ksi)	**Wall**	**f'_c** MPa (psi)	**E_c** GPa (ksi)
6 mm	386 (56)	210 (30458)	551 (79.9)	all walls	50 (7252)	34 (4931)

From results of the experiments, Marius concluded that all the walls with staggered opening patterns behaved in a ductile form since the vertical and horizontal reinforcement had yielded. However, the coupled wall exhibited a brittle failure mode due to crushing of the coupling beam which occurred in the same time as the horizontal bars in the coupling beams reached yielding. In addition to that, the maximum shear strength of the wall decreases as the openings are moved towards the ends of the walls while they are still stronger than the coupled wall. Ultimately, walls with staggered openings failed at a drift ratio between 0.75% to 1.0% but the maximum strength reached at a drift between 0.5% to 0.75%. In the case of the coupled wall, the total observed drift at failure was 0.25%.

4.2.8 Summary

Previous studies indicate that arrangement, size and location of the opening can affect the response of structural walls when subjected to cyclic loading. Some researchers concluded that these effects are negligible depending on the size and arrangement of the openings. However, there is no quantification of when the influence of the openings are significant. The drift capacity from the experiments indicates that openings openings have minimal impact on the deformation capacity of walls, but they cause a more drastic degradation of both stiffness and strength in these walls. When openings are nearer to the edges of the wall, they have the most impact on the response. In the case of flange presence, walls deformation capacity is significantly reduced.

Walls with openings can be classified according to the Figure 4.1. Majority of the experimental studies were focused on walls with staggered openings (ST) while less tests were focused on inline openings (IC & IE) and openings in the first floor (FC & FE). Furthermore, stress transfer through coupling beams needs to be further investigated. For this purpose, a number of shear walls are designed and simulated numerically using ATENA platform. The numerical model was validated in the previous chapter for non-planar walls. The model is also validated using walls with openings. In the next section, results of simulation of walls with openings are illustrated and explained.

4.3 Validation of the Analyses

A subset of the laboratory tests presented above were used to validate the finite element approach, presented in Chapter 2, for simulating the response of walls with openings. These are listed in Table 4.14. The sixteen test programs and walls from these test programs were chosen for use in validating the finite element modeling because not all the experiments provided all the data needed for simulation and comparison of the results or they did not have the minimum thickness of 3 inches. Table 4.14 summarizes simulated and measured wall response quantities. These data show the FEM model well predicts the response in comparison with planar (Lowes et al. [40]) and non-planar walls (Chapter 3), suggesting the numerical model is capable of depicting response parameters including strength, deformation capacity and failure mode. Figures and discussion below provide additional information.

In order to validate the approaches used for simulating walls with opening in ATENA software package, several experimental data are used. Section 4.2 described some of the previous experimental work performed to investigate the behavior of walls with openings. Some of these data are used for validating the finite element models. Table 4.14 tabulates walls used for the purpose of validation and their corresponding results.

Table 4.14: Simulation results for walls with openings.

ID	Configuration	$\frac{\ell_{\text{opening}}}{\ell_w}$	Stiffness to yield		Strength		Deformation		Failure mode	
			+	-	+	-	+	-		
			sim./exp.	sim./exp.	sim./exp.	sim./exp.	sim./exp.	sim./exp.	exp.	sim.
W1	SO	0.00	0.61	0.64	0.94	0.96	1.13	1.15	CB	CB
W2	ST	0.21	0.51	0.61	0.93	0.88	0.94	1.04	CS	CS
W3	ST	0.21	0.65	0.61	0.94	1.04	1.22	1.58	CS	CS
W4	ST	0.21	0.75	0.73	0.93	1.10	1.22	1.22	CS	CS
S1	SO	0.00	0.79	1.33	0.98	0.97	1.06	1.10	CB	CB
S2	ST	0.30	0.95	1.30	1.13	1.05	1.09	1.00	CB	CB
S3	ST	0.30	1.30	1.20	1.12	0.99	0.89	0.89	CB	CB
S4	ST	0.20	0.86	0.83	0.99	0.96	0.84	0.77	CB	CB
CI1	SO	0.00	0.98	0.72	0.88	0.87	0.96	0.97	SS	SS
PW1	IC	0.17	0.38	0.38	0.87	0.88	1.03	1.03	FS	FS
S-F1	SO	0.00	1.60	0.96	1.07	1.04	1.50	1.35	CB	CB
S-F3	ST	0.30	0.81	0.89	1.09	1.13	1.12	0.94	CB	CB
S-F4	ST	0.20	1.53	1.43	0.98	0.98	0.89	0.78	CB	CB
S-F2	ST	0.30	1.39	1.28	1.07	1.00	1.19	1.05	CB	CB
RW3-O	FE	0.25	0.72	0.70	1.02	1.15	0.95	1.18	CB	CB
BW1-O	FE	0.19	0.64	1.04	0.97	1.19	1.16	1.24	CB	CB
SW1	SO	0.00	0.95	1.05	0.92	0.93	0.96	0.97	CB	CB
SW23	ST	0.20	0.98	1.02	1.03	1.01	1.05	0.99	CB	CB
	mean		0.88	0.92	0.99	1.01	1.07	1.08		
	COV		0.42	0.33	0.08	0.09	0.15	0.19		

The data in Table 4.14 show that the ATENA modeling approach provides poor simulation of stiffness, relatively poor simulation of strength and excellent simulation of deformation capacity for specimens CI1 and PW1 tested by Shiu et al.; additionally, the model accurately simulates the observed failure mode. Errors in stiffness to yield are attributed to the shrinkage induced cracking that is not included in the numerical model. Yield strength is well simulated by the model; however, the model fails to capture the hardening observed in the laboratory. Review of the data for all tests presented earlier in this chapter shows that the hardening observed for these particular specimens exceed that observed for most others. Figure 4.20

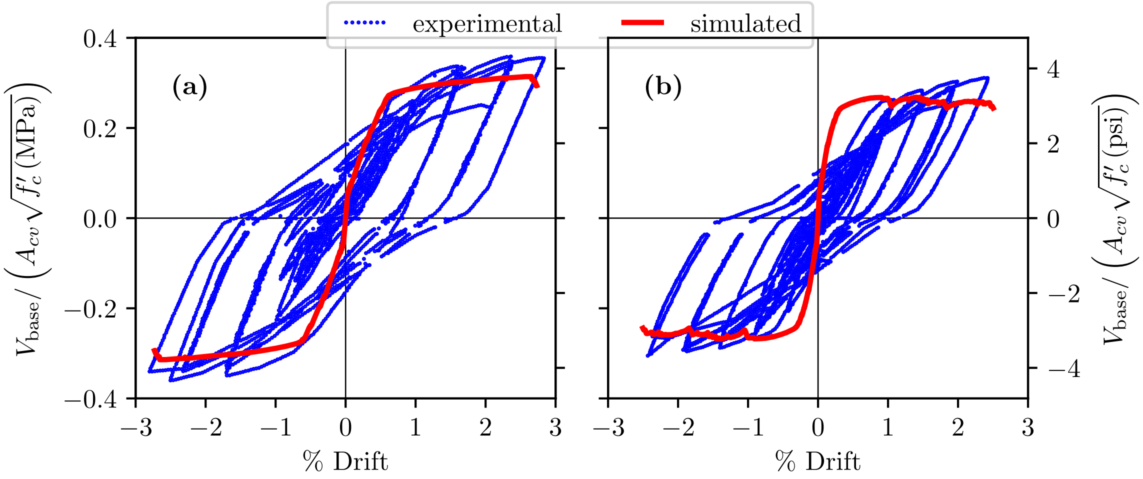

Figure 4.20: Load-deformation relationship for specimens **(a)** CI1 and **(b)** PW1 tested by Shiu et al. simulated in ATENA.

shows the simulated versus measured response of both specimens CI1 and PW1. Figure 4.23 compares simulated maximum principal strain with observed damage. The failure mode in specimen PW1 is well replicated in the analysis. The wall has failed by formation of diagonal cracks and compression struts. The maximum strain field in the simulation (left figure), shows the same failure mode in this specimen. The experimental crack pattern is for a cyclic loading case while the simulated strain field only shows a monotonic loading and the differences in both figures are due to that.

Figure 4.24 shows the simulated versus measured load deformation response of walls tested by Ali and Wight. Strength is well predicted for all the specimens. When the walls are loaded in the direction where the opening in the base is in compression the stiffness predictions are very close to the measured stiffness of the walls. However, in the opposite direction, when opening in the base is in tension, stiffness of the walls are overestimated. Deformation capacity and failure mode of the wall specimen was identified using the criteria discussed in the previous chapter. For the solid wall specimen (W1), deformation capacity is overestimated by about 13%. When the wall is loaded with opening in compression, the

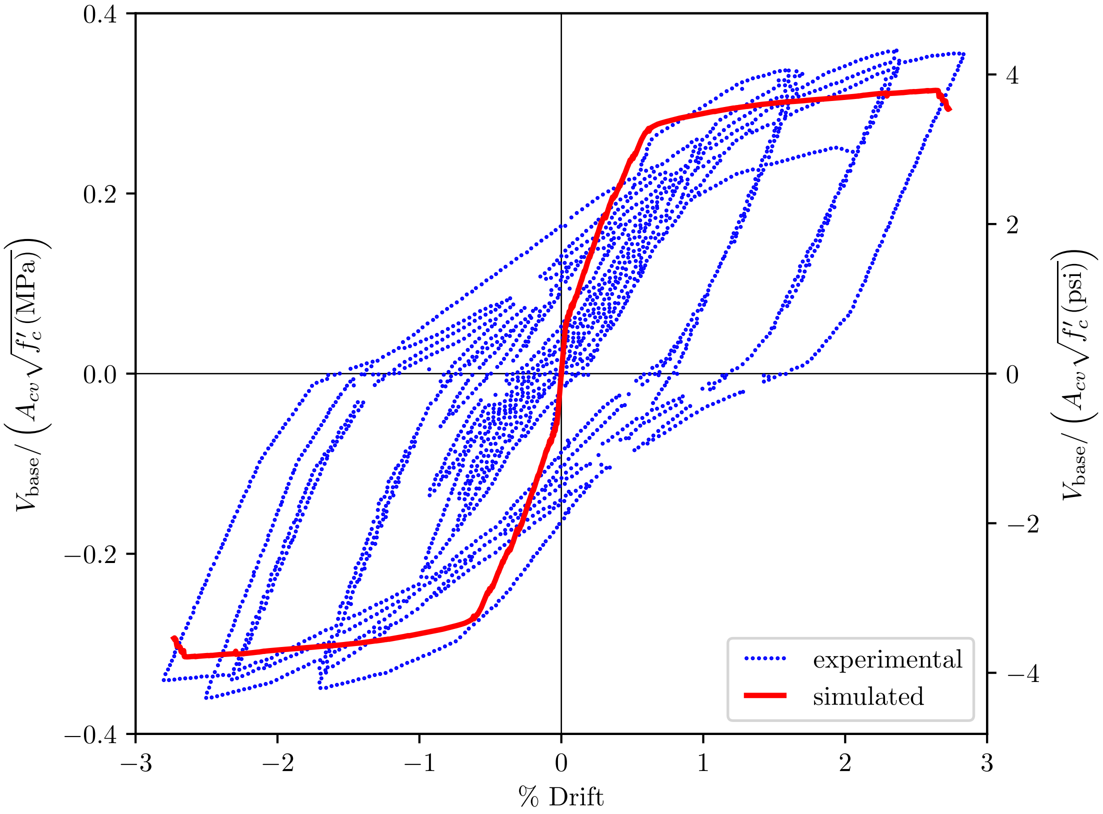

Figure 4.21: Load-deformation relationship for specimen CI1 tested by Shiu et al. simulated in ATENA.

drift capacity of the wall is better predicted where the average overestimation is less than 20%. When the wall specimen is loaded with the opening in tension, the average difference between simulated versus measured reaches to 25%. It should be noted that these specimens are loaded cyclically which might affect their capacities compared to the case with pushover loading. Additionally, when the specimen fails in one direction, the capacity in the opposite direction will be reduced. these specimens are loaded in the direction where the opening is in compression first and then the opposite direction.

Additionally, Figures 4.25, 4.26 and 4.28 show the simulated versus measured load-deformation relationships for specimens tested by Yanez et al., Wu and Marius, respectively.

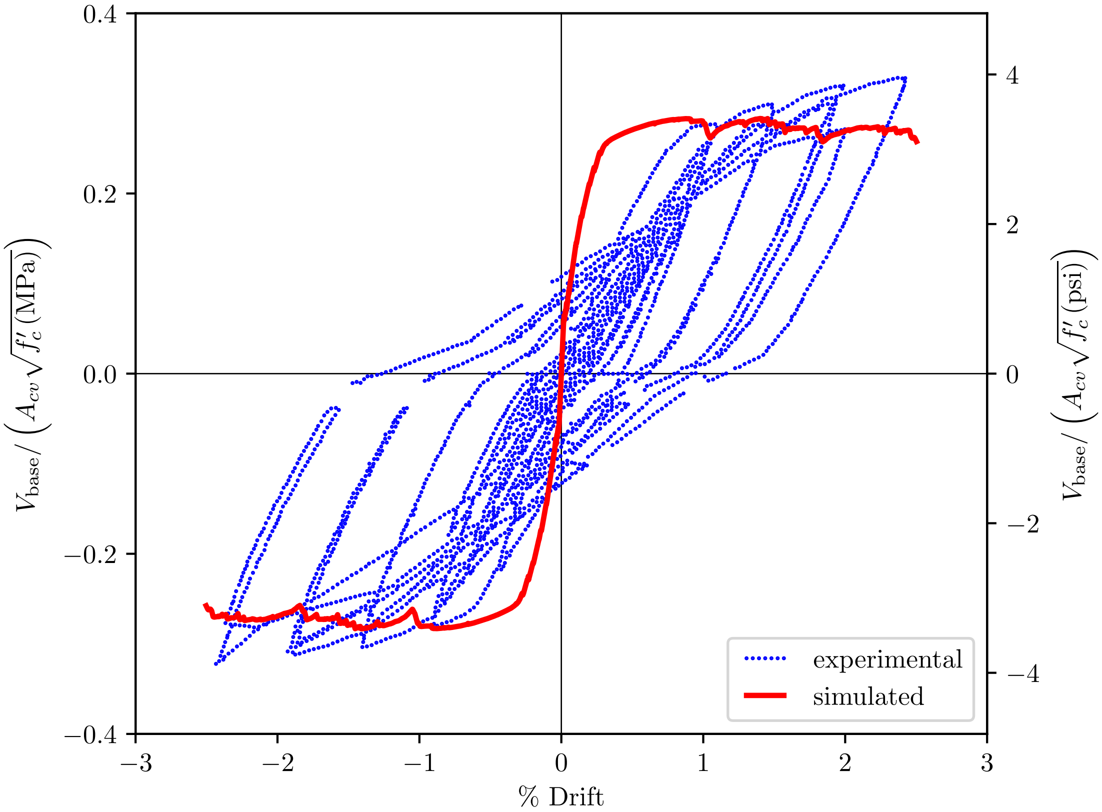

Figure 4.22: Load-deformation relationship for specimen PW1 tested by Shiu et al. simulated in ATENA.

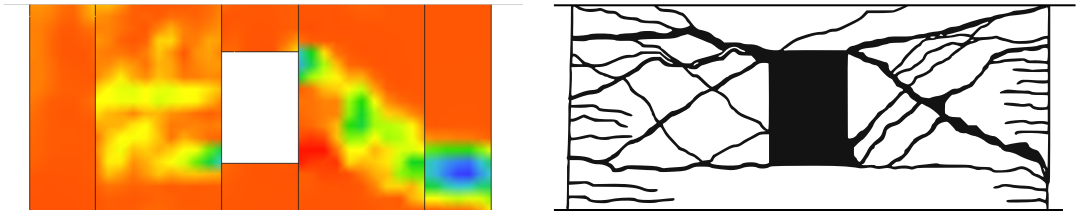

(a) Simulation

(b) Experimental

Figure 4.23: Simulated (maximum principal strain field) and measured (cracks) failure patterns in specimen PW1 (base story).

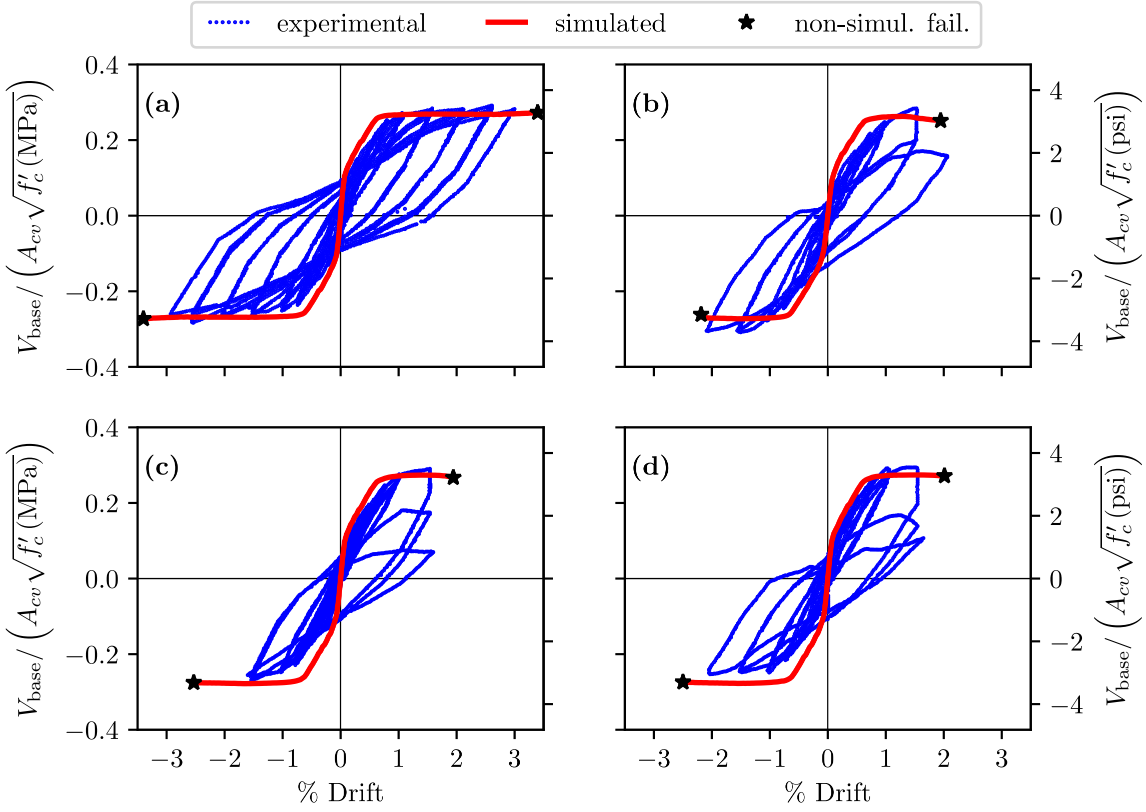

Figure 4.24: Load-deformation relationship for specimens **(a)** W1, **(b)** W2, **(c)** W3 and **(d)** W4, tested by Ali and Wight simulated monotonically in ATENA.

For walls tested by Wu, experimental material stiffness is provided by the researchers and are used in the simulations. The actual modulus of elasticity of concrete resulted in a lower stiffness prediction rather than over prediction compared to the previous cases where ACI 318-14 's formula used. The results of all the walls are shown Table 4.2. The mean and coefficient of variation (COV) indicates that, the stiffness is less accurately predicted while the strength is well predicted. Prediction of the deformation capacity is based on the criteria suggested by Whitman [68] and used in Chapter 3. The mean values for the prediction of the deformation capacity are reasonable but the COV is about 20%.

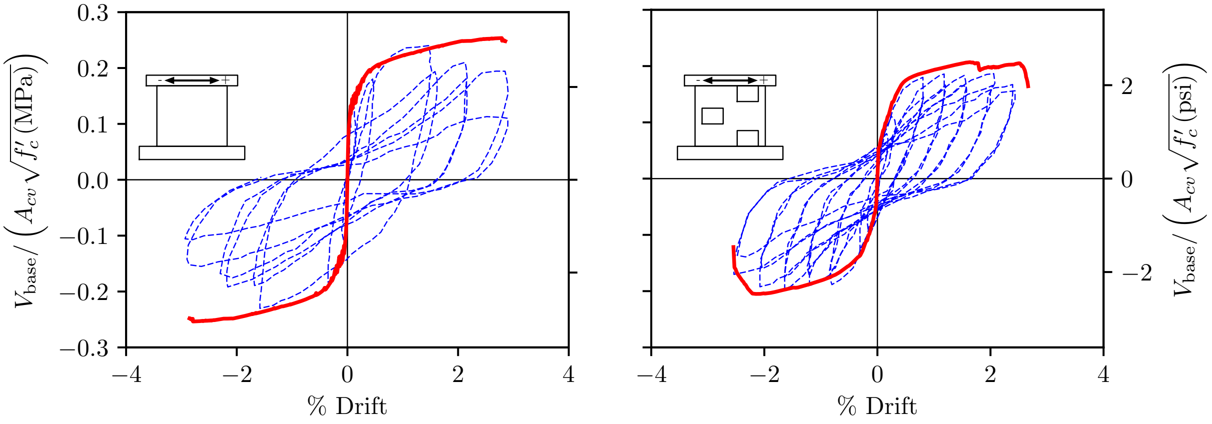

(a) Specimen S1 **(b)** Specimen S2

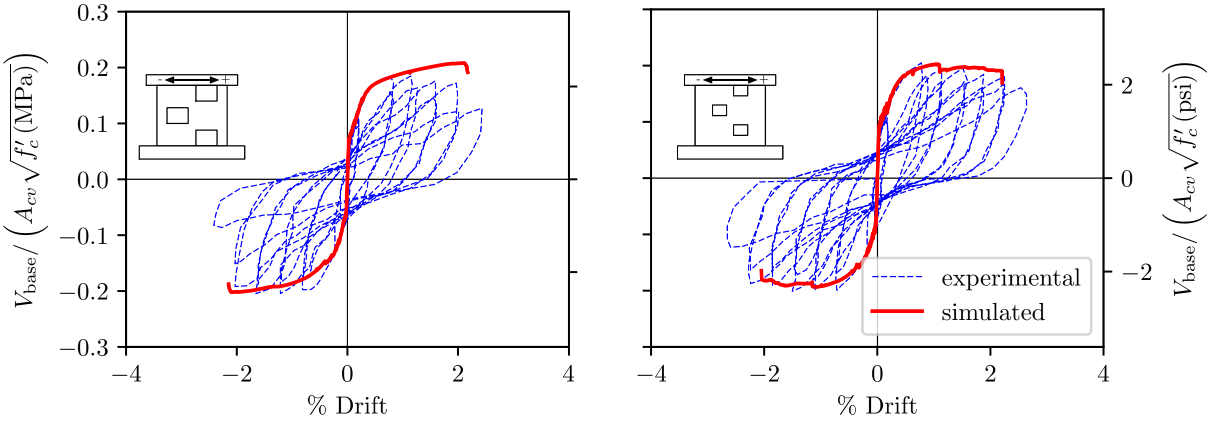

(c) Specimen S3 **(d)** Specimen S4

Figure 4.25: Load-deformation relationship for specimens tested by Yanez et al. simulated in ATENA.

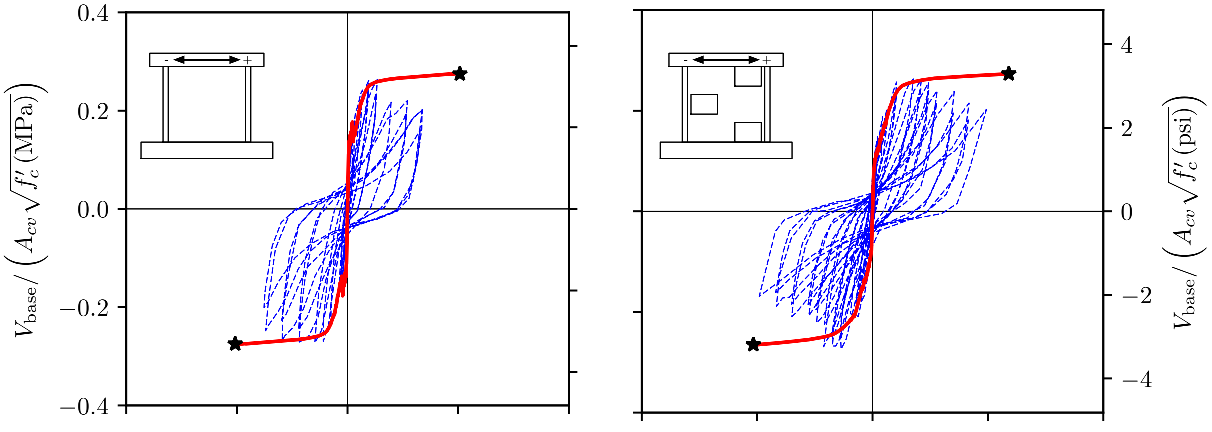

(a) Specimen S-F1

(b) Specimen S-F2

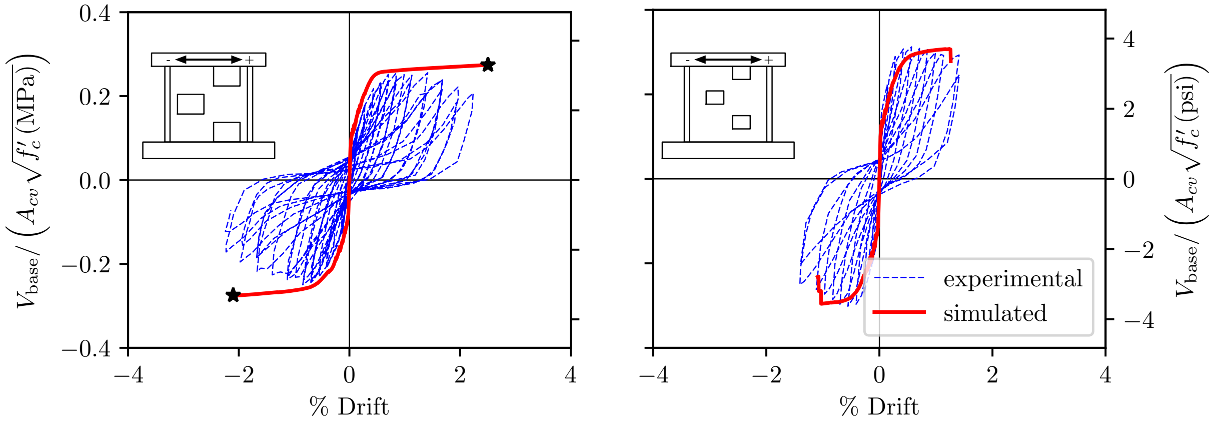

(c) Specimen S-F3

(d) Specimen S-F4

Figure 4.26: Load-deformation relationship for specimens tested by Wu simulated in ATENA.

4.4 Summary and Conclusion

4.4.1 Summary of What Was Done

A total of eighteen wall specimens were simulated using continuum FEM analysis in ATENA. Walls had planar cross-sections with different opening arrangements. Five specimens were

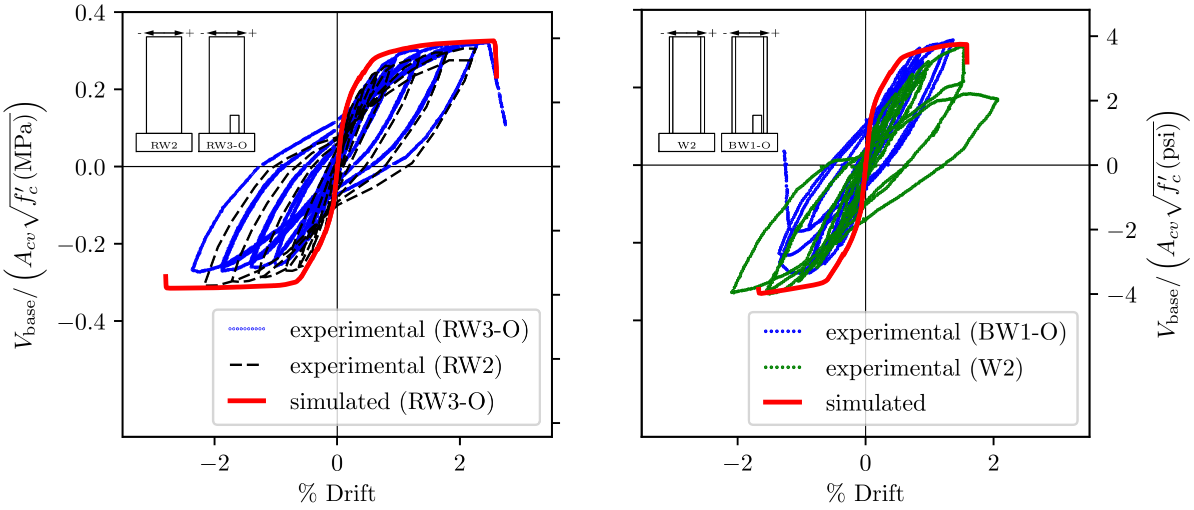

(a) Specimen RW3-O

(b) Specimen BW1-O

Figure 4.27: Load-deformation relationship for specimens tested by Taylor [55] simulated in ATENA.

solid, nine specimens had staggered openings, two specimens had one opening at the base and one specimen had openings at the center of each story. All simulation were monotonic with displacement controlled load at the effective height. Simulation results demonstrate the ability of the software to simulate response observed in the laboratory including strength and deformation capacity as well as provide improved understanding such walls with openings. ACI 318-14 [3], ASCE7 [8] were used to design twenty-nine walls with openings to investigate the impact of vertical irregularities.

4.4.2 Comparison of Simulated and Measured Responses

Data shows that

- Initial wall stiffness is overestimated,

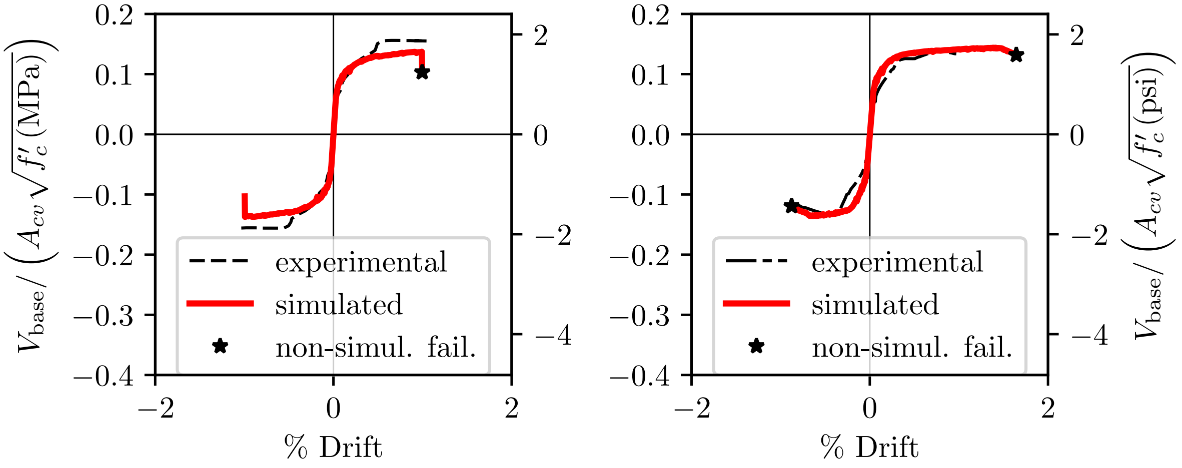

(a) SW1 **(b)** SW23

Figure 4.28: Load-deformation relationship for specimens tested by Marius [44] simulated in ATENA.

- Accurate prediction of the strength was achieved,
- Deformation capacity of the walls were well predicted for most of the walls.

4.4.3 New Understanding of the Behavior of Walls with Openings

The results of continuum analyses indicate

- Openings at center of the wall does not have a significant impact on the stiffness however, shear transfer mechanisms are affected the most,
- Deformation capacity is the most impacted by openings at the center of the wall, but proper design of the wall can improve the deformation capacity,
- Introducing an opening at the tension region of the wall, slightly reduces stiffness and strength but may result in a slight increase in deformation capacity,

- Introducing an opening in the compression region of the wall significantly reduces strength and deformation capacity,
- No difference observed between application of load at the effective height versus distributed loading for a solid wall.

Chapter 5

PARAMETRIC STUDY - FLANGED WALLS

5.1 Introduction and Motivation

Non-planar walls are used commonly in building construction to meet architectural constraints and to achieve required lateral stiffness and strength. Experimental and simulation data presented in Chapter 3 show that nonplanar walls can exhibit tension- and compression-controlled flexural failures as well as compression-shear failure; data show also that these failure modes result in a wide range of ductility capacities. While previous research identifies the factors that determine ductile and non-ductile failure modes for planar walls [9, 40], additional research is required to extend this work to non-planar walls. This chapter presents a simulation-based parameter study to investigate the behavior and response modes of nonplanar walls as well as the design parameters that determine the failure modes and ductility of these walls. As discussed in Chapter 3, the results of previous experimental research and simulation-based investigation of non-planar test specimens, demonstrates that

- Like planar walls, non-planar walls are vulnerable to compression-controlled and compression-shear failure modes; the potential for these failure modes is exacerbated in asymmetric non-planar walls where a larger "tension" flange can increase compression demand on a smaller "compression" flange (Section 3.4).

- Non-planar walls are vulnerable to compression-shear failure, characterized by onset of strength loss due to crushing at the web-boundary element interface, when high shear demands are coupled with high flexural compression demands (Section 3.4).

Past research on planar walls [40] shows that CSAR, shear demand and the depth of the confined region, all determine the likelihood of developing CB or CS (non-ductile) failure modes and that shear demand is a function of axial load, effective height and tension reinforcement. All of the above variable exist for non-planar walls. The large tension region exacerbates compression demands due to flexure, and that effective flange width in tension plays into this. These observations suggest opportunities for improving performance by preventing compression-shear failure, reducing compression demand by increasing flange width and expanding confinement in compression regions. Therefore, this study aim to evaluate: (1) a range of non-planar walls with different shear stress demands, (2) a range of non-planar walls with different flange widths, and (3) the ductility of non-planar walls compared to planar walls.

To achieve this, a simulation-based modeling parameter study was accomplished. The study employs reference wall specimens from the experimental dataset. For each reference wall specimen, shear span, strength of longitudinal bars, axial load ratio, and vertical boundary element reinforcement ratio were varied to achieve target peak shear stress demands; additionally, flange width and confinement length were varied to potentially improve performance. Study results provide improved understanding of performance.

5.2 Wall Designs Included in the Parameter Study

Three of the non-planar experimental test specimens used to validate the modeling approach were chosen as reference specimens for the parametric study. Each wall in the parametric study represents a modification of one of these reference test specimens. Modifications included variation in shear span, axial load ratio (ALR), reinforcement ratio ($\rho_{v,\mathrm{be}}$) and flange width to achieve higher peak shear stress demands, cross-sectional aspect ratio and higher deformation capacity. Cross-sectional aspect ratio is defined by the ratio of wall length to its thickness for planar walls. The study performed by Whitman [68] demonstrated that the planar walls are controlled by both cross-sectional aspect ratio and peak shear stress demand.

For parameter study, an ALR range of 0.0 to 20% applied to the specimens in addition to the variations in the shear span. The cross-sectional aspect ratio (CSAR) varied from 1.0

to 15.0 and shear span varied from 1.5 - 5.8. The CSAR calculation in flanged sections are more complex compared to planar walls. CSAR is defined as the ratio of the length of the wall (ℓ_w) to the associated thickness (t_w or b'_f). When flange is in compression, and the N.A. depth lies in the flange, flange width, b'_f, is used to calculate the CSAR. However, when N.A. depth is in the web portion of the wall, a weighted approach is employed in order to take into account the effects of both flange and web thicknesses. Therefore, CSAR is defined as:

$$\text{CSAR} = \frac{\ell_w A'_c}{b'_f A'_{c,f} + t_w A'_{c,w}} \tag{5.1}$$

where, t'_f , t_w and ℓ_w are the compression flange thickness, web thickness and wall length respectively, A'_c is the compressive area at nominal strength and c is the depth of neutral axis. The compression region for the case where N.A. lies in the web is shown in Figure 5.1. In order to observe the difference between weighted CSAR calculation versus regular calculation (i.e., ${}^{\ell_w}/_{t_w}$), the results for both methods are presented later in this chapter.

Tables 5.1 to 5.4 show the reinforcing properties, geometric properties and material properties of the reference specimens, respectively.

Table 5.1: Properties of parameter study reference specimens (SI units).

Specimen	ℓ_w	t_w	h	b_f	Shear span	ALR	${}^{V_{\max}}/_{A_{cv}\sqrt{f'_c}}$	${}^{V_{\max}}/_{V_n}$	Δ_u	$\delta_c^{1)}$	Failure mode
	mm	mm	mm	mm	–	%	MPa	–	%	%	
NTW1	2286	152.4	7925	1830	4.33	3	0.40		2.48	2.2	CB
NTW2	2286	152.4	7925	1830	4.33	3	0.43		1.65	3.7	CB
TC	1000	150.0	1800	850	1.2	6	0.17	1.16	3.5	3.9	CB

1) predicted wall displacement capacity per ACI 318-19 (Equation 18.10.6.2b)

5.2.1 Selection of Reference Specimens

Experimental specimens NTW1 and NTW2 (Figure 5.2) are selected to ensure half-scale models. The geometry of these walls are given in Tables 3.1 and 3.2. These specimens do

Table 5.2: Properties of parameter study reference specimens (Imperial units).

Specimen	ℓ_w	t_w	h	b_f	Shear span	ALR	$^{V_{\max}}/_{A_{cv}\sqrt{f'_c}}$	$^{V_{\max}}/_{V_n}$	Δ_u	$\delta_c^{1)}$	Failure mode
	in.	in.	in.	in.	–	%	psi	–	%	%	
NTW1	90.0	6.0	312.0	72.0	4.33	3	4.8		2.48	2.2	CB
NTW2	90.0	6.0	312.0	72.0	4.33	3	5.2		1.65	3.7	CB
TC	39.4	5.9	70.9	33.5	1.2	6	2.1	1.16	3.5	3.9	CB

1) predicted wall displacement capacity per ACI 318-19 (Equation 18.10.6.2b)

Table 5.3: Reinforcing properties of parameter study reference specimens

Specimen	**Reinforcing steel**						**Confinement**		
	$\rho_{\text{v,BE}}$	$\rho_{\text{v,web}}$	ρ_{gross}	$\rho_{\text{t,web}}$	ρ_{vol}	h_x	s_{vert}	s_{vert}/d_b	h_x/s
	%	%	%	%	%	mm (in.)	mm (in.)	-	-
NTW1	3.70	0.30	3.5	0.33	3.5	89 (3.5)	50.8 (2.0)	3.56	1.75
NTW2	3.34	0.25	3.5	0.33	3.5	89 (3.5)	50.8 (2.0)	3.56	1.75
TC	2.10	1.30	3.5	1.27	3.5	130 (5.12)	35 (1.38)	6.89	3.71

Table 5.4: Material properties of parameter study reference specimens

Specimen	f'_c	$f_{y,\text{be}}$	$f_{u,\text{be}}$	$\epsilon_{u,\text{be}}$	$f_{y,v}$	$f_{u,v}$	$\epsilon_{u,v}$
	MPa (psi)	MPa (ksi)	MPa (ksi)	–	MPa (ksi)	MPa (ksi)	–
NTW1	50.3 (7300)	439 (63.6)	707 (102.5)	0.14	514 (74.5)	727 (105.5)	0.14
NTW2	50.3 (7300)	439 (63.6)	707 (102.5)	0.14	514 (74.5)	727 (105.5)	0.14
TC	37.7 (5468)	355 (51.5)	483 (70.0)	0.18	355 (51.5)	483 (70.0)	0.18

not contain confinement in the web-flange intersection, therefore, in order to be compliant with the ACI 318-19 [4] requirements of special BE, confinement was added in the simulation. The main difference between the two specimens is in the reinforcement configuration in the flange. Speciment NTW1 is provided with heavier lumped reinforcement on both ends of the flange while in specimen NTW2 a rather uniformly distributed heavy reinforcement is used. Also, specimen NTW2 has a longer depth of confinement in the two of the web. Additionally, wall specimen TC [21] shown in Figure 5.2c is added to the list of reference specimens since it provided a smaller CSAR compared to specimens NTW1 and NTW2. These specimens were chosen because they are representative of modern construction and a range of reinforcement configurations.

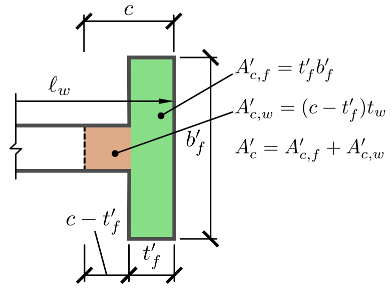

Figure 5.1: Compression region for a flanged wall when c lies in the web.

5.2.2 Study Parameters

The purpose of this study was to investigate the behavior and performance of walls subjected to higher shear stress demands, different flange widths, and axial load ratios. To investigate the impact of design parameters on non-planar wall performance, a series of new wall designs was created by modifying the reference specimen designs as follows:

- Normalized peak shear stress = ${}^{V_{\max}}/_{A_{cv}\sqrt{f'_c}}$: peak shear stress directly affects the failure mode of the wall specimens [40, 68] (see Section 5.1). Therefore, it is a key parameter for this study. In this study the normalized peak shear stress varied from $3\sqrt{f'_c}$ to $18\sqrt{f'_c}$ psi ($0.25\sqrt{f'_c}$ to $1.49\sqrt{f'_c}$ MPa).

- Wall length (CSAR): variation in the ℓ_w resulted in variation in cross-sectional aspect ratio. According to Lowes et al. [40], CSAR has an essential role in developing ductile

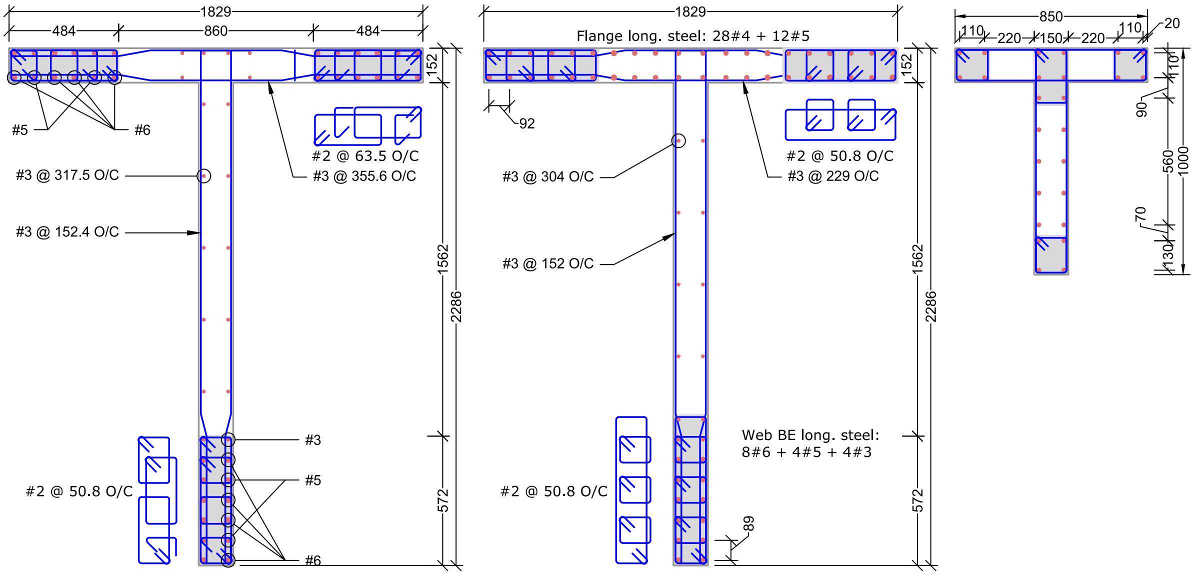

(a) Specimen NTW1 **(b)** Specimen NTW2 **(c)** Specimen TC

Figure 5.2: Cross-sectional view of Specimens NTW1, NTW2 and TC (dimensions in mm).

(CB) versus non-ductile (CS) failure mode. The CSAR computation is based on Equation (5.1) and Figure 5.1 and it ranged from 6.67 to 20.0 in this study.

- Flange width (b'_f): existence of a flange in the compression region could affect the performance of the wall and the way it could potentially fail. This is a difficult parameter to be studied experimentally. b'_f varied from no flange to a flange width equal to the one provided on the other end of the wall. As a result, three main geometrical configurations were used; T-shaped, semi-I-shaped, and I-shaped. Where the I-shaped cross-section is symmetric and Semi-I-shaped has the flange width in compression narrower than the one in tension. The flange length for all the T– and I–shaped specimens is the same as the associating reference walls. For the Semi–I–shaped walls the narrower flange width is either 33% or 55% of the wider flange; i.e., $b'_f = (0.33 \text{ or } 0.53)b_f$. (Note that if the flange width is denoted as b_f, i.e., without the prime, it refers to the flange width in tension).

- Axial Load Ratio (ALR): the axial load ratio for the reference specimens and experimental dataset was ranged from 0 to 6.0%. For parameter study, the range of ALR varied from 0.0 to 20%.

- Depth of confinement (ℓ_{be}/c): depth of confinement relative to the depth of neutral axis was varied from 0.25 to 1.19.

The main parameters used to acquire different shear stress demands were shear span, axial ratio, and reinforcement ratio in the BE. These parameters were varied as follows:

- Shear Span (${}^{M}/_{\ell_w V}$): for all the walls, shear span changed in order to achieve different shear stress demands.

- Axial Load Ratio (ALR): the axial load ratio for each wall specimen varied from 0.0 to 20%.

- Reinforcement Ratio ($\rho_{\mathrm{v,BE}}$): to preserve ACI compliancy of the wall BE detailing and reinforcement configuration due to the increase in the shear stress demand and ALR, the reinforcement ratio was increased. Accordingly, the reinforcement ratio in the web of the walls modified whenever required by the ACI code.

Simulation matrix is categorized based on the shape (generally width of the flange) and presented in Tables 5.5 to 5.7. The models are labeled as:

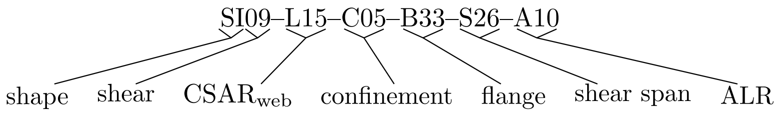

- Shape: T, SI (Semi–I), I
- Shear: peak shear stress demand at M_n ranging from $3\sqrt{f_c'}$ to $18\sqrt{f_c'}$ psi ($0.25\sqrt{f_c'}$ to $1.49\sqrt{f_c'}$ MPa)
- CSAR$_{\text{web}}$: ℓ_w/t_w ranging from 1.18 to 20.0
- Confinement: $(\ell_{\text{be}}/c) \times 10$ ranging from 0.25 to 1.19
- Flange: $b_f'/b_f \times 100$ ranging from $b_f' = t_w$ to $b_f' = b_f$
- Shear span: shear span ×10 ranging from 1.2 to 5.78
- ALR: axial load ratio ranging from 0% to 20%.

For instance, model SI09–L15–C05–B33–S26–A10 is a Semi–I–shaped wall with a shear stress demand of about $9\sqrt{f_c'}$ psi, wall length to wall thickness ratio of 15, confined length to depth of N.A. ratio of 0.5, compression flange width to tension flange with ratio of 0.33, shear span of 2.6 and an axial load ratio of 10%. For T–shaped and I–shaped walls the symbol `B--` is not included since it is apparent from the shapes whether b_f' is equal to b_f (i.e., I–shaped) or no flange is provided in compression (i.e., T–shaped). For example, model T03–L15–C11–S43–A00 is a T–shaped wall with a shear stress demand of about $3\sqrt{f_c'}$ psi, ${}^{\ell_w}\!/_{t_w} = 15$, ${}^{\ell_{\text{be}}}\!/_{c} = 1.1$, shear span of 4.3 and no ALR.

Table 5.5: List of simulated T-shaped models.

Specimen	**Shear span**	$\mathbf{V_{\max}/A_{cv}\sqrt{f_c'}}$	$\mathbf{b_f}$	**ALR**	$\mathbf{f_y}$	$\rho_{\mathbf{BE}}$	$\rho_{\mathbf{t},\text{web}}$	$\rho_{\mathbf{BE},\text{flange}}$
		MPa (psi)	mm (in.)	%	MPa (ksi)	%	%	%
T03–L15–C11–S43–A00	4.33	0.28 (3.4)	1829 (72)	0	439 (63.6)	3.7	0.3	3.34
T04–L15–C07–S43–A05	4.33	0.36 (4.3)	1829 (72)	5	439 (63.6)	3.7	0.3	3.34
T05–L15–C05–S43–A10	4.33	0.43 (5.2)	1829 (72)	10	439 (63.6)	3.7	0.3	3.34
T06–L15–C04–S43–A20	4.33	0.55 (6.6)	1829 (72)	20	439 (63.6)	3.7	0.3	3.34
T05–L15–C02–S43–A15	4.33	0.48 (5.8)	1829 (72)	15	439 (63.6)	3.3	0.4	3.34
T06–L15–C02–S43–A20	4.33	0.53 (6.4)	1829 (72)	20	439 (63.6)	3.3	0.4	3.34
T05–L15–C11–S35–A00	3.47	0.38 (4.6)	1829 (72)	0	439 (63.6)	3.7	0.3	3.34
T06–L15–C07–S35–A05	3.47	0.46 (5.5)	1829 (72)	5	439 (63.6)	3.7	0.3	3.34

Table 5.5: (continued)

Specimen	**Shear span**	$\mathbf{V_{max}/A_{cv}\sqrt{f'_c}}$	$\mathbf{b_f}$	**ALR**	$\mathbf{f_y}$	$\rho_{\mathbf{BE}}$	$\rho_{\mathbf{t},\text{web}}$	$\rho_{\mathbf{BE},\text{flange}}$
		MPa (psi)	mm (in.)	%	MPa (ksi)	%	%	%
T07–L15–C04–S35–A15	3.47	0.62 (7.5)	1829 (72)	15	439 (63.6)	3.7	0.3	3.34
T08–L15–C04–S35–A20	3.47	0.70 (8.4)	1829 (72)	20	439 (63.6)	3.7	0.3	3.34
T08–L15–C05–S27–A10	2.67	0.69 (8.3)	1829 (72)	10	439 (63.6)	3.7	0.3	3.34
T10–L15–C04–S27–A15	2.67	0.80 (9.6)	1829 (72)	15	439 (63.6)	3.7	0.3	3.34
T11–L15–C04–S27–A20	2.67	0.89 (10.7)	1829 (72)	20	439 (63.6)	3.7	0.3	3.34
T14–L10–C07–S12–A12	1.20	1.13 (13.6)	850 (33.46)	12	356 (51.6)	3.7	0.3	3.34
T15–L10–C06–S12–A18	1.20	1.27 (15.3)	850 (33.46)	18	356 (51.6)	3.7	0.3	3.34
T09–L10–C05–S12–A00	1.20	0.75 (9.0)	850 (33.46)	0	356 (51.6)	3.3	0.4	3.34
T11–L10–C04–S12–A06	1.20	0.94 (11.4)	850 (33.46)	6	356 (51.6)	3.3	0.4	3.34
T08–L10–C05–S15–A00	1.50	0.63 (7.5)	850 (33.46)	0	356 (51.6)	3.7	0.3	3.34
T09–L10–C04–S15–A06	1.50	0.78 (9.4)	850 (33.46)	6	356 (51.6)	3.7	0.3	3.34
T11–L10–C03–S15–A12	1.50	0.93 (11.2)	850 (33.46)	12	356 (51.6)	3.7	0.3	3.34
T13–L10–C02–S15–A18	1.50	1.06 (12.8)	850 (33.46)	18	356 (51.6)	3.7	0.3	3.34
T05–L10–C05–S24–A00	2.40	0.42 (5.1)	850 (33.46)	0	356 (51.6)	3.7	0.3	3.34
T06–L10–C04–S24–A06	2.40	0.49 (6.0)	850 (33.46)	6	356 (51.6)	3.7	0.3	3.34
T07–L10–C03–S24–A12	2.40	0.59 (7.1)	850 (33.46)	12	356 (51.6)	3.7	0.3	3.34
T08–L10–C02–S24–A18	2.40	0.67 (8.1)	850 (33.46)	18	356 (51.6)	3.7	0.3	3.34
T04–L09–C12–S58–A00	5.78	0.35 (4.2)	1829 (72)	0	439 (60.3)	3.7	0.3	3.34
T05–L09–C08–S58–A05	5.78	0.40 (4.8)	1829 (72)	5	439 (60.3)	3.7	0.3	3.34
T05–L09–C07–S58–A10	5.78	0.45 (5.4)	1829 (72)	10	439 (60.3)	3.7	0.3	3.34
T06–L09–C06–S58–A15	5.78	0.50 (6.0)	1829 (72)	15	439 (60.3)	3.7	0.3	3.34
T07–L09–C05–S58–A20	5.78	0.54 (6.5)	1829 (72)	20	439 (60.3)	3.7	0.3	3.34
T04–L11–C12–S47–A00	4.72	0.36 (4.4)	1829 (72)	0	439 (60.3)	3.7	0.3	3.34
T06–L11–C08–S47–A05	4.72	0.42 (5.1)	1829 (72)	5	439 (60.3)	3.7	0.3	3.34
T06–L11–C07–S47–A10	4.72	0.49 (5.9)	1829 (72)	10	439 (60.3)	3.7	0.3	3.34
T07–L11–C06–S47–A15	4.72	0.55 (6.6)	1829 (72)	15	439 (60.3)	3.7	0.3	3.34
T07–L11–C05–S47–A20	4.72	0.60 (7.3)	1829 (72)	20	439 (60.3)	3.7	0.3	3.34
T05–L20–C11–S24–A00	2.37	0.40 (4.9)	1829 (72)	0	439 (60.3)	3.7	0.3	3.34
T06–L20–C07–S24–A05	2.37	0.50 (6.0)	1829 (72)	5	439 (60.3)	3.7	0.3	3.34
T07–L20–C05–S24–A10	2.37	0.60 (7.2)	1829 (72)	10	439 (60.3)	3.7	0.3	3.34
T08–L20–C06–S26–A15	2.60	0.70 (8.4)	1829 (72)	15	439 (60.3)	3.7	0.3	3.34
T09–L20–C05–S26–A20	2.60	0.79 (9.5)	1829 (72)	20	439 (60.3)	3.7	0.3	3.34

Table 5.6: List of simulated Semi–I–shaped models.

Specimen	Shear span	$\frac{V_{max}}{A_{cv}\sqrt{f'_c}}$	b_f	b'_f	ALR	f_y	ρ_{BE}	$\rho_{t,web}$	$\rho_{BE,flange}$
		MPa (psi)	mm (in.)	mm (in.)	%	MPa (ksi)	%	%	%
SI06–L15–C19–B33–S26–A00	2.60	0.53 (6.4)	1829 (72)	610 (24)	0	439 (63.6)	3.7	0.3	3.3
SI07–L15–C15–B33–S26–A03	2.60	0.59 (7.1)	1829 (72)	610 (24)	3	439 (63.6)	3.7	0.3	3.3
SI08–L15–C09–B33–S26–A06	2.60	0.65 (7.8)	1829 (72)	610 (24)	6	439 (63.6)	3.7	0.3	3.3
SI09–L15–C05–B33–S26–A10	2.60	0.72 (8.6)	1829 (72)	610 (24)	10	439 (63.6)	3.7	0.3	3.3
SI10–L15–C03–B33–S26–A15	2.60	0.82 (9.9)	1829 (72)	610 (24)	15	439 (63.6)	3.7	0.3	3.3
SI11–L15–C03–B33–S26–A20	2.60	0.92 (11.0)	1829 (72)	610 (24)	20	439 (63.6)	3.7	0.3	3.3
SI05–L15–C19–B33–S35–A00	3.47	0.43 (5.1)	1829 (72)	610 (24)	0	439 (63.6)	3.7	0.3	3.3
SI07–L15–C15–B33–S35–A03	3.47	0.52 (6.2)	1829 (72)	610 (24)	3	439 (63.6)	3.7	0.3	3.3
SI07–L15–C09–B33–S35–A06	3.47	0.63 (7.6)	1829 (72)	610 (24)	6	439 (63.6)	3.7	0.3	3.3
SI09–L15–C05–B33–S35–A10	3.47	0.79 (9.5)	1829 (72)	610 (24)	10	439 (63.6)	3.7	0.3	3.3
SI11–L15–C03–B33–S35–A15	3.47	0.94 (11.3)	1829 (72)	610 (24)	15	439 (63.6)	3.7	0.3	3.3
SI11–L15–C05–B33–S35–A20	3.47	0.93 (11.2)	1829 (72)	610 (24)	20	439 (63.6)	3.7	0.3	3.3
SI04–L15–C19–B33–S43–A00	4.33	0.34 (4.1)	1829 (72)	610 (24)	0	439 (63.6)	3.7	0.3	3.3
SI06–L15–C11–B33–S43–A05	4.33	0.47 (5.6)	1829 (72)	610 (24)	5	439 (63.6)	3.7	0.3	3.3
SI08–L15–C05–B33–S43–A10	4.33	0.62 (7.5)	1829 (72)	610 (24)	10	439 (63.6)	3.7	0.3	3.3
SI09–L15–C05–B33–S43–A15	4.33	0.74 (9.0)	1829 (72)	610 (24)	15	439 (63.6)	3.7	0.3	3.3
SI11–L15–C14–B53–S15–A00	1.5	0.94 (11.3)	850 (33.46)	450 (17.72)	0	356 (51.6)	2.1	1. 3	2.1
SI14–L15–C20–B53–S15–A06	1.5	1.13 (13.6)	850 (33.46)	450 (17.72)	6	356 (51.6)	2.1	1. 3	2.1
SI16–L15–C15–B53–S15–A12	1.5	1.32 (15.9)	850 (33.46)	450 (17.72)	12	356 (51.6)	2.1	1. 3	2.1
SI17–L15–C11–B53–S15–A18	1.5	1.45 (17.4)	850 (33.46)	450 (17.72)	18	356 (51.6)	2.1	1. 3	2.1

5.3 Results

The parametric models shown in the Section 5.2.2 were modeled in ATENA . The numerical techniques developed and validated in Chapters 3 and 4 were used to analyze the models. Failure modes were identified using the procedure presented in Section 2.3.5, and ductility and hinge rotation were calculated using the methods presented belowe in Section 5.3.1.

5.3.1 Computed Response Quantities

For the study, simulated wall response and performance was defined on the basis of maximum shear stress demand, displacment ductility, drift capacity, and failure mode. These quantities were defined as follows:

Table 5.7: List of simulated I-shaped models.

Specimen	**Shear span**	$\mathbf{\frac{V_{max}}{A_{cv}\sqrt{f'_c}}}$	$\mathbf{b_f}$	**ALR**	$\mathbf{f_y}$	$\rho_{\mathbf{BE}}$	$\rho_{\mathbf{t},\text{web}}$	$\rho_{\mathbf{BE},\text{flange}}$
		MPa (psi)	mm (in.)	%	MPa (ksi)	%	%	%
I12–L01–C37–S18–A00	1.80	0.95 (11.4)	850 (33.46)	0	356 (51.6)	2.1	1.3	2.1
I15–L01–C25–S18–A06	1.80	1.20 (14.5)	850 (33.46)	6	356 (51.6)	2.1	1.3	2.1
I17–L01–C20–S18–A12	1.80	1.43 (17.2)	850 (33.46)	12	356 (51.6)	2.1	1.3	2.1
I09–L01–C37–S18–A00	1.80	0.73 (8.8)	850 (33.46)	0	356 (51.6)	2.1	1.3	2.1
I11–L01–C25–S18–A06	1.80	0.92 (11.1)	850 (33.46)	6	356 (51.6)	2.1	1.3	2.1
I13–L01–C20–S18–A12	1.80	1.10 (13.3)	850 (33.46)	12	356 (51.6)	2.1	1.3	2.1
I07–L01–C25–S26–A00	2.60	0.56 (6.8)	1829 (72)	0	439 (63.6)	3.7	0.3	3.34
I08–L15–C19–S26–A05	2.60	0.67 (8.0)	1829 (72)	5	439 (63.6)	3.7	0.3	3.34
I09–L15–C15–S26–A10	2.60	0.79 (9.5)	1829 (72)	10	439 (63.6)	3.7	0.3	3.34
I11–L15–C07–S26–A15	2.60	0.92 (11.0)	1829 (72)	15	439 (63.6)	3.7	0.3	3.34
I12–L15–C03–S26–A20	2.60	1.04 (12.5)	1829 (72)	20	439 (63.6)	3.7	0.3	3.34
I05–L15–C25–S35–A00	3.46	0.43 (5.2)	1829 (72)	0	439 (63.6)	3.7	0.3	3.34
I06–L15–C19–S35–A05	3.46	0.51 (6.1)	1829 (72)	5	439 (63.6)	3.7	0.3	3.34
I07–L15–C15–S35–A10	3.47	0.60 (7.2)	1829 (72)	10	439 (63.6)	3.7	0.3	3.34
I08–L15–C07–S35–A15	3.46	0.70 (8.5)	1829 (72)	15	439 (63.6)	3.7	0.3	3.34
I10–L15–C03–S35–A20	3.47	0.80 (9.7)	1829 (72)	20	439 (63.6)	3.7	0.3	3.34

- Normalized peak shear stress = ${V_{\max}}/\left(A_{cv}\sqrt{f'_c}\right)$: where $V_{\max}$ is the maximum base shear force developed in the analysis, A_{cv} is the gross area of concrete section bounded by web thickness and length of section in the direction of shear force, and f'_c is the concrete compressive strength.

- Deformation capacity, defined by onsent of simulated or non-simulated strength loss as discussed in Chapter 3, and quanitified using displacmenet ductility, drift capacity, and hinge rotation capacity:
  - Ductility: defined as the maximum displacement (Δ_u) reached by the model divided by the displacement at yielding (Δ_y).
  - Drift: defined at the effective height of the wall (Δ_u/h_{eff}).

  - Hinge rotation: vertical displacements at each end of the model at a distance equal to $\ell_w/2$ above the model base were computed and used to calculate hinge rotation. The distance $\ell_w/2$ is assumed to be the hinge length i.e., the critical section.

$$\text{Hinge Rotation [rad]} = (\Delta_{\text{vert,left}} - \Delta_{\text{vert,right}})/\ell_w \tag{5.2}$$

  For non-planar walls, drift capacity and hinge rotation magnitudes are dependent on stiffness of non-planar systems and thus cannot be compared for different wall configurations. Yet, ductility is not dependent on stiffness (see Figure 5.3). Figure 5.3 shows different approaches used to compute deformation capacity; i.e., hinge rotation (Figure 5.3a), drift (Figure 5.3b) and ductility (Figure 5.3c). The figure indicates that ductility is the only measure that can present the deformation capacity without any biases. Therefore, only ductility is presented as part of deformation capacity in this chapter and other quatities of deformation capacity (drift and hinge rotation) are provided in Appendix B.

- Failure mode: Analysis results were post-processed to characterize the cause of lateral strength loss as compression-buckling (CB), compression-shear (CS) or buckling rupture (BR) (i.e., CB, CS, or BR); these failure modes are discussed in detail in Chapter 2.

5.3.2 Tabular Results

The results of each set of analyses are shown in Tables B.1 to B.3. The results include normalized shear stress demand, drift, ductility and failure mode. For T–shaped walls shear span ranged from 1.2 to 5.78, CSAR ranged from 9 to 20, peaks shear stress demand ranged from $3.9\sqrt{f'_c}$ psi to $15.3\sqrt{f'_c}$ psi. For SemiI–shaped walls shear span ranged from 1.5 to 3.47, CSAR ranged from 2.22 to 15, peaks shear stress demand ranged from $6.0\sqrt{f'_c}$ psi to $17.4\sqrt{f'_c}$ psi. For T–shaped walls shear span ranged from 1.8 to 3.47, CSAR ranged from 1.18 to 15, peaks shear stress demand ranged from $6.0\sqrt{f'_c}$ psi to $17.2\sqrt{f'_c}$ psi.

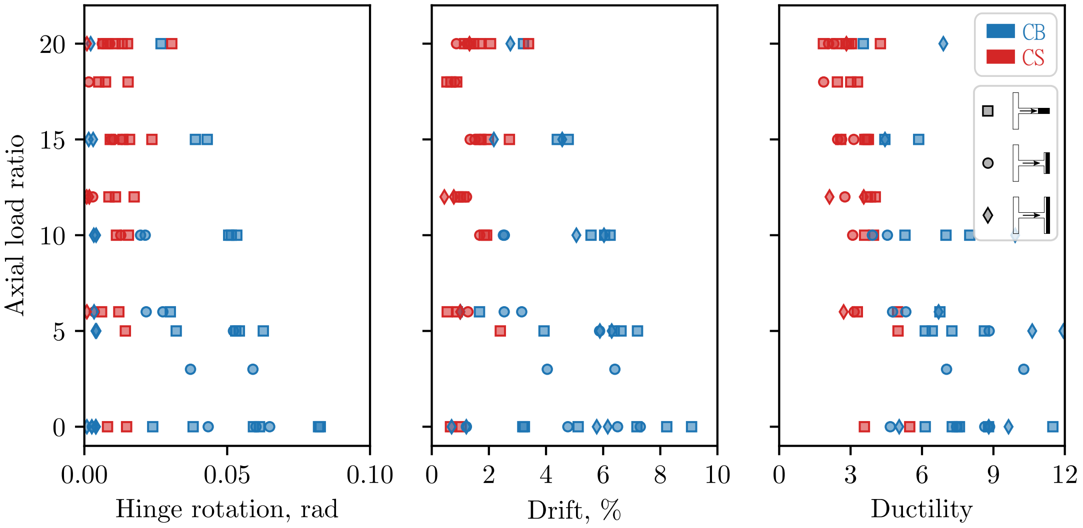

(a) Hinge rotation **(b)** Drift **(c)** Ductility

Figure 5.3: Comparison between different approaches used to compute deformation capacity.

5.3.3 Results

Figures 5.4 to 5.13 and B.7 investigate the relationship between design parameters (shear stress demand, CSAR, axial load ratio and configuration) and performance measures (ductility, drift capacity, hinge rotation and failure mode), they are plotted against each other. The data in these figures includes the simulation data for I– , semi–I– and T–shaped walls created as part of the current study as well as simulation data generated for planar walls by Whitman [68].

5.3.3.1 Depth of Confinement

Depth of confinement in walls with toes is an important parameter. Earlier research [40] has shown that an increase in the depth of confinement for planar walls, could significantly decrease the possibility of a CS failure [40, 68]. Results shown in Figure 5.4 indicates that similar conclusions could be made for T–shaped walls. As the depth of confinement increases, T–shaped walls tend to behave more ductile by exhibiting a CB failure.

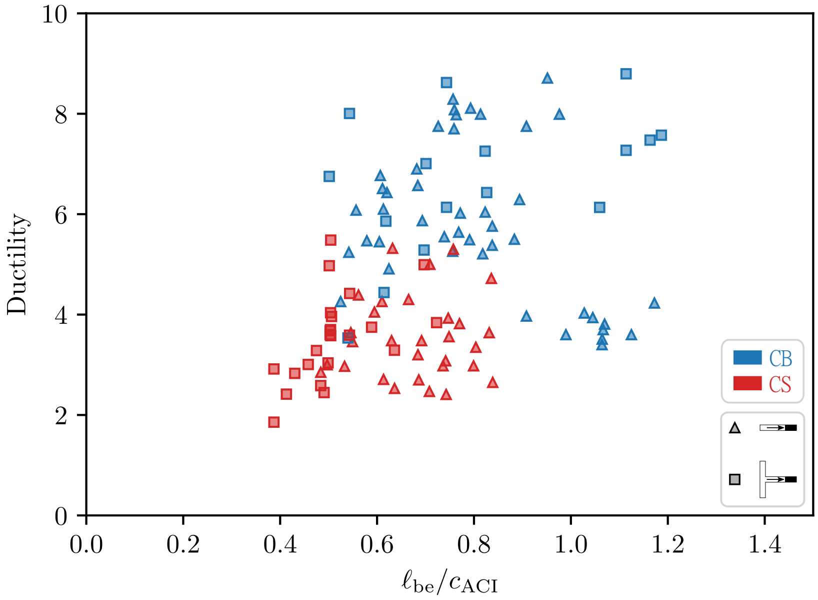

Figure 5.4: Relationship between ductility and confined length for planar and T-shaped walls when toe is in compression.

5.3.3.2 Axial Load Ratio

Figure 5.5 shows ductility versus axial load ratio for the three wall configurations simulated as part of the current project as well as for planar walls [68]. The data show that ductility increases with reduced axial load for planar, T– and Semi–I but not for I–shaped walls. This is attributed to the fact that for low axial loads, the flexural compression zone remains in the wall flange and ACI Code requirements for confinement of the web-flange interface that result in the depth of confinement extending well into the web of the wall and well-beyond the flexural compression zone such that there is not an opportunity for shear and flexure induced compression to compound in the unconfined web region of the wall. The data show that CS failures results in less ductility than CB failures, for a given axial load level. Ultimately, the data in Figure 5.5 suggest that axial load ratio, is not a primarily design parameter determining wall response; this is consistent with the results of the previous study (Lowes et al., 2019).

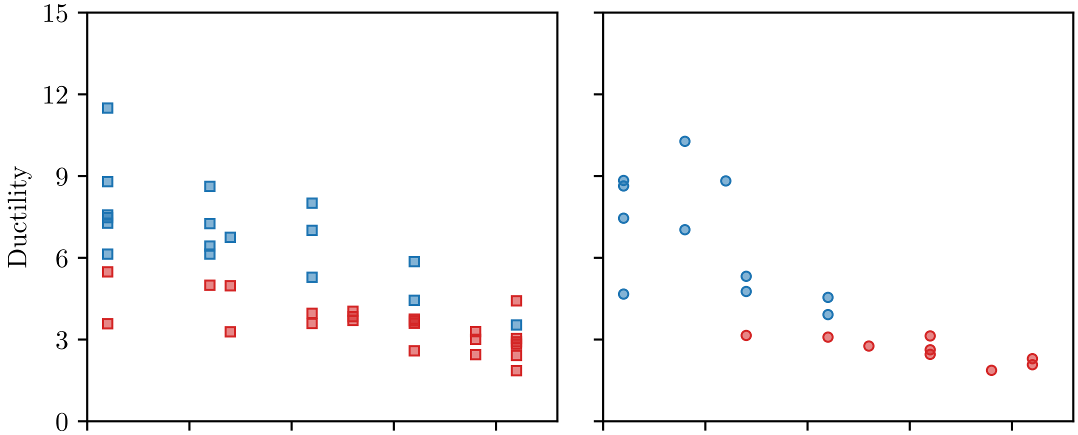

(a) T-shape **(b)** Semi-I-shape

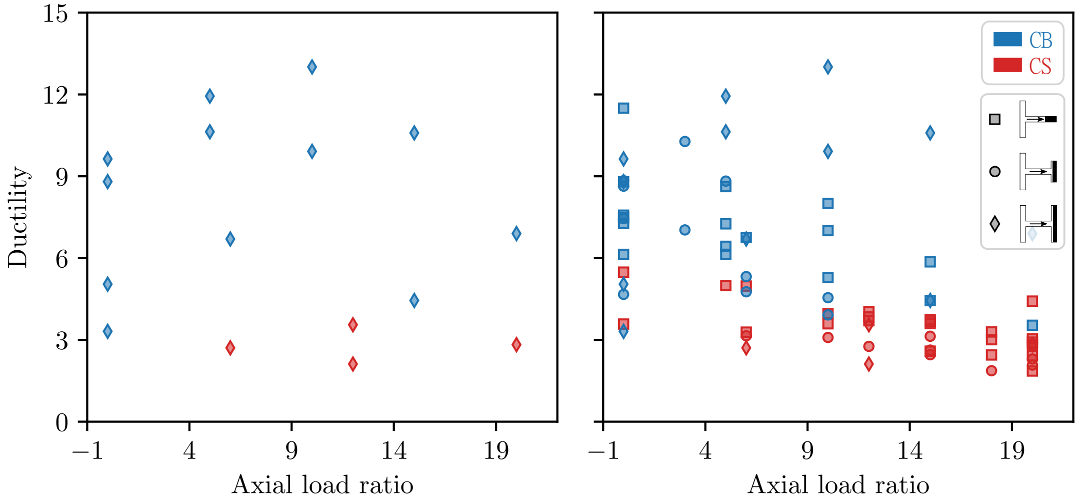

(c) I-shape **(d)** All shapes

Figure 5.5: Relationship between deformation capacity and axial load ratio for T–, Semi–I–, and I–shaped walls.

5.3.3.3 Cross-Sectional Aspect Ratio

The data in Figures 5.6 and 5.7 show ductility versus cross-sectional aspect ratio for the the three wall configurations simulated as part of this study as well as for planar walls [68]. These data show no correlation between these variables. As noted previously, the data show that the CS failure mode is associated with lower levels of ductility.

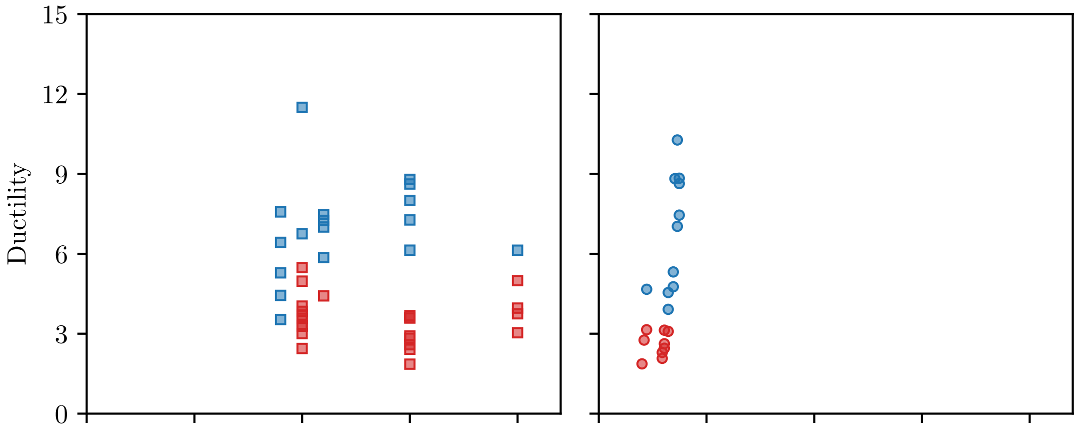

(a) T-shape **(b)** Semi-I-shape

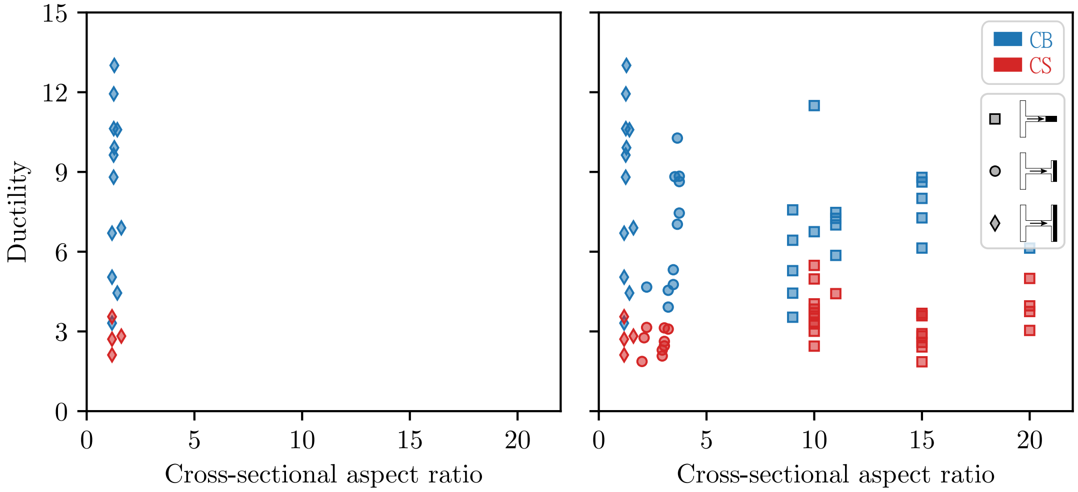

(c) I-shape **(d)** All shapes

Figure 5.6: Relationship between ductility and *weighted* cross-sectional aspect ratio for T–, Semi–I–, and I–shaped walls.

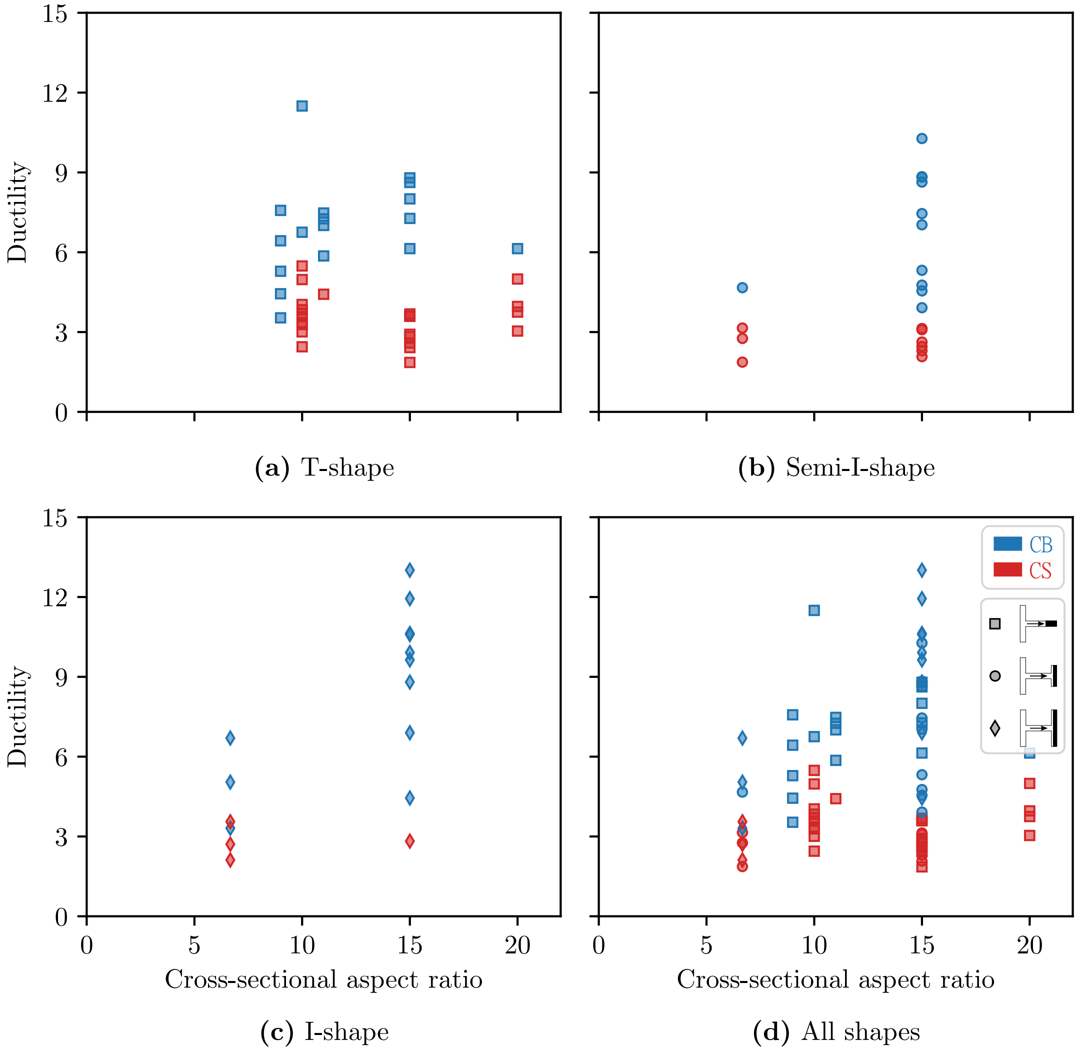

(a) T-shape **(b)** Semi-I-shape

(c) I-shape **(d)** All shapes

Figure 5.7: Relationship between ductility and *regular* cross-sectional aspect ratio for T–, Semi–I–, and I–shaped walls.

For T–shaped walls which behave very similar to the rectangular walls. For lower cross-sectional aspect ratios, T–shaped walls exhibit relatively higher deformation capacity. This is consistent with the conclusions made by Whitman [68] where the study showed that for the same failure mode, walls with smaller CSAR could undertake higher deformation capacity. When flanges are present, depth of neutral axis could lie either in the flange or in the web of the wall. This causes different walls with similar geometries to have different cross-sectional aspect ratios. Therefore, unlike walls without flanges, CSAR seems to be a more complex parameter for studying the behavior of flanged walls and could not demonstrate the behavior by itself. Rather, the behavior could be better demonstrated by combining CSAR along with confining depth and categorized on bases of ductility.

5.3.3.4 Peak Shear Stress Demand

Figure 5.8 shows the impact of maximum shear stress demand on deformation capacity as defined by ductility and hinge rotation; again data developed as part of the current study are compared with data for planar walls developed during a previous study. The data in these figures show that

1. high shear stress demand results in low ductility

2. the shear demand limit, which cannot be exceeded, to achieve high ductility increases as compression flange area is added, i.e progressing from planar and T–shpared walls, to semi–I–shaped walls, to I-shaped walls.

For T–shaped walls, similar to planar walls, when shear stress demand exceeds $0.42\sqrt{f'_c}$ MPa ($5\sqrt{f'_c}$ psi) , wall is more likely to fail in CS. However, adding flanges to the walls, causes a shift in this limit to about $0.75\sqrt{f'_c}$ MPa ($9\sqrt{f'_c}$ psi) if moderate flange width is used (Semi–I–shaped) and even up to $1.0\sqrt{f'_c}$ MPa ($12\sqrt{f'_c}$ psi) for larger flange widths. Consequently, flanges increase ductility. These dividing borders are shown in Figure 5.8.

As studied and concluded by Whitman [68], the CS failure mode only occurs for walls with a shear stress demand greater than $6\sqrt{f'_c}$ psi ($0.5\sqrt{f'_c}$ MPa). When such walls provided with a confinement length of about the depth of neutral axis, they can exhibit a CB failure instead of a CS failure. The specimens in the Figure 5.9 that exhibit a CB failure while having a shear stress demand of greater than $5\sqrt{f'_c}$ are having a boundary element length between 0.8c to 1.15c, where c is the neutral axis depth. ACI 318-19 [4] requires the boundary element length to be the greater of $c - 0.1\ell_w$ and $c/2$, where c is the depth of N.A. at M_n.

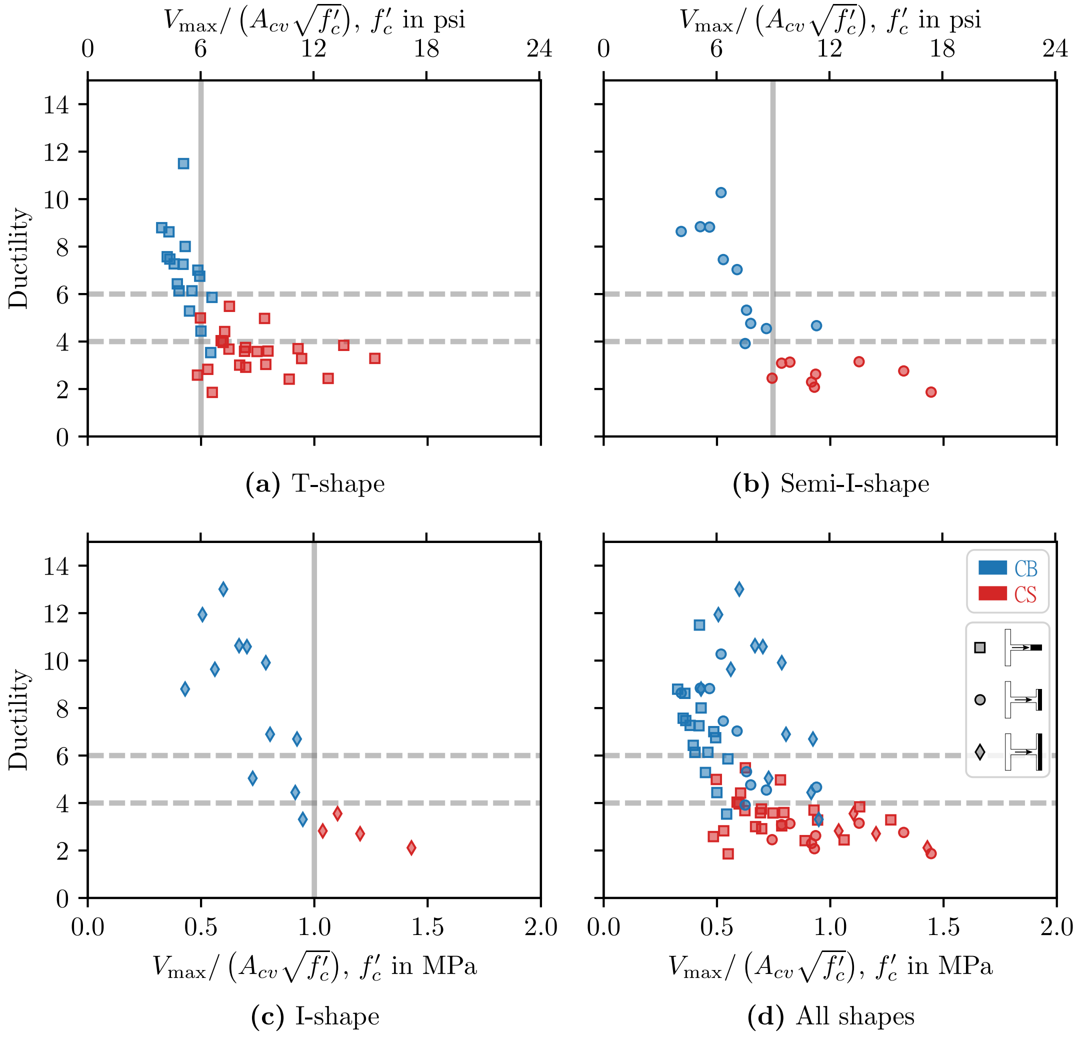

(a) T-shape **(b)** Semi-I-shape

(c) I-shape **(d)** All shapes

Figure 5.8: Relationship between peak shear stress and ductility for T–, Semi–I–, and I–shaped walls.

5.3.3.5 *Deformation Capacity*

As shown in Figures 5.9 to 5.12 deformation capacity and failure mode are influenced by the shear stress demand, cross-sectional aspect ratio (CSAR), confinement depth and ALR.

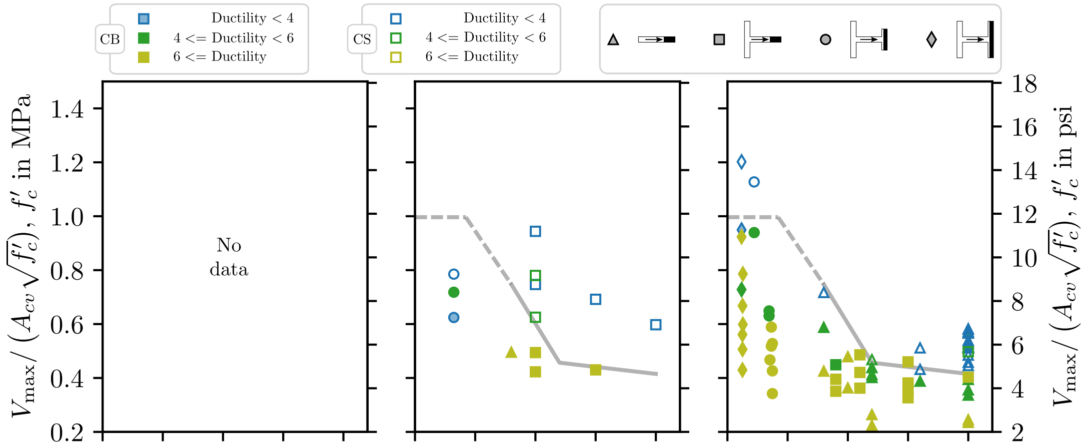

(a) $\ell_{\mathrm{be}}/c <= 0.4$
ALR<= 10%

(b) $0.4 < \ell_{\mathrm{be}}/c <= 0.6$
ALR<= 10%

(c) $0.6 < \ell_{\mathrm{be}}/c$
ALR<= 10%

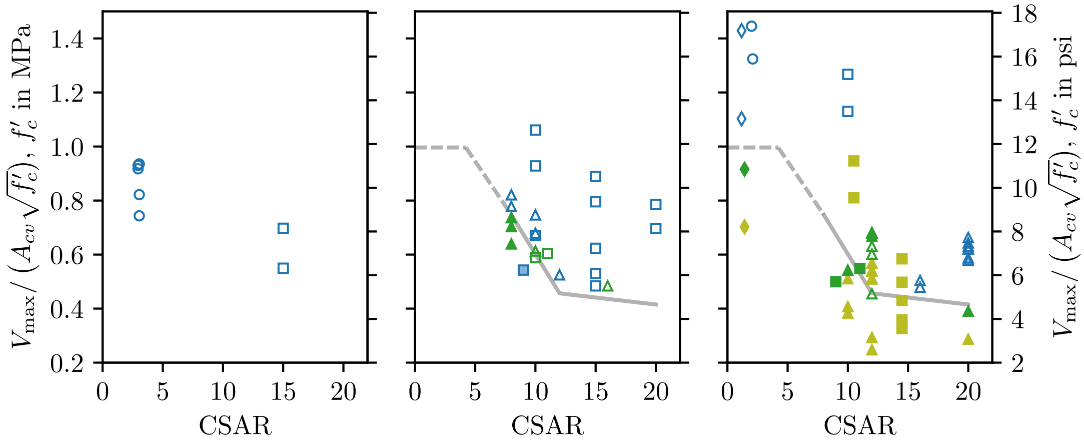

(d) $\ell_{\mathrm{be}}/c <= 0.4$
ALR> 10%

(e) $0.4 < \ell_{\mathrm{be}}/c <= 0.6$
ALR> 10%

(f) $0.6 < \ell_{\mathrm{be}}/c$
ALR> 10%

Figure 5.9: Relationship between peak shear stress and *weighted* cross-sectional aspect ratio, confinement length and axial load ratio for T–, Semi–I–, I–shaped and planar walls.

The data presented in Figures 5.9 to 5.12 show that T–shaped walls behave very similarly to planar walls when the toe is in compression.

Data shown in Figures 5.9 to 5.12 indicate that failure mode and ductility are influenced by the CSAR, shear stress demand and length of confinement. Figure 5.9, shows CSAR versus normalized peak shear stress with failure mode and ductility and ALR identified

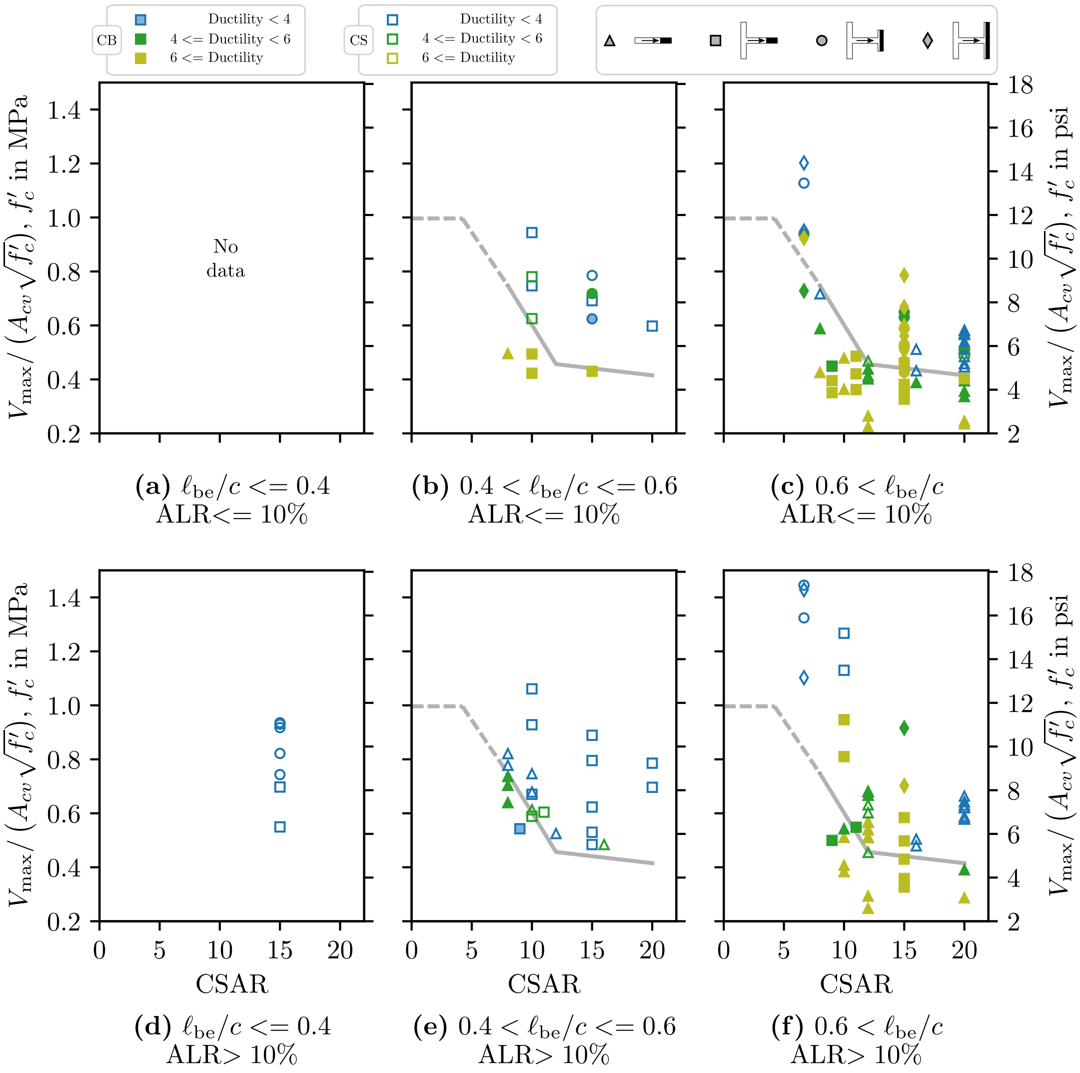

(a) $\ell_{\text{be}}/c <= 0.4$ ALR<= 10%

(b) $0.4 < \ell_{\text{be}}/c <= 0.6$ ALR<= 10%

(c) $0.6 < \ell_{\text{be}}/c$ ALR<= 10%

(d) $\ell_{\text{be}}/c <= 0.4$ ALR> 10%

(e) $0.4 < \ell_{\text{be}}/c <= 0.6$ ALR> 10%

(f) $0.6 < \ell_{\text{be}}/c$ ALR> 10%

Figure 5.10: Relationship between peak shear stress and *regular* cross-sectional aspect ratio, confinement length and axial load ratio for T–, Semi–I–, I–shaped and planar walls.

for each specimen. Figure 5.9 shows that walls with CSAR of smaller than 12, can carry shear stress demands larger than $6\sqrt{f'_c}$ psi ($0.5\sqrt{f'_c}$ MPa) without experiencing a CS failure. Additionally, the data in Figures 5.9 and 5.11 show that, providing longer confining lengths at the toe of the specimen, prevents the wall from incurring a CS failure and exhibit a CB failure.

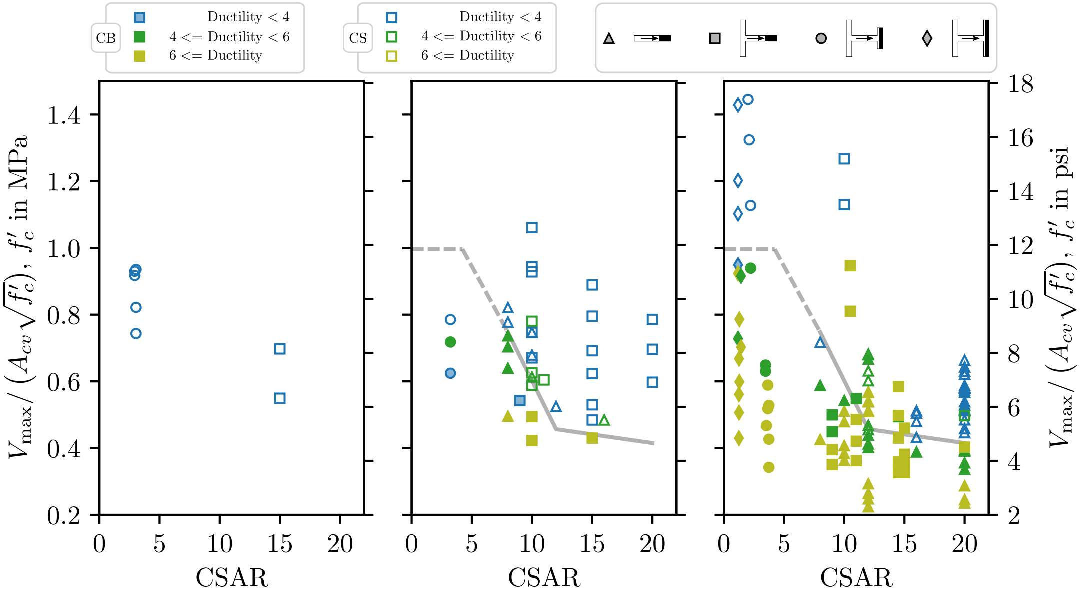

(a) $\ell_{\text{be}}/c <= 0.4$ **(b)** $0.4 < \ell_{\text{be}}/c <= 0.6$ **(c)** $0.6 < \ell_{\text{be}}/c$

Figure 5.11: Effects of *weighted* CSAR, shear stress demand and confinement length on failure mode and ductility.

When confinement is inadequate, i.e., $\ell_{\text{be}}/c <= 0.4$, walls exhibit a rather low ductility regardless of the shape and geometry (Figure 5.11). Additionally, they are more prone to fail in compression-shear type of failure. when minimum required confinement length is provided, ductility increases and the behaviour improves. Many walls in this range of confinement level exhibit high ductility when shear stress demand is small and ALR is smaller than 10% For a CSAR of great than 12, and peak shear stress of greater than $6\sqrt{f'_c}$ $(0.5\sqrt{f'_c})$, the wall fail in CS. However, when the confinement length is increased and provided confinement is greater than code requirement, failure mode is changed to CB and ductile capacity of the walls improve. Again if the ALR is smaller, higher ductility is observed. Moreover, when flanges are added in the compression region of the wall, higher ductility levels are observed which improves the behavior of the wall.

Figure 5.13 shows the effects of expanding the length of confinement in the compression region for T-shaped walls. When the length of confinement is not satisfactory, the wall is

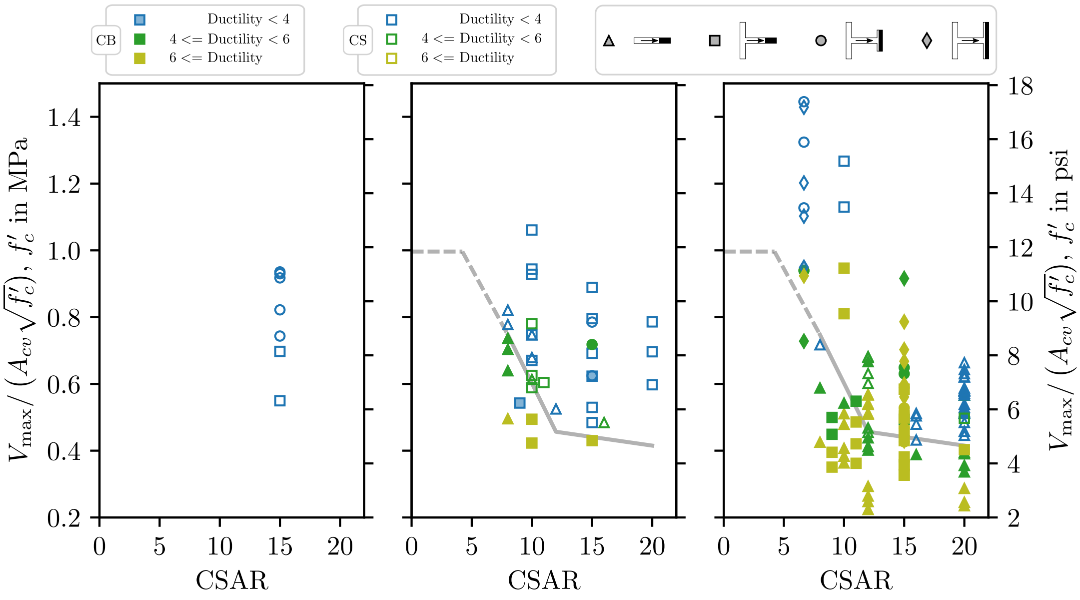

(a) $\ell_{\text{be}}/c <= 0.4$ **(b)** $0.4 < \ell_{\text{be}}/c <= 0.6$ **(c)** $0.6 < \ell_{\text{be}}/c$

Figure 5.12: Effects of *regular* CSAR, shear stress demand and confinement length on failure mode and ductility.

more likely to fail in compression shear. ACI's limit on confinement is based on the depth of the neutral axis and only a length equal to the greater of $c - 0.1\ell_w$ and $c/2$, where c is the depth of N.A. at M_n, is required to be confined. This limit, as investigated by Whitman [68] for planar walls, is not always adequate to prohibit the wall to undergo a CS failure. This can also be seen for the T–shaped walls as shown in Figure 5.13. This is another observation that confirms T–shaped, when toe is in compression, perform similar to planar walls. Instead, Whitman suggested increasing the length of confinement to a distance equal to the length of neutral axis. And the author simulated walls with $\ell_{\text{be}} = c/2$ and ℓ_{be} up to a distance c from the extreme compression fiber. In this study, T-shaped walls were simulated with $\ell_{\text{be}} = c/2$ and $\ell_{\text{be}} > c/2$. Similar to planar walls, providing adequate confinement length, can avoid a CS failure as it can be observed in Figure 5.13.

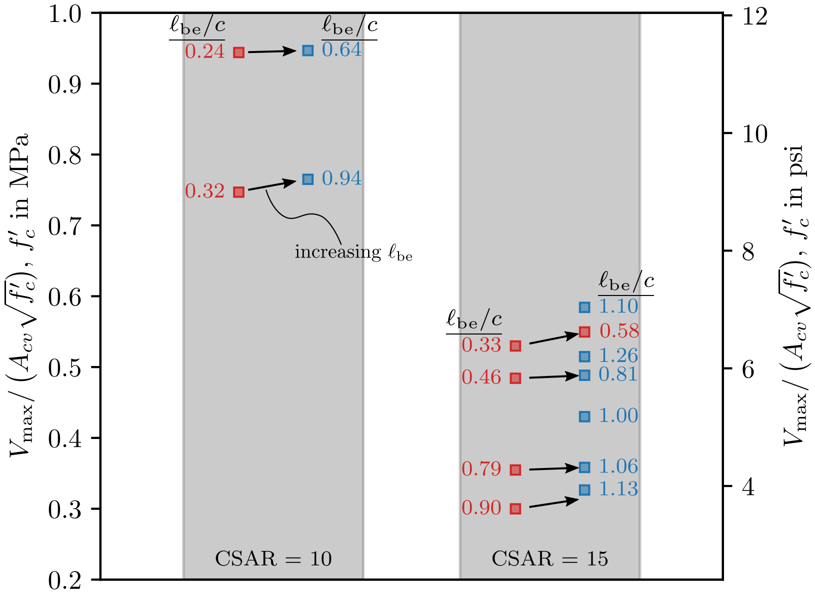

Figure 5.13: Effect of expanding length of confinement on failure mode (T-shaped walls).

5.4 *Impact of Flange Width on the Behavior and Failure Mode*

Providing flanges at the ends of the wall can improve the behavior of the wall by avoiding a CS failure and increasing ductility for walls with higher peak shear stress.

For T–shaped walls, similar to planar walls, when shear stress demand exceeds $5\sqrt{f'_c}$ psi ($0.42\sqrt{f'_c}$ MPa), wall is more likely to fail in CS. However, adding flanges to the walls, causes a shift in this limit to about $10\sqrt{f'_c}$ psi ($3.81\sqrt{f'_c}$ MPa) and improves the behavior. These dividing borders are shown in Figure 5.8. Figure 5.14 shows same specimens that initially failed in CS and flanges added to the compression zone to prevent the CS failure. For most of the specimens when peak shear stress demand is not very high, the behavior highly improved in terms of deformation capacity and failure mode. Failure mode for these specimens changed to CB which is the desired type of failure compared to CS. Additionally, wall response grew more ductile when flanges were added to the compression zone. The larger the flange width, the more ductile the response will be.

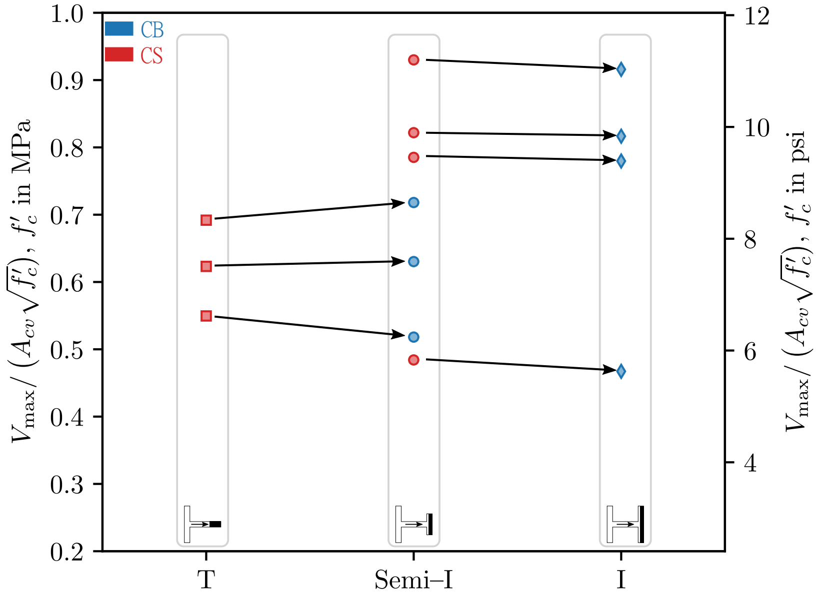

Figure 5.14: Migration from no flanged wall (T–shaped) to flanged walls (Semi–I & I–shaped)

5.5 *Effective Flange Width*

Simulation of walls with flanges in Chapter three showed that the effective flange width can vary depending on the reinforcement configuration and size of hte wall. The results indicated that the strain distribution in the flanges was neither constant across the flange width nor linear. ACI 318-19 [4] specifies the effective flange width to be extended from the face of the web a distance equal to the lesser of one-half the distance to an adjacent wall web and 25 percent of the total wall height.

To study the effective flange width, the first two reference specimens considered in Section 5.2 to study non-planar walls, were considered (i.e., specimens NTW1 and NTW2). For both specimens, width of the flange increased by factors of 1.5×, 2.0×, 4.0× and 6.0× the original width of the flange. In all new cases, the goal was to keep the strength change to a minimum. In order to keep the minimum reinforcement ratio in the flanges of specimen NTW1, additional longitudinal bars were added to the unconfined region for wider flanges accordingly.

All walls were loaded via displacement-controlled load increments in the direction parallel to the web in both positive and negative directions resulting in Flange In Tension (FIT) and Flange In Compression (FIC), consequently.

5.5.1 Results

The followings show the stress fields in the longitudinal bars and in the concrete for the models simulated with different flange widths.

5.5.1.1 Flange in Tension

Figure 5.15 shows the axial stress in the longitudinal bars and vertical strain distribution in the flanges of the models with different flange widths. The results indicate that the entire longitudinal bars in the flange are being engaged in the strength of the wall and the strain profile of the wall section. However, the rate at which the farther longitudinal bars are engaged is dependent on the width of the flange and reinforcement configuration. For narrower flanges, the rate at which the bars reach yielding and hardening is fairly uniform. Though, the strain profile is nonuniform when lumped reinforcement configuration is used. For uniform configuration, the strain distribution turns to be uniform. As the flange width grows, the rate at which the distant bars are reaching yielding and post-yielding, is not the same as the bars located nearer to the center of the wall. The same observation can be made by looking at the vertical strain distribution in the flanges of the walls.

5.5.1.2 Flange in Compression

When flange is in compression, the depth of neutral axis is mainly affected by the flange width. As the flange width grows, N.A. depth reduces. Due to the large width of flanges in the case of only the outer curtain of the flange reinforcement stays in compression and the other curtain of reinforcement will eventually reach tension. It is conceivable that the depth of neutral axial to be close to the cover thickness. This occurs when the inadequate

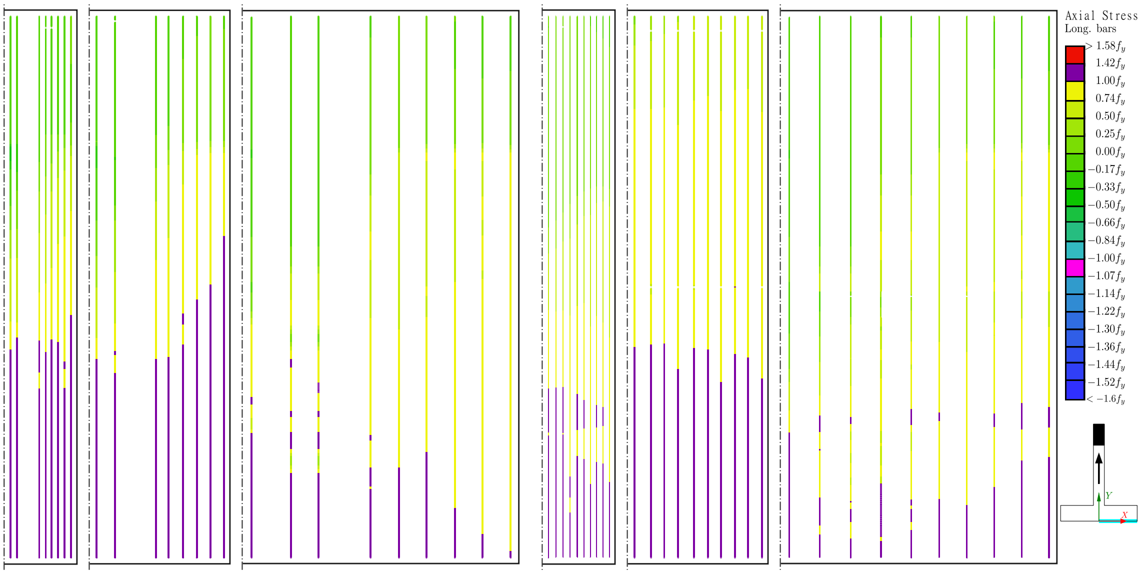

$b_f = 72''$ $b_f = 108''$ $b_f = 288''$ $b_f = 72''$ $b_f = 108''$ $b_f = 288''$

Lumped configuration Uniform configuration

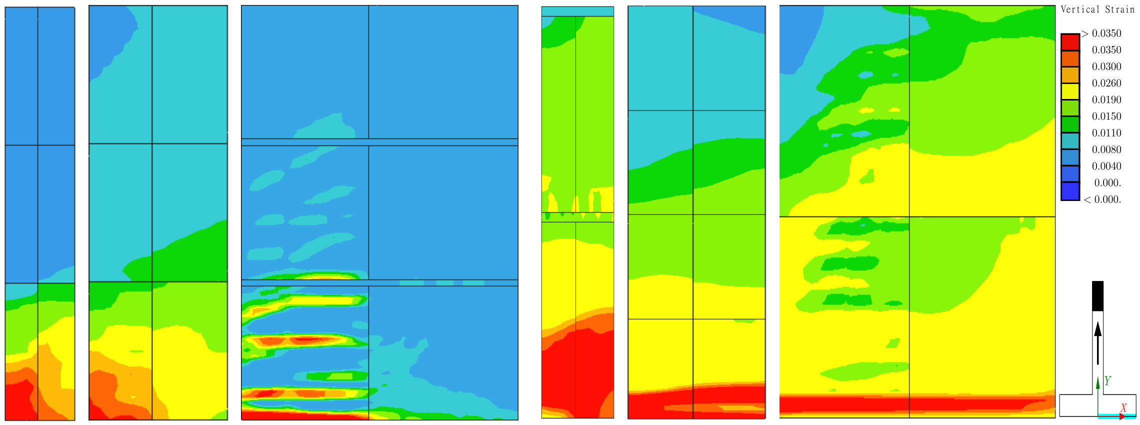

$b_f = 72''$ $b_f = 108''$ $b_f = 288''$ $b_f = 72''$ $b_f = 108''$ $b_f = 288''$

Lumped configuration Uniform configuration

Figure 5.15: Axial stress in longitudinal stress and vertical strain in concrete in flanges of T–shaped walls when the flange is in tension. Note that the highlighted cyan color shown on the cross-section indicates the portion of the wall shown. For vertical strain distribution, for clarity only the bottom two stories are shown.

tension reinforcement in the toe of the wall is provided and the wall undergoes enormous deformation.

5.6 *Nonlinear Strain Profiles*

ACI 318-19 [4] assumes a plane section remains plane when calculating the moment capacity of shear walls. However, similar to RC deep beams, RC shear walls could have a relatively long length in the direction of lateral load application. In general, this assumption overestimates the depth of N.A. as it can be seen in Figure 5.16.

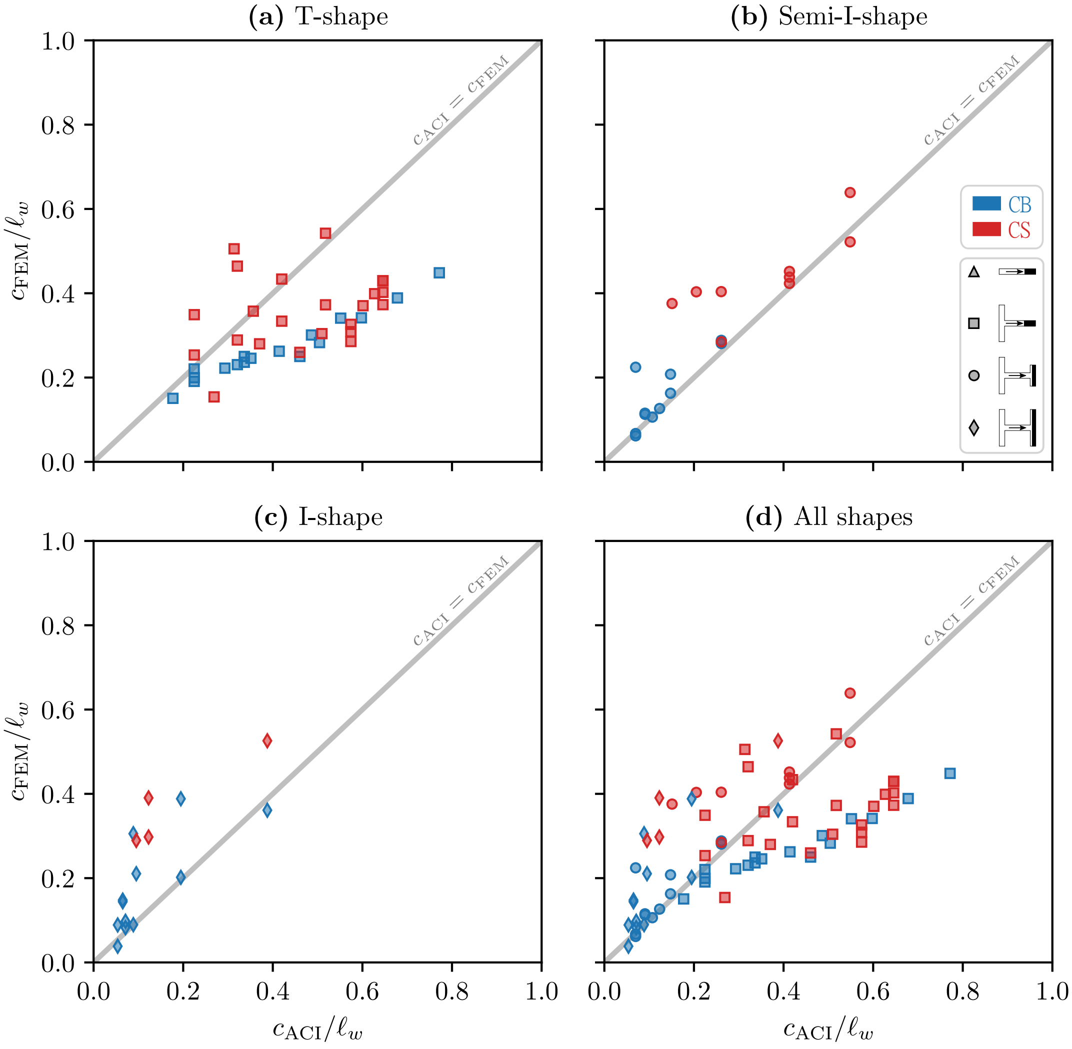

Figure 5.16: Ratio of the depth of N.A. computed by ACI and FEM.

This assumption for walls lacking a flange in compression zone, mostly overestimates the depth of neutral axis and, when flanges are added to this zone, it mostly underestimates the depth of compression zone. Therefore, for walls without flanges, it is more conservative since overestimation of the depth of the neutral axis leads to a confinement length larger than that required by the code. When the depth of neutral axis is underestimated by this linear assumption, a lesser confinement length is provided which could impair wall behavior and its capability to avoid a CS failure mode.

5.6.1 Strain Profile in Compression Flange

Figure 5.17 shows the strain profile in the compression zones of the T–, Semi–I and I–shaped walls. The figures are the vertical views of the first stories of the compression end of the walls. The strain profile is shown in three different points; (1) at M_n, (2) at an intermediate point between M_n and failure (3) right before failure. The compression strain magnitude of 0.003 is shown in purple. For T–shaped walls, due to the thin flange width ($b'_f = t_w$), the entire width gets engaged as soon as the cross-section reaches nominal capacity. When a relatively small flange is added (Semi–I–shaped walls), at first the outer regions of the flange reach a compression strain of 0.003 and then it propagates into the center of the flange. For wider flanges (I–shaped walls), specially when unconfined regions are available, compression strain of 0.003 first observed in these unconfined regions and then it expands into the center of the flange. The boundary elements at the two ends of the flange though, reach this strain level at a much later time. The main difference between the flanges for Semi–I, and I–shaped walls, in addition to the width, is the confinement detailing. The entire flange is confined in the case of Semi–I–shaped walls since the flange is not long enough to provide different regions with and without confinement. However, for I–shaped walls, in addition to the web-flange interface, only the two flange ends are provided with confinement and the remaining portion of the flange is left unconfined. If the entire flange width for the I–shaped walls is confined, a strain profile similar to that of Semi–I–shaped walls is expected.

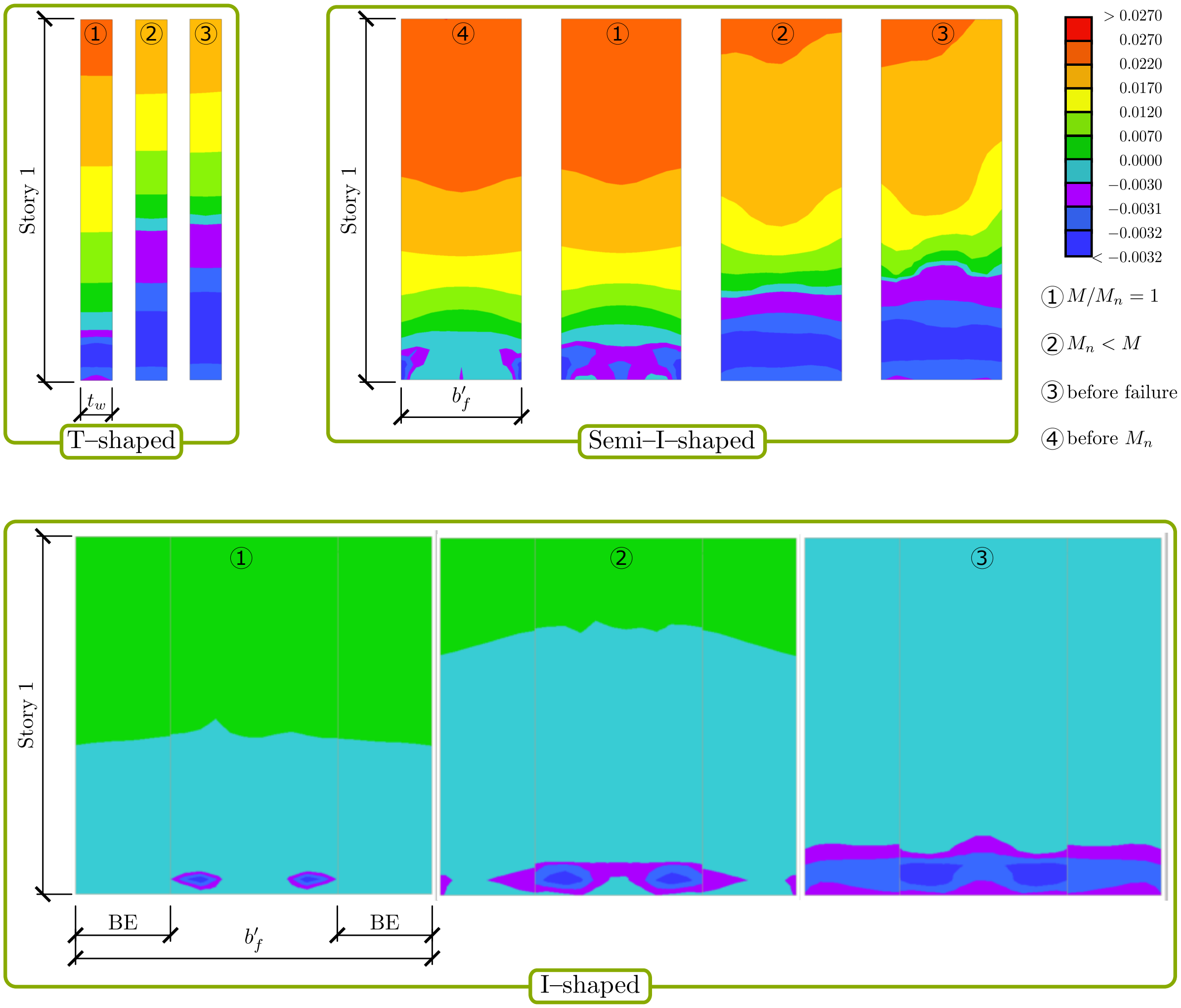

Figure 5.17: Strain profile in the compression flanges

5.7 *Findings*

Simulations were completed for seventy-six (fourty T–, twenty Semi–I– and sixteen I–shaped) concrete walls to study the effects peak shear stress demand, flange, depth of confinement and axial load ratio. Analysis results supports the following observations:

- Plane sections do not remain plane. The difference in the depth of neutral axis computed using ACI code provisions and simulated by numerical analysis shows this.

- T-shaped walls exhibit similar response to planar walls when toe is in compression,
  - Higher shear stress demands & aspect ratio lead to a more brittle CS failure modes,
  - Higher axial load leads to more brittle CS failure modes.
- Flanges in the compression zone, can prevent CS failure and increase ductility,
  - improves the borderline at which the wall is more susceptible to CS failure by about double of the one for planar and T–shaped walls,
- As ALR increases, ductility drops for walls regardless of the shape,
- Confinement of flange and web interface (i.e., higher ℓ_{be}/c), improves deformation capacity and failure mode.
- Shear stress limit to avoid CS failure is dependent on the shape:
  - Planar and T–shaped walls for high seismic regions need to have the shear stress demand limited to $0.5\sqrt{f'_c}\,\text{MPa}$ ($6\sqrt{f'_c}\,\text{psi}$).
  - For symmetric flanged walls (here I–sections), the shear stress demand could be up to $1.0\sqrt{f'_c}\,\text{MPa}$ ($12\sqrt{f'_c}\,\text{psi}$).
  - For asymmetric flanges walls, the shear stres demand should be less than $0.75\sqrt{f'_c}\,\text{MPa}$ ($9\sqrt{f'_c}\,\text{psi}$).

Chapter 6

PARAMETRIC STUDY - WALLS WITH OPENINGS

6.1 Introduction and Motivation

Similar to non-planar walls, walls with openings are arisen from architectural constraints in addition to the utility passage ways. However, openings in walls, or in other words; discontinuities in walls, might result in a reduction in stiffness and strength. These drops in strength and stiffness are expected to depend on the location and size of the openings. In Chapter 4 the results of experimental data and simulation data showed that, when opening size is larger the stiffness drops and when openings are wider and located closer the wall ends, more significant drop is observed in the strength of the wall.

The experimental data mostly includes planar walls and previous studies and experiments for non-planar walls with opening are rare. This could be due to the laboratory limitations for testing of such walls. Therefore, numerical methods are needed to understand the seismic response and develop guidelines for the design of walls with openings.

In the Chapters 3 and 4, the numerical model was validated for both non-planar walls and walls with openings. Results of the experiments and simulations showed that the behavior of walls with openings, similar to non-planar walls, is complex. The experimental results and continuum simulation of walls with openings in Chapter 4 provided some new understandings about the performance of such walls. Deformability of the walls was affected by the size and arrangement of the openings as well as the cross-sectional shape of the walls. Moreover, the shear stress demand on the wall can directly influence the deformability of the structural wall and could potentially impact the failure mode that is expected to occur. Also, data showed, the normal-strain distribution is not linear. To better understand the impacts of shear stress demand, cross-section, opening size and arrangement on the deformability and failure mode, a parametric study was conducted. The study also includes the effects of flanges on the behavior of walls with discontinuities.

This study specifically evaluates: (1) impact of vertical irregularities, (2) shear stress demand, (3) opening sizes, (4) a range of walls with different opening arrangements (patterns), and (5) flange in the compression region.

To achieve this, a comprehensive modeling parameter study was developed and conducted. The study is based on reference wall designed according ACI 318-14 and ASCE7. The wall consists of 8 stories and 30 ft long and 2 ft thick. These wall designs combined with the experimental dataset span a range of cross-sections and shear stress demand, opening size and arrangements. Next, for each reference wall, shear span, axial load ratio, and vertical boundary element reinforcement ratio were varied to achieve target peak shear stress demands. For each set of walls different opening arrangements were considered. The arrangements of openings include: (1) solid (SO), (2) first centered (FC), (3) first eccentric (FE), (4) inline centered (IC), (5) inline eccentric (IE), and (6) staggered (ST). The shape of these opening arrangements are shown in Figure 4.1. Note that for the case of FE, openings at the edge are also considered.

ASCE7 (2016) standard characterizes openings on the basis of change in stiffness from solid to walls with openings. In this study, openings with two different sizes were considered: (1) no openings (solid), (2) openings that result in 25% reduction in stiffness compared to the floor without opening, and (3) openings that result in 50% reduction in stiffness compared to the floor without opening.

6.2 Scope of the Parameter Study

The outline of the parametric study is as follows. First, the wall design to investigate the vertical irregularities is presented. Next, the variable parameters as well as their range of values are defined.

6.2.1 Selection of Reference Designs

A number of RC walls were designed according to ACI 318-14 and ASCE7 (2016) as part of a FEMA-sponsored project managed by the Applied Technology Council [23] to investigate the impact of vertical irregularities. Then these walls were used as reference designs for the parametric studies. For each parameter, the wall design was updated in order to be compliant with the current provisions of the code. The details of the building prototype, footprint, loading and wall design are presented in Section 6.3.

For solid walls shear stress demand is normalized by the gross area of concrete section bounded by web thickness and length in the direction of shear force and concrete compressive strength. When openings are present in the cross-section, the area associated with the opening at the base of the wall (critical section) is subtracted from the gross area of concrete. And therefore, A_{cv} is defined as $(\ell_w - \ell_{\text{opening}}) \times t_w$.

6.2.2 Study Parameters

The purpose of this study was to investigate the structural response of walls with openings subjected to higher shear stress demands, and axial load ratios. Additionally, the effects of flanges on improving the behavior. The study parameters are as follows:

- Vertical stiffness irregularity: ASCE7 (2016) standard characterizes openings on the basis of change in stiffness from solid to walls with openings. In this study, openings with two different sizes were considered in the 1st, 1st and 2nd and 5th (8-story building) or 8th (12-story building) to investigate the impacts of vertical irregularities.

- Normalized peak shear stress $({}^{V_{\max}}/_{A_{cv}\sqrt{f'_c}})$: In this study the normalized peak shear stress varied from $3.0\sqrt{f'_c}$ to $10\sqrt{f'_c}$ psi ($0.25\sqrt{f'_c}$ to $0.83\sqrt{f'_c}$ MPa).

- Axial Load Ratio (ALR): most of the experimental dataset for walls with openings has no axial load applied or just a small axial load is applied to the specimens. For parameter study, the range of ALR varied from 0.0 to 15%.

- Normalized opening length ($\ell_{\text{opening}}/\ell_w$): varied from 0.0 (solid wall) to almost 0.4.

- Different arrangements of openings were studied, as shown in Figure 4.1).

- Compression pier cross-sectional aspect ratio (CSAR$_{\text{cp}}$): CSAR$_{\text{cp}}$ represents the compression pier in the walls with openings (Figure 6.1). It is defined as the ratio of the length of the compression pier (ℓ_{cp}) to its thickness (t_{cp}). This parameter is used to quantifying safe distance from the extreme compression end at which the opening could be placed.

- Flange: improved the ductility of walls, in particular those with high shear stress demands. This is studied for walls with openings as well.

The main parameters used to acquire different shear stress demands were shear span, axial ratio, and reinforcement ratio. These parameters were varied using the same approaches for non-planar walls discussed in the previous chapter.

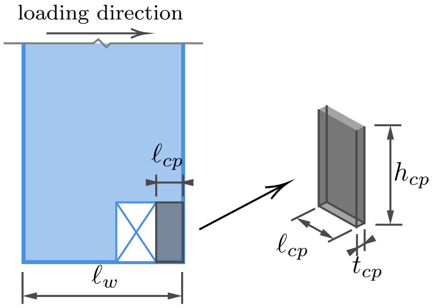

Figure 6.1: Compression pier in walls with openings.

6.3 Wall Design to Investigate the Impact of Vertical Irregularities

To study the influence of openings on the performance of mid-rise walled buildings, a number of buildings were designed using planar walls. Initially solid walls were designed. Then, walls with openings located at the 1st story, 1st and 2nd story, and an upper story (5th story for

8-story building and 8th story for 12-story building) were designed to compare to the solid walls.

6.3.1 Stiffness of the Walls

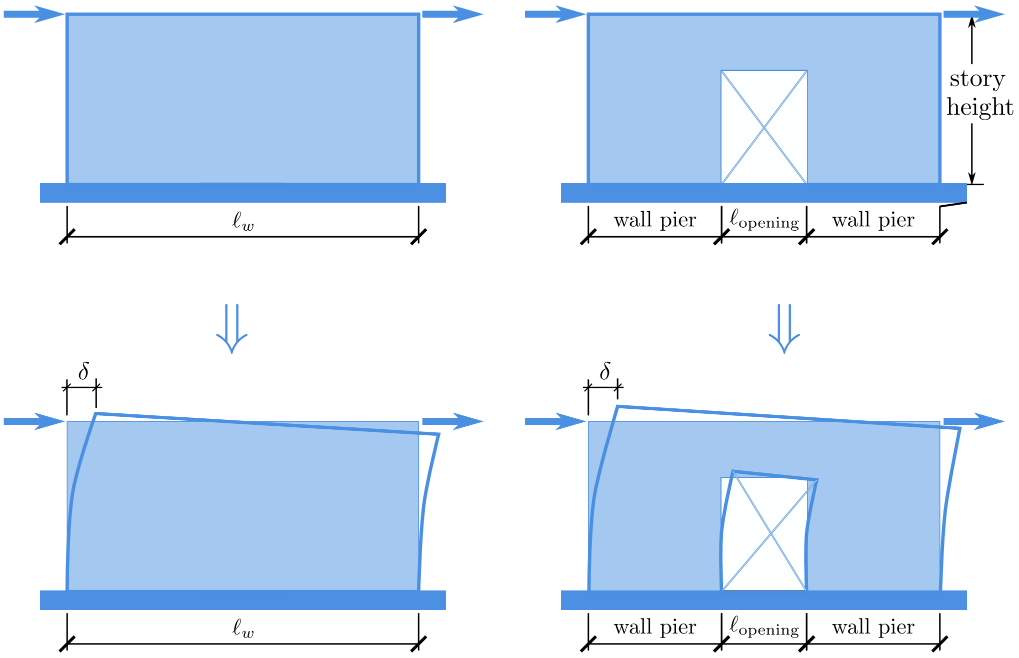

Figure 6.2: Approach used to find stiffness of the wall in SAP2000.

Opening length was determined to achieve a reduction in lateral stiffness for the stories with the opening that was either 50% of the stiffness of the above story or 75% of the average stiffness of the three higher stories. To determine the length of the openings, “racking” stiffness was considered with a closed-form solution. Figure 6.2 shows the details of the approach used in SAP2000 software platform to find lengths of the openings for the aimed stiffness. As shown in the figure, a unit force is applied to the wall in both top corners and the displacement of the wall portion (δ) is divided by the height at which the unit load is applied. Shell elements are used for modeling of the walls in SAP2000 software platform. After several iterations the following sizes were found for each case (Table 6.1):

Table 6.1: Length of openings in the walls designed [8- & 12-story buildings].

Target stiffness	**Wall with 30′ (9.144 m) length**		**Wall with 20′ (6.096 m) length**	
	length of opening	**length of pier**	**length of opening**	**length of pier**
% of solid	ft (m)	ft (m)	ft (m)	ft (m)
75	2.5 (0.762)	13.75 (4.191)	1.5 (0.762)	9.25 (2.896)
50	7.5 (2.286)	11.25 (3.429)	5.0 (2.286)	7.50 (2.286)

Wall demands were determined using the ASCE 7 (ASCE/SEI 2016) ELF procedure and, for the case of the $D_{\max}$ design spectrum, using the results of a modal response spectrum analysis (MRSA). Table 6.2 presents the design space; details of the building design process and wall designs are provided in Appendix C.

Each wall design has a unique identification tag that includes information about all relevant design characteristics. The 8-story walled building designed using the MRSA method to determine demands for the $D_{\max}$ spectrum with no wall openings is identified as 8-D-0-0-MRSA while the 12-story walled building designed using the ELF procedure to determine demands with openings in the 1st and 2nd stories to produce a story stiffness equal to 50% of the third story is identified as 12-D-2S-50-ELF.

6.3.2 Walled Building Configurations

The following section are based on the final report for the *Applied Technology Council*'s project (Assessing seismic performance of buildings with configuration irregularities) [23].

Designs were completed for building heights of 8 stories (32.31 m = 106 ft.) and 12 stories (48.16 m = 158 ft.); for all designs, the first story has a height of 4.57 m (15 ft.) and all other stories have a height of 3.96 m (13 ft.). Figure 6.5 shows elevation views for all of the 8-story walled buildings; 12-story elevations are similar. All buildings have a 36.58 m by 36.58 m

---

[1] For buildings with openings on the 5th or 8th story, only the case of a wall with an opening producing a section stiffness equal to 50% of the section stiffness on adjacent walls was considered.

Table 6.2: Design characteristics for walled buildings.

Number of designs	**Building height (stories)**	**Method used to determine demands**	**Design spectrum used for design**	**Stories with openings**	**Stiffness of floor with opening normalized by stiffness of floor above**[1]
6	8	ELF	D_{max}	None, 1st, 1st & 2nd, 5th	50% and 75%
5	8	MRSA	D_{max}	None, 1st, 1st & 2nd	50% and 75%
6	8	ELF	B_{max}	None, 1st, 1st & 2nd, 5th	50% and 75%
6	12	ELF	D_{max}	None, 1st, 1st & 2nd, 8th	50% and 75%
6	12	ELF	B_{max}	None, 1st, 1st & 2nd, 5th	50% and 75%

(120 ft. by 120 ft.) footprint (Figures 6.3 and 6.4). In all cases, the seismic force resisting system comprises two planar walls in each direction. Walls are located such that the center of stiffness and mass coincided. For 8- and 12-story buildings with earthquake demands defined by the D_{max} spectrum, walls were 9.14 m long by 0.61 m thick (30 ft. by 2 ft.); for these buildings, wall dimensions were determined by flexural demands and the requirement to use a longitudinal reinforcement ratio of less than 3%. For 8- and 12-story buildings with earthquake demands defined by the B_{max} spectrum, walls were 6.10 m long by 0.61 m thick (20 ft. by 2 ft.); for these buildings wall dimensions were determined by flexural demands and the requirement that the requirement that the longitudinal reinforcement ratio be less than 4%.

Initially, an 8-story reference wall was designed using the ASCE 7 ELF procedure for the D_{max} spectrum with no openings (Figure 6.5). Then, designs were created with openings introduced to create vertical stiffness irregularities. Openings were introduced at the horizontal center of the wall on the 1st floor, 1st and 2nd floors or the 5th (8-story building) or 8th (12-story building) floor (Figure 6.5). Openings have a height of 3.05 m (10 ft.) and a length that resulted in the story with the opening having a lateral stiffness equal to 75% or 50%

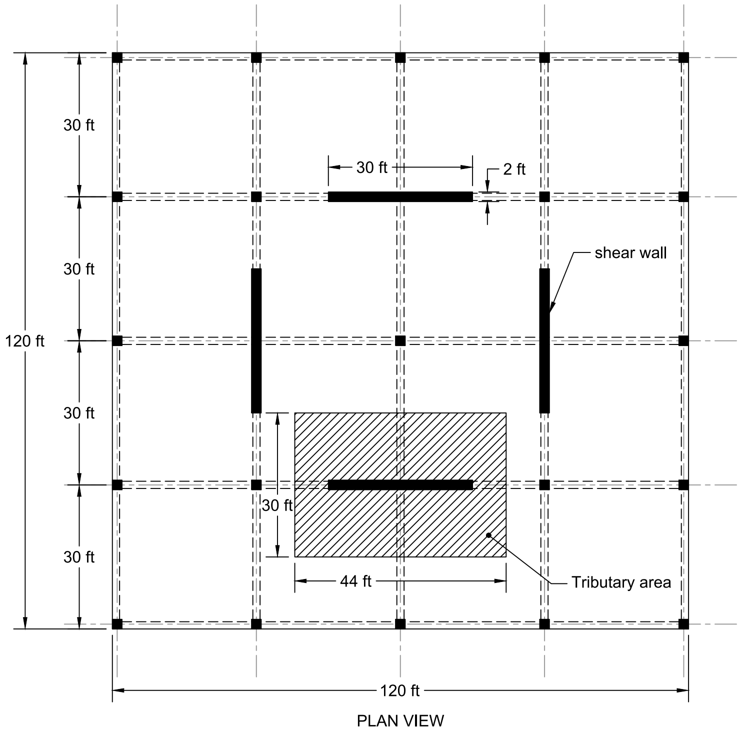

Figure 6.3: Building plan view for 8-story buildings designed for $D_{\max}$ and $B_{\max}$ spectra. Note that wall length is 20 ft. for $B_{\max}$ designs.

of an unadulterated story, where story stiffness was computed as $K = P/\Delta$ with P and Δ defined as shown in Figure 6.2. ASCE-7 [8] defines a wall in which a story stiffness is 75% of the average adjacent story stiffness as irregular and a wall in which a story stiffness is 50% of the adjacent story stiffness as extremely irregular.

The 8-story reference wall was designed with a length of 9.14 m (30 ft.) and a thickness of 0.61 m (2 ft.); ultimately, it was found that these dimensions were appropriate for all other 8- and 12-story continuous (no openings) wall designed for $D_{\max}$ loads. Thus, opening dimensions were the same for all $D_{\max}$ designs. An opening of 0.76 m (2.5 ft.) was used to create a story stiffness equal to 75% of the average adjacent story stiffness and an opening of 2.29 m (7.5 ft.) was used to create a story with a stiffness equal to 50% of the adjacent story stiffness. For $B_{\max}$ designs, wall dimensions were 6.10 m long by 0.61 m thick (20 ft.

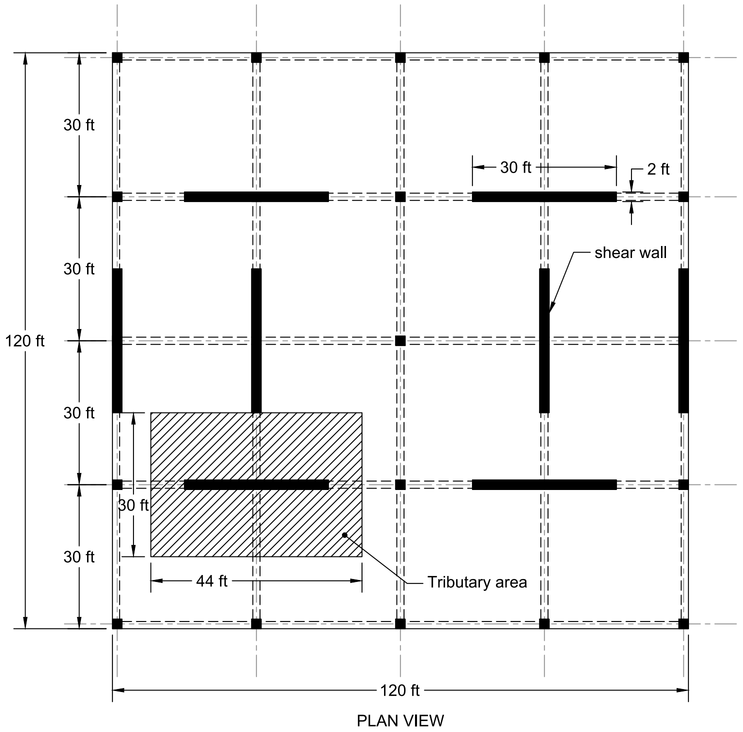

Figure 6.4: Building plan view for 12-story buildings designed for $D_{\max}$ and $B_{\max}$ spectra. Note that wall length is 20 ft. for $B_{\max}$ designs.

by 2 ft.) and openings of 0.46 m (1.5 ft.) and 1.52 m (5 ft.) were used, respectively, to create story stiffness equal to 75% and 50% of the adjacent story stiffness.

6.3.3 Design Demands

Walls were designed for gravity load on the basis of assumed dead and live loads and the framing pattern shown in Figure 6.3. The following dead and live loads were used for all designs:

Dead load (materials and mechanical) on all floors = 175 psf
Dead load (materials and mechanical) on roof = 140 psf
Live load (area load plus partitions) on all floors = 50 + 15 psf = 65 psf
Live load (area load plus partitions) on roof = 20 + 0 psf = 20 psf

The tributary area assigned to the wall was defined, in the direction perpendicular to the

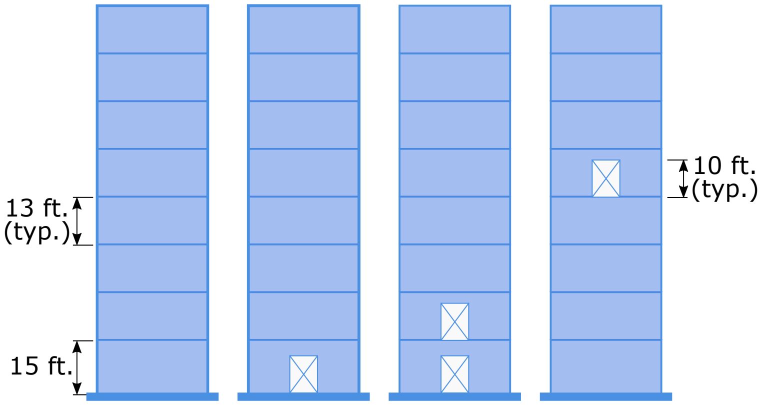

Figure 6.5: Building elevations showing wall with no openings and with openings in 1st story, 1st and 2nd stories and upper stories (5th for 8-story building and 8th for 12-story building).

length of the wall, by half the distance from the centerline of the wall to the center of the columns in the gravity framing system and, in the direction parallel to the length of the wall, half the distance from the end of the wall to the center of the columns in the gravity framing system. Figure 6.3 shows the wall tributary area for one of the 8-story walled buildings.

Walls were designed for earthquake load using the $D_{\max}$ and $B_{\max}$ design spectra specified in FEMA P-695. Designs were developed using demands determined from both modal response spectrum analysis (MRSA) and the equivalent lateral force (ELF) procedure as required in ASCE 7. Seismic weight was defined by dead load plus partition load, with partitions assumed to be attached to the floor and ceiling:

Seismic weight on all floors $= 175 + 15\,\text{psf} = 190\,\text{psf}$
Seismic weight on roof $= 140 + 7.5\,\text{psf} = 147.5\,\text{psf}$

Base shear demands determined using the ELF procedure employed the ASCE 7 specified design period, C_uT_a to determine earthquake demand. Base shear demands determined using MRSA were typically less than those determined using the ELF procedure and were scaled to 100% of the ELF base shear as required by ASCE7 [8]. In computing demands using MRSA, a line-element model was employed in which flexural stiffness was defined equal to 50% of the gross-section stiffness and axial and shear stiffness were taken equal to 100% of the section stiffness. Individual wall demands determined using the ELF and MRSA procedures were amplified to account for accidental torsion. Table 6.3 provides seismic design parameters for walls.

Table 6.3: Design properties for walled buildings and individual walls

Design ID	**MRSA period** (sec)	$\mathbf{C_u T_a}$ (sec)	**Building design base shear**
8-D-0-0-*	1.14	0.93	0.11W
8-D-*-*-*	1.14 - 1.18	0.93	0.11W
8-B-0-0-*	2.21	1.12	0.01W
8-B-*-*-*	2.23	1.12	0.01W
12-D-0-0-*	2.41	1.25	0.08W
12-D-*-*-*	2.41 - 2.42	1.25	0.08W
12-B-0-0-*	3.07	1.15	0.01W
12-B-*-*-*	3.07	1.15	0.01W

For D_{max} designs, the following ASCE 7 load cases were considered:

$$\text{Load case 5 (LC5): } (1.2 + 0.2S_{DS})D + \rho E + 0.5L \tag{6.1}$$

$$\text{Load case 7 (LC7): } (1.2 - 0.2S_{DS})D + \rho E \tag{6.2}$$

with $\rho = 1.0$ used for all designs. For all designs, Load case 7 controlled. Wall design was driven by flexural demands and wall axial loads were relatively low; thus, more longitudinal reinforcement was required to achieve flexural demands when lower axial loads were applied to the walls.

6.3.4 Design of Walls

Individual walls were designed to achieve required strength and detailed to achieve deformation capacity per ACI 318-14 (ACI Committee 318 2014). Specified material strengths used for design were $f'_c = 34.5\,\text{MPa}$ ($f'_c = 5000\,\text{psi}$) and $f_y = 414\,\text{MPa}$ ($f_y = 60\,\text{ksi}$). Walls were sized to achieve required strength and stiffness and to keep longitudinal reinforcing ratios in heavily reinforced boundary element regions below 4%. Appendix C presents in detail the baseline 8-story walled building designed using the ASCE 7-16 ELF procedure (8-D-0-0-ELF) as well as presents all 8- and 12-story wall designs.

Design of the baseline 8-story walled building (8-D-0-0-ELF) resulted in walls 9.14 m long by 0.61 m thick (30 ft. by 2 ft.). At the base, the wall included 1.83 m (6 ft.) long boundary elements with 2.5% longitudinal reinforcement ratios, web region longitudinal and horizontal reinforcement was approximately equal to the ACI Code minimum of 0.25%, and maximum shear stress demand was $0.16\sqrt{f'_c\,(\text{MPa})}$ ($1.9\sqrt{f'_c\,(\text{psi})}$). To facilitate comparison of the different wall designs, the 30 ft. by 2 ft. gross wall dimensions were maintained for all 8-story wall designs. Table 6.4 provides relevant design details for all 8-story wall designs, with ρ_{BE} equal to the boundary element longitudinal reinforcement ratio at the base of the wall (two values are provided by walls with openings as different reinforcement ratios are provided for boundary elements on the interior and exterior of the wall pier), ρ_{web} and ρ_h equal to the web region longitudinal and horizontal reinforcement ratios at the base of the wall, $\rho_{h,\text{opening}}$ equal to the horizontal reinforcement ratio in the wall above the openings, and ρ_{CB} equal to the coupling beam diagonal reinforcement ratio (total diagonal or horizontal bar area divided by coupling beam cross-sectional area).

6.4 *Modeling Wall Response*

Nonlinear analysis using continuum-type solid element models and the ATENA software platform were used to simulate the response of the walls to earthquake loading. The models were used to study the deformation capacity and stress fields of the walls under the influence of openings. The analysis method used has been shown using large experimental data set (Whitman 2015) to accurately simulate stiffness, strength and deformation capacity for planar walls exhibiting flexure-controlled response. The modeling approach is described in details in Section 2.3.

Table 6.4: Design propreties for walls.

Wall ID	**opening length** m (ft)	ℓ_{BE} m (ft)	ρ_{BE} %	ρ_{BE} %	$\rho_{\mathbf{h}}$ %	$\rho_{\mathbf{h},\mathrm{opening}}$ %	ρ_{CB} %
8-D-*-*-ELF walls are 30 ft. long by 2 ft. thick							
8-D-0-0-ELF	-	1.83 (6)	2.5	0.25	0.25	-	-
8-D-1S-75-ELF	0.76 (2.5)	1.52 (5)	3.5	0.25	0.25	0.65	-
8-D-1S-50-ELF	2.29 (7.5)	1.52 (5)	3.7	0.25	0.25	0.42	-
8-D-2S-75-ELF	0.76 (2.5)	1.52 (5)	3.7	0.25	0.25	0.65	0.71 (diag)
8-D-2S-50-ELF	2.29 (7.5)	1.52 (5)	3.9	0.25	0.25	0.65	0.87 (diag)
8-D-5S-75-ELF	0.76 (2.5)	1.83 (6)	2.5	0.25	0.25	0.25	-
8-D-5S-50-ELF	2.29 (7.5)	1.83 (6)	2.5	0.25	0.25	0.25	-
8-B-*-*-ELF walls are 20 ft. long by 2 ft. thick							
8-B-0-0-ELF	-	-	0.25	0.25	0.25	-	-
8-B-1S-75-ELF	0.46 (1.5)	-	0.25	0.25	0.25	0.25	-
8-B-1S-50-ELF	1.52 (5.0)	-	0.25	0.25	0.25	0.25	-
8-B-2S-75-ELF	0.46 (1.5)	-	0.25	0.25	0.25	0.25	-
8-B-2S-50-ELF	1.52 (5.0)	-	0.25	0.25	0.25	0.25	-
8-B-5S-75-ELF	0.46 (1.5)	-	0.25	0.25	0.25	0.25	-
8-B-5S-50-ELF	1.52 (5.0)	-	0.25	0.25	0.25	0.25	-

6.5 Preliminary Analyses to Investigate Reference Wall Response and Modeling Assumptions

Pushover analyses using ATENA software platform were used to assess the behavior and performance of the 8-story ELF baseline model (8-D-0-0-ELF) in addition to the investigation of the modeling assumptions.

According to the ATENA results for a planar wall, introduction of an opening in the middle of the bottom story does not have a major influence on the stiffness, strength and deformation capacity. When the opening is located in the tension region of the wall, it results in a reduced stiffness, reduced strength and slightly increased deformation capacity. If the opening is in the compression region of the wall, both strength and deformation capacity will significantly drop.

6.5.1 Modeling Assumptions used for ATENA Analyses

In addition to the impact of various modeling assumptions employed and the modeling procedure described in Section 6.4 some other modeling details are described here.

Expected material properties were employed in all nonlinear analyses. To define the expected material strengths, the recommendations of the PEER Tall Building Initiative (TBI 2010) were followed. According to these recommendations, unconfined compressive strength of concrete was increased by 30% and yield strength of reinforcing steel was increased by 17%. As a result, the 34.5 MPa (5000 psi) concrete compressive strength increased to 44.8 MPa (6500 psi) and the 414 MPa (60 ksi) yield strength of steel increased to 496.4 MPa (72 ksi). The ultimate strength of the longitudinal steel bars was assumed to be 724 MPa (105 ksi) with a corresponding strain of 20%.

All analyses included gravity load which is defined according to the recommendations of the FEMA P695 [7] . FEMA P695 defines the gravity load by

$$1.05D + 0.25L \tag{6.3}$$

where D is defined as the nominal dead load and L as the nominal live load as follows:

Dead load (materials and mechanical) on all floors = 175 psf
Dead load (materials and mechanical) on roof = 140 psf
Live load (area load plus partitions) on all floors = 50 + 15 psf = 65 psf
Live load (area load plus partitions) on roof = 20 + 0 psf = 20 psf

The corresponding gravity load determined for the wall tributary area shown Figure 6.3.

Lateral load, for ATENA analyses, was applied as a single point load via displacement increments at the effective height associated with the ELF load distribution.

6.5.2 Observations and Results

All the walls are analyzed using ATENA software platform. Simulations were performed by application of displacements at the effective height of the wall. As mentioned in Chapter 2 it is suitable to control the analysis by applying prescribed displacements rather than loads. The axial load is also applied through the centroid of the wall and maintained constant throughout the analysis period. Additionally, the boundary conditions are also applied at the beginning and held constant during the analysis. The boundary conditions consisted of the fixity of the foundation which was the same case for all the walls and applying horizontal roller representing the symmetry wherever applicable. Additionally, due to the lack of a buckling model in the program, failure points of the walls are identified using the criteria described in Section 2.3.5.

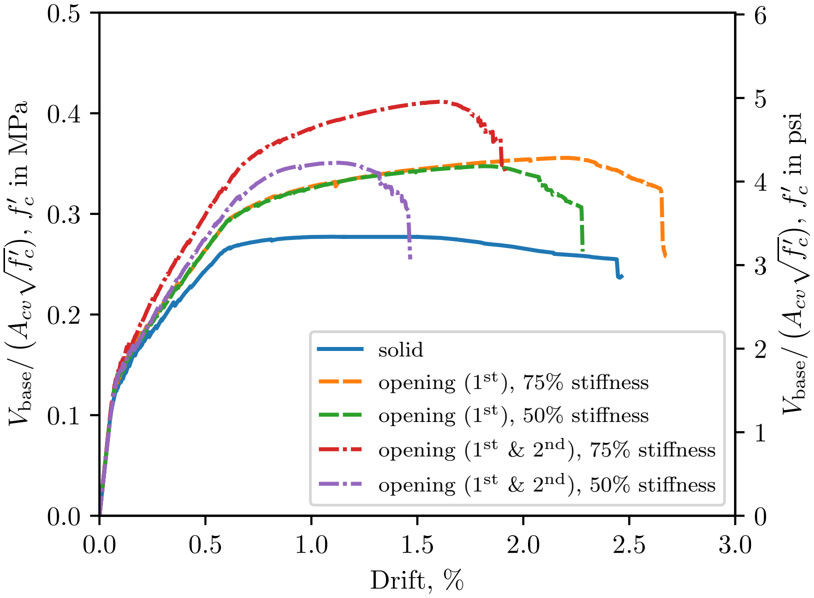

Figure 6.6: Normalized base shear versus drift at the point of loading for the 12-story walls using ELF approach for the D_{max} category.

Figure 6.6 illustrates the simulation results of the 8-story wall designed for the D_{max} category using the equivalent lateral force (ELF) procedure. The main cause of varying strength is the reinforcement configuration. Where openings existed, each pier was designed separately for the demands calculated using a static analysis for the equivalent lateral forces.

In the case where the stiffness is reduced to 50% of the adjacent story, the wall pier length is smaller and there is more reinforcement in the boundary elements. This is to satisfy the moment demand including the gravity load. When the whole cross-section is considered the moment capacity is going up due to the higher rate of reinforcement congestion at the ends. The details of the cross-section and design procedure is explained and shown in Appendix C.

Additionally, the results of the continuum analyses shows that the openings in the center of the wall does not have a big impact on the stiffness of the walls but the transfer mechanism of the shear stresses are affected the most. This raises this question whether the application of the lateral load through a point is a valid assumption or not. This is studied and explained in details in Section 6.9. Also, the location of the opening has a more significant effect on the strength, stiffness and deformation capacity of the walls.

Deformation capacity of the walls seems to have undergone the most influence by openings. For the 8-story wall, designed using ELF procedure for the D_{max} category (Figure 6.6) when an opening is added in the first story to reduce the stiffness to 75%, the deformation capacity is reduced significantly. And when the opening is added to two stories, the drift ratio is even smaller. For the wall with opening in the first story with 50% stiffness of the adjacent story, the strength is increased but the drift did not change too much. This is mainly because the design of the wall resulted in a higher rate of reinforcement towards the ends of the wall which directly affects the deformation capacity of the wall. This indicates that, it is possible to improve the behavior of walls with openings in the first story. All the walls with openings are designed with extra reinforcement provided at the sides of the wall and also confined according to the requirements of the ACI 318-14 (2014) code. The code does not exactly specify what percentage of reinforcement is needed next to the openings. For the walls designed in this study, the additional shear force is calculated using the approach proposed by Moehle [48]. This method is based on the strut-and-tie model and it is a conservative method. Additionally, where applicable, diagonal reinforcement is designed for the coupling beam. The details of the designs are shown in Appendix C.

When designed, in all cases the demands of the walls using modal response spectrum

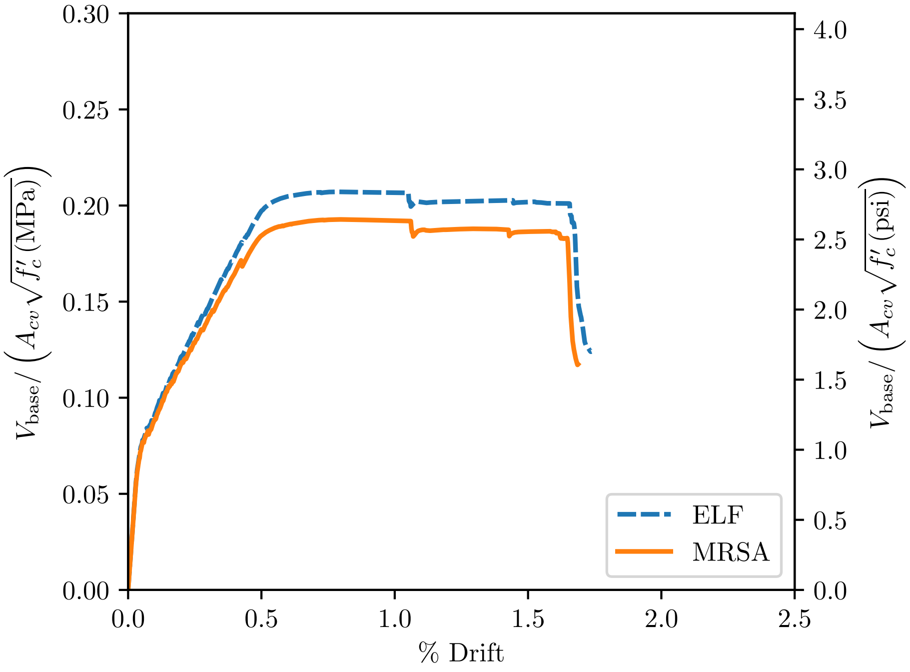

Figure 6.7: Comparison of normalized base shear versus drift at the point of loading for ELF and MRSA procedures for the solid 8-story wall for the $D_{\max}$ category.

analysis (MRSA) were smaller than he demands calculated from equivalent lateral force (ELF) procedure. As a result, even though the base shear was scaled to the one calculated using ELF procedure, the moment demands were less for the MRSA approach and less reinforcement were required. Figure 6.7 shows the comparison of normalized base shear versus drift at the effective height for ELF and MRSA procedures for the solid 8-story walls designed for the $D_{\max}$ category. As it can be observed from the figure, both walls resulted in the same deformation capacity and the difference in the stiffness is insignificant. The strength, however, is the only major difference between the response of both walls. It is clearly smaller for the wall designed for MRSA demands as it has less reinforcement provided.

Figure 6.8 shows the concrete minimum principal stress distribution for the 12-story walls (solid, with opening at the base story, with opening at the bottom two stories with

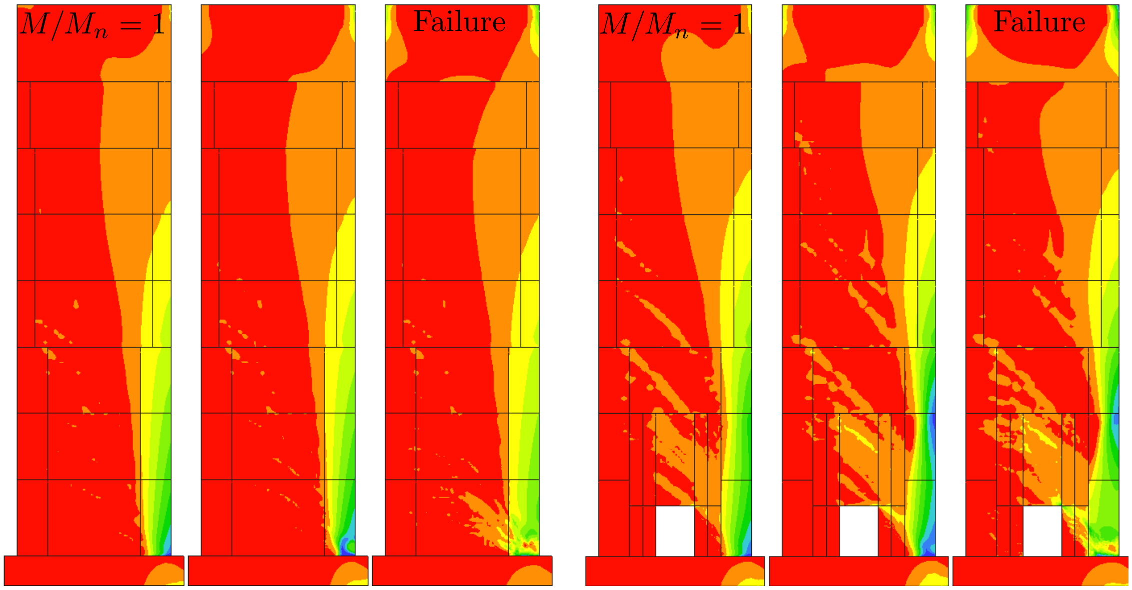

(a) Solid **(b)** Opening at 1st story

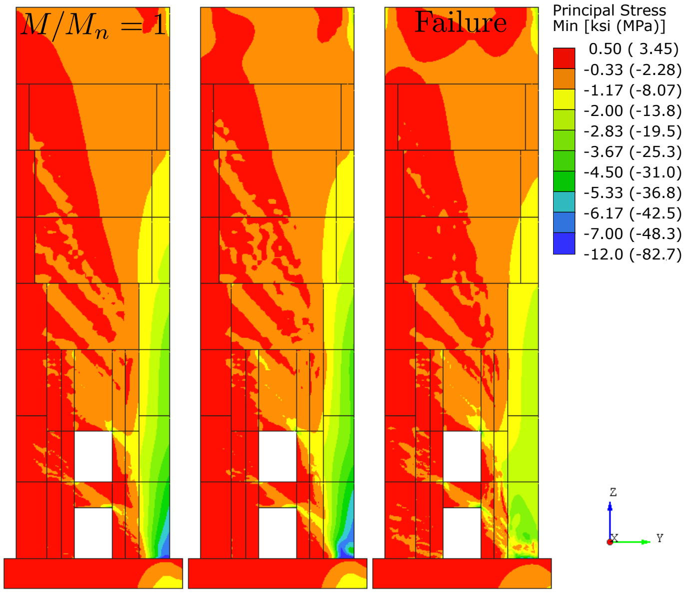

(c) Opening at bottom two stories

Figure 6.8: Minimum principal stress distribution in the 12-story walls (stiffness stories with opening is equivalent to 50% of the adjacent story).

stiffness reduced to 50%) for the case of $D_{\max}$ category. The figure shows the stress at nominal moment strength of the wall, an intermediate point between the nominal moment and failure and at failure. There is not a significant change in the mode of failure between the three walls. The only major difference is the transfer of stresses to the compression peir and compression boundary element. When there is no opening, the wall web area contributes in the transfer of the stresses but when there is one opening, the web region above the opening has the most of the shares to transfer the stress. For the case with two opening most of the stresses are transferred via the coupling beam and because of that, the corners of the coupling beam are undergoing a huge stress concentration as is apparent from the figure. In the cases of opening, the stresses are transferred to the compression boundary element sooner and as a result the failure reaches sooner and as a result the deformation capacity will be reduced. Since the rotation of the wall before failure is smaller for the case with openings, the neutral axis depth is bigger. The same observations can be made for these walls when the opening size reduces the stiffness to 75% of the adjacent story (see Figure 6.9). Except the inclination of the compression strut from the top of the opening in the second story to the lower compression corner is smaller for the wall with reduced to 75% of stiffness.

6.6 Investigation of Vertical Irregularity Using Nonlinear Continuum Analysis

As part of the current study, nonlinear continuum-type analysis was used to investigate the impact on wall performance of the horizontal location of an opening introduced in the bottom story of a mid-rise wall. The ATENA software platform was used to conduct nonlinear continuum analyses of walls subjected to gravity plus lateral loading; details of the ATENA modeling procedure are discussed in Section 2.3. Four opening locations were considered: no opening and openings at the center of the wall, on the right side of the wall and on the left side of the wall. All analyses employed a monotonically increasing lateral load pushing the wall to the right such that an opening on the right side of the wall affected the compression region of the wall while an opening on the left affected the tension region. Ultimately, the analysis results suggest that openings located in the middle of the wall have less impact on

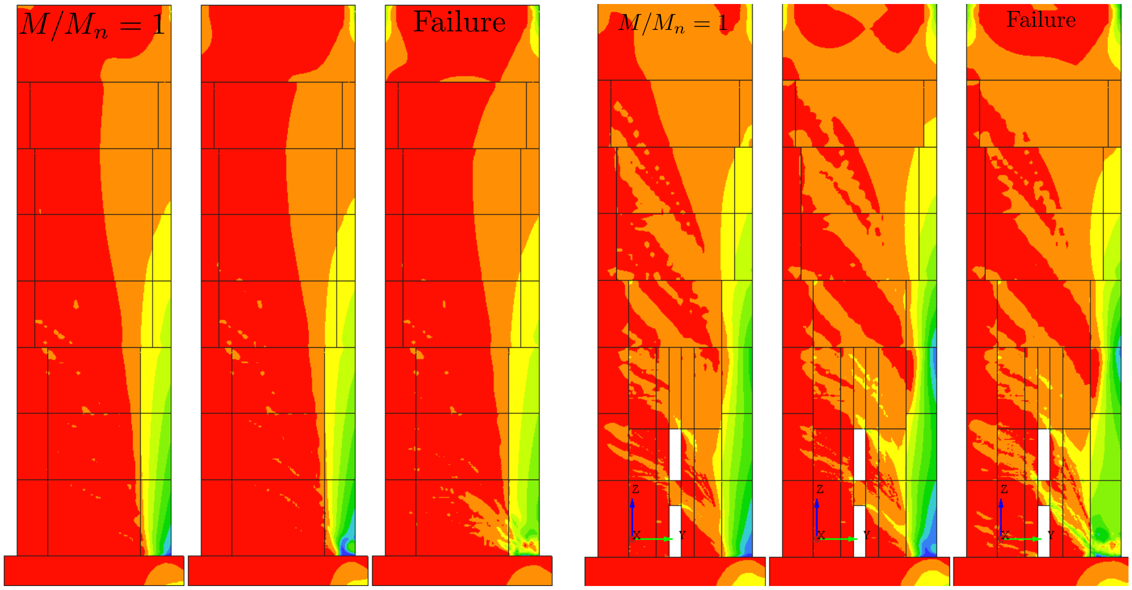

(a) Solid **(c)** Opening at bottom two stories

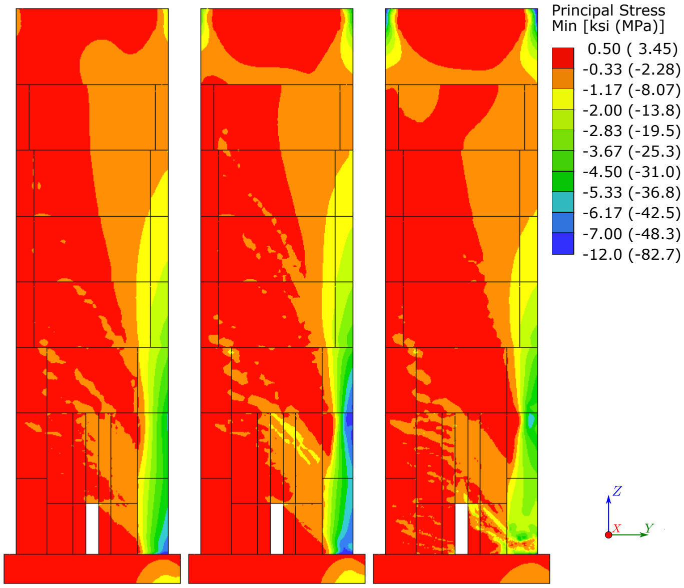

(b) Opening at 1st story

Figure 6.9: Minimum principal stress distribution in the 12-story walls (stiffness stories with opening is equivalent to 75% of the adjacent story).

stiffness, strength and deformation capacity than do openings near or at the tension and compression edges of the wall.

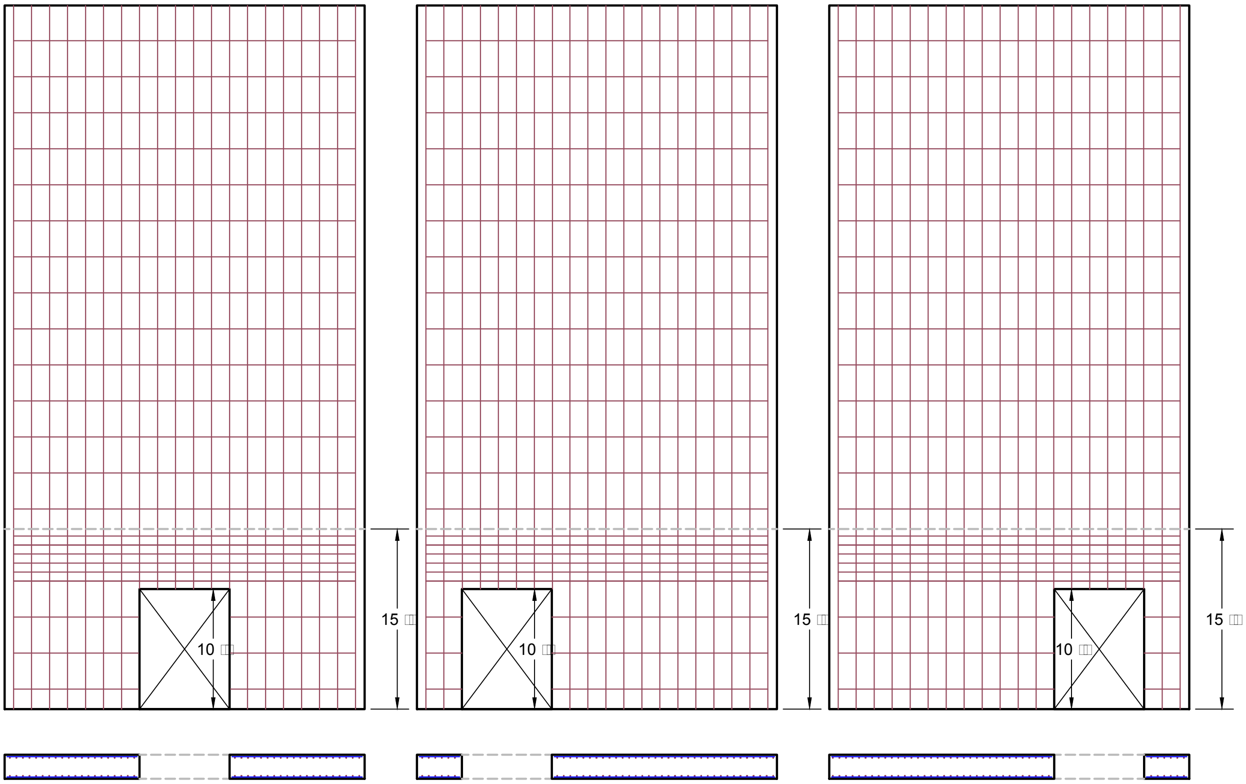

(a) Opening at center **(b)** Opening at left **(c)** Opening at right

Figure 6.10: Wall configurations and designs used for ATENA analyses to investigate the impact of opening location.

An 8-story wall (30 ft. long by 2 ft. thick by 106 ft. tall) with uniformly distributed vertical and horizontal reinforcement was used in the study. Figure 6.10 shows this reference wall configuration with openings (7.5 ft long by 10 ft. tall) introduced and supplemental horizontal reinforcement added above the opening to prevent damage directly above the opening. Figure 6.11 shows base shear, normalized by $\sqrt{f'_c}A_g$ with $f'_c = 6500$ psi and A_g equal to the area of the reference wall ($A_g = 60\,\mathrm{ft}^2$), versus drift at the point of the applied load. The data in Figure 6.11 show

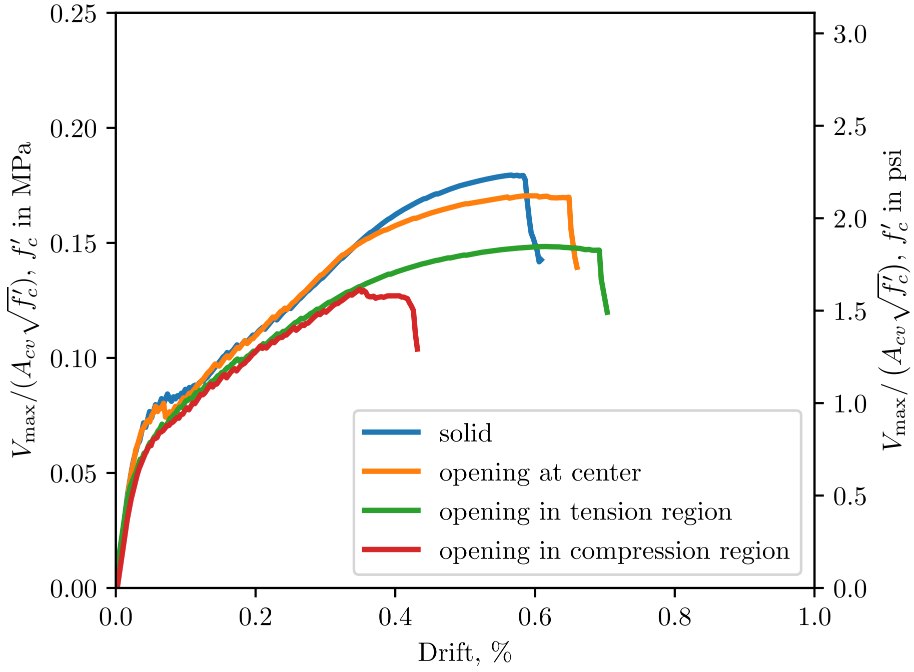

Figure 6.11: Normalized base shear versus drift at the effective height.

- Introducing an opening at the middle of the wall has minimal impact on the stiffness, strength and deformation capacity of the wall,

- Introducing an opening in the tension region of the wall (left side) reduces stiffness and strength slightly, as it reduces the volume of longitudinal reinforcement activated to resist lateral loading, and increases deformation capacity, as it reduces compression demands and thereby delays on set of compression failure, which triggers overall strength loss,

- Introducing an opening in the compression region of the wall (right side) significantly reduces strength and deformation capacity, as it reduces capacity of the flexural compression region resulting in early onset of compression failure, and thus early onset of overall strength loss.

Figure 6.12 shows concrete minimum principal stress before onset of strength loss (left wall in each subfigure) and at onset of strength loss (right wall in each subfigure) for the different wall configurations. These data shows a reduction in the magnitude of the minimum principal stress at failure; this is consistent with a compression-controlled flexural failure. These data show also a very different stress field for the wall with the opening on the right; this is consistent with the reduced strength and deformation capacity of this wall.

As opening movies to the right (compression region), the compression strut from the loading region splits into two separate struts, and it is divided between both left and right pier. When opening is closer to the end, the compression strut on the right pier becomes smaller and more stresses are transferred to the bottom right corner of the left pier.

6.6.1 Openings Located on the Edge of the Walls.

Additional wall were designed to investigate the effects of the opening on the edges of the walls. Figure 6.13 shows the changes in the deformation capacity when openings are further moved to the edge of the wall resulting in a smaller wall length as a result of this discontinuity. The results show that these discontinuities result in a significant drop in the strength of the walls. Change in the length, complicates the design of the wall since to reach the same capacity, more reinforcing bars are needed. Also, the region above the opening will need additional confined regions and horizontal bars to allow load transfer to the lower portion of the wall. Therefore, based on the current study results, this type wall with openings on the edges are not recommended. Rather, it is more advantageous to ignore the region above the opening and design for a short wall length.

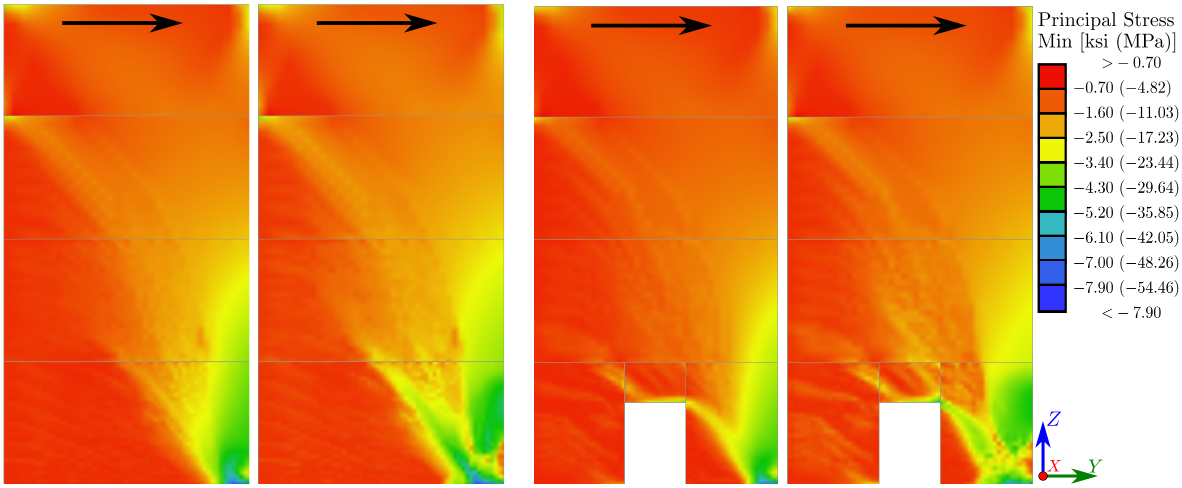

(a) Solid **(b)** Opening at center

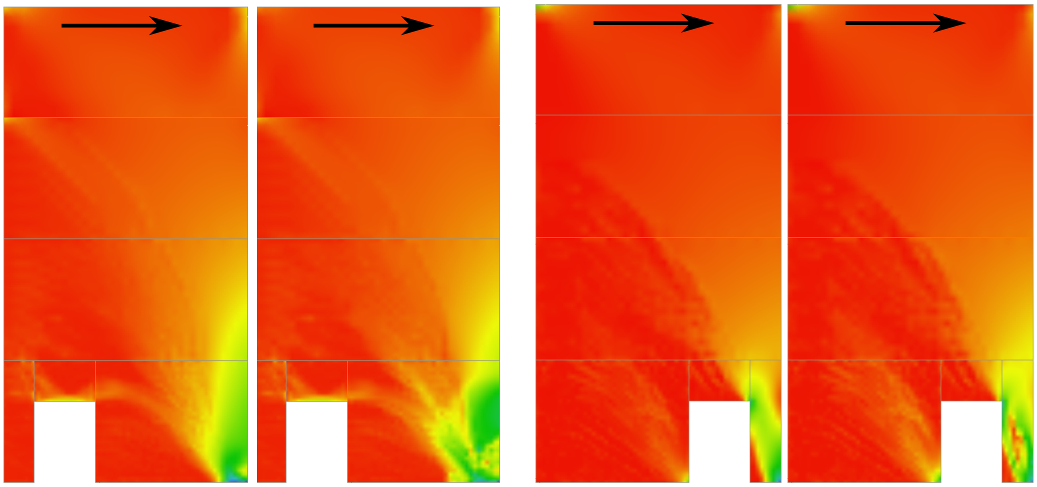

(c) Opening in tension region **(d)** Opening in compression region

Figure 6.12: Minimum Principal stress before failure and at failure for walls with and without Openings.

6.6.2 Further Investigation of Walls with Opening in the Compression Region

From the previous section it was observed that when openings are located in the compression region of the wall, the load transfer becomes more complex. In order to better understand the effect of the opening location in the compression region of the wall, a separate parametric

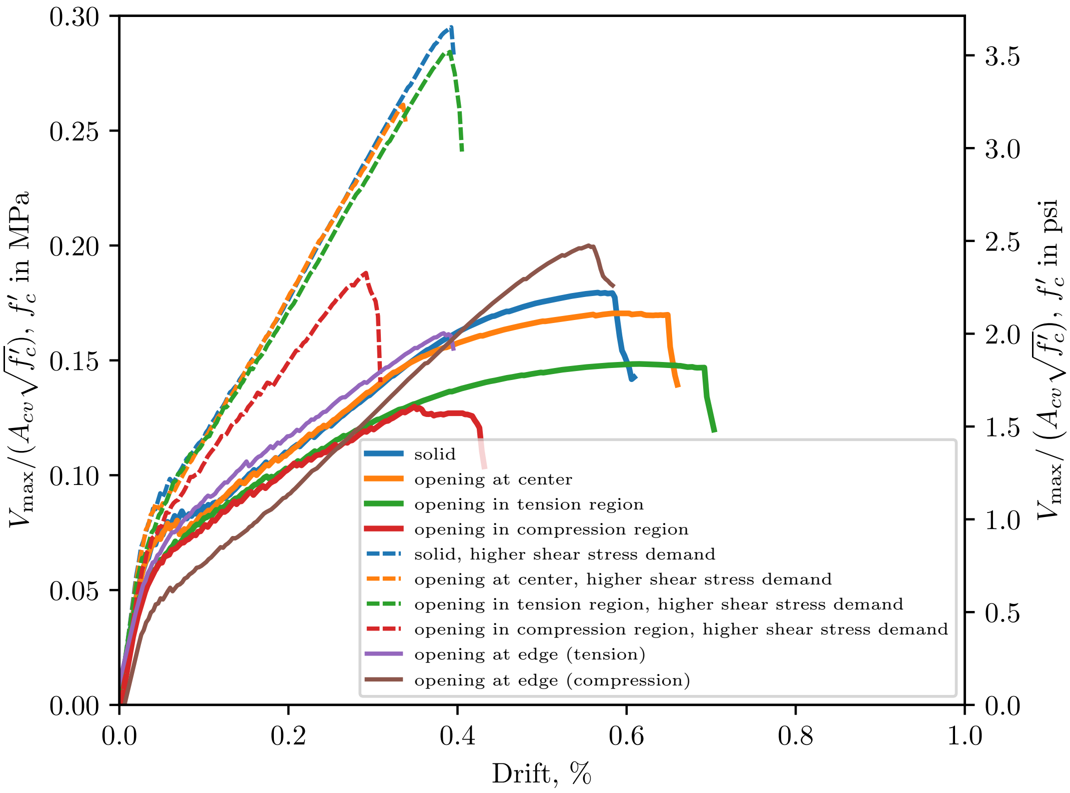

Figure 6.13: Load-deformation relationship for walls containing openings on the edges.

study was performed that includes openings in the compression region. The study takes into account the distance from the edge of the wall, cross-sectional aspect ratio of the pier in compression region as well as the axial load ratio on the wall. In such cases the confining length is bounded by the pier length and could fall below the code requirements. The opening size was kept constant for all the cases. The opening size is identical to the opening size that resulted in 50% reduction in strength for the reference wall. The models simulated for this study are listed in Table 6.5.

Additional model were simulated to investigate the effects of stacked openings (both inline and staggered) on the performance of walls. Table 6.6 shows list of models considered for impact of inline openings and Table 6.7 shows list of models considered for impact of staggered openings. For walls with inline openings planar walls were designed with inline openings in the compression region. Then flanges were added to the same specimens but the openings were moved next to the flanges. For staggered openings, center-to-center horizontal distance between the two vertical stacks of openings (s_{ho}) changed from $0.35\ell_w$ to $0.62\ell_w$. The confined regions and vertical bar configurations were adjusted accordingly while the difference in strength was kept minimum between the two configurations.

Table 6.5: List of simulated walls with openings with different compression pier sizes.

Specimen	**CSAR**	**CSAR$_{\mathbf{cp}}$**	$\ell_{\mathbf{be,tens}}$ mm (in.)	$\ell_{\mathbf{be,comp}}$(1) mm (in.)	**drift** %	$\mathbf{V}_{\text{max}}/\left(\mathbf{A_{cv}}\sqrt{\mathbf{f'_c}}\right)$ MPa (psi)
FE24–A00	15	1.00	1524 (60)	610 (24)	4.33	0.28 (3.49)
FE24–A03	15	1.00	1524 (60)	610 (24)	3.84	0.30 (3.66)
FE24–A06	15	1.00	1524 (60)	610 (24)	6.33	0.33 (3.94)
FE24–A10	15	1.00	1524 (60)	610 (24)	5.23	0.35 (4.18)
FE24–A15	15	1.00	1524 (60)	610 (24)	6.11	0.37 (4.44)
FE30–A00	15	1.25	1524 (60)	762 (30)	4.33	0.31 (3.69)
FE30–A03	15	1.25	1524 (60)	762 (30)	8.78	0.33 (3.95)
FE30–A06	15	1.25	1524 (60)	762 (30)	8.31	0.35 (4.21)
FE30–A10	15	1.25	1524 (60)	762 (30)	11.31	0.37 (4.43)
FE30–A15	15	1.25	1524 (60)	762 (30)	10.07	0.39 (4.71)
FE45–A00	15	1.88	1524 (60)	1143 (45)	2.03	0.29 (3.52)
FE45–A03	15	1.88	1524 (60)	1143 (45)	2.92	0.32 (3.83)
FE45–A06	15	1.88	1524 (60)	1143 (45)	2.53	0.34 (4.12)
FE45–A10	15	1.88	1524 (60)	1143 (45)	2.35	0.37 (4.48)
FE45–A15	15	1.88	1524 (60)	1143 (45)	3.80	0.40 (4.84)
FE60–A00	15	2.50	1524 (60)	1524 (60)	4.83	0.30 (3.73)
FE60–A03	15	2.50	1524 (60)	1524 (60)	5.70	0.33 (4.02)
FE60–A06	15	2.50	1524 (60)	1524 (60)	4.00	0.35 (4.26)
FE60–A10	15	2.50	1524 (60)	1524 (60)	3.03	0.38 (4.55)
FE60–A15	15	2.50	1524 (60)	1524 (60)	2.70	0.41 (4.88)

(1) $\ell_{\text{be,comp}}$ is bounded by the pier length; i.e., $\ell_{\text{be,comp}} = \ell_p$.

The models are labeled as: (1) the shape of the specimen; only if it is a T–shaped model and for planar walls no shape symbol is included, (2) opening location; this is according to

Table 6.6: List of simulated walls with stacked (inline) openings.

Specimen	**ℓ_p** mm (in.)	**CSAR**	**$\mathbf{CSAR_{cp}}$**	**ALR** %	**$\mathbf{V_{max}/\left(A_{cv}\sqrt{f'_c}\right)}$** MPa (psi)	**Drift** %	**Ductility**
(a) Planar walls with inline eccentric stacked openings							
IE72–A00	1830 (72)	15	3	0	0.31 (3.72)	3.77	6.51
IE72–A03	1830 (72)	15	3	3	0.33 (3.99)	5.96	5.99
IE72–A06	1830 (72)	15	3	6	0.35 (4.23)	7.64	5.36
IE72–A10	1830 (72)	15	3	10	0.38 (4.55)	6.95	4.21
IE72–A15	1830 (72)	15	3	15	0.41 (4.89)	6.06	2.69
(b) T–shaped walls							
T–IE24–A00	610 (24)	15	1	0	0.33 (3.94)	3.07	4.52
T–IE24–A03	610 (24)	15	1	3	0.36 (4.33)	3.84	8.53
T–IE24–A06	610 (24)	15	1	6	0.38 (4.61)	6.33	6.17
T–IE24–A10	610 (24)	15	1	10	0.42 (5.05)	5.23	6.92
T–IE24–A15	610 (24)	15	1	15	0.46 (5.57)	4.90	5.24
(c) Coupled walls - planar							
IC–A00	3430 (135)	15	5.6	0	0.34 (4.06)	2.96	4.09
IC–A03	3430 (135)	15	5.6	3	0.38 (4.57)	2.08	2.88
IC–A06	3430 (135)	15	5.6	6	0.40 (4.77)	1.72	2.54
IC–A10	3430 (135)	15	5.6	10	0.43 (5.13)	2.04	3.34
IC–A15	3430 (135)	15	5.6	15	0.45 (5.38)	1.58	3.05

Figure 4.1 and followed by the two digits representing the length of the compression pier in inches, and (3) the axial load ratio; illustrated by letter `A` and ranging from 0% to 20%. For instance, model FE24–A03 has an eccentric opening in the first story with a compression pier length of 24 in. and an axial load ratio of 3%. Model IE72–A00 contains inline eccentric openings with $\ell_p = 72$ in. and no ALR. And model ST24–A03 contains staggered openings with $\ell_p = 24$ in. and ALR=3%.

Table 6.7: List of simulated walls with staggered openings.

Specimen	$\mathbf{s_{ho}/\ell_w}$	$\boldsymbol{\ell_p}$ mm (in.)	**CSAR**	$\mathbf{CSAR_{cp}}$	**ALR** %	$\mathbf{V_{max}/\left(A_{cv}\sqrt{f'_c}\right)}$ MPa (psi)	**Drift** %	**Ductility**
ST24–A00	0.62	610 (24)	15	1	0	0.42 (5.09)	4.18	7.11
ST24–A03	0.62	610 (24)	15	1	3	0.45 (5.40)	3.12	5.74
ST24–A06	0.62	610 (24)	15	1	6	0.47 (5.68)	6.6	13.86
ST24–A10	0.62	610 (24)	15	1	10	0.50 (6.08)	4.47	9.83
ST24–A15	0.62	610 (24)	15	1	15	0.53 (6.44)	4.89	11.91
ST72–A00	0.35	1830 (72)	15	3	0	0.48 (5.79)	1.31	2.07
ST72–A03	0.35	1830 (72)	15	3	3	0.50 (6.06)	1.31	2.32
ST72–A06	0.35	1830 (72)	15	3	6	0.53 (6.35)	1.27	2.44
ST72–A10	0.35	1830 (72)	15	3	10	0.53 (6.38)	1.08	2.67
ST72–A15	0.35	1830 (72)	15	3	15	0.50 (5.99)	0.45	1.82

6.6.3 Deformation Capacity

Figure 6.14 shows the load-deformation capacity for simulated models presented in Table 6.5. As it can be observed from the figure, deformation capacity is affected by both cross-sectional aspect ratio of the pier in compression region ($\mathrm{CSAR_{cp}}$), and ALR. When $\mathrm{CSAR_{cp}}$is relatively small the pier undergoes a double curvature (see Figure 6.16a) and as a result the deformation capacity increases. However, when the pier length becomes smaller the deformation capacity drops. On the other hand, when pier length is larger, the behavior is more similar to a solid wall by means that the pier does not undergo a double curvature (Figure 6.16b) and crushing occurs within the boundary element. Figure 6.15 shows the trend by which the deformation capacity varies as ALR increases.

6.6.3.1 Failure Mode

When the cross-sectional aspect ratio of the pier in compression is relatively large, the failure mode is expected to be similar to walls without discontinuities unless inadequate shear, confining or transverse reinforcement is provided in the regions around the opening including

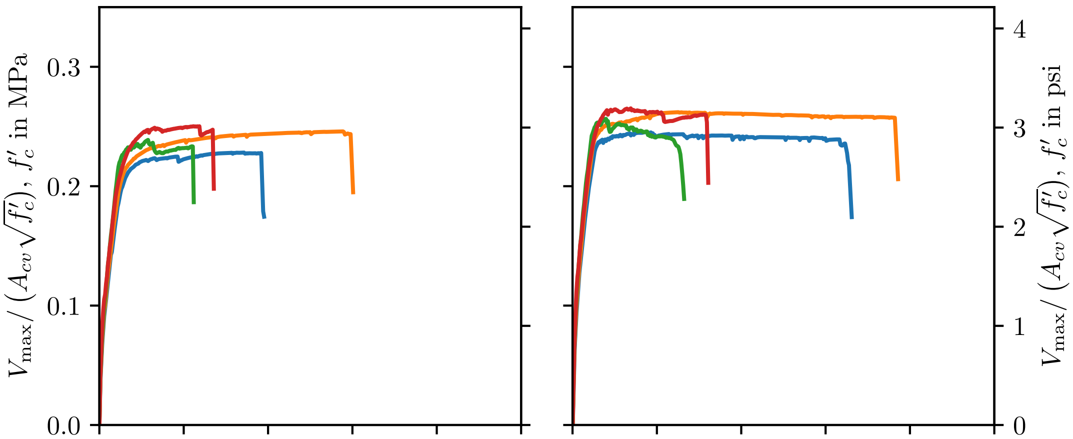

(a) ALR= 3% **(b)** ALR= 6%

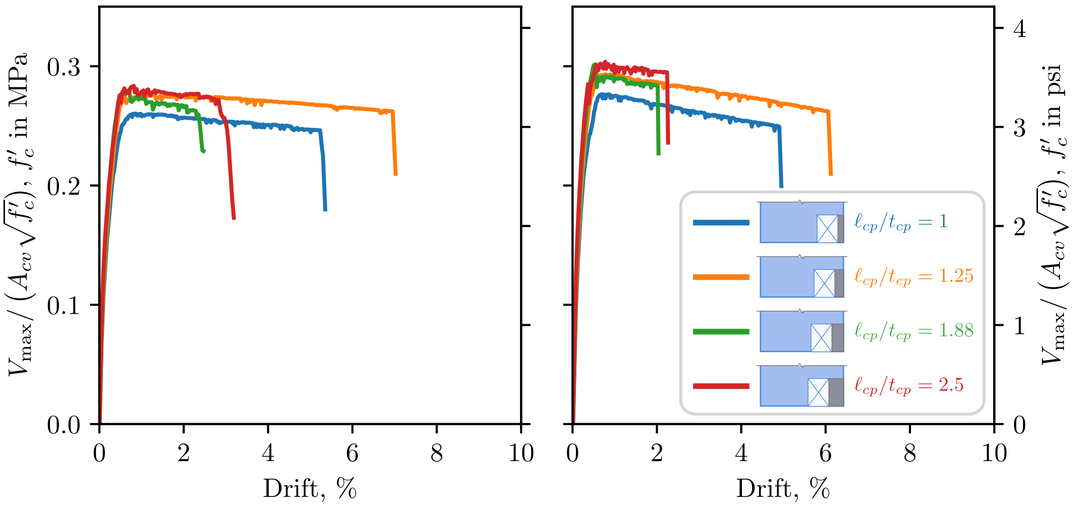

(c) ALR= 10% **(d)** ALR= 15%

Figure 6.14: Load-deformation relationships for walls with openings having different compression pier sizes.

the region above. In this study all the simulated models with CSAR_{cp} of 2.5 and 1.88 failed in compression-buckling. For shorter CSAR_{cp} and when the pier undergoes a double curvature, the failure would either occur at the interior side of the pier or at the upper portion of the pier where it is closer to the region above. For walls with large ALR, the rate of axial load and shear stresses that goes to the tension pier is much higher compared to the walls with

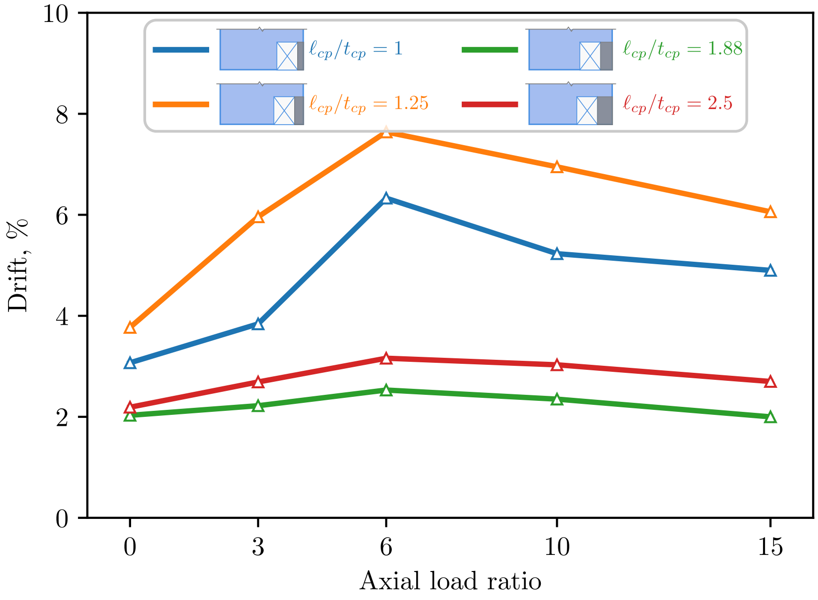

Figure 6.15: Variation in deformation capacity influenced by axial load ratio and distance of opening from the edge of wall in compression region.

smaller ALR. In such cases, the stresses are transferred to the lower bottom corner of the tension pier via larger compression struts. Consequently, the compression demand exerted to this corner could potentially be higher than the compression pier and lead to failure. This type of failure can be observed in Figure 6.17b. Note that only failure mode for four of models are shown in Figure 6.17.

If the deformation caused by the double curvature of the pier is significant, instead of a CB failure, a shear type failure is plausible. The results show that to avoid a potential shear failure in the compression pier of the wall, it is recommended to avoid pier dimensions that lead to double curvature.

6.7 Impact of Flanges on Walls with Stacked Openings

When stacked openings are in the middle of the cross-section, i.e., coupled walls, the design of the two piers are usually identical. And due to symmetry, the reinforcement configuration

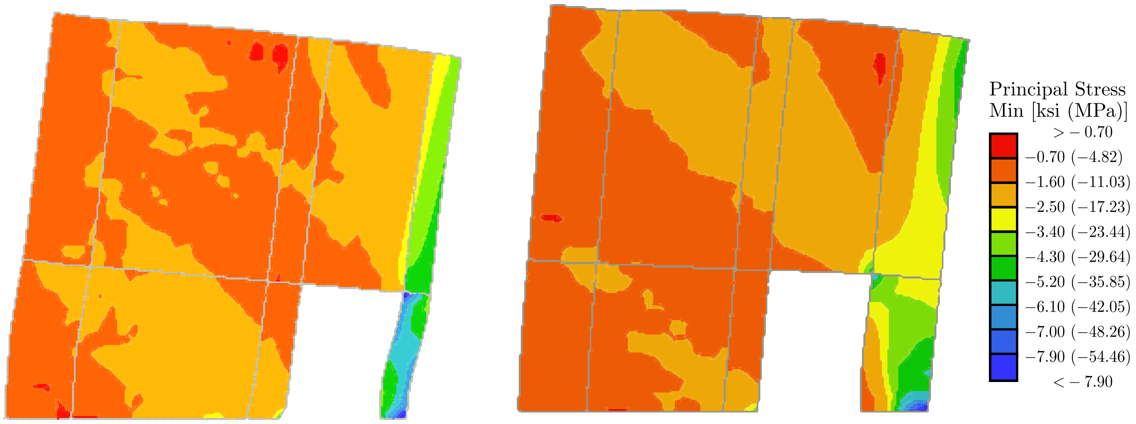

(a) $\ell_{cp}/t_{cp} = 1.0$ **(b)** $\ell_{cp}/t_{cp} = 2.5$

Figure 6.16: Pier deformation when opening is located in the compression region. Note that, for clarity only the bottom two stories of each wall is shown.

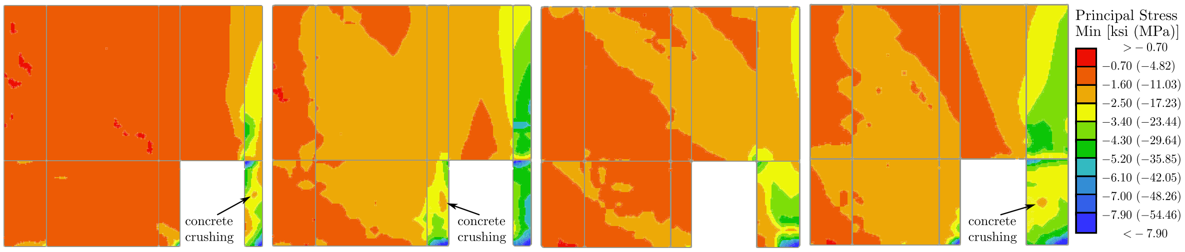

(a) $\ell_{cp}/t_{cp} = 1.0$, ALR=0% **(b)** $\ell_{cp}/t_{cp} = 1.0$, ALR=15% **(c)** $\ell_{cp}/t_{cp} = 2.5$, ALR=0% **(d)** $\ell_{cp}/t_{cp} = 2.5$, ALR=15%

Figure 6.17: Failure mode in walls having an opening in the compression region of the bottom story with different pier sizes and ALR. Note that, for clarity only the bottom two stories of each wall is shown.

for both piers are identical. However, when the openings are closer to one of the edges, the design becomes more complex and the rate of stress transfer is different depending on the proximity of the openings to the edges. In Section 6.6, it was observed that openings are most impactful when they are located in the compression region of the wall. A parameter study performed considering stacked openings in the compression region of the walls with and without flanges. Flanges were only provided to the compression region since they have a minor impact on the behavior of the wall when in tension.

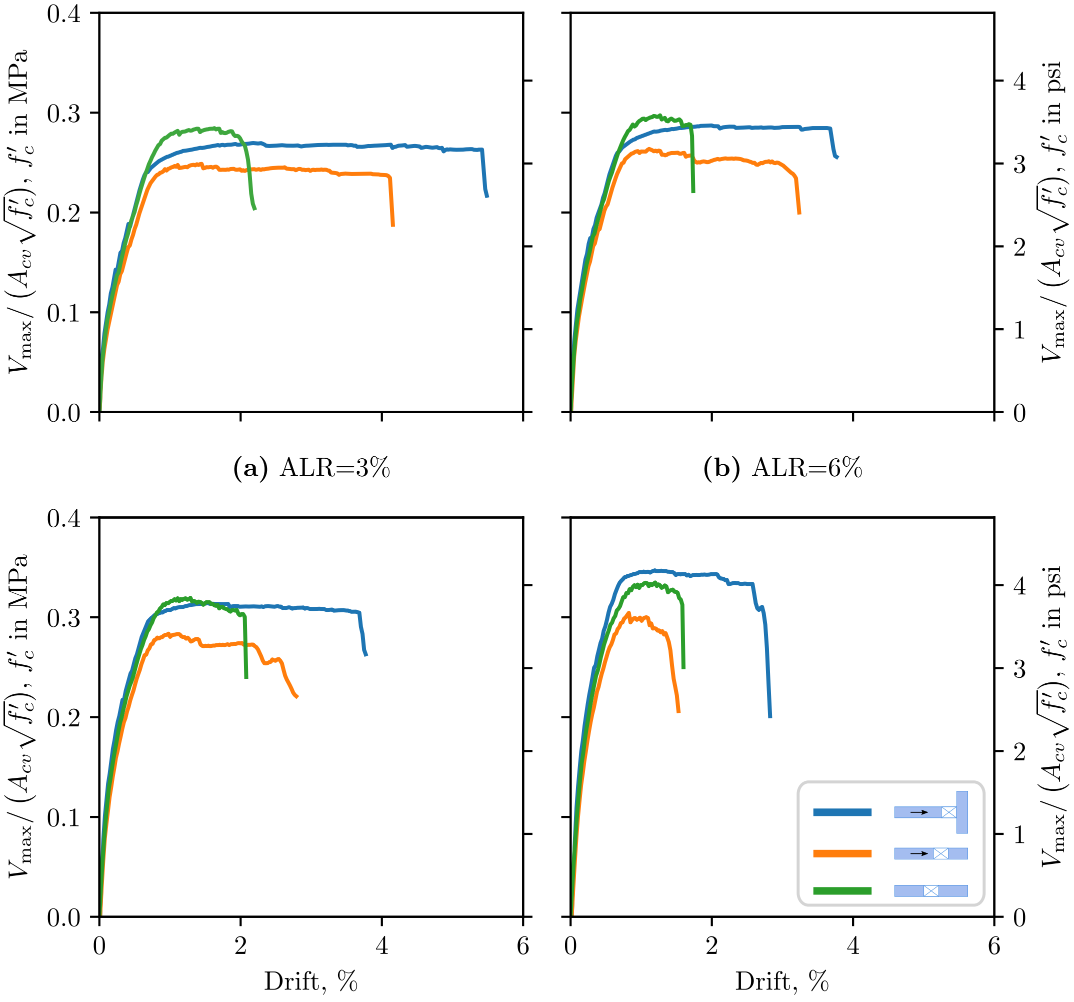

(a) ALR=3%

(b) ALR=6%

(c) ALR=10%

(d) ALR=15%

Figure 6.18: Impact of flanges on the deformation capacity of walls with stacked openings with different axial load ratios.

Figure 6.18 shows load-deformation relationship for walls with inline stacked openings for both planar and T–shaped walls while varying axial load ratio. For each ALR case, the strength was kept constant and the slight difference in the strength is due to rounding of required area of longitudinal steel (A_s) in the wall. As it can be observed from Figure 6.18, in all ALR cases, adding flanges were advantageous and the performance of the walls improved by the growth in the deformation capacity.

Figure 6.19 shows the load-deformation relationship for walls with staggered openings. Two configuration of walls were considered for this type of walls with discontinuities. The main difference between the two configurations is the center-to-center horizontal spacing between the two vertical stacks of the openings which is denoted by s_{ho}. The s_{ho}, for both cases, represents the two extreme cases with the largest and smallest spacing between the openings. For the smaller spacing, s_{ho} is 35% of the total length of the wall while it is 62% for the bigger case. Reinforcement configuration is accordingly adjusted for both cases but the difference in strength is kept minimum. Figure 6.19 shows that reducing the distance between the openings has a damaging effect on the deformation capacity. In all cases, regardless of the ALR, the drift capacity reduced by more than 50%. In the case of ALR= 15% the compression region of the wall next to the opening, started crushing as soon as the wall reached yielding.

The reduction in the deformation capacity is due to the redistribution of the stress transfer to the compression toe of the wall. When there is enough spacing between the two vertical stacks of openings for the compression struts and tension ties to form, the stress transfer is not that difference from a solid wall (Figure 6.20a and b). The difference is negligible as long as adequate spacing is provided. However, when the spacing provided is small, the transfer of the stress is redistributed. The stress reaches to the compression side on a higher elevation from the base of the wall creating a semi-vertical strut to the compression toe of the wall (Figure 6.20c and d). This results in a much higher demand on the compression toe of the wall and consequently, leads to an early failure.

6.8 Effect of Peak Shear Stress Demand on Deformation Capacity

Figures 6.21 and 6.22 shows the load-deformation relationships and effect of peak shear stress demand on deformation capacity for walls with different opening arrangements, respectively.

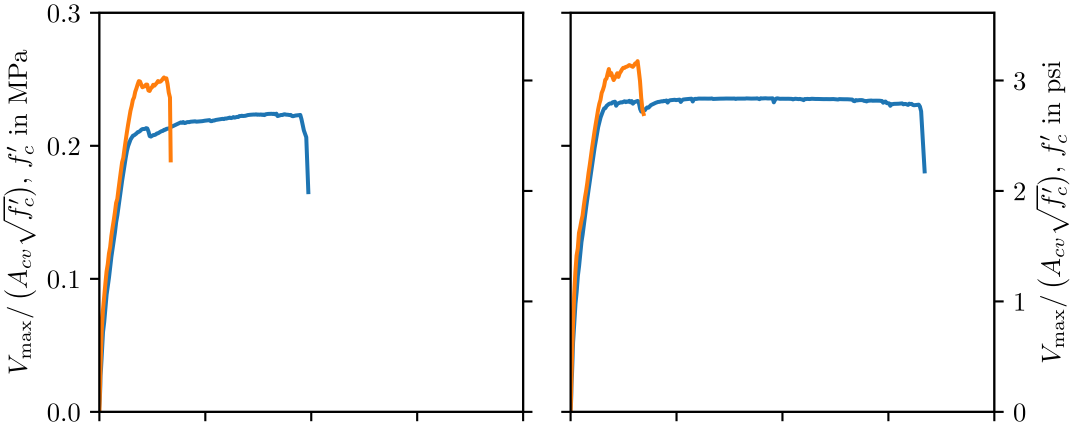

(a) ALR=3% **(b)** ALR=6%

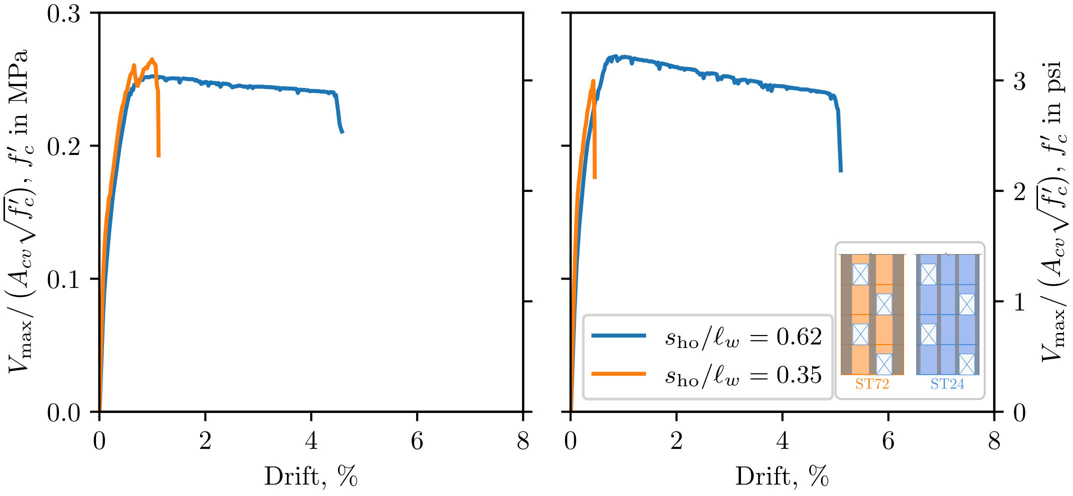

(c) ALR=10% **(d)** ALR=15%

Figure 6.19: Load-deformation relationship for walls with different staggered openings and varying axial load ratio. Note that s_{ho} represents the center-to-center horizontal spacing between the two vertical stacks of openings.

As expected, deformation capacity, drops by increasing the peak shear stress demand on the walls. However, the rate of drop is not the same for all opening arrangements. Walls having eccentric openings (FE and IE) undergo a larger deformation for smaller peak shear stress demands compared to coupled systems (IC). For larger magnitudes of peak shear stress, all walls exhibit similar deformation capacities, meaning, FE and IE walls undergo a larger drop

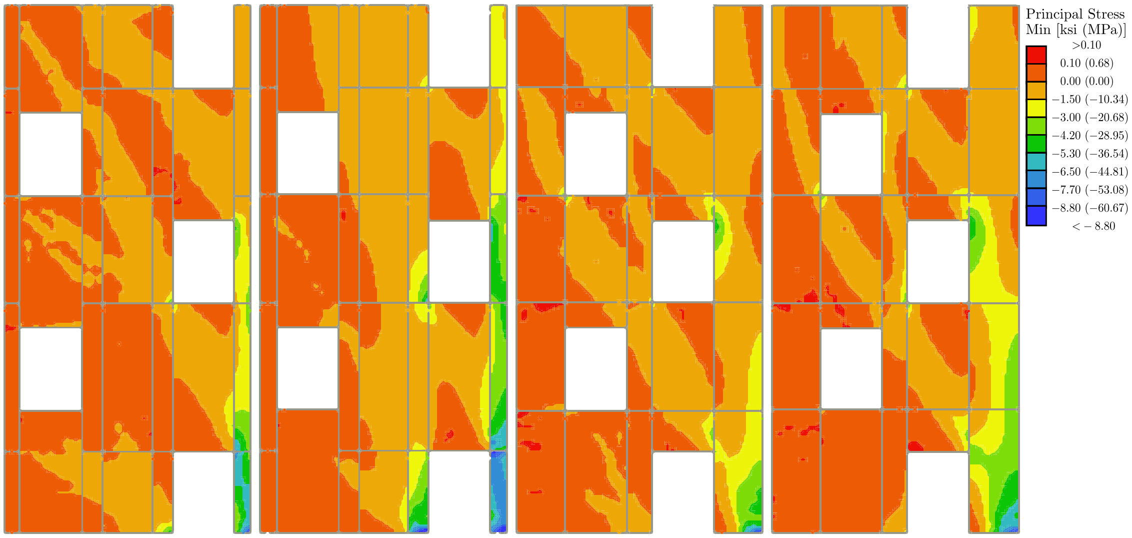

(a) Specimen ST24, ALR= 3%

(b) Specimen ST24, ALR= 15%

(c) Specimen ST72, ALR= 3%

(d) Specimen ST72, ALR= 15%

Figure 6.20: Stress transfer in walls with staggered openings.

in the deformation capacity compared with increase in peak shear stress demand.

6.9 Distributed Lateral Loading versus Loading at Effective Height

When a structural wall is simulated using a finite element analysis software, the mechanism of applying the load can influence the simulation results. In practice, when the wall is subjected to an earthquake loading, the seismic forces are distributed on each floor proportionally based on the mass intensity of each floor. Therefore, even during the design, the loads are distributed along the height of the building (or wall). However, for simulation purposes and to reduce the complexity of the model, a single force is usually applied to the effective height of the structure (see Figure 6.23) rather than a distributed loading. This is more common for pushover analyses.

In order to study the influence of the loading scheme, these loading schemes are applied to a continuous wall, and walls with different opening arrangements (IC, IE, ST). For the distributed loading case, a displacement- controlled lateral load increments applied to a rigid

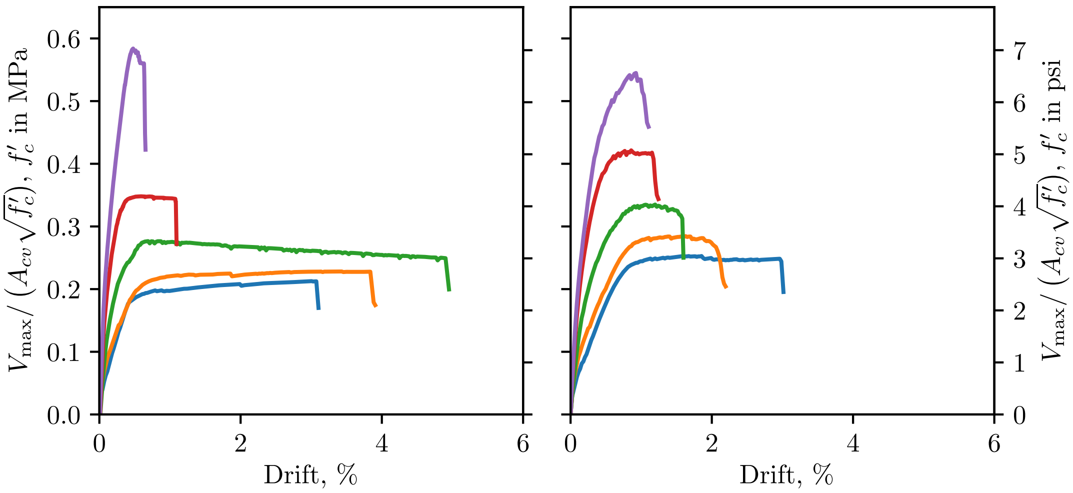

(a) FE, $\ell_{cp}/t_{cp} = 1$ **(b)** IC, $\ell_{cp}/t_{cp} = 5.6$

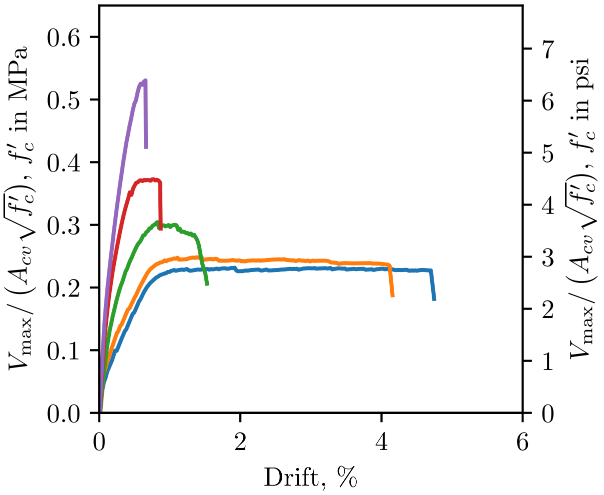

(c) IE, $\ell_{cp}/t_{cp} = 2.5$

Figure 6.21: Load-deformation relationship for walls with different opening patterns and different peak shear stress demand.

vertical beam at the effective height (Figure 6.23a). The beam is connected to each floor by links. For the loading at effective height case, displacement-controlled lateral loading applied to the effective height of the wall through a few layers of elastic finite elements (Figure 6.23b).

Figure 6.24 shows the load-deformation relationship for walls with different load patterns.

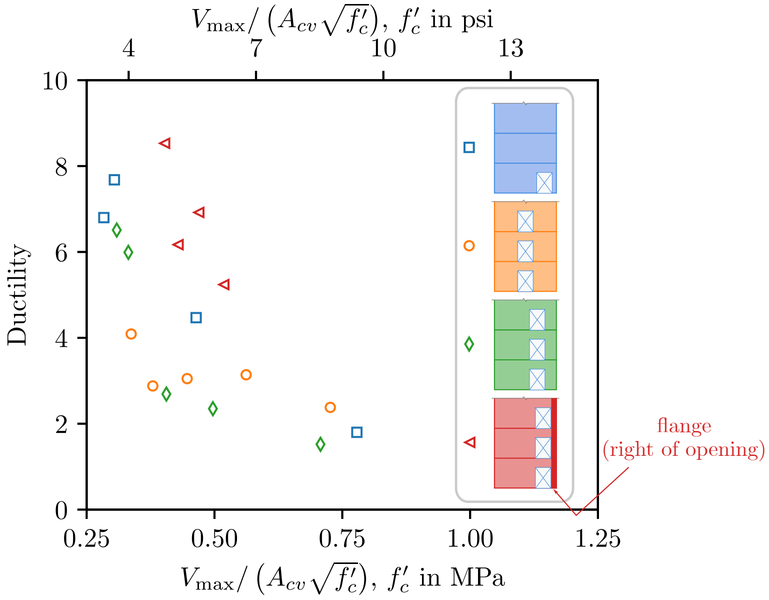

Figure 6.22: Effect of peak shear stress demand on deformation capacity for walls with different opening patterns.

The figure indicates that in some cases there is a significant post-crack stiffness change. Figures 6.25 and 6.26 show the average axial and shear stress traveled through the coupling beams for walls with stacked openings. As it can be observed from the figures, in the case of lateral distributed loading the amount of shear and axial stress carried by each coupling beam is larger than the case with lateral loading at effective height. Additionally, when the load is applied at effective height for IE walls, all coupling beams except for the first story carry negligible amounts of shear and axial stress. However, for distributed loading case in these walls, the average stresses carried by the coupling beams are substantially larger. This can also be observed in Figure 6.27. This indicates the significance of loading pattern for simulation and potentially for experiments. In distributed loading case, the stress is transferred to the right (compression region) through struts in each floor. The amount of shear stress in each coupling beam is similar but the average axial stress in each coupling

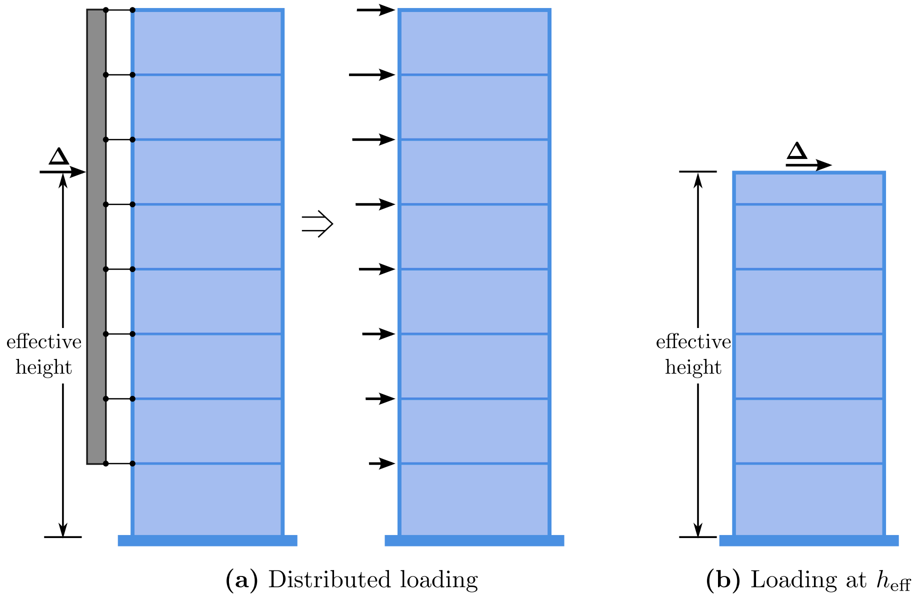

(a) Distributed loading **(b)** Loading at h_{eff}

Figure 6.23: Methods used to apply lateral loading to structures in numerical analyses.

beam is varying for IC walls. For IE walls, the variation in average axial stress in the coupling beams is less significant compared to IC walls (Figures 6.25 and 6.26).

Figure 6.28 shows the amount of stress transferred to each pier for IC and IE walls. The pier on the compression side of the wall carries a more significant amount of axial stress. For IC walls the difference between the two loading patterns is small while for IE walls, a rather larger difference is observed.

Loading pattern did not change the failure mode for any of the specimens. However, when a distributed loading pattern is used for IE walls, failure is not at the extreme fiber.For the case of IE, when the specimen is laterally loaded via a point load at the effective height, a larger portion of the compression pier is in tension compared to a distributed loading pattern (Figure 6.27c and d).

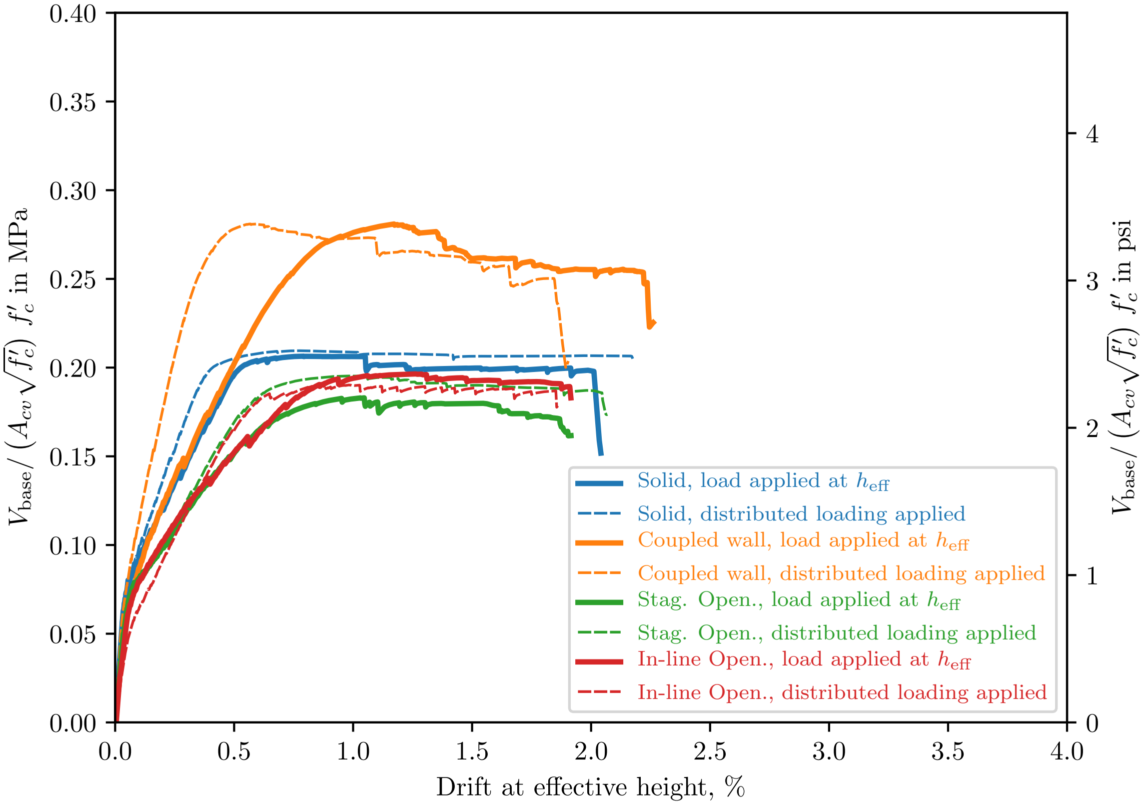

Figure 6.24: Load-deformation relationship for walls with distributed loading and point load at effective height. Note that for consistency the drift is computed at effective height.

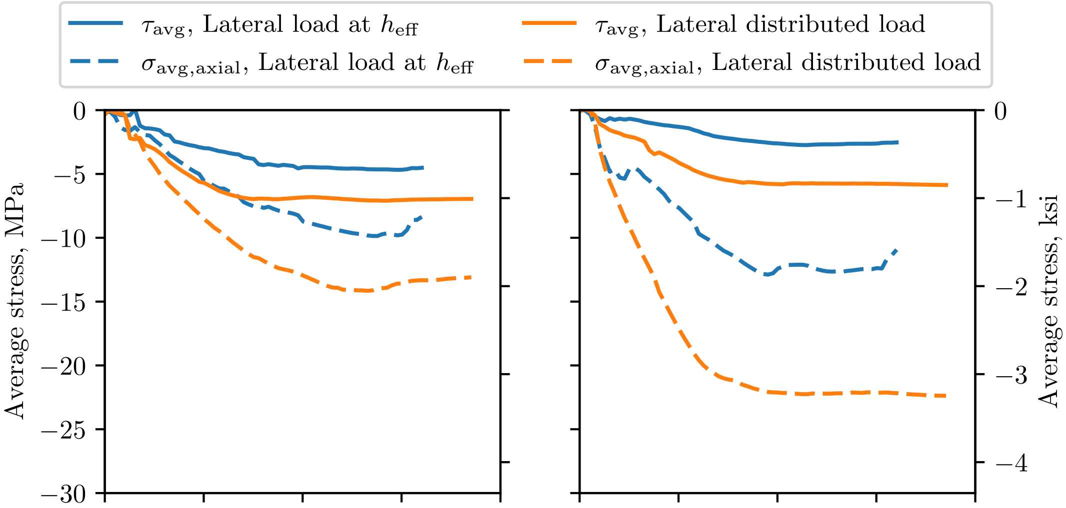

(a) 1st story coupling-beam **(b)** 2nd story coupling-beam

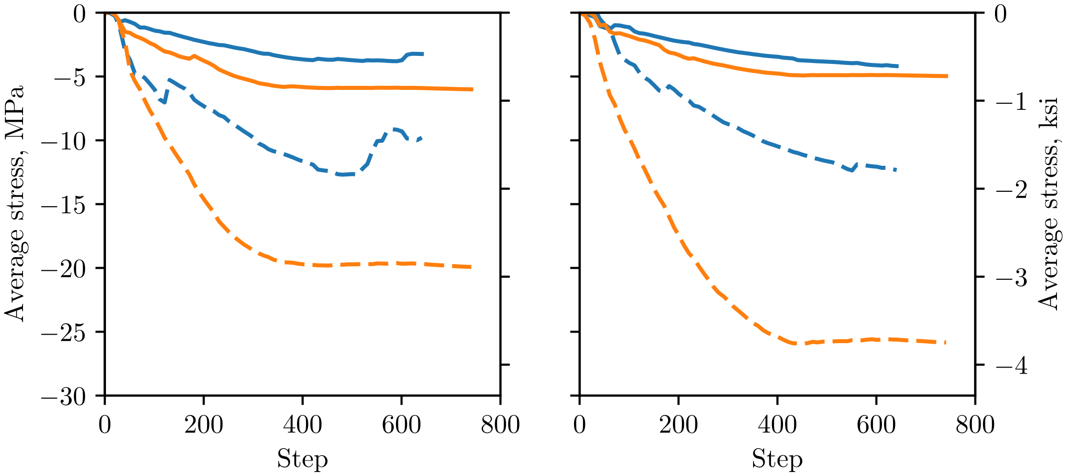

(c) 3rd story coupling-beam **(d)** 4th story coupling-beam

Figure 6.25: Average axial stress on coupling beams for coupled-walls loaded laterally with a point load at effective height and with distributed loading. Note that negative sign indicates compression stress.

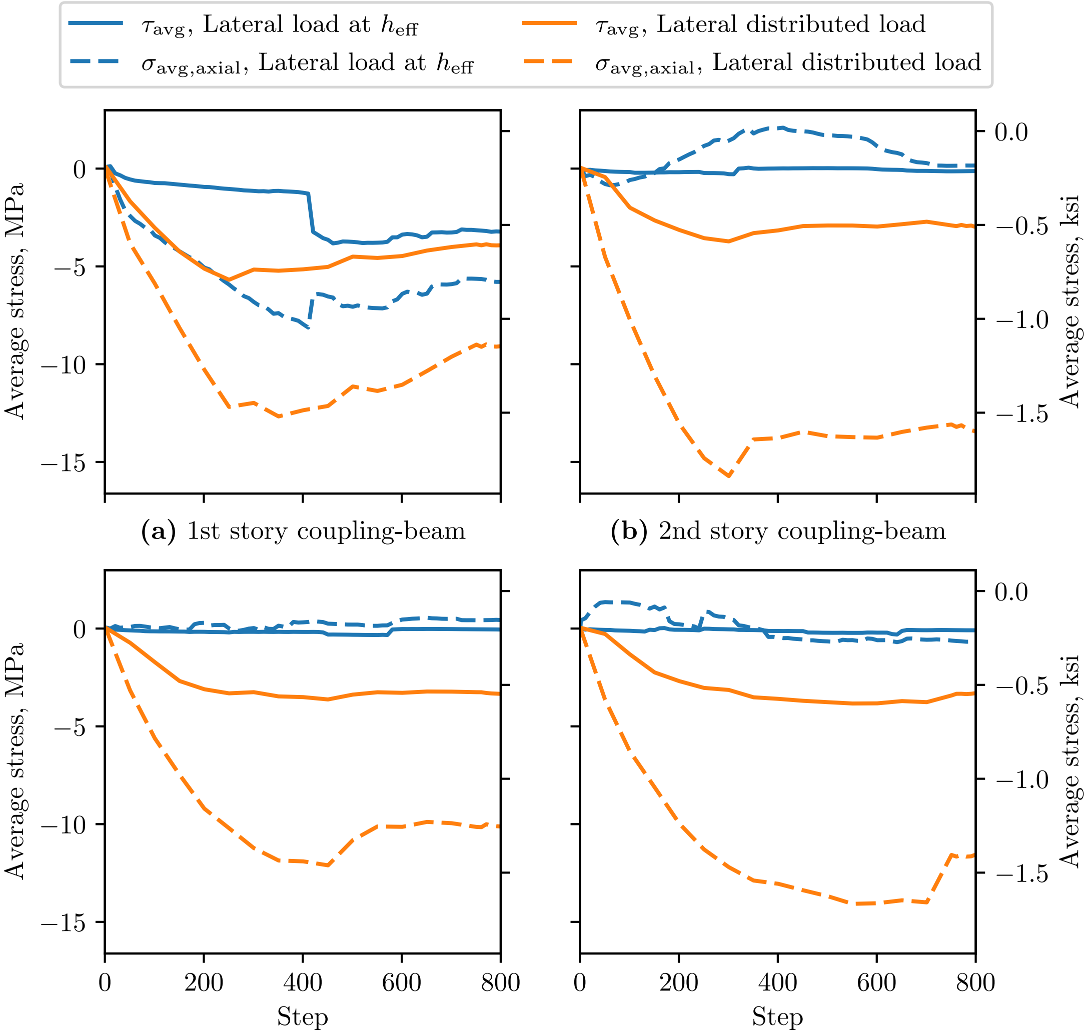

(a) 1st story coupling-beam

(b) 2nd story coupling-beam

(c) 3rd story coupling-beam

(d) 4th story coupling-beam

Figure 6.26: Average axial stress on coupling beams for walls with inline eccentric openings loaded laterally with a point load at effective height and with distributed loading. Note that negative sign indicates compression stress.

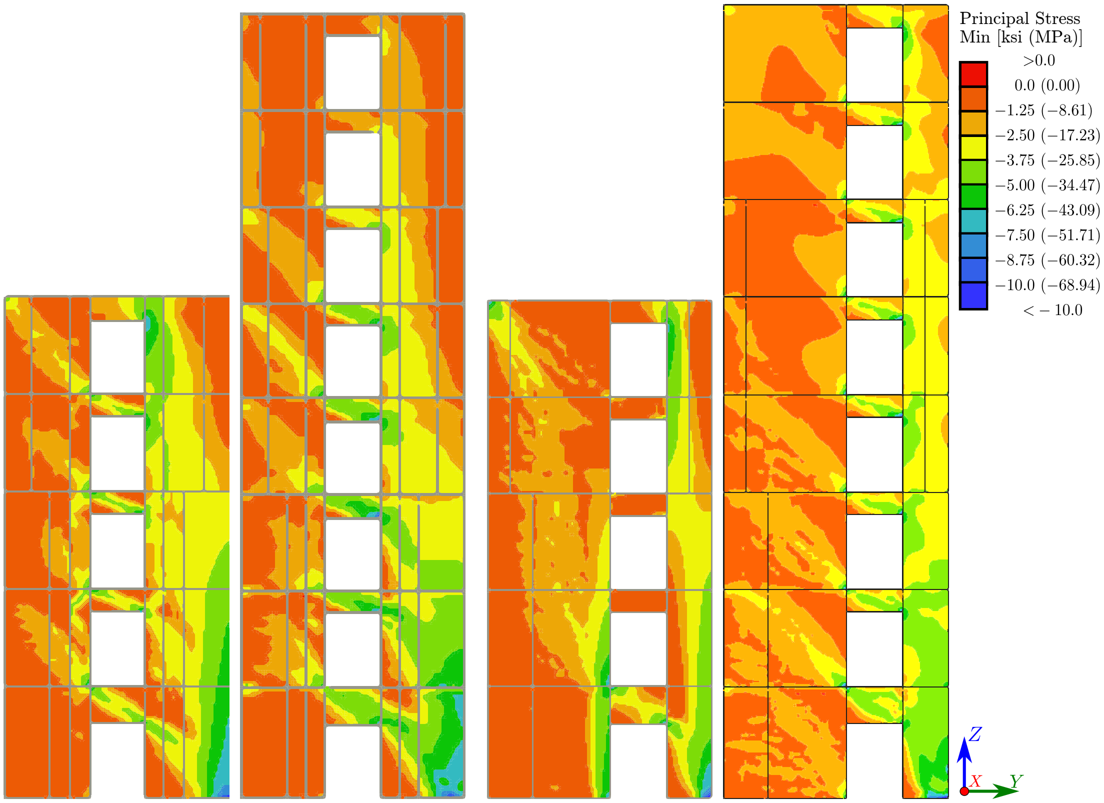

(a) IC, lateral loading at h_{eff}
(b) IC, lateral distributed load
(c) IE, lateral loading at h_{eff}
(d) IE, lateral distributed load

Figure 6.27: Minimum principal stress field for walls with stacked openings load laterally with a point load at effective height and with distributed loading. Note that for the case of lateral load at h_{eff}, the portion of the wall above the h_{eff} is not modeled. Loading direction is to the right.

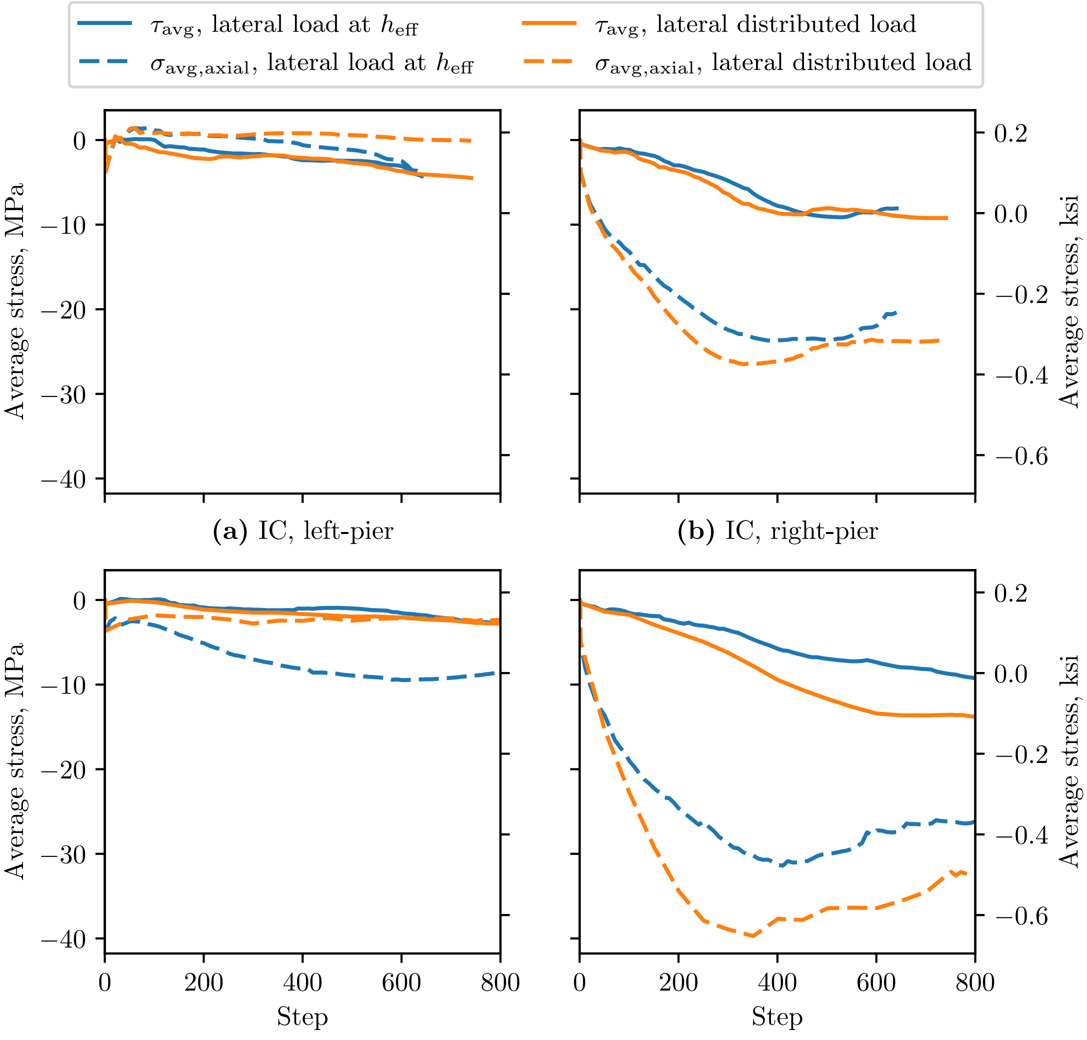

(a) IC, left-pier **(b)** IC, right-pier

(c) IE, left-pier **(d)** IE, right-pier

Figure 6.28: Average axial stress in the piers next to the openings in walls with stacked openings loaded laterally with a point load at effective height and with distributed loading. Note that negative sign indicates compression stress.

6.10 Findings

Simulations were completed for sixty-nine concrete walls with openings to study the effects peak shear stress demand, vertical irregularity, flange, arrangements and size of openings and axial load ratio. Analysis results supports the following observations:

- Openings at center of the wall does not have a significant impact on the stiffness however, shear transfer mechanisms are affected the most,

- Deformation capacity is the most impacted by openings in the compression of the wall, but proper design of the wall can improve the deformation capacity,

- Introducing an opening at the tension region of the wall, slightly reduces stiffness and strength but may result in a slight increase in deformation capacity,

- Introducing an opening in the compression region of the wall significantly reduces strength and deformation capacity,

- Flanges in the compression zone, could improve wall performance and increase ductility,

- Higher ALR redistributes the stress transfer mechanism and could potentially change the location of the failure from the compression pier to the compression region on the other side of the opening,

- For walls with staggered openings, the distance between the openings can have damaging effects if it is inadequate.

- Higher peak shear stress demands reduces the deformation capacity for walls with different opening arrangements. The rate of drop is higher for walls with eccentric openings,

- Higher shear stress demands could also affect failure mode.

Chapter 7

SUMMARY, CONCLUSIONS, AND RECOMMENDATIONS FOR FUTURE WORK

Review of the experimental and simulation data indicate that RC wall configuration, peak shear stress demand, and axial load ratio determine flexural wall performance, as characterized by deformation capacity and failure mode. Specifically, these data show that RC walls with high shear or axial stress demand or with configurations that result in locally high compression demands, exhibit a compression-shear failure mode and low ductility. These aspects of wall behavior are not fully captured by modern building codes, and practicing engineers expect flexure-controlled response and ductile behavior for walls designed in accordance with current design codes.

Since, an extended and broad-ranging experimental investigation of wall behavior and design was not feasible due to cost and the limitations of laboratory testing, a numerical study was conducted to investigate the effects of different design parameters on the response mechanisms, failure mode and deformation and ductility capacity of walls with basic and complex configurations.

This study employed a modeling approach employing the ATENA software to expand the existing experimental data and investigate the impact on wall performance of shear stress demand, axial load ratio, distribution of vertical reinforcement, extent of confining reinforcement, cross-sectional configuration presence and pattern of openings within the wall. The main objective of this study were

- Validate nonlinear three-dimensional finite element (FE) model developed and validated previously for simulating the response, including strength, deformation capacity and failure mode, of planar walls [40, 68] for walls with flanges and walls with discontinuities.

- Utilize the validated model to investigate the impact of critical parameters for walls with complex configurations. The parameters include shear stress demand, axial load ratio, distribution of vertical reinforcement, extent of confining reinforcement, cross-sectional configuration presence and pattern of openings within the wall.

- Provide design recommendations to improve response of RC structural walls.

7.1 Research Summary

7.1.1 Validation of the Numerical Model

Simulations were performed using the finite element program ATENA (). The previous investigation [40, 68] as well as preliminary research conducted as part of this study found the software to be incapable of simulating the full cyclic response histories of wall specimens tested in the laboratory. However, the previous investigation and preliminary research conducted as part of this study found that wall response, simulated for the case of constant axial loading and monotonically increasing lateral displacement demand, over predicted initial wall stiffness accurately represented the strength, deformation capacity, damage patterns, and failure modes observed in the laboratory. Thus, the simulations were performed using a monotonically increasing lateral displacement demand.

An experimental database comprising thirteen non-planar walls and eighteen walls with openings was used to validate the FE model for the current study. The model calibration was identical to that used for the previous study of planar walls [40, 68], with the exception that the model parameter controlling concrete dilation under compressive load was modified slightly. The need for this modification was attributed to changes introduced into the concrete material model in updating the software to the version used in the current study. Analysis results demonstrate that the software successfully simulates the response observed in the laboratory, including the failure mode, as well as provides improved understanding of the behavior (stress fields, damage patterns, and failure modes) of walls with complex configurations.

7.1.2 Parameter Study to Investigate Impacts of Design Parameters on Walls with Flanges

A comprehensive parametric study was conducted to study the effects of peak shear stress demand, cross-sectional configuration, axial load ratio, and depth of confinement within the concrete compression region, on the non-planar walls subjected to lateral loading. The study employed three reference specimens which modified to achieve a range of peak shear stress demands and cross-sectional configurations. Modifications of the reference specimens included axial load ratio, shear span, flange width, wall length and longitudinal reinforcement ratio, reinforcement distribution, and depth of confinement within the compression zone. The results showed that similar to planar walls, higher shear stress demands and axial load ratios lead to a more brittle, compression-shear (CS) and that including a flange in the compression zone, can increase ductility and prevent CS failure. High shear stress and axial load demand increase the likelihood of CS failure and increasing the depth of confinement within the compression region and/or adding flanges to the compression region improve deformation capacity and failure mode.

7.1.3 Parameter Study to Investigate Impacts of Design Parameters on Walls with Openings

This study investigated also the behavior of walls with openings, including consideration of the on response of the addition of vertical irregularities, shear stress demand, opening arrangements and sizes and flanges in the compression zone. This study utilized, as reference specimens, a series of wall designs developed for a FEMA-sponsored project managed by the Applied Technology Council [23]. The walls were designed according to the current code requirements. For each reference wall specimen, shear span, axial load ratio, and vertical boundary element reinforcement ratio were varied to achieve target peak shear stress demands. Additionally, reference specimens modified to include different opening arrangements, including solid, first centered, first eccentric, inline centered, inline eccentric and staggered. The results of these simulations showed that openings in the compression region are the most critical and that flanges result in higher ductility, higher axial load can relocate the failure, higher shear stress demand reduces deformation capacity and affects failure mode.

7.2 Conclusions

7.2.1 Modeling

Finite element modeling using the ATENA software package provided an accurate simulation of wall response including strength, deformation capacity and failure mode for walls with different configurations.

7.2.2 Parametric Study for Non-planar Walls

A parametric study was conducted to investigate the impacts of flanges, high shear stress demand, axial load ratio and cross-sectional configuration on the behavior of flanged walls; i.e., deformation capacity and failure mode.

1. Flexural walls can exhibit a compression-shear type failure where the compression stresses associated with flexure and shear transfer combined to create a region of high compression. This failure mode results in reduced deformation capacity in comparison with flexural compression failure.

2. Five design parameters have the most impact on failure mode and ductility of walls with flanges; shear stress demand, axial load ratio, addition of flanges that expand the area of compression region and the extent of confinement in compression region. Higher shear stress demand and axial load ratio made wall more vulnerable to undergo a compression-shear failure. Flanges alter the cross-sectional configuration of walls (weighted cross-sectional aspect ratio) and consequently, walls with flanges potentially less likely to fail in compression-shear. That, in addition to the confinement length will boost the possibility of a ductile failure in walls.

3. Increased axial load ratio increases the likelihood of compression-shear failure and results in reduced ductility for T– and Semi–I– shaped walls. Data suggest no correlation between increasing axial load and ductility of I–shaped walls. This is attributed to the I–shaped configuration providing a large compression region.

4. T-shaped walls loaded in the direction that puts toe of the web in compression exhibit similar failure mode and ductility to planar walls.

5. As has been shown previously for planar walls, the ATENA continuum analyses show that the vertical strain profile along the length of non-planar walls is not linear as it is commonly assumed in practice. When flanges are added, nonlinearity of the vertical strain profile is exacerbated. This nonlinearity is an indication of different local deformations across the length of the wall and therefore, the assumption that plane section remains plane after deformation is not accurate.

6. The vertical strain profile in the flanges of non-planar walls in tension is determined by the width of the flange and the reinforcement layout. When flanges are uniformly reinforced, the vertical strain profile ranges from uniform for short flanges to a triangular distribution (higher towards the center of wall) for wider flanges. For non-uniformly reinforced flanges, strains are substantially higher in the lightly reinforced regions regardless of flange width.

7. The behavior of flanges in compression is fairly similar to the behavior of flanges when they are in tension with uniformly reinforced flanges having approximately uniform strain fields if they are relatively short and higher strains being absorbed earlier in the lightly reinforced regions of the non-uniformly reinforced flanges.

7.2.3 Parametric Study for Walls with Openings

1. introducing an opening at the base of the wall has minimal impact on overall stiffness, strength and deformation capacity of the system if the opening is in the middle of the wall. As the opening moves towards the perimeter of the wall, the stiffness and deformation capacity begin to reduce. When the opening is close to the edge of the wall such that cross-sectional aspect ratio of the wall is small (small $\mathrm{CSAR_{cp}}$), then the pier goes into double curvature,

    - Openings at center of the wall that reduce story stiffness by 25 to 50% affect the shear transfer mechanism, strength of the wall and deformation capacity of the wall.
    - For walls with openings near the perimeter of the wall, when the opening is in tension, wall strength is reduced because there is less longitudinal reinforcement at the perimeter of the wall and when the opening is in compression, strength and deformation capacity are significantly reduced.
    - When openings on the first story are located in the compression region the wall will act like a solid wall unless the pier between the opening and edge of the wall has a small cross-sectional aspect ratio (small $\mathrm{CSAR_{cp}}$) in which case the pier goes into double curvature
    - Higher ALR redistributes the stress transfer mechanism and could potentially change the location of the failure from the compression pier to the compression region on the other side of the opening.

2. Walls with stacked openings,

    - The opening pattern has an effect on the deformation capacity of the wall; deformation capacity is reduced when the wall contains staggered openings with short horizontal distance between the openings. However, if the distance is adequate, a high ductile response can be achieved.

- The location of the opening impacts the stress field and response mode. For stacked openings, similar to other walls, increasing shear stress demand and axial load ratio reduces the deformation capacity. Higher shear stress demands could also affect failure mode. The location of stacked openings and detailing determine the rate at which ductility diminishes with stress demand.
- The loading distribution applied in the analysis has significant impact on the stress field but relatively little impact on the global load-displacement response with the exception of the coupled walls. The simulated minimum principal stress fields differ fairly substantially between the model with the distributed lateral loading and lateral point load at effective height. The coupling beam loads vary significantly between the two loading patterns.

3. Flanges in the compression zone, could improve wall performance and increase ductility. Adding flanges in the compression zone improves the performance and deformation capacity of walls with a single opening at base, with one opening, two openings and stacked openings.

7.2.4 Design Recommendations

1. The design shear stress capacity of walls should be a function of flange width based on the observation that to achieve a ductility in excess of 4.0, T–shaped walls must have a shear stress demand of $6.0\sqrt{f'_c}$ psi ($0.5\sqrt{f'_c}$ MPa), Semi–I–shaped walls must have a shear stress demand of $9.0\sqrt{f'_c}$ psi ($0.75\sqrt{f'_c}$ MPa), and I–shaped walls must have a shear stress demand of $12.0\sqrt{f'_c}$ psi ($1.0\sqrt{f'_c}$ MPa).

2. In order to avoid a compression-shear failure, extend the length of confinement to the full depth of the compression region if peak shear stress demand is larger than

$6.0\sqrt{f_c'}$ psi ($0.5\sqrt{f_c'}$ MPa).

3. When designing flanged walls, use uniform reinforcement configuration because a reinforcement pattern with heavily reinforced boundary elements and lightly reinforced web concentrates the strain demands in the lightly reinforced regions.

4. Where the opening is of substantial size, then the compression pier is going to attract a lot of shear stress and that can lead to reduced deformation capacity. If it is a skinny pier, then it does not attract very much shear, and it responds almost purely in flexure and not so much in shear and if it is wider, like a coupled wall, it attracts a lot of shear, and it can result in premature shear failure or a premature compression-shear failure.

5. Design walls with staggered openings with adequate horizontal spacing between the openings and between the openings and wall ends.

7.3 Future Work

Future research is needed to address the following.

1. Opening in flanges: Architectural requirements and utility passage ways may sometimes result in discontinuities in the flanges of the walls. Issues that turned up for walls with openings in the web, are likely to be more significant when openings are in the flanges.

2. Higher axial load ratios: Walls with high axial load ratio are more likely to behave differently when the axial load ratio is more than 20% which is not considered in this study.

3. Concrete strength: High strength and ultra-high performance concretes are more common nowadays in RC structures and very few studies focused on walls with high strength concrete and walls with ultra-high performance concrete.

4. Reinforcement distribution: More studies are required to study the effects of uniformly distributed reinforcement in the entire wall configuration versus lumped reinforced configuration is required.
5. Bar buckling: Current concrete models lack the simulation of bar buckling.
6. Cyclic loading: To further study the behavior of walls, different load patterns including cyclic loading pattern need to be considered.

REFERENCES

[1] Saman Ali Abdullah. *Reinforced Concrete Structural Walls: Test Database and Modeling Parameters*. PhD thesis, 2019.

[2] ACI 318-02. *Building Code Requirements for Structural Concrete (ACI 318-02) and Commentary*. American Concrete Institute, 2002.

[3] ACI 318-14. *Building Code Requirements for Structural Concrete (ACI 318-14) and Commentary*. American Concrete Institute, 2014.

[4] ACI 318-19. *Building Code Requirements for Structural Concrete (ACI 318-19) and Commentary*. American Concrete Institute, 2019.

[5] ACI 318-99. *Building Code Requirements for Structural Concrete (ACI 318-99) and Commentary*. American Concrete Institute, 1999.

[6] Aejaz Ali and James K. Wight. RC Structural Walls with Staggered Door Openings. *Journal of Structural Engineering*, 117(5):1514–1531, 1991. doi: 10.1061/(ASCE)0733-9445(1991)117:5(1514). URL `http://ascelibrary.org/doi/abs/10.1061/%28ASCE%290733-9445%281991%29117%3A5%281514%29`.

[7] Applied Technology Council (ATC). Quantification of building seismic performance factors. *Fema P695*, page 421, June 2009. URL `https://www.fema.gov/media-library-data/20130726-1716-25045-9655/fema{_}p695.pdf`.

[8] ASCE7. *Minimum Design Loads for Buildings and Other Structures*. ASCE/SEI Standard 7-16, 2016.

[9] A. Behrouzi, T. Welt, D. Lehman, L. Lowes, J. LaFave, and D. Kuchma. *Experimental and numerical investigation of flexural concrete wall design details*, pages 418–433. American Society of Civil Engineers (ASCE), 2017. doi: 10.1061/9780784480410.035. URL `https://ascelibrary.org/doi/abs/10.1061/9780784480410.035`.

[10] Anahid Behrouzi, Andrew Mock, Laura Lowes, Dawn E. Lehman, and Daniel Kuchma. Summary of Large-Scale Nonplanar Reinforced Concrete Wall Tests. Technical report, Charles Pankow Foundation, 2015.

[11] Anahid A. Behrouzi. *Impact of Cross Section, Web Reinforcement and Load History on the Seismic Performance of Slender Concrete Walls*. PhD thesis, University of Illinois at Urbana-Champaign, 2016.

[12] K Beyer, A Dazio, and MJN Priestley. Quasi-static Cyclic Tests of Two U-Shaped Reinforced Concrete Walls. *Journal of earthquake engineering*, 12(7):1023–1053, 2008.

[13] Beth L. Brueggen, Catherine E. French, and Sri Sritharan. T-Shaped RC Structural Walls Subjected to Multidirectional Loading: Test Results and Design Recommendations. *Journal of Structural Engineering*, 143(7):04017040, 2017. ISSN 0733-9445. doi: 10.1061/(ASCE)ST.1943-541X.0001719. URL `http://ascelibrary.org/doi/10.1061/{%}28ASCE{%}29ST.1943-541X.0001719`.

[14] Beth Louise Brueggen. *Performance of T-shaped Reinforced Concrete Structural Walls under Multi-directional Loading*. PhD thesis, University of Minnesota, 2009.

[15] CEN, ENV1998. *Eurocode 8: Design Provisions for Earthquake Resistance of Structures 1994. : European Committee for Standardization.* Brussels, 1998.

[16] CEN, preEN1998. *Eurocode 8: Design Provisions for Earthquake Resistance of Structures. 2003: European Committee for Standardization.* Brussels, 1998.

[17] Jan Cervenka and Vassilis K Papanikolaou. Three dimensional combined fracture–plastic material model for concrete. *International Journal of Plasticity*, 24(12):2192–2220, 2008.

[18] Vladimir Cervenka, Jan Cervenka, and Libor Jendele. Atena program documentation, part 1: Theory, 2013, 2013.

[19] Cervenka Consulting. *ATENA 3D: Computer Program for Nonlinear Finite Element Analysis of Rienforced Concrete Structures*. Prague, Czech Republic, 2015. URL `http://www.cervenka.cz`.

[20] Q. Chen. *Static inelastic analysis of reinforced concrete coupled shear wall*. PhD thesis, Tsinghua University, 2002.

[21] Chang-Sik Choi, Sang-Su Ha, Li-Hyung Lee, Young-Hun Oh, and Hyun-Do Yun. Evaluation of deformation capacity for RC T-shaped cantilever walls. *Journal of earthquake engineering*, 8(03):397–414, 2004.

[22] Raluca Constantin and Katrin Beyer. Non-rectangular RC walls: A review of experimental investigations. In *2nd European Conference on Earthquake Engineering and Seismology*, 2014.

[23] Applied Technology Council. *Assessing seismic performance of buildings with configuration irregularities*. Federal Emergency Management Agency : National Earthquake Hazards Reduction Program (U.S.), Washington, D.C., 2018.

[24] René De Borst. *Non-linear analysis of frictional materials*. PhD thesis, Delft University of Technology, The Netherlands, 1986.

[25] J H Doh and S Fragomeni. Evaluation of Experimental Work on Concrete Walls in One and Two-Way Action. *Australian journal of structural engineering*, 6(1):37–52, 2005. ISSN 1328-7982. doi: 10.1080/13287982.2005.11464943.

[26] M. Fethi Gullu and Kutay Orakcal. Nonlinear Finite Element Modeling of Reinforced Concrete Walls with Varying Aspect Ratios. *Journal of earthquake engineering : JEE*, 25(10):2033–2064, 2021. ISSN 1363-2469.

[27] Kent A. Harries. Ductility and Deformability of Coupling Beams in Reinforced Concrete Coupled Walls. *Earthquake Spectra*, 17(3):457–478, aug 2001. ISSN 8755-2930. doi: 10.1193/1.1586184. URL `http://journals.sagepub.com/doi/10.1193/1.1586184`.

[28] International Code Council IBC 2003. *International Building Code 2003*. International Building Code. International Code Council, 2003. ISBN 9781892395559.

[29] N Ile and JM Reynouard. Behaviour of U-Shaped Walls Subjected to Uniaxial and Biaxial Cyclic Lateral Loading. *Journal of Earthquake Engineering*, 9(01):67–94, 2005.

[30] Sanya Johnson. Comparison of Nonlinear Finite Element Modeling Tools for Structural Concrete. 2006.

[31] Daisuke Kato, Hiroshi Noda, and Yoichi Sugishita. Strength and deformation capacity of cantilever structural walls with openings. *PEER report*, 10:311–321, 1999.

[32] Kristijan Kolozvari, Kutay Orakcal, and John W. Wallace. Modeling of Cyclic Shear-Flexure Interaction in Reinforced Concrete Structural Walls. I: Theory. *Journal of Structural Engineering*, 141(5):04014135, 2015. doi: 10.1061/(ASCE)ST.1943-541X.0001059. URL `https://ascelibrary.org/doi/abs/10.1061/%28ASCE%29ST.1943-541X.0001059`.

[33] Kristijan Kolozvari, Thien A. Tran, Kutay Orakcal, and John W. Wallace. Modeling of Cyclic Shear-Flexure Interaction in Reinforced Concrete Structural Walls. II: Experimental Validation. *Journal of Structural Engineering*, 141(5):04014136, 2015. doi: 10.1061/(ASCE)ST.1943-541X.0001083. URL `https://ascelibrary.org/doi/abs/10.1061/%28ASCE%29ST.1943-541X.0001083`.

[34] Kristijan Kolozvari, Ross Miller, and Kutay Orakcal. Finite Element Modeling of Reinforced Concrete Structural Walls for Performance-Based Seismic Design. In *WIT Transactions on the Built Environment*, volume 172, pages 35–46, jul 2017. doi: 10.2495/ERES170041. URL `http://library.witpress.com/viewpaper.asp?pcode=ERES17-004-1`.

[35] D. J. Lee, H. Guan, J. H. Doh, and S. Fragomeni. Finite element analysis of reinforced concrete walls with openings in one- and two-way action. *Progress in Mechanics of Structures and Materials - Proceedings of the 19th Australasian Conference on the Mechanics of Structures and Materials, ACMSM19*, (May 2014):681–686, 2007.

[36] D.J. Lee, H. Guan, S. Fragomeni, and J.H. Doh. Preliminary Analysis of Normal Strength Concrete Walls with Openings using Layered Finite Element Method. In *Computational Methods*, number November 2016, pages 1783–1791. Springer Netherlands, Dordrecht, 2007. ISBN 9781402039539. doi: 10.1007/978-1-4020-3953-9_115. URL `http://link.springer.com/10.1007/978-1-4020-3953-9_115`.

[37] Bing Li, Kai Qian, and Hui Wu. Flange effects on seismic performance of reinforced concrete squat walls with irregular or regular openings. *Engineering Structures*, 110: 127 – 144, 2016. ISSN 0141-0296. doi: https://doi.org/10.1016/j.engstruct.2015.11.051. URL `http://www.sciencedirect.com/science/article/pii/S0141029615007580`.

[38] Hui Liu. *Effect of Concrete Strength on the Response of Ductile Shear Walls*. PhD thesis, McGill University, Montréal, Canada, 2004.

[39] Laura Lowes, Dawn Lehman, D Kuchma, A Mock, and Anahid Behrouzi. Large scale tests of C-Shaped Reinforced Concrete Walls: Summary Report. *NEES project warehouse*, 2013.

[40] Laura N. Lowes, Dawn E. Lehman, and Zach Whitman. Investigation of failure mechanisms and development of design recommendations for flexural reinforced concrete

walls. *Engineering Structures*, 186:323 – 335, 2019. ISSN 0141-0296. doi: https://doi.org/10.1016/j.engstruct.2019.01.122. URL `http://www.sciencedirect.com/science/article/pii/S0141029617321363`.

[41] Xilin Lu and Yuntao Chen. Modeling of Coupled Shear Walls and Its Experimental Verification. *Journal of structural engineering (New York, N.Y.)*, 131(1):75–84, 2005. ISSN 0733-9445.

[42] Xilin Lu, Ying Zhou, Juhua Yang, Jiang Qian, Cheng Song, and Ying Wang. Shear wall database. *Network for Earthquake Engineering Simulation*, 2010.

[43] Xinzheng Lu, Linlin Xie, Hong Guan, Yuli Huang, and Xiao Lu. A Shear Wall element for Nonlinear Seismic Analysis of Super-Tall Buildings using OpenSees. *Finite Elements in Analysis and Design*, 98:14–25, 2015. ISSN 0168-874X. doi: https://doi.org/10.1016/j.finel.2015.01.006. URL `https://www.sciencedirect.com/science/article/pii/S0168874X15000074`.

[44] Mosoarca Marius. Seismic behaviour of reinforced concrete shear walls with regular and staggered openings after the strong earthquakes between 2009 and 2011. *Engineering Failure Analysis*, 34:537–565, dec 2013. ISSN 13506307. doi: 10.1016/j.engfailanal.2013.05.014. URL `http://dx.doi.org/10.1016/j.engfailanal.2013.05.014http://linkinghub.elsevier.com/retrieve/pii/S1350630713001908`.

[45] F McKenna, S Mazzoni, and GL Fenves. Open System for Earthquake Engineering Simulation (OpenSees) Software Version 2.3.0. *University of California, Berkeley, CA. Available from http://opensees.berkeley.edu*, 2011.

[46] Marco Menegotto and Paolo Emilio Pinto. Method of Analysis for Cyclically Loaded RC Plane Frames Including Changes in Geometry and Non-elastic Behaviour of Elements Under Combined Normal Force and Bending. In *IABSE Congress Reports of the Working Commission*, volume 13, 1973.

[47] Philippe Menetrey and KJ Willam. Triaxial failure criterion for concrete and its generalization. *ACI structural Journal*, 92(3):311–318, 1995.

[48] Jack Moehle. *Seismic Design of Reinforced Concrete Buildings.* McGraw Hill Professional, 2014. ISBN 9780071839457.

[49] A. Niroomandi, S. Pampanin, R.P. Dhakal, and M. Soleymani Ashtiani. Finite Element Analysis of RC Rectangular Shear Walls Under Bi-Directional Loading. In *2016 NZSEE Conference*, 2016.

[50] Hiroshi Noda, Yoichi Sugishita, and Daisuke Kato. Tests of reinforced concrete cantilever walls with openings. *Transactions of the Japan Concrete Institute*, 19:311–316, 1997. ISSN 09118985.

[51] K Orakcal and JW Wallace. Flexural modeling of reinforced concrete walls - experimental verification. *ACI structural journal*, 103(2):196–206, 2006. ISSN 0889-3241.

[52] Robert Park. Evaluation of ductility of structures and structural assemblages from laboratory testing. *Bulletin of the New Zealand national society for earthquake engineering*, 22(3):155–166, 1989.

[53] Joshua S Pugh. *Numerical simulation of walls and seismic design recommendations for walled buildings*. PhD thesis, University of Washington, 2012.

[54] K. N. Shiu, J. I. Daniel, J. D. Aristizabal-Ochoa, A. E. Fiorato, and W. G. Corley. Earthquake resistant structural walls: Test of walls with and without openings. *NASA STI/Recon Technical Report N*, 82, July 1981.

[55] Christopher P Taylor. Design of Slender Reinforced Concrete Structural Walls with Openings. Thesis, Clarkson University, 1995.

[56] Christopher P Taylor, Paul A Cote, and John W Wallace. Design of Slender Reinforced Concrete Walls with Openings. *ACI Structural Journal*, 95(4), 1998. ISSN 0889-3241. doi: 10.14359/558. URL `http://www.concrete.org/Publications/ACIMaterialsJournal/ACIJournalSearch.aspx?m=details&ID=558`.

[57] TBI Guidelines Working Group. Guidelines for Performance-Based Seismic Design of Tall Buildings. Technical Report 2010/05, Pacific Earthquake Engineering Research Center, University of California (PEER), Berkeley, California, Novermber 2010.

[58] J.H. Thomsen and J.W. Wallace. *Displacement-based Design of RC Structural Walls: An Experimental Investigation of Walls with Rectangular and T-shaped Cross-sections*. Report (Clarkson University. Department of Civil and Environmental Engineering). Clarkson University, Department of Civil Engineering, 1995.

[59] John H Thomsen and John W Wallace. Displacement-based Design of Slender Reinforced Concrete Structural Walls: experimental verification. *Journal of Structural Engineering*, 2004.

[60] Thien Anh Tran. *Experimental and analytical studies of moderate aspect ratio reinforced concrete structural walls*. PhD thesis, UCLA, 2012.

[61] Jacob A. Turgeon. The seismic performance of coupled reinforced concrete walls. Master's thesis, Virginia Polytechnic Institute and State University, 2011.

[62] Jan GM Van Mier. *Fracture of concrete under complex stress*. Faculty of Civil Engineering, Delft University of Technology, 1986.

[63] Frank J Vecchio and Michael P Collins. The modified compression-field theory for reinforced concrete elements subjected to shear. *ACI J.*, 83(2):219–231, 1986.

[64] John W Wallace. New methodology for seismic design of RC shear walls. *Journal of Structural Engineering*, 120(3):863–884, 1994.

[65] John W Wallace. Seismic design of RC structural walls. Part I: new code format. *Journal of Structural Engineering*, 121(1):75–87, 1995.

[66] Travis S Welt, Leonardo M Massone, James M LaFave, Dawn E Lehman, Steven L McCabe, and Pablo Polanco. Confinement Behavior of Rectangular Reinforced Concrete Prisms Simulating Wall Boundary Elements. *Journal of Structural Engineering*, page 04016204, 2016.

[67] Travis Steven Welt. *Detailing for compression in reinforced concrete wall boundary elements: experiments, simulations, and design recommendations*. PhD thesis, University of Illinois at Urbana-Champaign, 2015.

[68] Zachary J Whitman. Investigation of Seismic Failure Modes in Flexural Concrete Walls Using Finite Element Analysis. Master's thesis, University of Washington, 2015.

[69] Mark L Wilkins. Calculation of elastic-plastic flow. Technical report, 1964.

[70] Edward L Wilson and A Habibullah. Structural Analysis Program SAP2000. *Computers and Structures Inc., California*, 2016.

[71] Hui. Wu. *Design of reinforced concrete walls with openings for strength and ductility*. Thesis, Nanyang Technological University, 2005.

[72] Fernando V. Yanez, R. Park, and T. Paulay. Seismic behaviour of walls with irregular openings. In *The 10th World Conference on Earthquake Engineering*, volume 6, pages 3303–3308, Balkema, Rotterdam, 1992.

[73] Mu-Zi Zhao, Dawn E. Lehman, and Charles W. Roeder. Modeling recommendations for RC and CFST sections in LS-Dyna including bond slip. *Engineering Structures*, 229: 111612, 2021. ISSN 0141-0296. doi: https://doi.org/10.1016/j.engstruct.2020.111612.

Appendix A

ATENA SOFTWARE PACKAGE

A.1 Model Configuration and Meshing

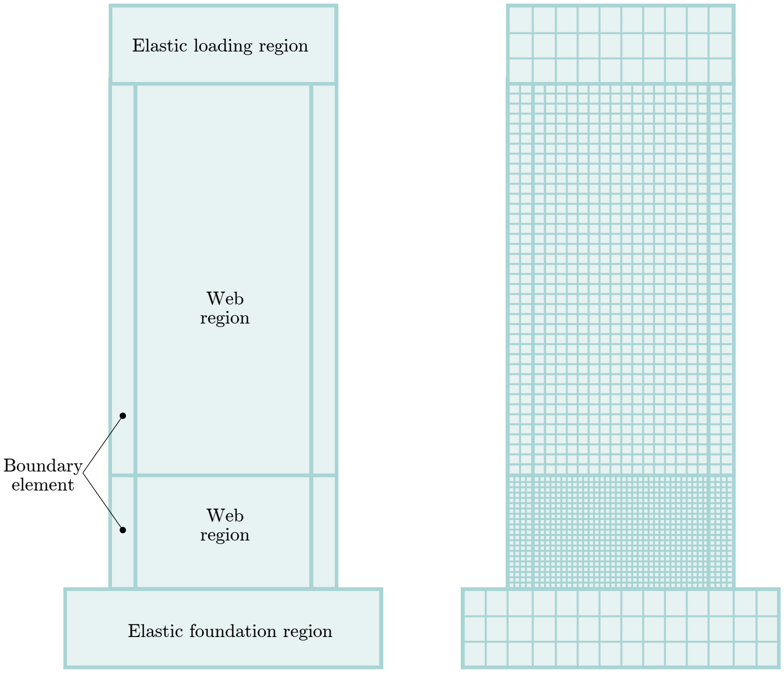

Figure A.1: Geometric layout (left) and characteristic mesh scheme (right) in ATENA model.

Figure A.1 shows the geometric layout and characteristic mesh scheme of the models used for simulation of walls. The wall models consist of different parts; confined regions (boundary elements), unconfined regions (web elements) and elastic regions (foundation and loading elements). Greater mesh refinement and nonlinear material model are used in regions where more inelastic action is expected. Size of elements used for concrete in these regions are 2 inches ($\approx 50\,\text{mm}$) and at least two elements are used over half of the thickness of the wall. For these portions 90% of the reinforcements are modeled discretely including the confinement and only 10% is smeared evenly in each region. In the web regions, the entire horizontal reinforcement is smeared. In regions where the nonlinear response is not as significant as the base of the wall, all the confining reinforcement are smeared and bigger mesh size is used. Nonlinear material models are used for all these regions. Elastic regions, are modeled using an elastic material with the same elastic modulus used for the concrete material in the rest of the wall. No reinforcement is used in these regions. Coarse element size is used in these regions ($\geq$ 4 in. (100 mm)). Due to the different mesh sizes between different sections (known as *macro elements* in ATENA) in the model and to ensure continuity between mesh elements, there exists contact surfaces as “perfect connection” between the macro elements. The contact relationships have to be defined in a way that the coarser elements’ size is the master and the finer elements’ size is the slave. This is automatically specified by the software, however, sometimes it needs manual adjustment for stability of the analysis and compatibility. For further details about the model configuration and element types refer to Appendix A.

A.2 Modeling Concrete Material Response using ATENA

In ATENA the material model formulation assumes small strains and is based on the strain decomposition into elastic, plastic and fracture components. The *Rankine criterion* is used for concrete cracking, which results in the onset of cracking when the principal tensile stress exceeds the user-defined concrete tensile strength and crack opening or widening occurring when the tensile stress normal to the crack surface exceeds the post-cracking concrete tensile strength.

There are multiple concrete constitutive models included in the ATENA software package. `CC3DNonLinCementitious2` (NC2) is the most suitable model for the current study. The NC2 model uses continuum damage mechanics along with fixed or rotating cracks to simulate response in tension, plasticity theory with softening and hardening to simulate behavior in compression and the strain decomposition method as proposed by De Borst [24] to merge tensile and compressive response. It is suitable for concrete that is subjected to three-dimensional stress states and this model can produce the mesh-objective results through material regularization. Figure 2.11 shows the uniaxial stress-strain law for concrete used in ATENA.

Concrete constitutive model in ATENA [19] uses a *Fracture-Plastic* constitutive model that combines constitutive models for compressive (plastic) and tensile (fracturing) responses. One of the advantages of using this model is that it can handle physical changes such as crack closure of concrete and can be used for any shape of hardening or softening laws. Furthermore, plastic and fracture models can be combined using a different algorithm or model as well. Additionally, the two models can be formulated separately as well. The proposed method by De Borst [24] is used in ATENA to combine the plasticity and fracture models. Return mapping approach developed by Wilkins [69] are the base of both models [19]. The strain decomposition proposed by De Borst [24] is

$$\varepsilon = \varepsilon_e + \varepsilon_p + \varepsilon_f \tag{A.1}$$

where ε_e, ε_p and ε_f are the elastic, plastic and fracture strains. And the new stress state (σ_n) is calculated as

$$\sigma_n = \sigma_{n-1} + \mathbf{E}\left(\Delta\varepsilon - \Delta\varepsilon_p - \Delta\varepsilon_f\right) \tag{A.2}$$

where $\mathbf{E}$ is elasticity tensor and $\Delta\varepsilon_p$ and $\Delta\varepsilon_f$ are increments of plastic and fracturing strain, respectively and are based on the material model employed.

In the plasticity model for concrete crushing, nonlinear compressive response is defined using plasticity theory and the assumption of non-associated flow rule. The failure surface developed by Menetrey and Willam [47] is used in ATENA and defined as

$$F^p = \left[\sqrt{1.5}\frac{\rho}{f_c'}\right] + m\left[\frac{\rho}{\sqrt{6}f_c'}r(\theta, e) + \frac{\xi}{\sqrt{3}f_c'}\right] - c = 0 \tag{A.3}$$

where

$$m = 3\frac{f_c'^2 - f_t'^2}{f_c' f_t'}\frac{e}{e+1}, \qquad r(\theta, e) = \frac{4(1-e^2)\cos^2\theta + (2e-1)^2}{(1-e^2)\cos\theta + (2e-1)\sqrt{4(1-e^2)\cos^2\theta + 5e^2 - 4e}}$$

and (ξ, ρ, θ) are Heigh-Vestergaard coordinates, $e \in \langle 0.5, 1.0 \rangle$ is a parameter that defines the smoothness of the failure surface. If $e = 0.5$, the failure surface has sharp corner and if $e = 1.0$ it is completely circular around the hydrostatic axis. f'_c and f'_t are compressive and tensile strengths, respectively.

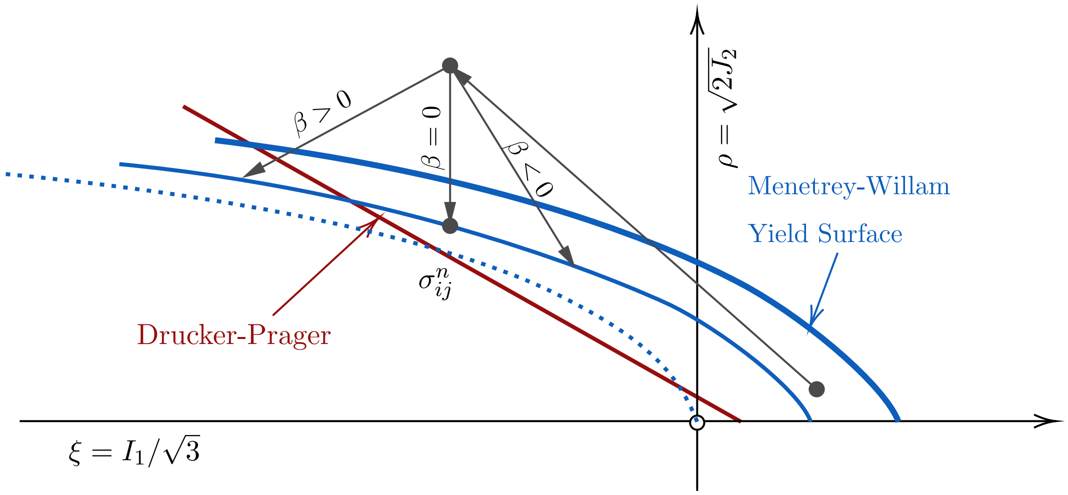

Figure A.2: Direction of the yield surface and plastic strain vector.

The return mapping function for the plastic corrector is

$$\Delta\varepsilon_p = \Delta\lambda \frac{\partial G^p(\sigma_{\text{trial}})}{\partial\sigma} \tag{A.4}$$

where $G(\sigma)$ is the flow rule and its derivative at the predictor stress state σ_{trial} is the return direction and is defined by

$$G^p(\sigma) = \beta \frac{1}{\sqrt{3}} I_1 + \sqrt{2J_2} \tag{A.5}$$

As mentioned earlier, the plastic model follows a non-associated flow rule which means the plastic flow is not perpendicular to the failure surface. Instead β defines the return direction. If $\beta < 0$ it means the material is being compacted and if $\beta = 0$ there is no change in the volume and when $\beta > 0$ the material is being dilated.

Figure A.2 shows the return mapping algorithm for the model. During each predictor-corrector, to account for hardening/softening, the failure surface shifts along the hydrostatic axis. The failure surface moves based on strain hardening and strain softening parameter. According to Menetrey and Willam surface, a parameter $c \in \langle 0, 1\rangle$ controls the hardening/softening and has the following relationship

$$c = \left(\frac{f_c'(\varepsilon_p)}{f_c'}\right)^2 \tag{A.6}$$

where $f_c'(\varepsilon_p)$ indicates the hardening/softening law shown in Figure A.3. Menetry-Willam has a quadratic nature and that is why the term in Equation (A.6) is squared. The linear part represents the softening curve which based on displacement and incorporate mesh objectivity in the finite element solution. Its shape is based on the work performed by Van Mier [62]. f_{co}' is the onset of the nonlinear behavior and ε_c^p is the strain at compressive strength. L_c is a parameter representing the projection of the element size into the direction of minimal principal stresses.

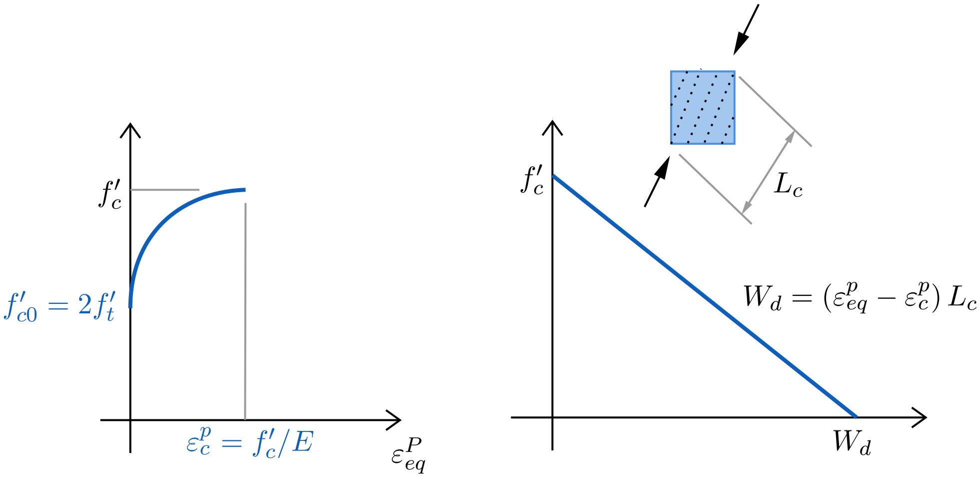

Figure A.3: Compressive Hardening/Softening and compression characteristic Length.

A.2.1 Effect of Crack Rotation Model

In ATENA there are two models to simulate the smeared cracks in concrete: *fixed crack model* and *rotated crack model*. In the fixed crack model, the direction of principal stress at the onset of cracking will be the direction of cracks. This direction is fixed and represents the axis of orthotropy of the material. In the rotated crack model, the direction of principal stress and principal strain coincide. Then the cracks rotate when the principal strain axes rotate [18]. Fixed Crack Model has been chosen for the analysis of the walls. It was found that fixing the crack model leads to a better behavior of the model in ATENA.

A.2.2 Confined Concrete

In order to account for the effect of confined concrete, the concrete crushing energy, G_{fc}, is usually increased as it leads to a more ductile behavior. In ATENA, this is represented by means of critical compressive displacement, W_d, in compression (see Figure A.4). However, in ATENA, the impact of confinement is modeled by the yield surface and flow rule and the same W_d is used for both confined and unconfined concrete.

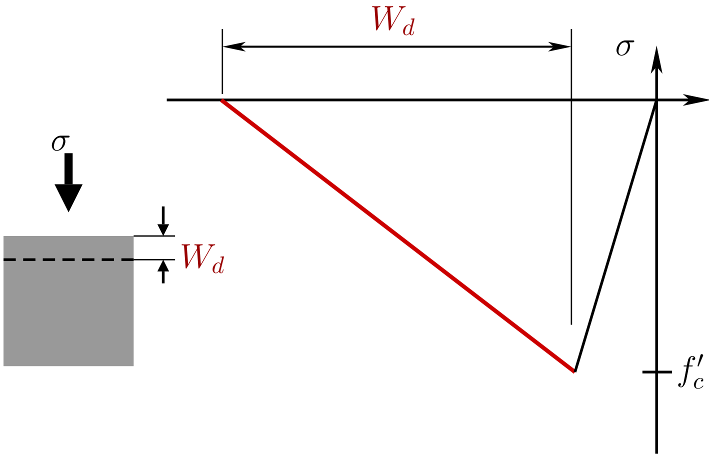

Figure A.4: Softening displacement law in compression

After concrete reached peak stress, the softening law in compression is linearly decreasing. This strain softening of concrete in compression can be represented by two models. One of them is based on dissipated energy, and the other based on local strain softening. The end point of the softening curve is defined by means of the plastic displacement W_d. ATENA

User's Manual [19] recommends to use a magnitude of 0.0196 inches (0.5 mm) for W_d which is based on the experiments performed by Van Mier [62]. But Whitman [68] found that a magnitude of 0.0425 inches (1.081 mm) works best.

A.2.3 Tension Stiffening

In reinforced concrete members, tensile stress is transferred from concrete to steel between cracks, with the result that steel tensile stress drops slightly between cracks and concrete tensile stress is non-zeor between fully formed cracks (i.e. cracks that are open to the point that concrete carries zero tensile stress. This phenomenon can be simulated by assigning a residual tensile strength to the concrete (see Figure A.5). Whitman [68] found that for fine meshes, such as used here, assigning a residual tensile strength factor of zero ($C_{ts} = 0$) provided more accurate results and increased numerical stability. Thus, in the majority of the simulations in this study, this factor is taken as zero, meaning there is no residual strength in the concrete in tension.

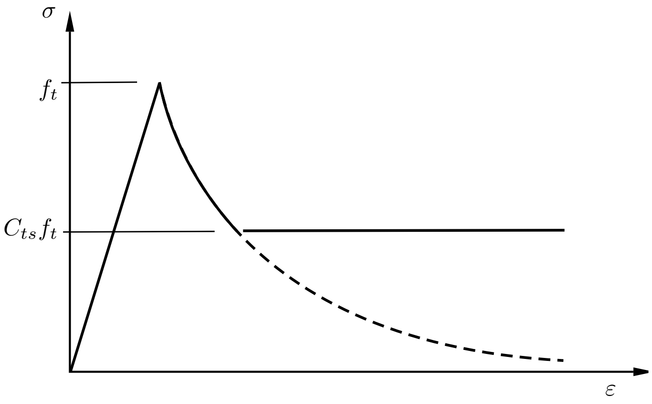

Figure A.5: Tension stiffening

A.2.4 Shear Factor (S_F) and Aggregate Interlock (MCF)

Another parameter in the concrete model definition which sometimes has a high impact on the behavior and mode of failure is the *shear factor* (S_F). Shear strength of a cracked concrete in ATENA is found using the Modified Compression Field Theory of Vecchio and Collins [63] [17, 18].

$$\sigma \leq \frac{0.18\sqrt{f_c'}}{0.31 + \dfrac{24w}{a_g + 16}} \tag{A.7}$$

Where f_c' is the compressive strength in MPa, a_g is the maximum aggregate size in mm and w is the maximum crack width in mm at the given location. This model is activated in the program if the aggregate size or aggregate interlock is specified. If not, the shear stress on a crack surface cannot exceed the tensile strength of concrete. The crack stiffness equals

$$E_{iiii}'^{cr} = \frac{f_t'\left(w_i^{max}\right)}{\hat{\varepsilon}_{ii}'^{f}}, \text{(no summation of indices)} \tag{A.8}$$

and

$$E_{ijij}'^{cr} = S_F \min\left(E_{iiii}'^{cr}, E_{jjjj}'^{cr}\right), \text{(no summation of indices)} \tag{A.9}$$

where $i \neq j$, and S_F is a shear factor coefficient that defines a relationship between the normal and shear crack stiffness. The default value of S_F is 20 but according to the parameter study conducted by Whitman [68], it was found that the value of S_F is best to be between $50 - 200$.

A.3 Model for Steel Reinforcement in ATENA

In ATENA reinforcement can be modeled in both discrete and smeared forms. Truss elements are used for discrete models while the smeared reinforcement is defined as a component of the composite material. In the current study both techniques are used for defining steel models. Generally, about 10% of the reinforcement in each region is smeared to avoid numerical instability during analysis. Only in the web region the horizontal reinforcement is smeared totally as it does not have a big impact on the simulation but reduces the computational time of the program.

A material model based on the work of Menegotto and Pinto [46] is provided by ATENA for modeling reinforcing steel. This model in ATENA is extended to account for isotropic hardening too by an arbitrary hardening law which can be selected for reinforcement. The stress in the cyclic model is computed using the formula:

$$\sigma = (\sigma_0 - \sigma_r)\,\sigma^* + \sigma_r$$

where

$$\sigma^* = b\varepsilon^* + \frac{(1-b)\varepsilon^*}{\left(1+\varepsilon^{*R}\right)^{1/R}}, \qquad \varepsilon^* = \frac{\varepsilon - \varepsilon_r}{\varepsilon_0 - \varepsilon_r}, \qquad R = R_0 - \frac{c_1\xi}{c_2+\xi}$$

where R_0, c_1 and c_2 are parameters which determined experimentally. The values of ε_0 (strain in the first cycle), ε_r (residual strain) and ξ (strain between two successive cycles) change for each cycle (see Figure A.6). All values with the subscript r specifies the point at which the cycle started, and the subscript 0 shows the theoretical yield point that will be reached during the unloading if the response would not have been modified by the hysteretic behavior.

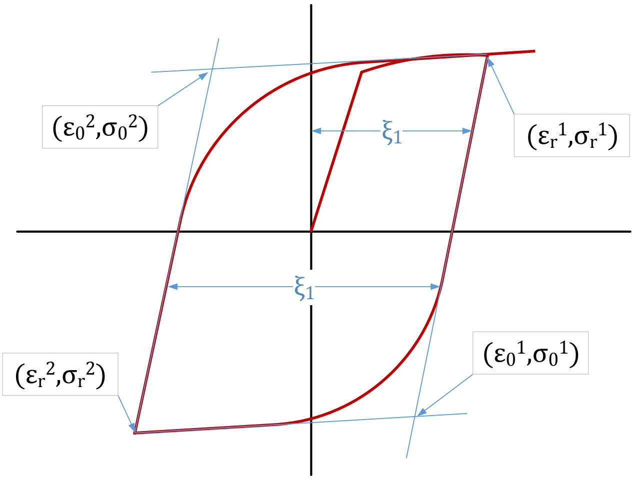

Figure A.6: Cyclic reinforcement model based on Menegotto and Pinto.

Table A.1 shows values of parameters used in the ATENA analyses. These values are suggested by Cervenka Consulting [19], Pugh [53] and calibrated by Lowes et al. [40], Whitman [68] for use in the ATENA models. For a study of the parameters refer to Lowes et al. [40], Whitman [68].

$$f'_t = 1.26 f'^{2/3}_{cu}\,(\text{psi}) \quad \left(0.24 f'^{2/3}_{cu}\,(\text{MPa})\right) \tag{A.10}$$

$$E_c = 57000\sqrt{f'_c\,(\text{psi})} \quad \left(4700\sqrt{f'_c\,(\text{MPa})}\right) \tag{A.11}$$

$$G_f = 0.000143 f'_t\,(\text{psi}) \quad \left(0.000025 f'_t\,(\text{MPa})\right) \tag{A.12}$$

Table A.1: List of concrete parameters used in ATENA analysis

Concrete Parameter	**Symbol**	**Description**	**Value**[1)]
Compressive strength	f'_c	Determines the peak compressive strength of concrete	Determined by experimental testing of 6 in. × 12 in. cylinders
Tensile strength	f'_t	Determines the peak tensile strength of concrete	Computed per recommendations of CEB-FIP (1990), (Equation (A.10))
Elastic modulus	E_c	Determines elastic modulus of concrete	Calculated according to ACI 318-14 [3], (Equation (A.11))
Fracture energy	G_f	Determines the fracture energy of concrete; enables material regularization in tension	Computed per the recommendations of Vos (1983), (Equation (A.12))
Plastic deformation	W_d	Determines the plastic deformation capacity of concrete at zero compressive stress; enables material regularization in compression	Range of potential values ($W_d = 0.025$ in. to 0.125 in. (0.635 mm to 3.175 mm))
Dilation parameter	β	Determines the extent to which concrete dilates under inelastic compression loading	$\beta = 0$ to 0.7
Shear retention factor	S_F	Determines the shear stiffness of cracked concrete	Range of potential values ($S_F = 20$ to 200)
Residual tensile strength factor	C_{ts}	Determines the residual tensile strength of concrete	Range of potential values ($C_{ts} = 0.00$ to 0.05)

[1)] Based on suggestions by Cervenka Consulting [19] and Pugh [53] and calibrations made by Whitman [68]. Details of the calibration study can be found in the thesis by Whitman [68].

Appendix B

NON-PLANAR WALL DATA AND RESULTS

This appendix complements the parameter study for non-planar walls and provides more inputs, response quantities, and load-displacement figures for all specimens simulated in this study. Additionally, some stress fields are provided for a selected number of specimens.

Table B.1: List of results for simulated T–shaped models .

Specimen	**Shear span**	**CSAR**	**ALR**	$\mathbf{V_{max}/A_{cv}\sqrt{f'_c}}$	**Drift**	**Ductility**	**Failure mode**
		–	%	MPa (psi)	%	–	
T03–L15–C11–S43–A00	4.33	15.00	0.0	0.33 (3.93)	8.2	8.80	CB
T04–L15–C07–S43–A05	4.33	15.00	5.0	0.36 (4.32)	6.6	8.62	CB
T05–L15–C05–S43–A10	4.33	15.00	10.0	0.43 (5.18)	6.2	8.01	CB
T06–L15–C04–S43–A20	4.33	15.00	20.0	0.55 (6.62)	1.5	1.86	CS
T05–L15–C02–S43–A15	4.33	15.00	15.0	0.48 (5.83)	2	2.59	CS
T06–L15–C02–S43–A20	4.33	15.00	20.0	0.53 (6.38)	2.1	2.83	CS
T05–L15–C11–S35–A00	3.47	15.00	0.0	0.38 (4.59)	5.1	7.27	CB
T06–L15–C07–S35–A05	3.47	15.00	5.0	0.46 (5.54)	3.9	6.14	CB
T07–L15–C04–S35–A15	3.47	15.00	15.0	0.62 (7.50)	2.7	4.47	CS
T08–L15–C04–S35–A20	3.47	15.00	20.0	0.70 (8.40)	1.7	2.92	CS
T08–L15–C05–S27–A10	2.67	15.00	10.0	0.69 (8.33)	1.9	3.59	CS
T10–L15–C04–S27–A15	2.67	15.00	15.0	0.80 (9.58)	1.7	3.60	CS
T11–L15–C04–S27–A20	2.67	15.00	20.0	0.89 (10.71)	1.1	2.42	CS
T14–L10–C07–S12–A12	1.20	10.00	12.0	1.13 (13.61)	1.1	4.06	CS
T15–L10–C06–S12–A18	1.20	10.00	18.0	1.27 (15.26)	0.7	3.83	CS
T09–L10–C05–S12–A00	1.20	10.00	0.0	0.75 (8.99)	1.9	5.52	CS
T11–L10–C04–S12–A06	1.20	10.00	6.0	0.94 (11.37)	1	4.18	CS
T08–L10–C05–S15–A00	1.50	10.00	0.0	0.63 (7.53)	1	5.48	CS
T09–L10–C04–S15–A06	1.50	10.00	6.0	0.78 (9.40)	0.9	4.97	CS
T11–L10–C03–S15–A12	1.50	10.00	12.0	0.93 (11.18)	0.9	3.70	CS
T13–L10–C02–S15–A18	1.50	10.00	18.0	1.06 (12.78)	0.5	2.45	CS

Table B.1: (continued)

Specimen	**Shear span**	**CSAR**	**ALR**	**$V_{max}/A_{cv}\sqrt{f'_c}$**	**Drift**	**Ductility**	**Failure mode**
		–	%	MPa (psi)	%	–	
T05–L10–C05–S24–A00	2.40	10.00	0.0	0.42 (5.09)	3.2	11.50	CB
T06–L10–C04–S24–A06	2.40	10.00	6.0	0.49 (5.95)	1.7	6.75	CB
T07–L10–C03–S24–A12	2.40	10.00	12.0	0.59 (7.09)	1	4.04	CS
T08–L10–C02–S24–A18	2.40	10.00	18.0	0.67 (8.07)	0.9	3.01	CS
T04–L09–C12–S58–A00	5.78	9.00	0.0	0.35 (4.22)	9.1	7.57	CB
T05–L09–C08–S58–A05	5.78	9.00	5.0	0.40 (4.76)	7.2	6.43	CB
T05–L09–C07–S58–A10	5.78	9.00	10.0	0.45 (5.41)	5.6	5.29	CB
T06–L09–C06–S58–A15	5.78	9.00	15.0	0.50 (6.02)	4.4	4.44	CB
T07–L09–C05–S58–A20	5.78	9.00	20.0	0.54 (6.54)	3.2	3.53	CB
T04–L11–C12–S47–A00	4.72	11.00	0.0	0.36 (4.36)	7.2	7.47	CB
T06–L11–C08–S47–A05	4.72	11.00	5.0	0.42 (5.06)	6.4	7.26	CB
T06–L11–C07–S47–A10	4.72	11.00	10.0	0.49 (5.85)	6.1	7.01	CB
T07–L11–C06–S47–A15	4.72	11.00	15.0	0.55 (6.60)	4.8	5.86	CB
T07–L11–C05–S47–A20	4.72	11.00	20.0	0.60 (7.28)	3.4	4.42	CS
T05–L20–C11–S24–A00	2.37	20.00	0.0	0.40 (4.85)	3.2	6.14	CB
T06–L20–C07–S24–A05	2.37	20.00	5.0	0.50 (5.99)	2.4	4.99	CS
T07–L20–C05–S24–A10	2.37	20.00	10.0	0.60 (7.20)	1.8	3.96	CS
T08–L20–C06–S26–A15	2.60	20.00	15.0	0.70 (8.39)	1.7	3.75	CS
T09–L20–C05–S26–A20	2.60	20.00	20.0	0.79 (9.46)	1.3	3.04	CS

B.1 Lateral Load-Displacement Response

Figures B.1 to B.3 present load-displacement relationship for the simulated specimens shown in Chapter 5.

Table B.2: List of results for simulated Semi–I–shaped models

Specimen	**Shear span**	**CSAR**	**ALR**	$\mathbf{V_{max}/A_{cv}\sqrt{f'_c}}$	**Drift**	**Ductility**	**Failure mode**
		–	%	MPa (psi)	%	–	
SI06–L04–C19–B33–S26–A00	2.60	3.75	0.0	0.53 (6.36)	4.8	7.45	CB
SI07–L15–C15–B33–S26–A03	2.60	15.00	3.0	0.59 (7.09)	4	7.03	CB
SI08–L15–C09–B33–S26–A06	2.60	15.00	6.0	0.65 (7.81)	2.5	4.76	CB
SI09–L15–C05–B33–S26–A10	2.60	15.00	10.0	0.72 (8.65)	2.5	4.55	CB
SI10–L15–C03–B33–S26–A15	2.60	15.00	15.0	0.82 (9.90)	1.7	3.13	CS
SI11–L15–C02–B33–S26–A20	2.60	15.00	20.0	0.92 (11.05)	1.2	2.30	CS
SI05–L04–C19–B33–S35–A00	3.47	3.75	0.0	0.46 (5.49)	5.4	4.41	CB
SI07–L15–C15–B33–S35–A03	3.47	15.00	3.0	0.56 (6.75)	6.9	4.68	CB
SI07–L15–C09–B33–S35–A06	3.47	15.00	6.0	0.56 (6.75)	5.6	7.03	CB
SI06–L02–C00–B33–S35–A08	3.47	15.00	8.0	0.53 (6.44)	1.2	2.27	CS
SI11–L07–C14–B53–S15–A00	1.50	2.22	0.0	0.94 (11.31)	1.2	4.67	CB
SI14–L07–C20–B53–S15–A06	1.50	6.67	6.0	1.13 (13.58)	1.3	3.90	CB
SI16–L07–C15–B53–S15–A12	1.50	6.67	12.0	1.32 (15.95)	1.2	2.89	CS
SI17–L07–C12–B53–S15–A18	1.50	6.67	18.0	1.44 (17.40)	0.8	1.87	CS

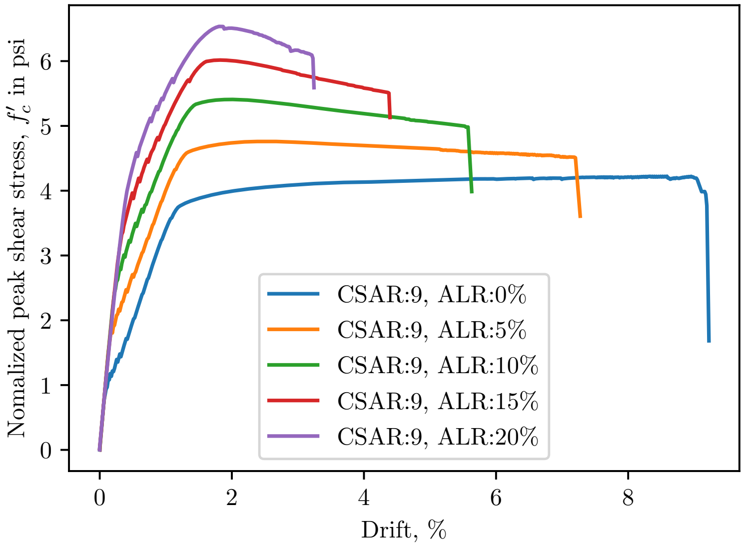

Figure B.1: Load-deformation relationship for specimens with $\ell_w/t_w = 9$ (shear-span = 5.78).

Table B.3: List of results for simulated I–shaped models

Specimen	**Shear span**	**CSAR**	**ALR**	$\mathbf{V_{max}/A_{cv}\sqrt{f'_c}}$	**Drift**	**Ductility**	**Failure mode**
		–	%	MPa (psi)	%	–	
I12–L01–C37–S18–A00	1.80	1.18	0.0	0.95 (11.43)	1.21	3.31	CB
I15–L01–C25–S18–A06	1.80	1.18	6.0	1.20 (14.48)	0.99	2.71	CS
I17–L01–C20–S18–A12	1.80	1.18	12.0	1.43 (17.20)	0.77	2.11	CS
I09–L01–C37–S18–A00	1.80	1.18	0.0	0.73 (8.77)	0.69	5.04	CB
I11–L01–C25–S18–A06	1.80	1.18	6.0	0.92 (11.12)	1.00	6.70	CB
I13–L01–C20–S18–A12	1.80	1.18	12.0	1.10 (13.28)	0.44	3.55	CS
I07–L01–C25–S26–A00	2.60	1.25	0.0	0.56 (6.76)	6.16	9.64	CB
I08–L15–C19–S26–A05	2.60	15.00	5.0	0.67 (8.04)	5.89	10.63	CB
I09–L15–C15–S26–A10	2.60	15.00	10.0	0.79 (9.47)	5.06	9.91	CB
I11–L15–C07–S26–A15	2.60	15.00	15.0	0.92 (11.03)	2.17	4.45	CB
I12–L15–C03–S26–A20	2.60	15.00	20.0	1.04 (12.49)	1.32	2.82	CS
I05–L15–C25–S35–A00	3.46	1.25	0.0	0.00 (0.00)	0.00	0.00	CB
I06–L15–C19–S35–A05	3.46	15.00	5.0	0.51 (6.10)	6.30	11.94	CB
I07–L15–C15–S35–A10	3.47	15.00	10.0	0.60 (7.21)	6.03	13.01	CB
I08–L15–C07–S35–A15	3.46	15.00	15.0	0.70 (8.46)	4.57	10.59	CB
I10–L15–C03–S35–A20	3.47	15.00	20.0	0.80 (9.69)	2.75	6.90	CB

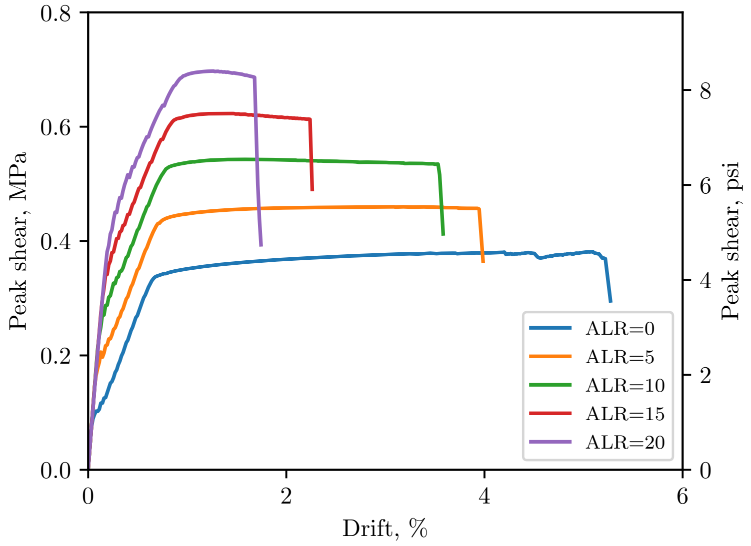

Figure B.2: Load-deformation relationship for T–shaped specimens with $\ell_w/t_w = 15$ (shear-span = 4.33).

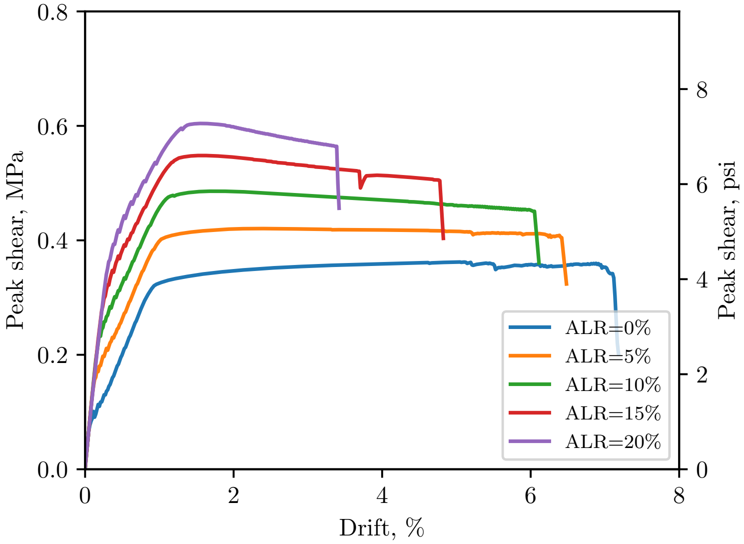

Figure B.3: Load-deformation relationship for T–shaped specimens with $\ell_w/t_w = 20$ (shear-span = 4.72).

B.2 Computed Response Quantities

Figures B.4 to B.7 present the computed response quantities for the simulated specimens. This set includes additional measures for deformation capacity and complements the set of plots provided in Chapter 5.

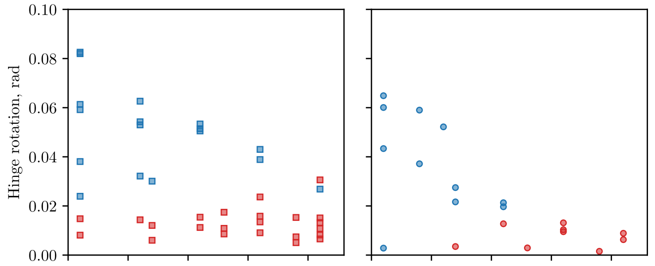

(a) T-shape **(b)** Semi-I-shape

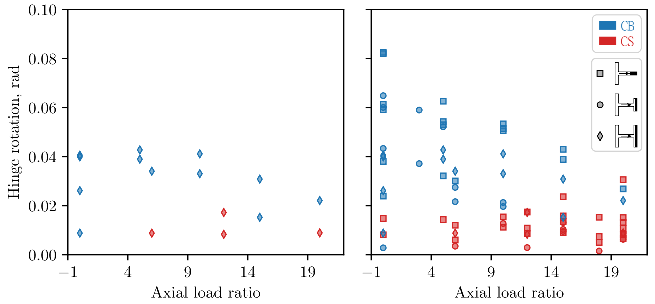

(c) I-shape **(d)** All shapes

Figure B.4: Relationship between peak shear stress and drift for T–, Semi–I–, and I–shaped walls.

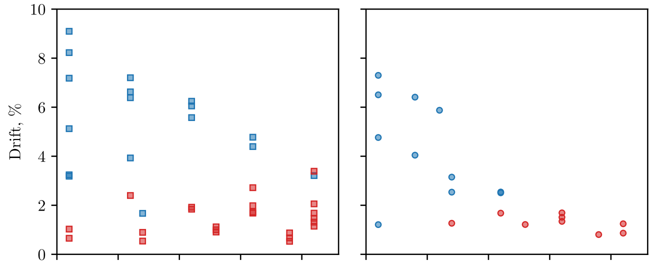

(a) T-shape **(b)** Semi-I-shape

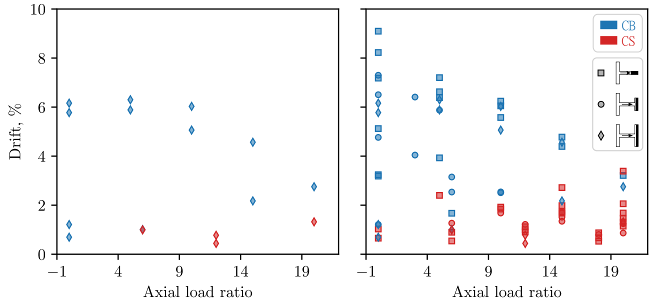

(c) I-shape **(d)** All shapes

Figure B.5: Relationship between peak shear stress and drift for T–, Semi–I–, and I–shaped walls.

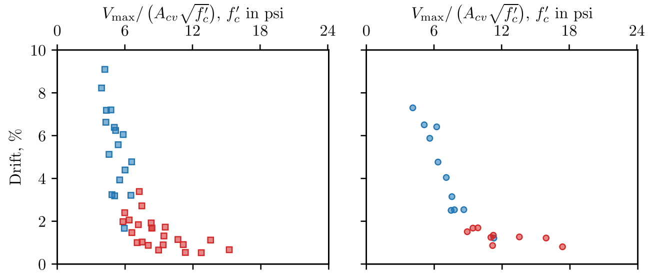

(a) T-shape **(b)** Semi-I-shape

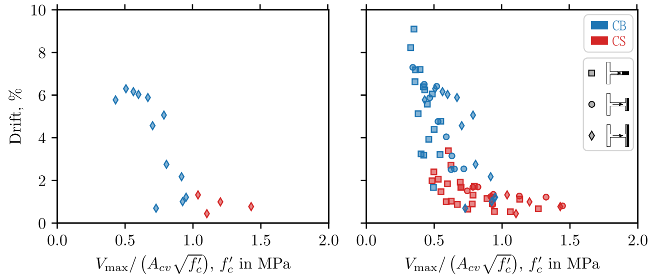

(c) I-shape **(d)** All shapes

Figure B.6: Relationship between peak shear stress and drift for T–, Semi–I–, and I–shaped walls.

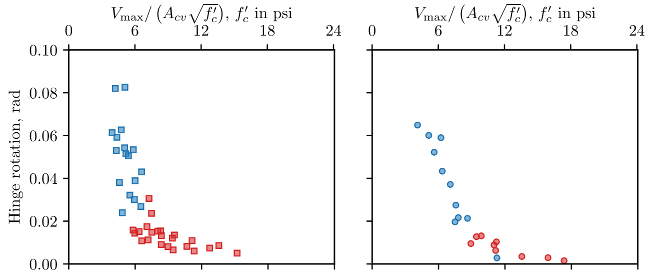

(a) T-shape **(b)** Semi-I-shape

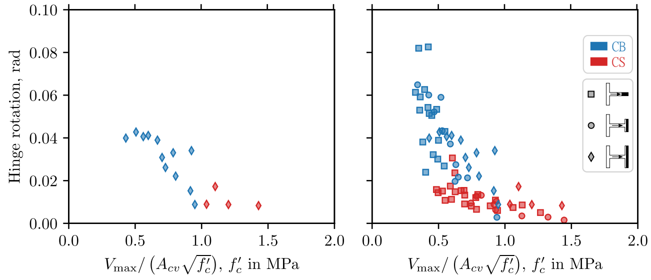

(c) I-shape **(d)** All shapes

Figure B.7: Relationship between peak shear stress and hinge rotation for T–, Semi–I–, and I–shaped walls.

Appendix C

WALLS WITH OPENINGS DATA AND RESULTS

This appendix details the design of the walls with stiffness irregularities, and it complements the parameter study for walls with openings and provides more inputs, response quantities, and load-deformation figures for all specimens simulated in this study. Additionally, some stress fields are provided for a selected number of specimens.

C.1 Wall Design and Building Prototype

The summary of the parameters used in the design and analysis for the 8-story building prototype is shown in Table C.1

The wall designed represents a structural RC wall as part of an 8-story building. The prototype of the building is shown in Figure C.1 and as it can be observed, two walls are used in each direction to resist lateral pressure. ASCE 7–16 code [8] is used to design the shear walls with the following assumptions:

- Seismic Design Category: **D (with maximum spectral acceleration)**
- Site Class: **C- Very dense soil and soft rock**
- Risk Category: **II**
- 8-story building:
    - 120 ft × 120 ft (1, 2, 4 story buildings are 120 ft (36.58 m) by 180 ft (54.86 m); 8, 12, 20 story building are 120 ft by 120 ft)
    - two planar walls in each direction

Table C.1: Summary of the parameters used in the design and analysis (8-story building)

8-story, Special Concrete Wall		**8-D-0-0-ELF**
DESIGN PARAMETERS		
Dead Load	Typical = 175 psf	Roof = 140 psf
Live Load	Typical = 65 psf	Roof = 20 psf
Seismic Weight	Typical = 190 psf	Roof = 147.5 psf
Total building seismic weight, $W = 21276$ kips		
Wind Speed	110 mph (strength)	85 mph (service)
Risk Category II	Importance Factor, $I_e = 1.0$	
Special Concrete Walls		
$R = 6$	$C_d = 5$	
Site Class C	$S_{DS} = 1.5$	$S_{D1} = 0.6$
Seismic Design Category D		
Material properties	$f'_{c,\text{beam}} = 5$ ksi	$f_y = 60$ ksi
ANALYSIS		
Centerline modeling of beams and columns		
Rigid diaphragms	$I_{\text{wall}} = 0.5 I_g$	
Design based on Equivalent Lateral Force Procedure		
Calculated period	$T_x = 1.14$ sec	
Upper limit period	$C_u T_{ax} = 0.925$ sec	
Seismic response coefficient	$C_{s,x} = 0.108$	
controlling equation	(12.8-3)	
Seismic base shear (two walls)	$V_x = 2300$ kips $= 0.108W$	
Drift limits applied	$0.020 h_{sx}$ (seismic)	$h/400$ (wind)
Controlling lateral design	Seismic Strength	Seismic Strength
Design base shear (including accidental torsion) (two walls)	$V = 2358$ kips $= 0.11W$	

- center of stiffness and mass coincide (no eccentricity)
- dead load (materials + mechanical) = 175 psf (floors)

$= 140$ psf (roof)

- live load (area load + partitions) $= 50$ psf $+ 15$ psf (partitions) $= 65$ psf (floors)

  $= 20$ psf $+ 0$ psf (partitions) $= 20$ psf (roof)

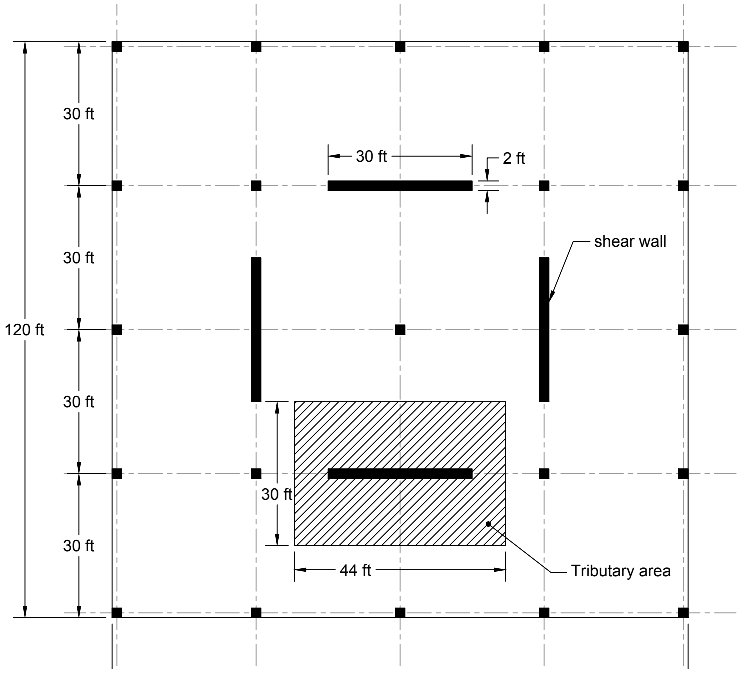

Figure C.1: Building prototype (8-story building)

C.1.1 Design spectrum parameters

$S_s = 1.5g$ FEMA P965 - $1.5g$ is max for Seismic Design Category D

$S_1 = 0.6g$ FEMA P965 - $0.6g$ is max for Seismic Design Category D

$F_a = 1.2$ ASCE 7–16, Table 11.4-1, Site Class C

$F_v = 1.4$ ASCE 7–16, Table 11.4-2, Site Class C

$$S_{DS} = 1.5g \quad \Rightarrow \quad S_{D1} = 0.6g$$

$$T_0 = 0.2\frac{S_{D1}}{S_{DS}} = 0.08\,s$$

$$T_s = \frac{S_{D1}}{S_{DS}} = 0.4\,s$$

$$T_L = 8\,s$$

C.1.2 Calculation of seismic weight

Seismic weight = dead + partitions

$= 175 + 15 = 190\,\text{psf}$ (floors)

$= 140 + 7.5 = 147.5\,\text{psf}$ (roof) (Note that this does not meet requirements of 12.7.2, which requires 10 psf minimum for partitions)

Table C.2: Determination of seismic weight for each story

Level	DL (psf)	Area (ft^2)	W_i (k)
Roof	147.5	14400	2124
Level 8	190	14400	2736
Level 7	190	14400	2736
Level 6	190	14400	2736
Level 5	190	14400	2736
Level 4	190	14400	2736
Level 3	190	14400	2736
Level 2	190	14400	2736
		Sum	21276

W = 21276 kip = total building seismic weight

C.1.3 Calculation of seismic loads

$R = 6$ B4, Table 12.2-1 Special reinforced concrete shear walls

$I_e = 1$ Table 1.5-2 Risk Category I/II

$C_d = 5$ Table 12.2-1 Special RC shear Walls

$C_u = 1.4$ Table 12.8-1 > 0.4

Using Modal Response Spectrum Analysis (MRSA), the period is found in SAP2000 [70]. Per SAP2000 the period is found to be: $T_{\text{MRSA}} = 1.14018$ s

Using Table 12.8-2 for the case (All other Structural Systems) it is found that $C_t = 0.02$ and $x = 0.75$ Height of each story is 13 ft (3.96 m) except for the first story which is 15 ft (4.57 m) high. Therefore, for the 8-story building:

$$h_n = (8-1) \times 13 + 15 = 106\,\text{ft.}$$

$$T_a = C_t h_n^x = 0.661\,\text{s} < T_L = 8\,\text{s}$$

$$T_{\text{MRSA}} > C_u T_a \quad \rightarrow \quad T = C_u T_a$$

$$C_s = \frac{S_{DS}}{\frac{R}{I_e} g} = 0.25 > \frac{S_{D1}}{T \frac{R}{I_e} g} = 0.108$$

$$\text{use } C_s = 0.108 \quad ([12.8\text{-}5]\ C_s > C_{s,min} = 0.044 S_{DS} I_e = 0.066 \ \ \text{OK})$$

$$\Rightarrow \quad V = C_s W = 2300.131\,\text{kips}$$

Table C.3: Calculation of equivalent loads for each story

Level	h_x (ft)	w_x	$w_x h_x$	C_{vx}	eq. load $F = C_{vx} \times V$ (kip)	Story Shear (kip)	Story Moment (kip-ft)
Roof	106	2124	225144	0.1788	411.2		
Level 8	93	2736	254448	0.2020	464.7	411.2	5345.8
Level 7	80	2736	218880	0.1738	399.8	875.9	16733.1
Level 6	67	2736	183312	0.1456	334.8	1275.7	33317.4
Level 5	54	2736	147744	0.1173	269.8	1610.5	54254.2
Level 4	41	2736	112176	0.0891	204.9	1880.4	78699.0
Level 3	28	2736	76608	0.0608	139.9	2085.3	105807.3
Level 2	15	2736	41040	0.0326	75.0	2225.2	134734.6
Base		21276	1259352	1	2300.1	2300.1	164636.3

C.1.4 Addition of shear due to accidental torsion

It is assumed there is no eccentricity, therefore, the stiffness and mass are coincident. Also, it is assumed that the walls are located in interior.

The arm $= 0.05 \times 0.5 \times L = 3$ ft.

Then the torsion can be calculated as $T = V \times 0.05L = 6F_x$

Total Stiffness $= K_t = 4\left(\frac{L}{4}\right)^2 = 3600 \text{ ft}^2$

$F_{xi} = \frac{L/4}{K_t} \times \text{arm} = 0.025$, $F_{yi} = F_{xi}$. Using these equations, shear and moment demands are calculated in Table C.4. Note that two walls are assumed in each direction (see Figure C.1).

Table C.4: Determination of shear and moment demand at each story for a single wall

Level	h_x (ft)	w_x	$w_x h_x$	C_{vx}	$F = C_{vx}V$	F/2	F/2×0.025	Story Load (kips)	Story Shear (kips)	Story Moment (kip-ft)	Story Moment (kip-in)
Roof	106	2124	225144	0.1788	411	206	5	211			
Level 8	93	2736	254448	0.2020	465	232	6	238	211	2740	32876
Level 7	80	2736	218880	0.1738	400	200	5	205	449	8576	102908
Level 6	67	2736	183312	0.1456	335	167	4	172	654	17075	204902
Level 5	54	2736	147744	0.1173	270	135	3	138	825	27805	333663
Level 4	41	2736	112176	0.0891	205	102	3	105	964	40333	483999
Level 3	28	2736	76608	0.0608	140	70	2	72	1069	54226	650715
Level 2	15	2736	41040	0.0326	75	37	1	38	1140	69051	828618
Base			1259352	1	2300	1150	1179	1179	1179	86734	1040805

Based on the calculations in Table C.4 the total moment at the base is 86734 kip-ft with a shear force of 1179 kips. Consequently, the effective height can be calculated:

$$\text{effective height} = h_{\text{eff}} = \frac{\text{Moment} = 86734}{\text{Shear} = 1179} = 73.57\,\text{ft}.$$

C.1.5 Determination of vertical loads used for design

According to section 12.4 load cases 5 and 7 are applied.

Load Case 5: $(1.2 + 0.2S_{DS})D + \rho E + 0.5L$ - Note that $0.5L$ allowed as live load is less than 100 psf

Load Case 7: $(1.2 + 0.2S_{DS})D + \rho E$

Per section 12.4.3.2 and as there is not any vertical irregularity in the building, the value of ρ is taken as 1.

Dead Load = 175 psf (floors)
= 140 psf (roof)
Live Load = 50 psf + 15 psf (partitions) = 65 psf (floors)
= 20 psf + 0 psf (partitions) = 20 psf (roof)

Based on the tributary area shown in Figure C.1 and the given loads, the vertical loads in each floor are calculated in Table C.5.

Table C.5: Vertical loads on each story

Level	Dead Load (psf)	Live Load (psf)	LC5 (lbs)	LC7 (lbs)	Story Load LC5 (kips)	Story Load LC7 (kips)	Wall Axial Load LC5 (kips)	Wall Axial Load LC7 (kips)
Roof	140	20	220	94	290.4	124.08		
Level 8	175	75	300	142.5	396	188.1	290.4	124.08
Level 7	175	75	300	142.5	396	188.1	686.4	312.18
Level 6	175	75	300	142.5	396	188.1	1082.4	500.28
Level 5	175	75	300	142.5	396	188.1	1478.4	688.38
Level 4	175	75	300	142.5	396	188.1	1874.4	876.48
Level 3	175	75	300	142.5	396	188.1	2270.4	1064.58
Level 2	175	75	300	142.5	396	188.1	2666.4	1252.68
Base					3062.4	1440.78	3062.4	1440.78

where: LC5 = $(1.2 + 0.2S_{DS})D + 0.5L$ and LC7 = $(0.9 - 0.2S_{DS})D$

C.1.6 Wall design

The demands on each floor are calculated as explained in the previous sections and are summarized in the table below. All the walls are designed according to *ACI 318–14* code [3]. The longitudinal reinforcements are designed such that the wall is a tension-controlled design. The design is based on the following:

Specified concrete compressive strength, $f'_c = 5000$ psi

Yield strength of steel bars, $f_y = 60$ ksi

Length of the wall, $L_{\text{wall}} = 30$ ft

Thickness of the wall, $t_{\text{wall}} = 2$ ft

The total axial load in the base floor is 1441 kips; therefore, the axial load ratio is

$$ALR = \frac{1441}{L_{\text{wall}} t_{\text{wall}} f'_c} = 3.34\%$$

Table C.6 shows the demands and designed capacities for each floor for the reference wall. The load case $(0.9 - 0.2S_{DS})D + 1.0E$ governs the design.

Table C.6: Demands and capacities on each floor.

Level	Story Shear (kips)	Axial Load (kips)	Story Moment (kip-ft)	ϕM_n (kip-ft)
Roof				
Level 8	211	124	2740	23492
Level 7	449	312	8576	23492
Level 6	654	500	17075	23492
Level 5	825	688	27805	57511
Level 4	964	876	40333	57511
Level 3	1069	1065	54226	57511
Level 2	1140	1253	69051	89164
Base	1179	1441	86734	89168

C.1.7 Design of Longitudinal Reinforcement (Flexural Design)

The model shown in Figure C.2 is used for designing the structural walls with boundary elements. The nominal moment capacity, M_n, is calculated when the strain in extreme concrete fiber in compression reaches a magnitude of 0.003. However, in all cases the tensile strain in the extreme tensile bar is more than 0.005 which ensures a tension-controlled failure mechanism. This is in compliance with the ACI code.

For calculation of the wall capacities, sectional analysis is chosen using OpenSEES [45]. Both `concrete01` and `steel01` are used for simulation of concrete and steel in the OpenSEES analyses. The reason for choosing `cocnrete01` is because it is the closest model in OpenSEES to the ACI's compression concrete block.

The strength reduction factor, ϕ, is according to ACI 21.2.2 and since the strain in the steel in more than 0 .005 in./in., ϕ is 0.9. Spacing of longitudinal reinforcement and reinforcement detailing are according to ACI 11.7 and chapter 25.

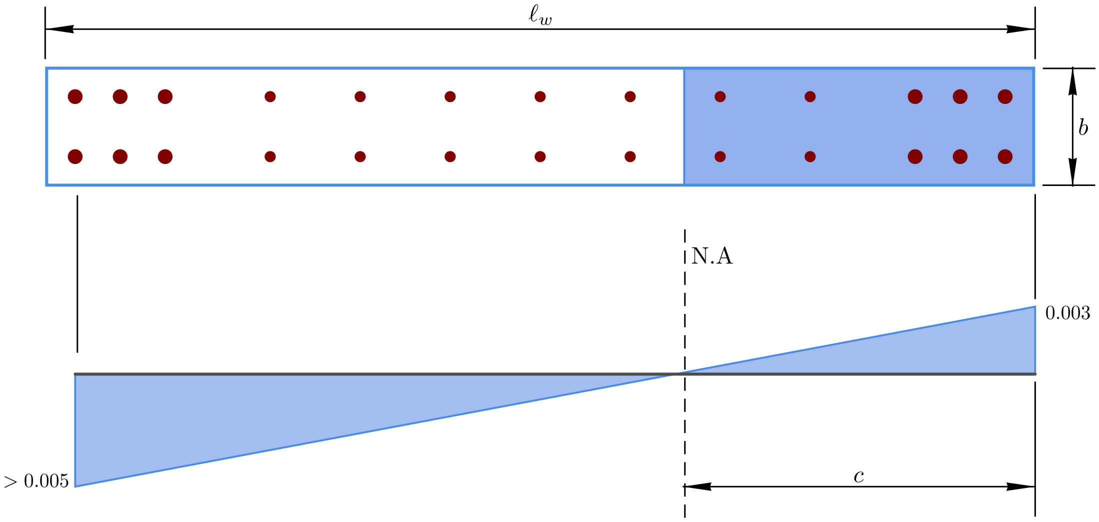

Figure C.2: Typical wall section and assumed strain distribution.

C.1.8 Design of Confining and Transverse Reinforcement

C.1.8.1 Design for shear

Shear design is in accordance to 18.10.2 and 18.10.4 of ACI 318–14. According to section 18.10.2.1, the minimum distributed web reinforcement ratio is 0.0025 for both vertical and transverse reinforcement. Almost in all the web regions of the walls, the demands are less than the minimum requirements, and a ratio of 0.0025 is provided for both ρ_ℓ and ρ_t. Except for the regions neighboring the openings in the wall where the demands increase due to non-continuity. The detailing of the reinforcement is according to ACI 11.7 and chapter 25.

C.1.8.2 Design of confining reinforcement

The transverse reinforcement in the boundary elements are designed in accordance with ACI 318–14, 18.10.6.4f following the detailing requirements of the ACI 11.7 and chapter 25.

C.1.9 Design of Wall Panel Zone

According to Moehle [48], *Panel Zone* is the region or element of a structural wall subjected to relatively uniform shear which can be with or without normal stresses. The forces from adjacent wall segments are resolved and as a result the nominal shear stress in the panel zone may be bigger than the ones in the adjacent wall segments. Moehle uses a useful solution by assuming no weights for the walls and equal dimensions ℓ_w as shown in Figure C.3. After assuming $T_2 = C_2$, and from horizontal equilibrium of the chord along **ab**, $T_2 = C_2 = v_1 \ell_h b_w / 2$. And from horizontal equilibrium of chords along **ef** and **ij**, $T_2 = C_2 = v_2 \ell_w b_w$. Both quantities should be equal and after rearranging it is found that:

$$v_2 = \frac{\ell_h}{2\ell_w} v_1$$

This relation indicates how different and bigger v_1 is relative to v_2. To find that, the vertical equilibrium of forces are taken in the vertical chords and that requires $T_1 = (v_1 + v_2) h_s b_w = \left(1 + {}^{\ell_h}\!/_{2\ell_w}\right) v_1 h_s b_w$. Hence, the shear stress in the panel zone can be found:

$$v_1 = \frac{1}{1 + {}^{\ell_h}\!/_{2\ell_w}} \left(\frac{T_1}{h_s b_w} \right)$$

The shear reinforcement above and below the punches, which resembles a panel zone, is designed both in accordance to the ACI code and using the method suggested by Moehle. In almost all the cases Moehle's method controls the design of shear reinforcement for the region above the punch. However, the depth of the panel zone, h_s, is extended whenever it would not meet the requirements of ACI code for shear strength (sec 18.10.4). Consequently, the amount of reinforcement in the chord is calculated by considering the moment induced by the couple from the two boundary elements on each side of the opening (tension and compression). In other words, the two horizontal chords above the opening, have the same or larger moment capacity as the ones from the boundary reinforcements on each side of the punch.

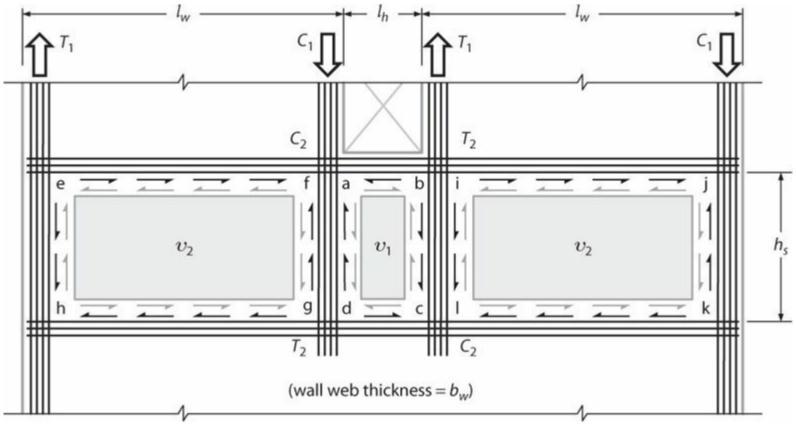

Figure C.3: Forces in the panel zone [48].

C.1.10 Design of Coupling Beam (ACI 18.7)

The coupling beams designed according to ACI code, section 18.7. Shear forces in the coupling beams were found using `Section Cut` in SAP2000. For each coupling beam, two groups of diagonally placed bars are used symmetric about the mid-span. ACI code requires transverse reinforcement to be provided for either diagonal bars or for the entire beam cross-section according to section 18.7.5.2 of the ACI code. For the current designs, transverse reinforcement is decided to be provided in the entire beam cross-section.

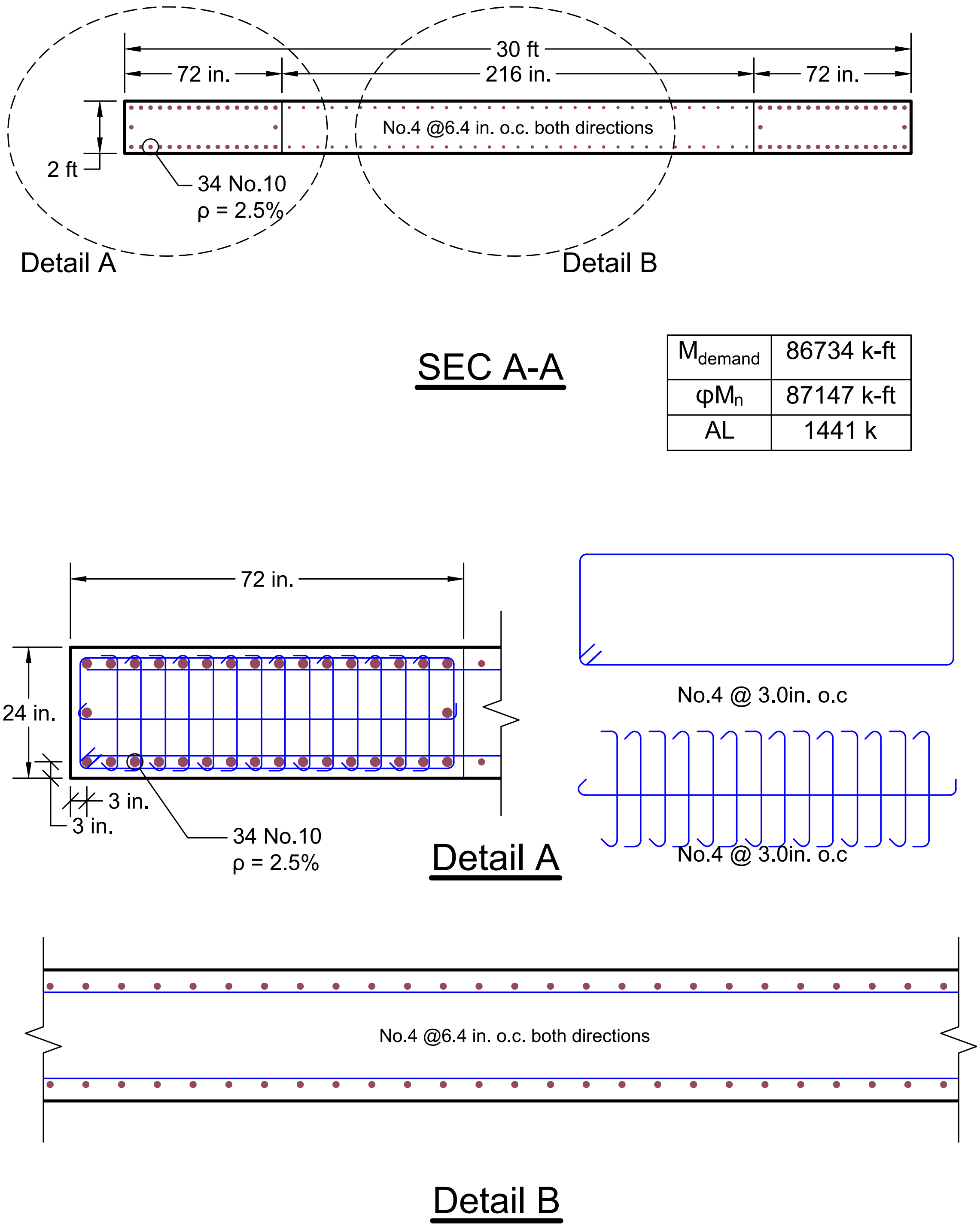

M_{demand}	86734 k-ft
φM_n	87147 k-ft
AL	1441 k

Figure C.4: Reinforcement configuration at the base for 8-story buildings designed for $D_{\max}$ spectrum.

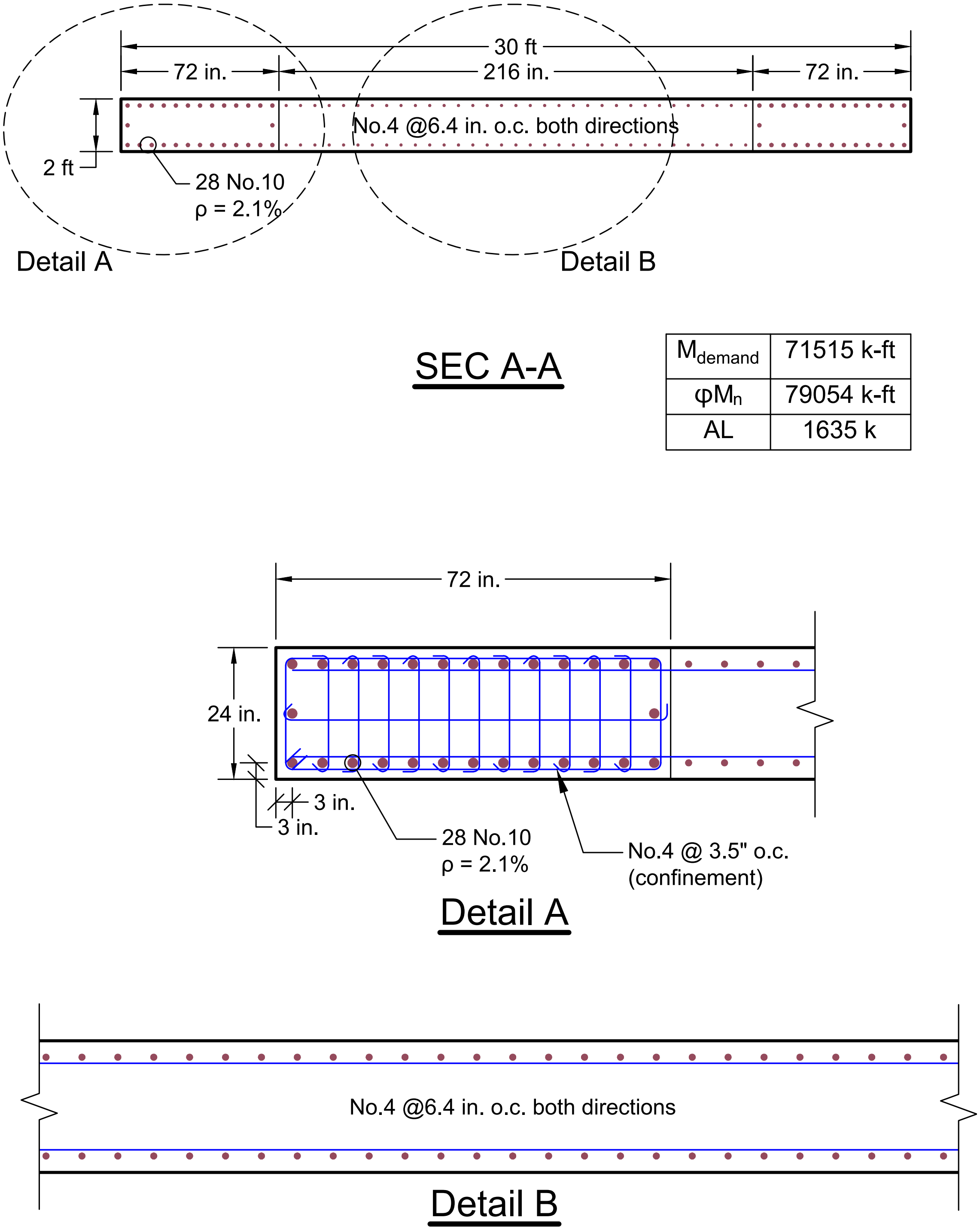

M_{demand}	71515 k-ft
φM_n	79054 k-ft
AL	1635 k

Figure C.5: Reinforcement configuration at the base for 12-story buildings designed for $D_{\max}$ spectrum.